

LASER SURFACE TEXTURING - FUNDAMENTAL  
STUDY AND APPLICATIONS

A THESIS  
SUBMITTED TO THE UNIVERSITY OF MANCHESTER  
FOR THE DEGREE OF  
DOCTOR OF PHILOSOPHY (PhD)  
IN THE FACULTY OF ENGINEERING AND PHYSICAL SCIENCES

2015

Tian Long See

SCHOOL OF MATERIAL SCIENCE, PROTECTION AND CORROSION CENTRE

# Contents

<b>Contents</b>	<b>1</b>
<b>List of Figures</b>	<b>6</b>
<b>List of Tables</b>	<b>17</b>
<b>List of Publications</b>	<b>20</b>
<b>Nomenclature</b>	<b>22</b>
<b>Abstract</b>	<b>26</b>
<b>Declaration</b>	<b>29</b>
<b>Copyright</b>	<b>30</b>
<b>Acknowledgements</b>	<b>31</b>
<b>1 INTRODUCTION</b>	<b>32</b>
1.1 Research Motivation - The Engineering Challenges . . . . .	32
1.2 Knowledge Gaps and Scientific Challenges . . . . .	34
1.3 Aim and Objectives . . . . .	36
1.4 Thesis Structure . . . . .	36
<b>2 LITERATURE REVIEW</b>	<b>39</b>
2.1 Introduction . . . . .	39
2.1.1 Lasers . . . . .	39
2.1.2 Characteristics of Laser Beams . . . . .	41

## CONTENTS

---

2.2	Laser Beam Interaction with Materials . . . . .	42
2.2.1	Electronic and Lattice Dynamics . . . . .	42
2.2.2	Laser Beam Absorption . . . . .	48
2.2.3	Ablation . . . . .	49
2.2.3.1	Influencing Factors in Laser Ablation . . . . .	50
2.2.4	Plasma . . . . .	60
2.2.5	Laser Induced Periodic Surface Structures . . . . .	61
2.3	Laser Surface Texturing . . . . .	63
2.3.1	Micro-Surface Texturing . . . . .	65
2.3.2	Laser Surface Cleaning . . . . .	69
2.4	Laser Surface Texturing Application . . . . .	74
2.4.1	Effect of Surface Properties on Adhesion . . . . .	74
2.4.1.1	Adhesion Theory . . . . .	75
2.4.1.2	Adhesion on CFRP . . . . .	80
2.4.1.3	Dust Adhesion on Polymer . . . . .	89
2.4.2	Surface Tribology . . . . .	97
2.4.2.1	Friction, Wear and Lubrication . . . . .	97
2.4.2.2	Improving Tool's Life Cycle . . . . .	105
2.4.2.3	Effect of Texturing Geometry on Wear . . . . .	109
2.5	Summary . . . . .	113
<b>3</b>	<b>MATERIALS AND EQUIPMENT</b>	<b>116</b>
3.1	Introduction . . . . .	116
3.2	Materials . . . . .	116
3.2.1	Carbon Fibre Reinforced Polymer Composite . . . . .	116
3.2.2	Epoxy resin . . . . .	117
3.2.3	Nickel Alloy . . . . .	118
3.2.4	Acrylonitrile Butadiene Styrene Polymer . . . . .	118
3.3	Equipment . . . . .	119
3.3.1	Laser Equipment . . . . .	119
3.3.1.1	Excimer Laser . . . . .	119
3.3.1.2	Femtosecond Laser . . . . .	121
3.3.2	Surface Characterisation Equipment . . . . .	123

3.3.2.1	Scanning Electron Microscope . . . . .	123
3.3.2.2	White Light Interferometer . . . . .	124
3.3.2.3	X-ray Photoelectron Spectroscope . . . . .	125
3.3.2.4	Microhardness Tester . . . . .	126
3.3.2.5	Optical Microscope . . . . .	126
<b>4</b>	<b>LASER BEAM INTERACTION WITH MATERIALS</b>	<b>128</b>
4.1	Introduction . . . . .	128
4.2	Experimental Procedures . . . . .	129
4.3	Results and Discussion . . . . .	131
4.3.1	Femtosecond Laser Beam Interaction with HR4 Nickel Alloy	131
4.3.1.1	Ablation Morphology . . . . .	131
4.3.1.2	Ablation Characteristic . . . . .	134
4.3.1.3	Comparison of Ablation Methods . . . . .	142
4.3.2	Excimer Laser Beam Interaction with CFRP . . . . .	145
4.3.2.1	Ablation Characteristics . . . . .	145
4.3.2.2	Surface Chemical Composition Analysis . . . . .	147
4.3.3	Excimer Laser and Femtosecond Laser Beam Interaction with ABS . . . . .	155
4.3.3.1	Ablation Morphology . . . . .	155
4.3.3.2	Ablation Characteristics . . . . .	159
4.3.3.3	Surface Chemical Composition Analysis . . . . .	163
4.3.3.4	Comparison of Ablation Characteristic . . . . .	169
4.4	Summary . . . . .	172
<b>5</b>	<b>LASER CLEANING AND ABRADING OF CFRP FOR IMPROVED PAINT ADHESION</b>	<b>175</b>
5.1	Introduction . . . . .	175
5.2	Methodology . . . . .	178
5.2.1	Material Preparation . . . . .	178
5.2.2	Surface Pre-treatment Methods . . . . .	178
5.2.2.1	Sand-paper Grinding Pre-treatment Method . . . . .	178
5.2.2.2	Laser Surface Pre-treatment Method . . . . .	179



## CONTENTS

---

5.2.3	Material Characterisation . . . . .	179
5.2.3.1	Paint Adhesion Tester . . . . .	179
5.3	Results and Discussion . . . . .	181
5.3.1	Basic Material Characterisation of the CFRP . . . . .	181
5.3.2	Investigation of Laser Surface Pre-treatment on Paint Ad- hesion Strength . . . . .	183
5.3.2.1	Morphological and Chemical Characteristics of the surface . . . . .	184
5.3.2.2	Wettability of the surface . . . . .	188
5.3.2.3	Paint Adhesion Performance . . . . .	190
5.3.3	Operating Window for Smooth CFRP Surface . . . . .	194
5.3.4	Operating Window for Rough CFRP Surface . . . . .	202
5.3.5	3D component cleaning . . . . .	205
5.4	Summary . . . . .	208
<b>6</b>	<b>LASER SURFACE TEXTURING OF NICKEL ALLOY AND TRIBOLOGY BEHAVIOUR</b>	<b>210</b>
6.1	Introduction . . . . .	210
6.2	Methodology . . . . .	213
6.2.1	Material Preparation . . . . .	213
6.2.2	Laser Surface Texturing . . . . .	213
6.2.3	Material Characterisation . . . . .	214
6.2.4	Friction and Wear Test . . . . .	214
6.2.5	Characteristic of Dimple . . . . .	216
6.2.6	Wear Characteristics . . . . .	218
6.2.6.1	In the Dry Environment (No Lubrication) at Room Temperature . . . . .	218
6.2.6.2	In the Oil Lubricated Environment at Room Tem- perature . . . . .	219
6.3	Summary . . . . .	225
<b>7</b>	<b>LASER SURFACE TEXTURING OF ABS AND DUST ADHE- SION BEHAVIOUR</b>	<b>227</b>

## CONTENTS

---

7.1	Introduction . . . . .	227
7.1.1	Factors Causing Dust Adhesion . . . . .	229
7.2	Methodology . . . . .	232
7.2.1	Material Preparation . . . . .	232
7.2.2	Laser Surface . . . . .	233
7.2.2.1	Surface Energy Modification . . . . .	233
7.2.2.2	Surface Texturing Modification . . . . .	233
7.2.3	Material Characterisation . . . . .	234
7.2.4	Dust Adhesion Test . . . . .	234
7.3	Results and Discussion . . . . .	236
7.3.1	Surface Morphology of the Textured Surface . . . . .	236
7.3.1.1	Surface Energy Modification . . . . .	236
7.3.1.2	Surface Texturing . . . . .	237
7.3.2	Particle Charge Property . . . . .	239
7.3.3	Dust Adhesion Test . . . . .	241
7.4	Summary . . . . .	246
8	<b>Conclusions</b>	<b>247</b>
9	<b>Future Work</b>	<b>252</b>
9.1	Laser Beam Interaction with Materials . . . . .	252
9.2	Paint Adhesion Improvement by Laser Surface Processing . . . . .	253
9.3	Tribology Performance Improvement by Laser Surface Texturing . . . . .	253
9.4	Dust Adhesion Control with Laser Surface Texturing . . . . .	254
	<b>References</b>	<b>255</b>

**Final word count:** 59487

# List of Figures

1.1	Illustration of the thesis structure . . . . .	37
2.1	Electronic and lattice temperature profiles (simulations obtained with the TTM) in copper irradiated by laser pulses of different durations (ranging from 50 <i>fs</i> to 500 <i>ps</i> ). With 50 <i>fs</i> pulses, electrons and lattice are completely decoupled and the lattice is substantially unaffected by the laser beam. With 500 <i>ps</i> pulses, electron and lattice follow almost identical temperature evolutions [16]. . . . .	47
2.2	Material removal mechanisms using laser beam [24]. . . . .	53
2.3	Illustration of laser beam frequency. . . . .	54
2.4	Ablation thresholds versus number of pulses for nickel-based superalloy C263 [27]. . . . .	54
2.5	Damage fluence versus pulse number curves for the different crystallographic orientations of chemically polished Cu surfaces [28]. .	55
2.6	Plot summarizing the data on short-pulse laser ablation of Ni, Cu, Mo, In, W, Au metals . [33] . . . . .	57
2.7	Ablation depth per pulse for copper versus the incident laser fluence for 150 <i>fs</i> laser pulses [35]. . . . .	58
2.8	Illustration of the occurrence of physical process when a material surface is radiated by a high power laser beam [69]. . . . .	61
2.9	SEM images of the diamond surface after irradiated with a 1000 number of pulse at a rate of 250 <i>kHz</i> with a pulse energy of (a) 120 <i>nJ</i> (b) 72 <i>nJ</i> and is processed sequentially using two scanning direction at 0° (bold arrow) and 300° (dotted arrow) [73]. . . . .	62

## LIST OF FIGURES

---

2.10 SHIM image (a) after 10 scans at 800 $mm/s$ with fluence of 13 $mJ/cm^2$ . (b) of coarse ripples with clustered particles with fluence of 4.1 $J/cm^2$ [74]. . . . .	63
2.11 SEM image of: (a) laser treated surface showing the formation of micro/nano structures after exposing Ti surface with approx- imately 500 laser shots at fluence 1.2 $J/cm^2$ . Inset is the pho- tograph of a control (gray colour) and micro-structured titanium piece (black in colour), (b)laser-irradiated spot after being exposed with approximately 2000 shots showing the self-organized forma- tion of micro/nanostructures, (c)cross-section of an individual con- ical microstructure and (d) nanoscale ripples formed on the conical microstructures [80]. . . . .	64
2.12 Classification of laser surface texturing. . . . .	65
2.13 3-dimensional topography measurement /profile of a single texture element [81]. . . . .	66
2.14 Optical images of pores on the disk surface produced by laser tex- turing. The pores with diameter of (a) 100 $\mu m$ ; (b) 150 $\mu m$ ; (c) 200 $\mu m$ [83]. . . . .	66
2.15 Profiles of the pore of diameter 150 $\mu m$ and the heat affected zone: (a) at the pore centre, and (b) at the heat affected zone [83]. . . .	67
2.16 (a) “Satisfactory” micro-hole, induced with pulse energy of 40 $mJ$ and a $1/e^2$ beam radius of 5 $mm$ . (b) Structure induced on a steel surface [85]. . . . .	67
2.17 Left: Damage on cemented tungsten carbide induced with one laser pulse of 54 (a), 35 (b), 12 (c) and 4.4 $\mu J$ (d). Right: Craters on diamond after 10 (a), 50 (b), 250 (c) and 1000 (d) pulses (150 $fs$ , 54 $\mu J$ ) [88]. . . . .	68
2.18 Crater in WC-Co produced with 10000 pulses (6.5 $J/cm^2$ ) using a Ti:Sapphire femtosecond laser of 100 $fs$ pulse width and 800 $nm$ wavelength [87]. . . . .	68

## LIST OF FIGURES

---

2.19	Surface profilometry and average roughness of glass/epoxy surfaces treated with different excimer laser beams conditions: (a) $150 \text{ mJ/cm}^2$ , 40 <i>NOP</i> ( $S_a$ $0.6 \text{ }\mu\text{m}$ ). (b) $150 \text{ mJ/cm}^2$ , 400 <i>NOP</i> ( $S_a$ $13.1 \text{ }\mu\text{m}$ ). (c) $500 \text{ mJ/cm}^2$ , 500 <i>NOP</i> ( $S_a$ $17.2 \text{ }\mu\text{m}$ ) [91]. . . .	70
2.20	SEM images of PEEK composite surface after treatment at various parameters (a) un-treated. (b) SiC-abraded. (c) laser-treated: $0.18 \text{ J/cm}^2$ , 50 <i>NOP</i> , (d) $0.18 \text{ J/cm}^2$ , 100 <i>NOP</i> , (e) $1 \text{ J/cm}^2$ , 10 <i>NOP</i> , (f) $6 \text{ J/cm}^2$ , 10 <i>NOP</i> using a ArF excimer laser of $193 \text{ nm}$ wavelength [89]. . . . .	72
2.21	Depths of matrix ablation, (a) as a function of the number of pulses, fluence - $1.01 \text{ J/cm}^2$ , pulse frequency - $5 \text{ Hz}$ and (b) fluence, number of pulses - 50, pulse frequency - $5 \text{ Hz}$ , showing linear relationship [92]. . . . .	73
2.22	Classification of fundamental theories related to adhesion theory. .	75
2.23	Interaction between PMMA surface and surfaces of different acidic and basic nature (After Leadley and Watts, 1997). <sup>a</sup> indicating hydrolysis of the ester and adsorption through the carboxylate anion [103; 104]. . . . .	77
2.24	Schematic representation of a local environment for an atom in the bulk of a material (B), on a plane surface (S), and on an asperity on a rough surface (A) [103]. . . . .	78
2.25	Illustration of an electric double layer formation. . . . .	79
2.26	Model of polymer film in which cross-linking of the surface has occurred. Highlighted is a cross-link tracer chain [113]. . . . .	81
2.27	SEM images of the surface before and after surface pre-treatment [94]. . . . .	84
2.28	Contact angle of water droplet on (a) un-treated and (b) plasma treated polyolefin samples [124]. . . . .	85
2.29	SEM images of (a) peel ply treated carbon/epoxy composite and (b) alumina grit blasted carbon epoxy composite [93]. . . . .	86
2.30	Possible particle geometries and surfaces for: (a,b) Real system. (c,d,e) Idealised models [133]. . . . .	90

## LIST OF FIGURES

---

2.31	Diagram illustrating the force interaction to a particle when adhere on a surface. . . . .	91
2.32	Illustration of capillary condensation effect between a spherical particle and a flat surface [133]. . . . .	93
2.33	Geometry illustration of forces interaction of a spherical particle adheres on a smooth surface. . . . .	94
2.34	(a) Contact between two mating surfaces, (b) adhesion between contacting asperities, (c) ploughing of softer surface by an asperity of harder surface, (d) ploughing by foreign particle entrapped between moving surfaces and (e) slip line deformation model of friction [146]. . . . .	98
2.35	Illustration of the typical event of an erosive wear process [146]. .	103
2.36	Pressure distribution of the lubricant film under hydrodynamic lubrication region [146]. . . . .	104
2.37	Stribeck curve that shows the relation between friction coefficient with the lubrication parameter [146]. . . . .	105
2.38	Laser Surface texturing of regular micro-surface structure in the form of micro-dimples with diameter of 100 $\mu m$ , depth of 10 $\mu m$ and dimple density of 20 % [161]. . . . .	108
2.39	Surface texture of different shapes: (a) circle, (b) ellipse, (c) triangle [175]. . . . .	111
2.40	Dimensionless pressure distribution of different textural shapes and orientations. (a) Circle, (b) Triangle $\Delta \uparrow$ , (c) Triangle $\Delta \downarrow$ , (d) Ellipse//, (e) Ellipse $\perp$ [174]. . . . .	112
3.1	Optical images of surface view of (a) smooth surface and (b) rough surface of the CFRP. . . . .	117
3.2	Image of the excimer laser layout. . . . .	120
3.3	Schematic diagram of the femtosecond laser layout (M1, M2, M3, M4, M5, M6: mirror). . . . .	122
3.4	Image of the femtosecond laser layout. . . . .	122
3.5	Schematic diagram of SEM setup [177]. . . . .	123
3.6	Schematic diagram of white light interferometer setup [178]. . . .	124

## LIST OF FIGURES

---

4.1	Optical images of the craters produced at (a) $9.55 \text{ J/cm}^2$ , 10 <i>NOP</i> , (b) $10.61 \text{ J/cm}^2$ , 30 <i>NOP</i> , (c) $15.21 \text{ J/cm}^2$ , 100 <i>NOP</i> and (d) $31.12 \text{ J/cm}^2$ , 200 <i>NOP</i> . . . . .	132
4.2	Schematic diagram illustrating the correlation between the Gaussian spatial distributions of the laser fluence with the resultant ablation morphology region. . . . .	133
4.3	Plot of ablation depth versus <i>NOP</i> for different laser fluence. . . .	134
4.4	Plot of $D^2$ versus $\ln(E_p)$ for different <i>NOP</i> on femtosecond laser spot ablation on nickel alloy. . . . .	136
4.5	Plot of $D^2$ versus logarithmic of peak laser fluence from which the ablation threshold for different <i>NOP</i> were determined for femtosecond laser spot ablation on nickel alloy. . . . .	136
4.6	Plot of (a) ablation threshold versus <i>NOP</i> and (b) $\log(N * F_{th}^N)$ versus $\log(N)$ for femtosecond laser spot ablation on nickel alloy using diameter measurement. . . . .	137
4.7	Plot of laser fluence in logarithmic scale versus ablation depth per pulse at a frequency of 1 <i>kHz</i> for femtosecond laser ( $\lambda = 800 \text{ nm}$ , <i>pulse width</i> = 100 <i>fs</i> ) spot ablation on nickel alloy using depth measurement. . . . .	138
4.8	Plot of (a) ablation threshold versus <i>NOP</i> and (b) $\log(N * F_{th}^N)$ versus $\log(N)$ for femtosecond laser spot ablation on nickel alloy using depth measurement. . . . .	140
4.9	Plot of $D^2$ versus logarithmic of peak laser fluence from which the ablation threshold for different <i>NOP</i> were determined for femtosecond laser ( $\lambda = 800 \text{ nm}$ , <i>pulse width</i> = 100 <i>fs</i> ) line ablation on nickel alloy. . . . .	141
4.10	Plot of (a) ablation threshold versus <i>NOP</i> and (b) $\log(N * F_{th}^N)$ versus $\log(N)$ for femtosecond laser line ablation on nickel alloy using diameter measurement. . . . .	142
4.11	Plot of laser fluence in logarithmic scale versus ablation depth per pulse at a frequency of 1 <i>kHz</i> for femtosecond laser line ablation on nickel alloy using depth measurement. . . . .	143

## LIST OF FIGURES

---

4.12	Plot of (a) ablation threshold versus NOP and (b) $\log(N * F_{th}^N)$ versus $\log(N)$ for femtosecond laser line ablation on nickel alloy using depth measurement. . . . .	143
4.13	Optical images of square crater produced by excimer laser on epoxy using $1.5 J/cm^2$ laser fluence, (a)100 NOP and (b)200 NOP. . . .	146
4.14	Plot of laser fluence in logarithmic scale versus ablation depth per pulse with excimer laser at a frequency of 10 <i>Hz</i> for epoxy resin. .	147
4.15	Plot of (a) ablation threshold versus NOP and (b) $\log(N * F_{th}^N)$ versus $\log(N)$ for epoxy resin using depth measurement. . . . .	148
4.16	Wide scan XPS spectrum for (a) as received smooth and rough CFRP surface and (b) different excimer laser surface treatment conditions for the smooth CFRP surface. . . . .	149
4.17	High resolution carbon scan XPS spectrum for excimer laser treated (a) smooth CFRP with $90 mJ/cm^2$ , 3 <i>NOP</i> and (b) rough CFRP with $50 mJ/cm^2$ , 20 <i>NOP</i> . . . . .	150
4.18	Illustration of (a) multi-photon ionisation mechanism and (b) cascade ionization mechanism [225]. . . . .	154
4.19	Optical images of the ablated region produced at (a) $0.05 J/cm^2$ , (b) $0.4 J/cm^2$ , (c) $0.8 J/cm^2$ and (d) $1.5 J/cm^2$ at 100 <i>NOP</i> using excimer laser ( $\lambda = 248 nm$ , <i>pulse width</i> = 15 <i>ns</i> ). . . . .	157
4.20	SEM images of the (a) ablation region produced at $0.05 J/cm^2$ , 100 <i>NOP</i> using excimer laser ( $\lambda = 248 nm$ , <i>pulse width</i> = 15 <i>ns</i> ) and (b) un-treated ABS surface. . . . .	157
4.21	SEM images of the craters produced at (a) $4.1 J/cm^2$ , 1 <i>NOP</i> , (b) $19.45 J/cm^2$ , 10 <i>NOP</i> , (c) $4.1 J/cm^2$ , 50 <i>NOP</i> and (d) $19.45 J/cm^2$ , 100 <i>NOP</i> using femtosecond laser ( $\lambda = 800 nm$ , <i>pulse width</i> = 100 <i>fs</i> ). . . . .	158
4.22	3D optical microscope image with ablated crater profile produced at $4.1 J/cm^2$ , 50 <i>NOP</i> using femtosecond laser. . . . .	158
4.23	Plot of laser fluence in logarithmic scale versus ablation depth per pulse at a frequency of 10 <i>Hz</i> for ABS polymer using excimer laser.	159



## LIST OF FIGURES

---

4.24	Plot of $D^2$ versus logarithmic of peak laser fluence from which the ablation threshold for different NOP were determined for spot ablation on ABS using femtosecond laser. . . . .	160
4.25	Plot of (a) ablation threshold versus NOP and (b) $\log(N * F_{th}^N)$ versus $\log(N)$ for femtosecond laser spot ablation on ABS polymer using diameter measurement. . . . .	161
4.26	Plot of laser fluence in logarithmic scale versus ablation depth per pulse with a femtosecond laser ( $\lambda = 800 \text{ nm}$ , <i>pulse width</i> = $100 \text{ fs}$ ) at a frequency of $1 \text{ kHz}$ for ABS using depth measurement.	162
4.27	High resolution carbon scan XPS spectrum for (a) non-treated ABS and (b) excimer laser ( $\lambda = 248 \text{ nm}$ , <i>pulse width</i> = $15 \text{ ns}$ ) treated ABS with $200 \text{ mJ/cm}^2$ , $50 \text{ NOP}$ . . . . .	163
4.28	High resolution carbon scan XPS spectrum for (a) non-treated ABS and (b) femtosecond laser ( $\lambda = 800 \text{ nm}$ , <i>pulse width</i> = $100 \text{ fs}$ ) treated ABS with $7.43 \text{ J/cm}^2$ , $8 \text{ NOP}$ . . . . .	164
5.1	Illustration of the mask projection technique using a “hole array” mask. . . . .	179
5.2	PosiTest AT-M Manual model [244] . . . . .	180
5.3	Pull-off test used for evaluating the adhesion of primer coating on CFRP. . . . .	181
5.4	Optical microscope images of cross section showing polymeric layer thickness for (a) smooth surface and (b) rough surface of CFRP. .	182
5.5	Optical images of the CFRP cross section showing the fibre diameter used in the composite. . . . .	182
5.6	3D optical profile of CFRC showing the thickness of the total polymer layer above the fibres around $10 \text{ }\mu\text{m}$ . . . . .	183
5.7	Illustration of the hole-array mask used in the experiment. . . . .	184
5.8	Surface morphology of the CFRP smooth surface before and after various treatments. (a) as-received, (b) sand-papered, (c) excimer laser treated with $50 \text{ mJ/cm}^2$ , $20 \text{ NOP}$ and (d) excimer laser treated with $250 \text{ mJ/cm}^2$ , $20 \text{ NOP}$ . . . . .	185

## LIST OF FIGURES

---

5.9	Surface morphology of the CFRP rough surface before and after various treatments. (a) as-received, (b) sand-papered, (c) excimer laser treated with $75 \text{ mJ/cm}^2$ , 6 NOP and (d) excimer laser treated with $175 \text{ mJ/cm}^2$ , 3 NOP. . . . .	186
5.10	Surface roughness for excimer laser treated and sand-papered CFRP surface in comparison with the as-received CFRP surface on (a) smooth surface and (b) rough surface. . . . .	186
5.11	Contact angle for excimer laser treated and sand-papered CFRP surfaces in comparison with the as-received CFRP surface on (a) smooth surface and (b) rough surface. . . . .	189
5.12	Top surface view of the composite after paint adhesion test. (a) smooth surface and (b) rough surface of the CFRP. . . . .	191
5.13	Paint adhesion improvement after excimer laser treatment in comparison with the sand-papered surface for (a) smooth surface and (b) rough surface of the CFRP. . . . .	192
5.14	3D optical profiles of the surface after excimer laser ( $\lambda = 248 \text{ nm}$ , $\text{pulse width} = 15 \text{ ns}$ ) cleaning at laser fluence of $200 \text{ mJ/cm}^2$ and NOP of (a) 10 (b) 20 (c) 40 (d) 100 and (e) 200. . . . .	196
5.15	Variation of removal depth with different laser pre-treatment parameters. . . . .	197
5.16	Optical images of the surface after excimer laser ( $\lambda = 248 \text{ nm}$ , $\text{pulse width} = 15 \text{ ns}$ ) cleaning at laser fluence of (a) $25 \text{ mJ/cm}^2$ , 100 NOP (No damage), (b) $50 \text{ mJ/cm}^2$ , 200 NOP (Threshold) and (c) $200 \text{ mJ/cm}^2$ , 200 NOP (Fibre exposed). . . . .	198
5.17	Operating window diagram for the smooth CFRP surface using hole-array mask. . . . .	199
5.18	Bar plot of adhesion strength increment vs different mask used at fluence of $100 \text{ mJ/cm}^2$ and 7 NOP for the smooth CFRP surface. . . . .	200
5.19	Illustration of the hybrid mask concept. . . . .	201
5.20	Dimension of the hybrid mask. . . . .	201
5.21	Bar plot of adhesion strength increment vs different laser parameters using the hybrid mask for the smooth CFRP surface. . . . .	202
5.22	Illustration of the square mask used in the experiment. . . . .	202

## LIST OF FIGURES

---

5.23	3D optical profiles of the surfaces with excimer laser ( $\lambda = 248\text{ nm}$ , pulse width = 15 ns) cleaning parameter (a) 50 $\text{mJ}/\text{cm}^2$ and 20 NOP (b) 100 $\text{mJ}/\text{cm}^2$ and 50 NOP, (c) 200 $\text{mJ}/\text{cm}^2$ and 100 NOP, (d) 400 $\text{mJ}/\text{cm}^2$ and 100 NOP. . . . .	203
5.24	3D optical profile of the laser cleaned surface with 200 $\text{mJ}/\text{cm}^2$ and 100 NOP with different magnifications. . . . .	203
5.25	Operating window diagram for the rough CFRP surface using a square mask. . . . .	204
5.26	Schematic diagram illustrating the measured beam angle relative to the sample. . . . .	205
5.27	Plot of adhesion strength increment vs plane angle relative to the laser beam. . . . .	206
5.28	(a) 3D component of the CFRP used for testing. (b) Hybrid mask used in the 3D component testing experiment. . . . .	207
5.29	Excimer laser layout used for the pre-treatment of the 3D CFRP component. . . . .	207
5.30	(a) Surface labeling of the 3D component used. (b) Bar plot of adhesion strength increment vs different 3D component surface with the fluence of 175 $\text{mJ}/\text{cm}^2$ and 3 NOP for the smooth CFRP surface. . . . .	208
6.1	Schematic of a single-sided SPF tool shown (a) before and (b) after gas pressure forming [250]. . . . .	211
6.2	POD-2 pin on disc wear tester [255]. . . . .	215
6.3	Schematic illustration of the parameters used in wear rate and wear volume calculation. . . . .	216
6.4	(a) SEM image of a dimple taken at 45° incline plane and (b) optical white light interferometer profile of the dimples produced at 4.2 $\text{J}/\text{cm}^2$ fluence and 15 NOP. . . . .	217
6.5	(a) The wear rate and (b) average steady state friction coefficient of textured surfaces with different dimple area ratio of depth 2.5 $\mu\text{m}$ under dry environment and room temperature condition. . . . .	218

## LIST OF FIGURES

---

6.6	SEM images of the grinded nickel alloy surface (a) before wear test and (b) after wear test. . . . .	220
6.7	(a) Plot of friction coefficient respond with sliding speed of $0.0042\text{ m/s}$ and (b) Peak to peak friction coefficient difference with different sliding speed for un-textured nickel surface in oil lubrication environment under the pressure of $5.66\text{ MPa}$ . . . . .	221
6.8	Plot of friction coefficient versus sliding speed under different contact pressure in oil lubrication environment. . . . .	222
6.9	Plot of friction coefficient versus sliding speed for textured (20 % dimple area ratio with $2.5\text{ }\mu\text{m}$ depth) and un-textured nickel surface in oil lubrication environment. . . . .	223
6.10	(a) The wear rate and (b) average steady state friction coefficient of textured surfaces with different dimple area ratio of depth $2.5\text{ }\mu\text{m}$ under oil lubricated condition. . . . .	223
6.11	(a) The wear rate and (b) average steady state friction coefficient of textured surfaces with different dimple depth of 20 % dimple area ratio under oil lubricated environment. . . . .	224
7.1	Illustration of the air flow in the separation system of Dyson DC37 bagless vacuum cleaner. . . . .	228
7.2	Separation system components of the of Dyson DC37 bagless vacuum cleaner. . . . .	229
7.3	Removal mechanisms involved in a particle adhesion system. . . . .	231
7.4	Factors influencing dust particle adhesion on a surface. . . . .	231
7.5	Aerodynamic particle size distribution plot for Thistle multi-finish plaster measured using APS. . . . .	232
7.6	Patterns used for ABS surface texturing. . . . .	234
7.7	Schematic diagram of the dust adhesion test rig used in the experiment. . . . .	235
7.8	The Sartorius 2024MP digital weighing machine manufactured by Data Weighing Systems Inc. . . . .	235

7.9	Optical white light interferometer contour plot illustrating surface morphology of different excimer laser ( $\lambda = 248 \text{ nm}$ , $\text{pulse width} = 15 \text{ ns}$ ) surface treatment conditions: (a) as-received, (b) $50 \text{ mJ/cm}^2$ , $10 \text{ NOP}$ , (c) $200 \text{ mJ/cm}^2$ , $10 \text{ NOP}$ and (d) $400 \text{ mJ/cm}^2$ , $50 \text{ NOP}$ for ABS surface. . . . .	236
7.10	Surface roughness plot for different excimer laser surface treatment conditions for ABS surface. . . . .	237
7.11	Optical white light interferometer surface morphology profile for femtosecond laser textured ABS with (a) circular pattern with separation distance of $100 \text{ }\mu\text{m}$ (needle shape) and (b) $200 \text{ }\mu\text{m}$ (dimple shape), (c) hatch pattern with separation distance of $100 \text{ }\mu\text{m}$ (fin shape) and (d) $200 \text{ }\mu\text{m}$ (hatch shape) and (e) line pattern with separation distance of $200 \text{ }\mu\text{m}$ (line shape). . . . .	238
7.12	Surface roughness plot for different femtosecond laser surface texturing conditions for ABS polymer. . . . .	239
7.13	SEM image of the dust particles used in the experiment. . . . .	240
7.14	Calibration plot for (a) capacitor of $10 \text{ nF}$ with varying voltage. (b) Capacitor of different capacitance charged with a constant $5 \text{ V}$ supply. . . . .	240
7.15	Plot of particle charge accumulation versus time. . . . .	241
7.16	Dust adhesion performance for different excimer laser ( $\lambda = 248 \text{ nm}$ , $\text{pulse width} = 15 \text{ ns}$ ) surface treatment conditions under air flow dust test. . . . .	242
7.17	Dust adhesion performance for different femtosecond laser ( $\lambda = 800 \text{ nm}$ , $\text{pulse width} = 100 \text{ fs}$ ) surface texturing conditions under air flow dust test. . . . .	244
7.18	SEM images of (a) dimple and (b) hatch texture on ABS after dust adhesion test. . . . .	245
7.19	SEM images of line pattern at an angle of (a) $45^\circ$ and (b) $0^\circ$ . . . .	245

# List of Tables

2.1	Common industrial lasers with their wavelength range and photon energy [21]. . . . .	51
2.2	Chemical composition (%) of epoxy matrix surface treated with KrF excimer laser of wavelength 248 nm and pulse width of 30 ns determined with ESCA analysis [91]. . . . .	70
2.3	Classification of secondary forces [103]. . . . .	76
2.4	Surface pre-treatment methods. . . . .	82
2.5	Typical primary pigments used in paint [130]. . . . .	88
2.6	Examples of low molecular weight and high molecular weight binders used in paint [130]. . . . .	89
2.7	Typical lubricant film properties in a machine element application [146]. . . . .	106
3.1	Elemental composition of the HR4 nickel alloy (weight %). . . . .	118
3.2	Range of wavelength for excimer laser with different gas mixtures [2]. . . . .	120
4.1	Excimer laser surface treatment parameters for CFRP. . . . .	130
4.2	Excimer laser surface treatment parameters for ABS polymer. . . . .	130
4.3	Femtosecond laser surface treatment parameters for ABS polymer. . . . .	131
4.4	Summary of ablation characteristics obtained using different geometry measurements for nickel alloy. . . . .	144
4.5	Elemental composition of the CFRP surface measured by XPS before and after various excimer laser treatment conditions. . . . .	148

## LIST OF TABLES

---

4.6	XPS chemical shifts of carbon 1s electrons for carbon-nitrogen and carbon-oxygen functional group and the relevant binding energy published [205; 207; 208; 209; 210; 211]. . . . .	151
4.7	Surface chemical composition changes of the CFRP surface measured by XPS carbon high resolution scan before and after various excimer laser treatment conditions. . . . .	151
4.8	Surface chemical composition changes of the CFRP surface measured by XPS oxygen and nitrogen high resolution scan before and after various excimer laser treatment conditions. . . . .	152
4.9	Elemental composition of the ABS surface measured by XPS before and after various excimer laser treatment conditions. . . . .	165
4.10	Elemental composition of the ABS surface measured by XPS before and after various femtosecond laser treatment conditions. . . . .	166
4.11	Surface chemical composition changes of the ABS surface measured by XPS carbon high resolution scan before and after various excimer laser treatment conditions. . . . .	167
4.12	Surface chemical composition changes of the ABS surface measured by XPS carbon high resolution scan before and after various femtosecond laser treatment conditions. . . . .	168
4.13	Surface chemical composition changes of the ABS surface measured by XPS oxygen and nitrogen high resolution scan before and after various excimer laser treatment conditions. . . . .	168
4.14	Surface chemical composition changes of the ABS surface measured by XPS oxygen and nitrogen high resolution scan before and after various femtosecond laser treatment conditions. . . . .	169
4.15	Summary of ablation characteristics obtained using different geometry measurement for ABS polymer. . . . .	170
5.1	Chemical composition (%) of CFRP surface [127]. . . . .	176
5.2	Roughness and surface free energy of bare composite surfaces [127].	176
5.3	Laser parameters used for CFRP surface pre-treatment experiment.	184
5.4	Elemental composition of the CFRP surface measured by XPS after abrasion by sand paper. . . . .	187

## LIST OF TABLES

---

5.5	Surface chemical composition changes of the CFRP surface measured by XPS carbon high resolution scan after abrasion using sand paper. . . . .	187
5.6	Surface chemical composition changes of the CFRP surface measured by XPS oxygen and nitrogen high resolution scan after abrasion using sand paper. . . . .	187
5.7	Solid-liquid and liquid-liquid interaction strength of different contact angle values [248]. . . . .	194
5.8	Observation of the smooth CFRP surfaces after laser pre-treatment using different laser parameters. . . . .	195
5.9	Observation of the rough CFRP surfaces after laser pre-treatment using different laser parameters. . . . .	204
6.1	Laser parameters used to produce the dimples. . . . .	214
6.2	Spacing between dimples for different dimple area ratio. . . . .	217
7.1	Summary of the feature height for different ABS textured surfaces.	237



# List of Publications

1. T.L. See, Z. Liu, S. Cheetham, S. Dilworth and L. Li, Laser abrading of carbon fibre reinforced composite for improving paint adhesion, *Appl. Phys. A* 117 (3) (2014), pp. 1045-1054
2. T.L. See, Z. Liu, H. Liu, L. Li, J. Chippendale, S. Cheetham, S. Dilworth, Effect of geometry measurement on characteristics of femtosecond laser ablation of HR4 nickel alloy, *Opt. Lasers Eng.* 64 (2015), pp. 71-78.
3. Y.Z. Yan, L. Li, T.L. See, L.F. Ji and Y.J. Jiang, CO2 laser peeling of Al<sub>2</sub>O<sub>3</sub> ceramic and an application for the polishing of laser cut surfaces, *Journal of the European Ceramic Society* 33 (2013), pp. 1893-1905
4. T.L. See, Z. Liu, L. Li, Short pulsed laser interaction with aerospace materials and its applications, School of Materials PGR conference, 2012, Manchester, UK.
5. T.L. See, Z. Liu, Excimer laser surface modification of carbon fibre composite for improvement of paint adhesion, School of Materials PGR conference, 2013, Manchester, UK. (Poster)
6. A. Mhich, T.L. See, P. Mbata, N. Edeh, A. Lemnifi, Daishu Qian, Z. Liu, L. Li, P. Mativenga, S. Cheetham and S. Dilworth, Excimer laser surface modification for improvement of paint adhesion, Industrial Laser Applications Symposium, ILAS, 2013, Nottingham, UK.
7. T.L. See, Z. Liu, S. Cheetham, S. Dilworth and L. Li, Laser surface cleaning and abrading/ texturing of carbon fibre reinforced composite for improving paint adhesion, MACE PGR Conference, 2014, Manchester, UK.

8. T.L. See, Z. Liu, S. Cheetham, S. Dilworth and L. Li, Laser surface cleaning and abrading/ texturing of carbon fibre reinforced composite for improving paint adhesion, School of Materials PGR conference, 2014, Manchester, UK.

# Nomenclature

Symbol	Nomenclature	Units
$N$	Conduction electron density	electrons per cubic bohr
$e$	Electronic charge	$nC$
$m$	Electron mass	$kg$
$\tau_{ee}$	Lifetime of excited electron	$s$
$\varepsilon_F$	Fermi energy	$eV$
$T_e$	Electron temperature	$K$
$T_L$	Lattice temperature	$K$
$\tau_{ep}$	Electron-phonon coupling time	$s$
$C_e$	Electronic specific heat	$J/m^3K$
$C_L$	Lattice specific heat	$J/m^3K$
$\lambda_p$	Coupling constant	—
$\omega_D$	Debye frequency of the irradiated solid	$Hz$
$S(t)$	Absorbed laser power per unit volume	$W/m^3$
$H(T_e, T_L)$	The rate of energy transfer between electrons and lattice	$W/m^3$
$I$	Laser intensity	$W/m^2$
$s$	Cross section of single-photon process	$m^2$
$\tau_D$	Mean time between two electronic collisions	$s$
$\varepsilon_o$	Dielectric constant	—

Symbol	Nomenclature	Units
$\omega_p$	Plasma frequency	$Hz$
$\sigma$	Conductivity	$S/m$
$R_o$	Reflectivity	—
$\kappa$	Extinction coefficient	—
$n$	Refractive index	—
$\rho$	Electrical resistivity, $\Omega m$	
$E$	Energy	$m^2kg/s^2$
$h$	Planck Constant	$Js$
$c$	Speed of light	$m/s$
$\lambda$	Wavelength	$m$
$L$	Ablation depth per pulse	$\mu m$
$\alpha^{-1}$	Optical penetration depth	$cm^{-1}$
$F$	Laser fluence	$mJ/cm^2$
$F_{th}$	Laser fluence threshold	$mJ/cm^2$
$F_n$	Laser fluence	$mJ/cm^2$
$\eta$	Quantum yield for chain scission	—
$R$	Surface reflection loss	—
$A$	Material constant	—
$z$	The radius of the contact area between the deformed particle and the surface	$m$
$\varepsilon_o$	Permittivity of vacuum	—
$\Delta U$	Potential difference between the two particles	$V$
$q$	Charge of the particle	$nC$
$2R$	Distance between the particle and the surface	$m$
$\gamma$	Surface tension of water	$N/m$
$F_A$	Particle adhesion force	$N$
$F_t$	Tangential external force	$N$

Symbol	Nomenclature	Units
$M_t$	External moment	$Nm$
$F_L$	Lift force	$N$
$d$	Diameter of the particle	$m$
$a$	Radius of the deformed contact area	$m$
$k$	Static friction coefficient	—
$W_A$	Thermodynamic work of adhesion	$J$
$z_o$	Minimum separation distance	$m$
$\rho$	Density	$kg/m^3$
$A$	Hamaker constant	—
$\Pi$	Adhesion parameter	—
$\nu$	Kinematic viscosity	$cm^2/s$
$W_{ad}$	Wear rate	$mN/mm^3$
$V$	Wear volume	$m^3/m$
$L$	Sliding distance	$m$
$K$	Wear coefficient	—
$F_N$	Normal load	$N$
$H$	Hardness of the softer material	—
$\eta$	Viscosity of the lubricant	$cm^2/s$
$v$	Sliding velocity	$mm/s$
$P$	Pressure exerted	$N/m^2$
$\lambda$	Specific film thickness	$nm$
$h_{min}$	Minimum film thickness	$nm$
$\sigma$	Rms surface roughness	$\mu m$
$r$	Radial distance from the centre of the Gaussian spatial beam profile	—
$F_0^{pk}$	Peak laser fluence when $r = 0$	$mJ/cm^2$
$D$	Crater diameter	$m$
$E_p$	Pulse energy	$mJ/cm^2$
$E_{th}$	Threshold pulse energy	$mJ/cm^2$

Symbol	Nomenclature	Units
$\xi$	Incubation factor	—
$N$	Number of pulses	—
$l$	Energy penetration depth	$cm^{-1}$
$C$	Volumetric specific heat	$J/kg$
$T$	Temperature	$K$
$d$	Number of pulses	—
$D_{area}$	Dimple area ratio	%

# Abstract

The increased demand in stringent requirements on engineered surfaces in the aerospace and manufacturing industries drove the need for developing advanced surface engineering techniques such as chemical etching, plasma etching, corona discharge and laser surface texturing in order to alter material surface physical and chemical properties. Among these techniques, laser surface texturing has been identified as one of the most efficient and effective surface treatment/ texturing techniques which utilizes laser ablation to meet the demand of practical engineering requirements. This thesis details three practical engineering challenges in the field of paint adhesion, dust adhesion and tribology performance of SPF sheet forming dies in which case the problems and motivation for development came from projects by industrial partner collaborations with BAe Systems, Rolls-Royce and Dyson Ltd. The proposed solutions to these challenges are formulated around laser surface texturing techniques using excimer and femtosecond lasers on three engineering materials which are CFRP, ABS polymer and HR4 nickel alloy.

As ablation is the main mechanism used in laser surface texturing techniques in achieving surface property changes, the understanding of laser beam interaction with materials is crucial. The fundamental understanding of laser beam interaction with different materials has been researched since the use of lasers in practical engineering applications by which laser material interaction parameters such as ablation threshold, incubation coefficient and optical penetration depth are of primary interest in addition to the ablation rate. Currently the published literatures are either material specific or laser specific with minimal or zero comparison between different types of lasers and materials as such which limits the understanding of laser beam interaction with materials. In addition, laser

beam interaction with polymers has always been done using ultraviolet wavelength lasers. In this thesis, the interaction between two types of lasers and three types of materials which includes metals and polymers are presented through comparison and discussion between different interactions.

It has been discovered that the ablation threshold value is lower for ABS interaction with excimer laser as compared to the interaction with femtosecond laser due to the difference in the ablation mechanism. The optical penetration depth value is higher for ABS interaction with the excimer laser as compared to the interaction with the femtosecond laser due to differences in the photon energy of the laser beam of different wavelength. Two ablation rate curves were identified on ABS interaction with infrared wavelength femtosecond laser beams which has not been reported before. Chemical composition of the laser treated layer changes through chain scission process, creating free radical carbons that reacted with oxygen, nitrogen and water vapour in air creating oxygen and nitrogen rich functional groups which increased with increasing laser fluence and number of pulses.

Laser ablation is known for its capability of altering surface morphology and surface chemistry of materials through excitation of electrons causing bond scission or melt where materials are vaporised, ejected or undergo chemical compositional changes. In the case of polymers, addition of oxygen and nitrogen rich functional groups are identified whereas in the case of metals, changes in crystallographic, orientation and oxidation states are identified. Such changes are deemed ideal for applications such as adhesion where it is mainly used for bonding and joining of similar or dissimilar materials. In this research, excimer laser surface treatment showed improvement in CFRP paint adhesion where a better adhesion is achieved than sand-papered surfaces. Paint adhesion of CFRP surfaces is affected by surface contaminants, surface chemical composition and surface roughness where the degree of influence is in the respective order.

In addition, excimer and femtosecond laser surface treated ABS also improved dust adhesion. The main factors that affect the ABS surface dust adhesion performance are surface roughness and surface chemical composition. The increase in surface roughness increases the surface area available for dust to adhere to. In addition, it also increases the drag coefficient of the air flow results in a higher re-



moval force exerted by the air flow onto the dust particles through changes in the localised aerodynamic flow. The increase in polar functional groups increases the adhesion of the dust particles onto the surface due to an induced dipole moment by the charged dust particles.

Laser micro-dimpled surfaces have been reported to be effective in reducing friction coefficient and wear rate of surfaces under oil lubricated conformal contact conditions where the dimples act as reservoirs to store lubricant and wear particles. But such surfaces have not been extensively researched under non-conformal contact conditions for different lubricated environments. In addition, there are contradictory results found between published literatures which observe under similar wear environments and conditions but with different dimple geometry. Hence a detailed investigation on dimpled surfaces under non-conformal contact conditions is being carried out. Laser surface texturing of 100  $\mu m$  size dimples shows a reduction in nickel alloy wear rate under dry and oil lubricated environments. A higher dimple area ratio reduces the wear rate under dry condition with abrasive wear as the main wear mechanism. Under oil lubricated environments, the friction coefficient is dependent on the surface contact pressure, sliding speed and the viscosity of the lubricant and the wear rate is dependent on the film thickness which correlates to the friction coefficient. The wear rate of a dimpled surface is dependent on three factors which are the dimple diameter to contact area diameter ratio, depth of the dimple produced and the density of the dimples.

Positive results are obtained in all three engineering applications indicating the feasibility of laser surface texturing techniques in providing suitable material surface properties for these applications.

# Declaration

The University of Manchester  
*PhD by published work Candidate Declaration*

**Candidate Name:** Tian Long See

**Faculty:** Engineering and Physical Sciences

**Thesis Title:** Laser Surface Texturing - Fundamental Study and Applications

**Declaration to be completed by the candidate:**

I declare that no portion of this work referred to in this thesis has been submitted in support of an application for another degree or qualification of this or any other university or other institute of learning.

Signed:

Date: Wednesday 7<sup>th</sup> October, 2015

# Copyright

The author of this thesis (including any appendices and/or schedules to this thesis) owns any copyright in it (the “Copyright”)<sup>1</sup> and s/he has given The University of Manchester the right to use such Copyright for any administrative, promotional, educational and/or teaching purposes.

Copies of this thesis, either in full or in extracts, may be made only in accordance with the regulations of the John Rylands University Library of Manchester. Details of these regulations may be obtained from the Librarian. This page must form part of any such copies made.

The ownership of any patents, designs, trade marks and any and all other intellectual property rights except for the Copyright (the “Intellectual Property Rights”) and any reproductions of copyright works, for example graphs and tables (“Reproductions”), which may be described in this thesis, may not be owned by the author and may be owned by third parties. Such Intellectual Property Rights and Reproductions cannot and must not be made available for use without the prior written permission of the owner(s) of the relevant Intellectual Property Rights and/or Reproductions.

Further information on the conditions under which disclosure, publication and exploitation of this thesis, the Copyright and any Intellectual Property Rights and/or Reproductions described in it may take place is available from the Head of School of Material Science, Protection and Corrosion Centre (or the Vice-President) and the Dean of the Faculty of Engineering and Physical Sciences, for Faculty of Engineering and Physical Sciences candidates.

---

<sup>1</sup>This excludes material already printed in academic journals, for which the copyright belongs to said journal and publisher. Pages for which the author does not own the copyright are numbered differently from the rest of the thesis.

# Acknowledgements

I dedicate this work to my parents for their endless support, patience, sacrifices, love and encouragement in everything that I do in life. I also like to take the opportunity to thank my sister for her support during my PhD in the UK.

I would like to express my sincere gratitude and appreciation to my supervisors, Dr Zhu Liu and Prof. Lin Li for their invaluable guidance and support throughout my PhD.

I am grateful to Dr David Whitehead and Dr Guo Wei for their help in using the laser facilities in LPRC. I would also like to thank Shirley Zhou and Teru Hashimoto for SEM, Dr John Walton for XPS, Dr Hong Liu for white light interferometer, Gary for XRD, Polly for FTIR and Andy for Raman spectroscopy. I would also like to thank Steve Blatch for his support and help in completing COSHH forms and risk assessments.

It has been a great pleasure working and interacting with other PhD students and post doc in the CPC and LPRC group. My appreciation goes to Daishu Qian, Mohsen, Dr A. Mhich, Dr Guo Wei, Yuanze Zhou, Ahmed Lemnifi and Guoshuo.

I would like to acknowledge BAe Systems, Roll-Royce and Dyson Ltd for funding my PhD and enable me to be involved in industrial driven projects. Specifically, I would like to thank Steve Dilworth, Clive Grafton-Reed, Owen Nicholson, Andrew Bower and Mark Johnson for their valuable discussion and suggestions.

# Chapter 1

## INTRODUCTION

### 1.1 Research Motivation - The Engineering Challenges

There has been an increased demand for surface engineered structures such as surface micro/nano textures to achieve desirable surface properties that are different from those of the bulk material for applications such as improved coating adhesion and wear resistance. Material surface properties for such applications are crucial as they involved contact of two material surfaces. There are many surface engineering processes available to modify the surface structures (e.g. surface texture) including the use of mechanical machining, sand blasting, chemical etching, plasma etching, corona discharge and laser surface texturing (LST). Among these techniques, LST is one of the most flexible and efficient techniques to meet the requirement for more stringent surface structure design requirements and tailoring surface properties of advanced engineering materials [1]. In addition, LST has the advantages of non-contact processing, zero tool wear, fast processing speed, non-dross ablation and ease for automation [2; 3; 4].

This research was motivated by the challenges in practical engineering. The industrial problems to be addressed in this research came from the collaborating partners including BAe Systems, Rolls-Royce and Dyson Ltd.

The demand for bigger airplanes, fuel saving, and reduction of environmental damages, has pushed the wider use of lightweight materials in aircraft structures

and components. The increase in composite and aluminium materials in the aircraft manufacturing has driven the needs for better understanding of the material property changes under severe weather conditions. In most cases, surface protection measures are used to prevent composite materials from deteriorating when they are exposed to ultraviolet (UV) radiation to avoid decomposition and delamination. The common surface protection measures used are coating or painting where surface pre-treatment is required to increase adhesion and durability due to the low adhesion property of the un-treated composite material surfaces. This is because the surfaces of carbon fibre reinforced plastic (CFRP) composites will usually have release agents to prevent them from sticking to the forming tools during manufacturing. These agents also reduce paint adhesion strength due to their low surface energy nature if they are not removed. In addition, their surface finish are also not ideal for paint adhesion. Therefore surface cleaning and abrading (roughening) are commonly needed as a manufacturing step for surface pre-treatment before painting.

The conventional methods of achieving these include the use of manual sandpapering, which is a slow and laborious process, in addition it is worker experience and efficiency dependent. Hence there is a need to develop a better surface pre-treatment technique that is more controllable and reliable. LST would be an ideal candidate. The original problem came from one of the project partners, BAe Systems, to improve composite coating quality, consistency, reliability, cost and speed. The performance of introducing LST for cleaning and abrading of CFRP composites for paint coating is unknown. It is therefore, one of objectives and work packages of the research to develop an appropriate laser based method for CFRP surface abrading (texturing) and to understand its basic characteristics and performances.

Tool wear has always been a topic of research related to manufacturing processes such as metal forming and forging. The increase in demand for more complex shapes and harder materials to be produced through dies and moulds drives the needs for better dies and lubricants to meet the manufacturing standards required. Dimpled surfaces have been known to improve tribological performances in terms of friction and wear reduction for conformal contacts, but the performance for non-conformal contact is still unknown. In addition, the effect

of dimple geometry such as size, spacing distance between dimples and dimple shape on tribology performance is not fully understood. As LST is capable of producing micro-dimples of different geometry achieving a resolution much smaller than that of conventional machining methods, there is a need to investigate the feasibility and characteristics of laser dimpled surface on tribology performance of super-plastic forming dies. The engineering problem came from BAe Systems for the improvement of tool life of HR4 nickel alloy dies for superplastic forming applications. A solution is therefore needed to be developed with full scientific understanding of the technology proposed. This forms another objective and second work package of the research.

The fundamental science behind dust adhesion has been a puzzle for many years and there are no reasonable explanations and theories that enable one to fully explain the phenomena of dust adhering to a surface. Dust adhesion phenomena is complex where it involves different forces and interactions depending on the environment and the surrounding conditions. As adhesion is closely related to the surface properties of the material, changes in these properties such as surface roughness/texture, surface chemical composition, wettability and surface energy will affect the adhesion performance. The engineering problem came from Dyson Ltd for the improvement of dust adhesion within the dust collection chamber to improve user satisfaction of the bag-less cyclone vacuum cleaners. The effect of LST on acrylonitrile butadiene styrene (ABS) polymer is unknown and a solution is therefore needed to be developed through understanding the technology proposed. This forms another objective and third work package of the research.

## **1.2 Knowledge Gaps and Scientific Challenges**

The research was driven by industrial needs of three engineering problems and the solutions can be all related to the use of LST techniques. It is therefore useful to understand the basic characteristics of laser interactions with different materials, especially the ABS polymer, HR4 nickel alloy and CFRP composites during laser surface processing/texturing. From these studies, generic and specific knowledge of laser beam interactions with materials is able to be obtained.

LST is a process that relies on the interaction of the laser beam and material to achieve specific micro/nano periodic surface structure by material removal through ablation. Meanwhile, the surface microstructure and chemical composition may be altered. The removal of material through LST is dependent on several factors such as laser fluence, frequency, number of pulses (NOP), laser beam wavelength, material surface reflectivity and absorptivity. There have been many publications in this field but most of the work are material or laser specific where the fundamental understanding of the generic laser beam and material interaction characteristics is not fully developed for different lasers and materials. The relevant knowledge gap in the field related to the research is the interaction of ultrashort pulsed infrared (IR) laser beam with polymeric material as the existing LST on polymer investigations use UV lasers. In addition, there are two commonly used methods to characterise laser material interaction parameters (i.e. ablation threshold, optical penetration depth and incubation factor) where the accuracy and reliability of these methods have not been investigated and discussed. As the characterisation method used influence the understanding of the laser beam and material interactions for different lasers and materials, the understanding of the discrepancy between different characterisation method results is crucial and needs to be investigated.

There are many publications on excimer laser texturing of polymers for the improvement of adhesion between similar or different polymers, fibre and matrix, and polymer and metal where the fundamental understanding of adhesion improvement in these cases are well understood. However, excimer laser texturing for improvement of coating adhesion has not been investigated. Although some of the knowledge from previous work can be used to establish the science behind coating adhesion improvement, further analysis and experimental work are required to verify the hypothesis.

Dimpled die materials using LST methods have been investigated by many researchers in which the published papers are specifically involving particular types of dimple geometry, lubrication and point of contact. Previous investigations concentrated on the specific tribological performance due to the effect of the dimples, including friction coefficients and wear rate responses. There is yet a lack of understanding of the effect of dimpled die materials on tribological



performance under different lubrication conditions and dimple geometries.

Dust adhesion is a complex phenomenon and has not been fully understood. Although there are a few theories on adhesion that have been proposed by researchers over the last 100 years dealing with material adhesion properties, they are not sufficient to understand all dust adhesion phenomena. Hence, there is a lack of knowledge on the science of dust adhesion and the effect of LST on ABS polymer on dust adhesion.

### 1.3 Aim and Objectives

The aim of the research is to develop and understand short and ultrashort pulsed laser surface texturing processes and laser interactions with CFRP, HR4 nickel alloy (high temperature die) and ABS polymer for engineering applications. The specific objectives of the research are:

- To understand the interactions of excimer laser beam with CFRP/ epoxy polymer and material characteristics.
- To understand the interactions of excimer laser and femtosecond laser beam with ABS plastic and material characteristics.
- To understand the interactions of femtosecond laser beam with HR4 nickel alloy and material characteristics.
- To investigate the feasibility of paint adhesion improvement by laser-abrading/ texturing of CFRP.
- To investigate the tribological behaviour of laser-textured HR4 nickel alloy.
- To investigate dust attachment behaviour on laser-textured ABS.

### 1.4 Thesis Structure

This thesis is divided into nine main chapters where the key chapter of the thesis is chapter 4 whereby the laser beam interaction with materials is detailed. Chapter

5–7 are structured in relation to three different laser texturing applications upon which each application investigated is detailed in a single chapter. The structural layout of the thesis is illustrated in Figure 1.1.

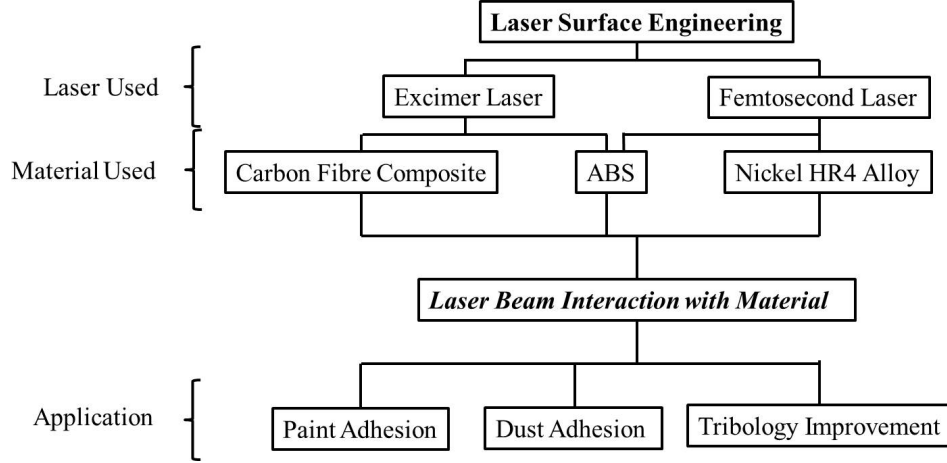


Figure 1.1: Illustration of the thesis structure

Chapter 2 provides a literature review on laser texturing processes for composite, metals and polymers with their relative applications related to adhesion and tribology improvements. In addition, literatures of laser beam interactions with these materials are reviewed and analysed where the fundamental laser ablation mechanisms and phenomena during ablation are discussed. This chapter also includes a brief overview of laser/optic fundamentals.

Chapter 3 describes the materials and equipment used in the research.

Chapter 4 details the experiments on the investigation of the excimer and femtosecond laser beam interaction with HR4 nickel alloy, CFRP and ABS materials. The basic phenomena and effects of laser beam interactions with the materials are described and analysed.

Chapter 5 details an investigation on the application of laser surface pre-treatment (combined laser cleaning and abrading) on CFRP for paint adhesion. Different surface pre-treatment methods examined are described. The mechanism of paint adhesion on textured and laser cleaned surfaces is discussed in this chapter.

Chapter 6 details an experimental investigation on tribological behaviour of laser textured HR4 nickel alloy. The effect of laser-textured nickel HR4 alloy

on wear characteristics with dry and oil lubrication are investigated where the mechanisms on the effect of surface textures on wear characteristics are discussed.

Chapter 7 details an experimental investigation on dust adhesion behaviour of laser textured ABS. The effect of laser textured ABS on adhesion of dust under airflow environment is investigated, and the mechanisms involved are discussed.

Chapter 8 concludes all the research results highlighting the main scientific contributions of this research.

Chapter 9 presents the authors suggestion for the future work with an analysis of additional knowledge gaps to be filled.

# Chapter 2

## LITERATURE REVIEW

### 2.1 Introduction

This chapter first introduces fundamentals of laser and the systems that include the classification of lasers and the characteristics of laser beams. Then, a literature review is given on laser beam interactions with materials, laser surface modification techniques in particular laser surface texturing techniques and applications aiming to identify knowledge gaps and new scientific challenges. The emphasis of the literature review is on the understanding of fundamental phenomena in material ablation with short and ultrashort pulsed lasers and mechanisms involved. A literature review on corresponding application fields relevant to this PhD research is also presented in this chapter, which provides the state of the art technologies in the relevant field and identify the knowledge gaps and technological challenges.

#### 2.1.1 Lasers

LASER is the abbreviation for Light Amplification by the Stimulated Emission of Radiation. A basic laser consists of two parallel mirrors that form an optical resonator to allow photons to oscillate between them [2]. One of the parallel mirrors (i.e. the output window) is partially transparent to allow part of the laser beam to transmit through and the other is fully reflective with a concave surface to minimize energy loss through diffraction. The active medium between the mirrors

can be gas such as  $CO_2$ ,  $KrF$ ,  $ArF$ ,  $He/Ne$ , or solid such as neodymium-doped yttrium aluminium garnet ( $Nd : YAG$ ), titanium-doped sapphire, neodymium-doped yttrium orthovanadate ( $Nd : YVO_4$ ), neodymium-doped yttrium calcium oxoborate ( $Nd : YCOB$ ) and neodymium-doped yttrium lithium fluoride ( $Nd : YLF$ ). The medium is pumped or excited often with another light such as flash lamp or laser such as a diode laser and pumped with direct current (DC) or radio frequency (RF) power supply [2]. When photon with energy similar to the energy gap of the medium material present during the excited state of the medium, the excited atoms can emit a photon of similar wavelength and phase as the photon, which then decays to a lower energy level producing light that has the characteristics of coherency and monochromaticity. This process is called stimulated emission, first proposed by Einstein.

There are many types of lasers available in the market with different configurations producing coherent light of different beam properties. They are characterized by laser beam properties such as wavelength, pulse width and transverse electromagnetic modes. In general, lasers are classified through the active medium that produced the laser beam. The three main types of laser classification are solid-state lasers (such as  $Nd : YAG$  lasers and semiconductor lasers), gas lasers (such as  $CO_2$  and excimer lasers) and liquid lasers (such as dye lasers).

Laser systems used in laser machining process typically consist of a number of elements and they are:

- A laser generator with its power supply and cooling system.
- A beam delivery system
- A work fixture with motion control system and associated controller
- A fume extraction system
- A beam focusing system.
- A work piece gas shielding system
- A system safety enclosure
- Sometimes, a process monitoring and control system

### 2.1.2 Characteristics of Laser Beams

Laser beams have very special properties that make them different from other light sources. These properties, originated from the coherence of the light, make a laser beam an ideal source for machining in industry. These properties include:

- Directionality
- Monochromaticity
- High brightness/ radiance
- Low beam divergence

A light source is said to be monochromatic when there is only one specific wavelength associated with the light source. Due to the monochromaticity property, a laser beam is capable of being focused to an extremely small spot, which results in high energy density on a single spot that is highly desirable for laser machining. A light source that is coherent must be both temporally coherent and spatially coherent. Temporal coherence means that the phase of each point of the beam does not change with time. Spatial coherence means that the phase difference between two points of the laser beam does not change with time. A real laser normally has infinite spatial coherence time in addition to a short temporal coherence time corresponding to the light transition time between the energy levels. Due to the directionality, low beam divergence and radiance property of a laser beam, beam delivery over long distance with large optical energy to a small spot is possible. Different lasers may have different wavelengths ranging from the infrared to the ultraviolet, which allows different lasers to be used for different applications and materials.

Laser comes in several resonator modes and different modes have different stability. The lowest-order mode known as the Gaussian Mode ( $TEM_{00}$ ) is one of the stable laser resonators. This mode provides optimal irradiance distribution and minimizes divergence caused by diffraction. A Gaussian mode beam does not change its form over distance and the mode quality is measured by the focusability of the laser beam.

## 2.2 Laser Beam Interaction with Materials

Laser beam interaction with material is crucial in laser processing as it helps explain the phenomena occurred during and after processing which aid in understanding and design suitable laser processing parameters to achieve better quality machining. Although there have been many previous investigations on the interaction of laser beam with materials, many knowledge gaps still exist. So far only a limited number of materials have been investigated on their interactions with laser beams. Generally, laser beam and material interactions involve electronic and lattice dynamics, beam absorption, material ablation mechanisms, plasma generation and its interactions with laser beams and laser induced periodic surface structure (LIPSS). The following sections provide a review on the above basic phenomena.

### 2.2.1 Electronic and Lattice Dynamics

Electronic and lattice dynamics play an important role in the energy transfer during interaction of a laser beam with materials. The interaction of laser beam with a material can be considered as an energy transfer process from the laser beam into the material where the Newton law of conservation of energy holds. Hence, part of the energy from a laser beam is absorbed by the material and part of the energy is transmitted, reflected and scattered to the surrounding media. The interaction of a material with an electromagnetic wave can be described by Maxwell's equations. This section summarises the basic electronic and lattice dynamics of solid materials where the emphasis is on the typical interaction time scales and their consequences on laser beam interaction with materials.

For any electromagnetic waves (which include a laser beam of any wavelength from IR to UV), energy transfer between the beam and material is through the absorption of photons by the electrons through inter- or intra-band electronic transitions which results in a non-equilibrium electronic distribution as some electrons are excited as a result of absorbing more energy from the photons. The thermalisation of a solid material is achieved via two mechanisms which are electron-electron and electron-phonon coupling interactions. The electron-electron thermalisation is a complex process and is influenced by the electronic

structure of the materials. In the case of conductors, electrons are mobile between the valance band and conduction band through excitation of electrons as there is no gap in between the two electronic bands. As for semiconductors and insulators, an electron-hole pairs are created as a result of electron excitation due to the band gap in between the conduction band and the valance band. The difference in electronic structures of materials causes variations in re-equilibrium of the electronic distribution and can be as long as nanoseconds depending on the material properties [5].

The electron-electron thermalisation process in a conductor (metal) is governed by an electron scattering event, which is known to be a very fast process (within the femtosecond time scale). The simplest approach in estimating the thermalisation time required is through Drude model where the electron scattering time,  $\tau_D$  is dependent on the electrical conductivity of the material,  $\sigma_{el}$  with the following equation [6]:

$$\tau_D = \frac{\sigma_{el}m}{Ne^2} \quad (2.1)$$

where  $N$  is the conduction electron density,

$e$  is the electronic charge,

$m$  is the electron mass

Under the non-equilibrium electronic distribution condition, the electrons re-equilibrate themselves through electron-electron collision and the time required to achieve equilibrium is known as the lifetime of excited electron,  $\tau_{ee}$  and is described using Fermi liquid theory which follows the equation [7]:

$$\tau_{ee} = \tau_0 \frac{\varepsilon_F}{\varepsilon - \varepsilon_F} \quad (2.2)$$



where  $\tau_0$  is in the order of femtosecond,

$\varepsilon_F$  is the Fermi energy,

$\varepsilon - \varepsilon_F$  is the excited electron energy with respect to the Fermi level

As the lifetime of excited electron,  $\tau_{ee}$  is short (usually in the range of femtoseconds or picoseconds), experimental investigation through time-resolved photoemission experiments is only possible through lasers with pulse width comparable to  $\tau_{ee}$ . This is achieved through femtosecond or picosecond lasers and has been experimentally proven by Qiu and Tien in their study on short-pulse laser heating on metals [8; 9]. When a longer pulse laser beam is used, the electron-electron thermalisation occurs within the pulse duration of the laser irradiation which hinders the observation of the actual lifetime of excited electrons. Instead, the electronic dynamic follows the time evolution of the laser pulse.

In addition to electron-electron scattering, electron-phonon scattering is also possible which describes the interaction between the electron and lattice. The theory of electron-phonon scattering process was developed back in 1960s due to the discovery of superconductivity where the basics of the interaction process were outlined in the work of Eliashberg [10]. A simplified approach to visualise the electron-phonon scattering process was proposed by P.B. Allen [11] through the rate of energy transfer in the form of thermal energy using a simple rate equation shown in equation 2.3. The thermalisation process is based on the collision between the electron and lattice [11].

$$\frac{\partial T_e}{\partial t} = \frac{(T_L - T_e)}{\tau_{ep}} \quad (2.3)$$

where  $T_e$  is the electron temperature,

$T_L$  is the lattice temperature,

$\tau_{ep}$  is the electron-phonon coupling time

The electron-phonon coupling time is dependent on the Debye frequency of the irradiated solid,  $\lambda_p$  and a constant related to the electronic temperature which is known as coupling constant,  $\omega_D$  with the following equation [12]:

$$\tau_{ep} = \frac{2\pi k_B T_e}{3\hbar \lambda_p \omega_D^2} \quad (2.4)$$

From Equation 2.4, the electron-phonon coupling time is estimated to be in the region of a few picoseconds which is roughly twice the order of magnitude slower than the electron-electron scattering time. Upon establishing the understanding on the interaction between the electron and the lattice, the time dependence of the electron and lattice energy (or temperature) can be described using two separate heat transfer equations as shown below:

$$C_e \frac{\partial T_e}{\partial t} = \nabla(k_e \nabla T_e) - H(T_e, T_L) + S(t) \quad (2.5)$$

$$C_L \frac{\partial T_L}{\partial t} = H(T_e, T_L) \quad (2.6)$$

where  $C_e$  is the electronic specific heat,

$C_L$  is the lattice specific heat,

$S(t)$  is the absorbed laser power per unit volume,

$H(T_e, T_L)$  is the rate of energy transfer between electrons and lattice,

$\nabla(k_e \nabla T_e)$  is the diffusive electronic heat transfer,

$\tau_{ep}$  is the electron-phonon coupling time

The two separate heat transfer equations are the result of the two-temperature model (TTM) developed by Anisimov et al. in 1974 [13]. Under proper experimental conditions, the energy transfer between the electron and lattice can be simplified using the equation [14; 15]:

$$H(T_e, T_L) = g_{ep}(T_L - T_e) \quad (2.7)$$

where  $g_{ep} = C_e/\tau_{ep}$

The effect of equations 2.5 and 2.6 can only be observed when the laser pulse width is shorter than the relaxation time for electron-electron and electron-phonon coupling. On the contrary if the pulse width is longer, then the electron and lattice thermalises within the pulse duration having  $T_e = T_L = T$ . This is illustrated through solving numerical simulation of temperature profile for copper metal using the required material properties such as thermal and optical parameters as shown in Figure 2.1, from which it is observed that at a 50 *fs* pulse width, only electron-electron scattering is observed where the temperature of the lattice is unchanged. When the pulse width increases to 5 *ps*, electron-electron scattering is still observed with a small amount of electron-phonon coupling effect as the temperature of the lattice increases slightly. When the pulse width increases further to 500 *ps*, the temperature of the electron and the lattice matches with the temperature of the material surface which was described earlier. Hence for longer laser pulses, the model can be simplified by the following equation [16]:

$$(C_L + C_e) \frac{\partial T_e}{\partial t} = \nabla(k_e \nabla T_e) + S(t) \quad (2.8)$$

Considering that the specific heat constant for electron,  $C_e$  is much smaller than the specific heat constant for lattice,  $C_L$ , the equation can be further simplified to [6; 16]:

$$C_L \frac{\partial T_e}{\partial t} = \nabla(k_e \nabla T_e) + S(t) \quad (2.9)$$

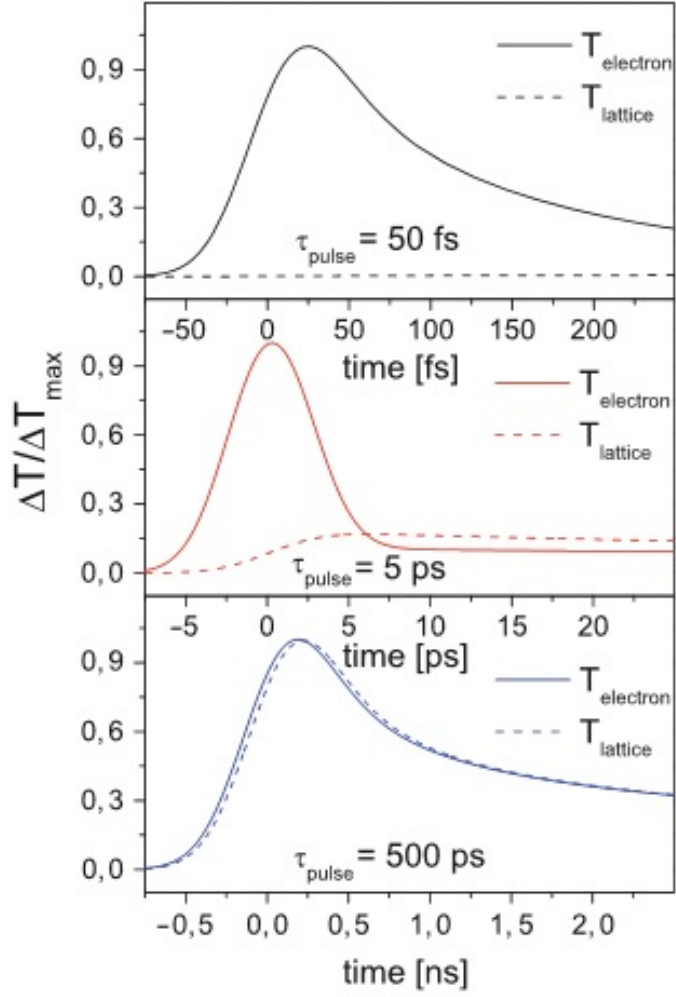


Figure 2.1: Electronic and lattice temperature profiles (simulations obtained with the TTM) in copper irradiated by laser pulses of different durations (ranging from 50 *fs* to 500 *ps*). With 50 *fs* pulses, electrons and lattice are completely decoupled and the lattice is substantially unaffected by the laser beam. With 500 *ps* pulses, electron and lattice follow almost identical temperature evolutions [16].

### 2.2.2 Laser Beam Absorption

The absorptivity of the material is related to the optical property of the material which is determined by the free electrons (valence electrons) because the inner electrons only interact weakly with the applied electric field. By using Drude model, the absorptivity,  $\alpha$  and reflectivity,  $R_o$  of the material can be obtained using extinction coefficient,  $\kappa$  and refractive index,  $n$  of the material through the equation [17]:

$$\alpha = \frac{2\omega\kappa}{c} = \frac{4\pi\kappa}{\lambda} \quad (2.10)$$

$$R_o = \frac{(n-1)^2 + \kappa^2}{(n+1)^2 + \kappa^2} \quad (2.11)$$

where  $\lambda$  is the wavelength,  
 $\omega$  is the angular frequency,  
 $C$  is the speed of light

In addition, the plasma frequency,  $\omega_p$  is related to the conductivity,  $\sigma$  of metal with the following equation [17]:

$$\sigma = \omega_p^2 \tau_D \varepsilon_o \quad (2.12)$$

where  $\tau_D$  = is the mean time between two electronic collisions,  
 $\varepsilon_o$  = is the dielectric constant

Hence for electromagnetic wave of wavelength,  $\omega \ll \tau_D^{-1}$ , the absorptivity and reflectivity of metal can be estimated using the electrical resistivity,  $\rho = \sigma^{-1}$  with the following equations [18; 19]:

$$\alpha = \sqrt{\frac{2\omega}{c^2 \varepsilon_o \rho}} \quad (2.13)$$

$$R_o = 1 - 2\sqrt{2\omega\epsilon_o\rho} \quad (2.14)$$

The inverse of absorptivity,  $\alpha^{-1}$  is known as the optical penetration depth or absorption length. Based on the equation, the reflectivity and optical penetration depth is about 90 – 99 % and 10 *nm* respectively for metallic material when is irradiated with beam intensity below the plasma frequency [18]. From the equation, it is clear that the absorptivity is related to the laser wavelength and resistivity of the material.

The absorptivity of materials depend on other factors as well including laser beam incidence angle, surface roughness and temperature of the material. The absorption increases with increasing surface roughness because a rougher surface enhances the absorption by a multi-reflection process [20]. For most metals, an increase in temperature results in an increase in absorptivity especially at the melting point of the material where the increase is significant [18].

### 2.2.3 Ablation

**Definition** Removal of material using a pulse laser beam through rapid vaporization or sublimation is commonly known as ablation. When a high intensity laser beam is incident on the surface of a material, some of the incident beam is absorbed by the material and the remaining intensity is lost to the surrounding through reflection or scattering process. The absorbed light energy converts to heat that raises the temperature of the material. When the material temperature exceeds their boiling point, it becomes vapour and is normally ejected from the surface. As laser ablation is related to the interaction between the laser beam and materials, the dynamic of the fundamental material structure (electron and lattice) as well as the absorptivity of the material with laser beam is crucial in determining the type of ablation mechanism involved in the process. Laser ablation process is a complex phenomenon where it is dependent on several factors such as material properties, laser wavelength, pulse width, frequency, fluence, number of pulses and the surrounding environmental conditions. Laser ablation of a material can be quantified through a term known as ablation depth per pulse or ablation rate and is usually in the range of nanometer per pulse for a ps or fs

laser. This quantification is used in the following sections in discussing the effect of different factors on laser ablation process.

### 2.2.3.1 Influencing Factors in Laser Ablation

**Laser Beam Wavelength** Laser beam wavelength affects the laser ablation process because it is related to the photon energy of the laser through the equation [2]:

$$E = \frac{hc}{\lambda} \quad (2.15)$$

where  $E$  is the photon energy,

$h$  is the Planck constant ( $6.626 \times 10^{-34}$ ),

$c$  is the speed of light ( $3 \times 10^8$ ),

$\lambda$  is the wavelength

From equation 2.15, it is clear that an increase in laser beam wavelength result in a smaller photon energy. Table 2.1 summarises the common industrial lasers used in the market with their respective wavelength and photon energy.

The absorption of photon energy by the material is achieved through either single-photon absorption or multi-photon absorption process. For electromagnetic wave with the wavelength within near IR and near UV region, the photon energy can only be absorbed or interact with the electrons rather than the ions as the ions are too heavy to follow the high frequency field [18]. For x-photon, the transition probability,  $W$  is given by a general expression [17]:

$$W = s^x I^x \quad (2.16)$$

where  $I$  = is the laser intensity,

$s$  = is the cross section of single-photon process

Table 2.1: Common industrial lasers with their wavelength range and photon energy [21].

Type	Lasing Species	Principle wavelength (nm)	Photon energy (eV)
Excimer	$F_2$	157	7.9
	$ArF$	193	6.4
	$KrF$	248	5
Nd:YAG - Frequency-quadrupled	$Nd^{3+}x^4$	266	4.7
	$XeCl$	308	4
	$XeF$	351	3.5
Nd:YAG - Frequency-doubled	$Nd^{3+}x^2$	532	2.3
Helium-neon	$Ne^*$	633	2
Ruby	$Cr^{3+}$	694	1.8
Ti:sapphire	$Ti^{3+}$	670 – 1100 (tunable)	1.9 – 1.1
AlGaAs diode	Band gap	700 – 900 (tunable)	1.8 – 1.4
Nd:YAG or Nd:glass	$Nd^{3+}$	1064	1.17
Yb:YAG or Yb:glass	$Yb^{3+}$	1030	1.2
Carbon monoxide	$CO$ vibration	5400	0.2
Carbon dioxide	$CO_2$ vibration	1064	1.17



From the expression, it is clear that the x-photon transition probability follows a non-linear expression and is dependent on the laser intensity if the cross section is constant. It indicates that the probability of multi-photon absorption process (nonlinear absorption) increases strongly with increasing laser intensity. This case holds true with shorter pulsed laser under constant laser fluence due to the nature of the laser beam having higher intensity.

The dependency of ablation rate with laser wavelength is investigated by D. Ashkenasi et al. [22]. It is observed that the NOP required to ablate sapphire at a fixed fluence is lower for shorter laser wavelength and this is believed to be due to the difference in photon energy of the laser as having a shorter wavelength result in higher photon energy.

**Laser Pulse Width** Laser pulse width is another laser parameter that affects the ablation rate of the material as the duration of the incident laser beam is one of the determining factors for the transfer of photon energy onto the material. As mentioned in the previous section, the transfer of photon energy onto the material is through electron-electron and electron-phonon coupling process where a determining factor is the pulse width of the laser beam. Hence the ablation process can be classified into two types depending on the photon energy transfer process. If the photon energy only transfers through electron-electron coupling process, it is known as non-thermal (photolithic) process. If electron-phonon coupling process is involved (for pulse width longer than picosecond), it is termed thermal (pyrolithic) process [23]. The two different processes can be illustrated in simple flow chart as shown in Figure 2.2.

The dependency of ablation rate with laser pulse width is investigated by D. Ashkenasi et al. and R. Le Harzic et al. [22; 25]. It is concluded that for laser pulse width up to 5 – 10 *ps*, the effect of laser pulse width is not significant as the main mechanism is within the optimal energy range. On the contrary, the effect of pulse width became significant when the laser pulse width is longer than picosecond as the ablation efficiency is reduced due to the decrease in effective energy penetration depth [25]. This is believed to be caused by plasma shielding effect as well as an increase in heat conduction losses and at longer pulse width, thermal ablation mechanism is involved.

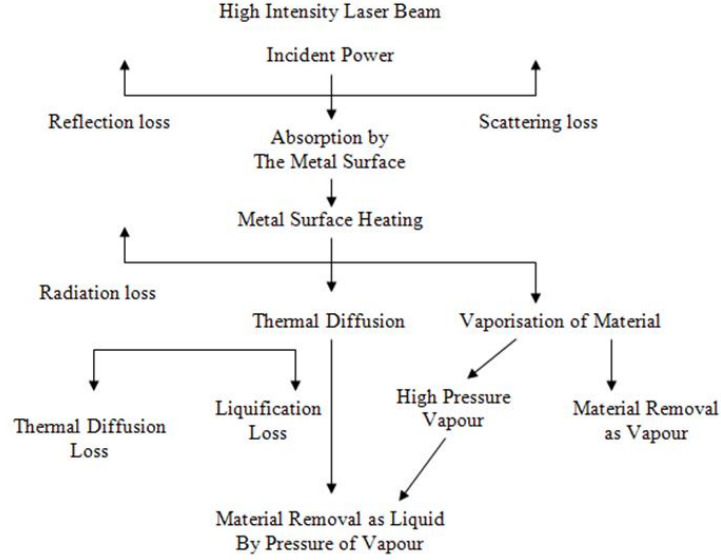


Figure 2.2: Material removal mechanisms using laser beam [24].

**Laser Frequency or Repetition Rate** Laser pulse frequency is defined as the NOP per second where higher frequency results in a shorter “off time” as the “on time” which is also known as the laser pulse width is constant. A continuous “on time” is achieved if the frequency is high enough which result in a continuous wave (CW) laser rather than a pulse laser. The definition of pulse frequency is illustrated in Figure 2.3. The decrease in “off time” result in shorter duration for heat dissipation after laser irradiation thus increase ablation rate as the ablation mechanism changes from non-thermal to thermal.

The dependency of ablation rate with pulse repetition rate was investigated by F.C. Burns and Stephen R. Cain [26]. It was observed that an increase in pulse repetition rate increased the ablation rate by reducing the ablation threshold of polyimide (PI) and Vacrel 8230 photoresist. From the observation, it was concluded that the effective absorption coefficient obtained from the ablation rate curve determines the magnitude of repetition rate factor [26].

**Number of pulses** The number of pulses is also one of the factors that affect the ablation rate where it increases with NOP due to the reduction of ablation

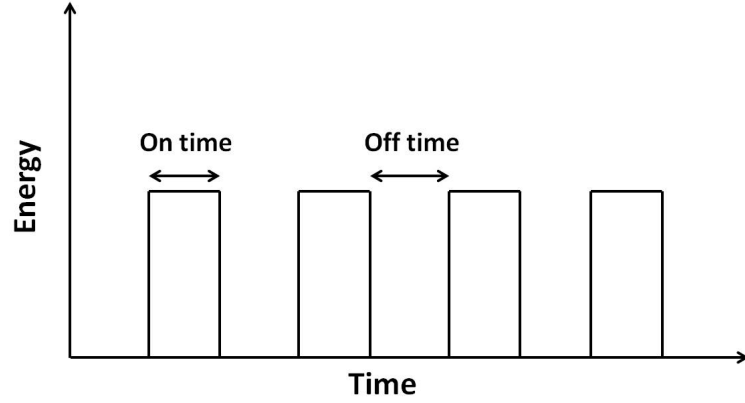


Figure 2.3: Illustration of laser beam frequency.

threshold. The term incubation is used to describe the dependency of ablation threshold on NOP where the ablation threshold decreases with increasing NOP in an exponential fashion till it reaches an asymptotical value as shown in Figure 2.4. Any fluence below that value requires an infinite NOP to initiate ablation of materials [27]. Such phenomenon is observed in both metallic materials and polymers [26; 27; 28; 29].

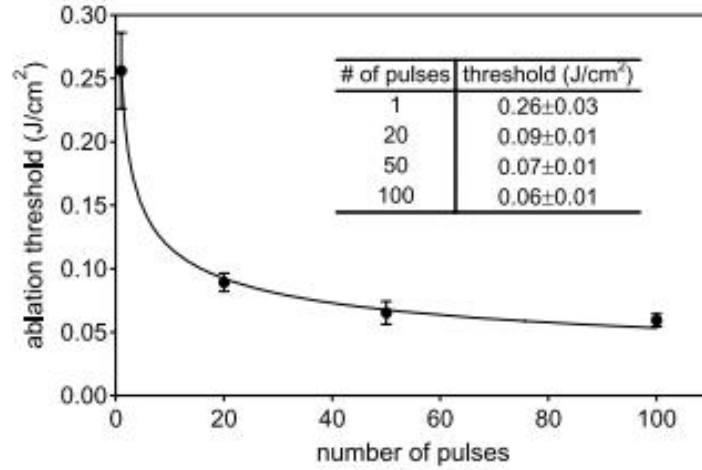


Figure 2.4: Ablation thresholds versus number of pulses for nickel-based superalloy C263 [27].

In metals, such phenomenon is believed to be caused by the degradation of the material properties as a result of the plastic stress-strain formation. The expla-

nation of the incubation effect is proven by Yong Jee et al. by investigating the effect on a single-crystal metal surface [28]. It is observed that the Cu(111) shows a more rapid decrease in the threshold fluence with increase NOP as compared to Cu(100) as shown in Figure 2.5 as FCC crystal structure has low resistance to laser-induced damage.

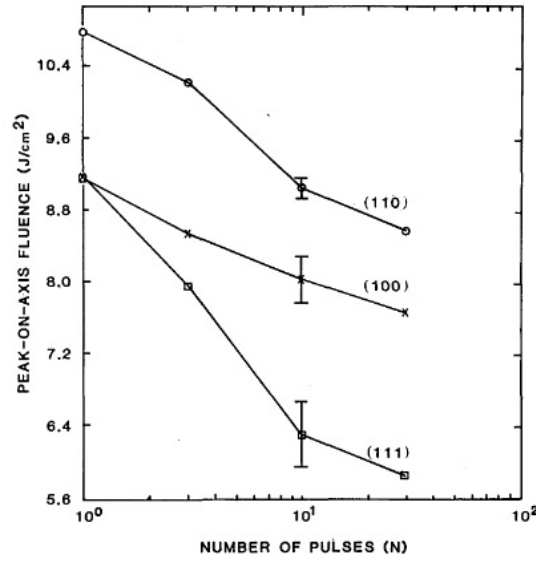


Figure 2.5: Damage fluence versus pulse number curves for the different crystallographic orientations of chemically polished Cu surfaces [28].

As for polymer, it is believed to be caused by the weakening of the polymer chain through changes in the polymer structure where the chromophoric group (side-chain of the polymer that undergoes changes in orientation) increases the absorptivity of the material reported by Stephen R. Cain et al. on the investigation done using PI and PMMA [29].

**Material properties** Metallic materials consist of crystal structures with specific lattice arrangement of overlapping valance bands where the electrons are mobile forming a sea of electrons. Such bonding is termed metallic bond that has a high binding energy ( $> 10$  eV per atom). As the main building block of metallic materials are based on electrons and lattice, the properties of electron and lattice play an important role in determining the ablation mechanisms involved when

interacting with a laser beam.

Occurrence of bond dissociation through photon energy in metals is unlikely due to the high binding energy of the metallic bond. This is because the highest achievable photon energy through laser beam is  $6.4 \text{ eV}$  ( $\lambda = 193 \text{ nm}$ ) which is smaller than the binding energy of metallic bond. Hence, the governing ablation mechanism for metallic materials is thermal ablation for laser pulse width  $> ns$ . This is because the incident photon energy that is absorbed by the electrons increases the kinetic energy of the electrons which is then further transferred onto the lattice causing vibrations resulting in thermal energy that heats up the material causing dissociation of material [30; 31]. The ablation phenomenon is governed by the Beer-Lambert law where the logarithmic ratio of the incidence fluence to the threshold fluence is constant. This equation is then derived into another form that relates the change in fluence with ablation depth per pulse which is known as the logarithmic law of ablation per pulse as shown in Figure 2.6 where the constant is termed optical penetration depth as shown in the equation below [32; 33]:

$$L = \frac{1}{\alpha} \ln\left(\frac{F}{F_{th}}\right) \quad (2.17)$$

where  $L$  = Ablation depth per pulse  
 $\alpha^{-1}$  = Optical penetration depth  
 $F$  = Laser fluence  
 $F_{th}$  = Laser fluence threshold

Optical penetration depth is defined as the penetration distance of the laser beam from the material surface where the intensity of the laser beam is  $1/e$  of the initial laser beam intensity. Hence, this parameter is dependent on material properties but independent on material surface conditions and initial laser beam intensity.

A slightly different phenomena is observed when metallic materials are ablated using ultrashort pulse laser (pulse width  $< 1 \text{ ns}$ ). There exist two trend lines

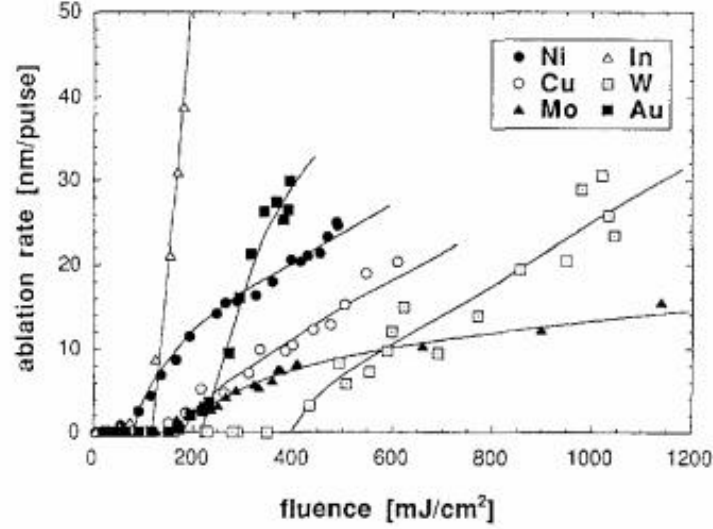


Figure 2.6: Plot summarizing the data on short-pulse laser ablation of Ni, Cu, Mo, In, W, Au metals . [33]

between ablation depth per pulse and laser fluence where a well-known two temperature model is proposed as shown in Figure 2.7 [27; 34; 35]. In the proposed model, it is argued that the electrons and lattice have different heat capacity and thermal conductivity constant. Due to the higher heat capacity of the electron and the ultrashort laser pulse width, when the incident photon energy is absorbed by the electrons [35], the thermal energy (kinetic energy) obtained result in dissociation of material without transferring to the lattice as the thermalization time for electron-phonon coupling is in the range of a few picosecond ( $1.5 - 3 \text{ ps}$ ) [36]. As a result, the ablation rate is dependent on the incident energy intensity of the laser beam but independent on the pulse width of the ultrafast laser beam [37]. As most of the ultrashort pulsed lasers have very high incident intensity due to the short pulse, they do not follow the Beer-Lambert law that is normally applied in explaining the light absorption for moderate intensity. This non-linear effect is more pronounced at a high intensity and is dependent on the incidence intensity of the laser beam [38]. Hence there exist two trend lines in the form similar to equation 2.17 that are governed by two different constants. In the low fluence regime, the constant is termed optical penetration, as the ablation mechanism in-

involved is non-thermal in nature whereas in the high fluence regime, the constant is termed energy or heat penetration depth, as the ablation mechanism involved is thermal in nature.

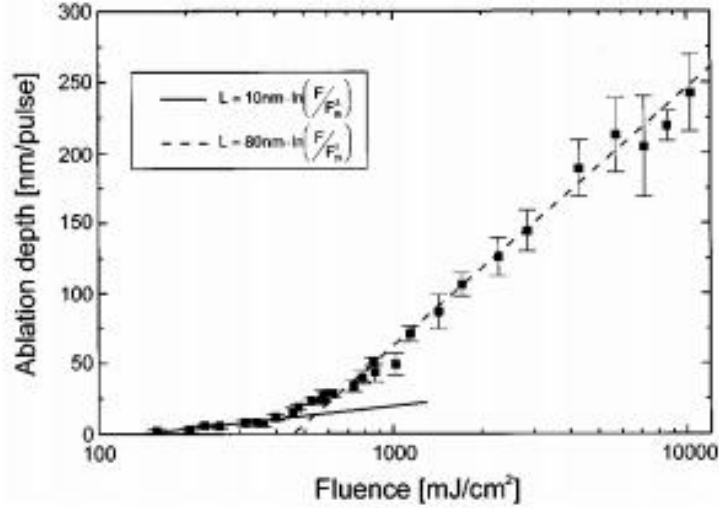


Figure 2.7: Ablation depth per pulse for copper versus the incident laser fluence for 150 *fs* laser pulses [35].

The first polymer ablation was reported by R. Srinivasan et.al [39] and Y. Kawamura et.al. [40] simultaneously in 1982 due to the growing availability of high pulse energy UV gas halide (RGH) lasers which provided the platform for laser beam material interactions. Srinivasan then continued in this field of research and became the leader of polymer ablation. He introduced the term laser ablation and ablative photodecomposition which are now commonly used. Till today, ablation mechanism study of polymers have been concentrated on UV wavelength lasers as polymers have the highest absorptivity of photon energy in the UV spectrum. The threshold fluence,  $F_{th}$  is dependent on the material properties and laser wavelength and it varies from tens of  $mJ/cm^2$  to more than  $1 J/cm^2$  where the typical threshold for UV laser beam is around 20–200  $mJ/cm^2$  [41; 42; 43; 44; 45; 46]. At a limited range of fluence above the ablation threshold, the etching rate versus laser fluence obeys Beer's law that follows the logarithmic law of ablation per pulse as shown in equation 2.17.

Srinivasan proposed the mechanism of ablative photodecomposition (non-

thermal ablation) due to the absence of significant thermal damage on ablated polymer using UV lasers [47] which is also known as photochemical models by some authors. This is explained through the high photon energy generated by the UV laser ( $6.4 - 4.9$  eV) that is close to the bond energy of polymeric chain which result in direct chain scission upon excitation of the electronic state from the valance band to the band gap in between the valance and conduction band that exist due to material imperfection (defect) or trap state [45; 48; 49; 50; 51; 52; 53; 54]. It is argued that the photon energy absorbed used in the bond-breaking process restricts the rise in temperature on the surface which then restricts on the thermal damage on the substrate and such mechanism is termed cold ablation. However, this model is difficult to be justified when the laser pulse width is longer than the thermalisation time of the non-radiative excited electrons. In this model, it is assumed that when a single laser pulse is irradiated on the material surface,  $n$  bonds per unit volume must be broken to achieve material removal and the required fluence to achieve that is estimated using [55]:

$$F_n = \frac{nh\nu}{\eta\alpha(1 - R)} \quad (2.18)$$

where  $\eta$  is the quantum yield for chain scission,

$h\nu$  is the photon energy,

$R$  is the surface reflection loss

In addition to the photochemical model, another model termed photothermal model is also proposed to explain the decomposition of the polymer via thermal energy [56; 57; 58; 59; 60]. The model is based on the thermalisation of the excited electronic state on a picosecond time scale through vibrational mode of the molecules. This model is confirmed by a number of investigation using  $CO_2$  lasers where effective polymer ablation is seen through pure thermal process [61; 62; 63]. The threshold fluence is estimated using the following equation [46]:

$$F_T = \frac{C(T_D - T_R)}{\alpha(1 - R)} \quad (2.19)$$



where  $C$  is the volumetric specific heat of polymer,  
 $T_D$  is the corresponding temperature,  
 $T_R$  is the initial surface temperature

In most scenarios, it seems that polymer laser ablation cannot be quantified through pure photo-ablation or thermal-ablation alone and hence another model is proposed which is known as photophysical model where both thermal and non-thermal process is involved in the ablation mechanism. The model itself is built on two different assumptions where one assumes that the bond breaking of the polymer is done through two independent channels (thermal and non-thermal) [64; 65]. The other assumption is that the bond breaking of the polymer is done through excitation of different excited electronic states and chromophores [66; 67]. The photophysical model is deemed important to help explain the ablation phenomena using ultrashort pulse lasers (ps and fs) where the frequency of the laser beam is high enough to initiate multi-photon absorption [68].

#### 2.2.4 Plasma

Plasma generation is another phenomenon that occurs during ablation above certain laser fluence, NOP and frequency. During ablation, material is removed through absorption of photon energy by the electron where the absorbed energy is then transformed into thermal energy via electron-phonon coupling the result of which is material removal in vapour form. The vapour produced causes the formation of plasma where the vapour ejected from the material surface stayed in between the laser beam and the ablated region producing a shield that prevent the laser beam from penetrating through as the laser beam is partially absorbed by the plasma [69]. The propagating plasma is also known as laser supported absorption wave (LSAW). If LSAW moves with subsonic velocity with respect to the environment medium, it is known as laser-supported combustion wave (LSCW). When the LSAW speed exceeds the speed of sound due to the increase in laser intensity, it is known as laser-supported detonation wave (LSDW) [17].

Plasma is usually observed at laser power density of  $> 10^{10} \text{ W/cm}^2$  where an inverse Bremsstrahlung process occurs [69]. During this process, the photon energy of the laser beam is absorbed by the free electrons in the plasma which further increase the energy of the electrons and at the same time result an ion recoil to take up the residual momentum. At higher laser power density ( $> 10^{13} \text{ W/cm}^2$ ), this process turns into a collective plasma effect where ion/plasma wave and electromagnetic wave are produced [69]. This process is illustrated in Figure 2.8.

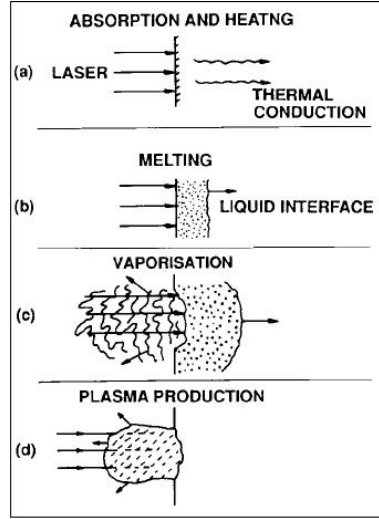


Figure 2.8: Illustration of the occurrence of physical process when a material surface is radiated by a high power laser beam [69].

### 2.2.5 Laser Induced Periodic Surface Structures

Laser induced periodic surface structures (LIPSS) were discovered several years after laser was invented and have been observed for over 40 years. LIPSS can be produced on all materials by all lasers when the surface of a material is irradiated with a certain fluence and NOP. LIPSS is mainly referring to the formation of ripples on the material surface after laser radiation and was considered as laser surface damage in the past [70]. In recent years, such structures have gain interest as periodic structured surfaces have certain applications such as self-cleaning surfaces or enhancing lubrication or tribology of the material surface. The forma-

tion of the ripples is caused by the interference between the incident and surface wave scattered on sub-wavelength imperfections such as corrugations [71]. The orientation and wavelength of the ripples formed by laser irradiation is dependent on the polarization, wavelength, NOP, angle of incidence and fluence of the laser beam [72].

Masataka Shinoda et al. investigated the ripple formation on undoped synthetic single-crystal diamond using a Ti:Sapphire femtosecond laser of 800 nm wavelength. The laser is capable of forming grooves of approximately 300  $\mu\text{m}$  long perpendicular to the laser polarization direction with pulse energy between 72–240 nJ [73]. The grooves have an aspect ratio of  $> 12$  and the average groove spacing is about 146 nm. The formation of the grooves does not change the diamond composition and such grooves are useful for fabricating sub-micrometer devices or nano-imprinting mould in diamond [73]. Figure 2.9 shows the SEM images of the grooves produced on diamond after irradiated with laser beam.

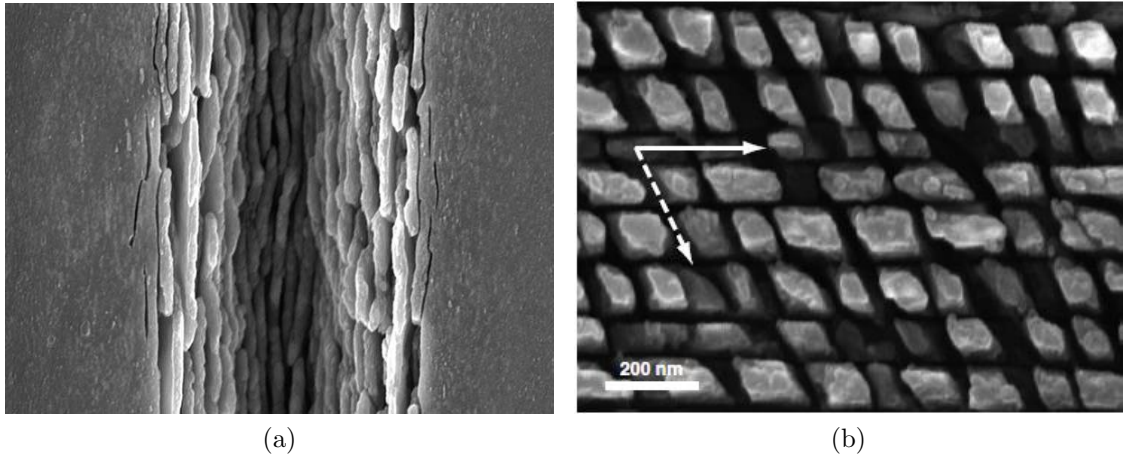


Figure 2.9: SEM images of the diamond surface after irradiated with a 1000 number of pulse at a rate of 250 kHz with a pulse energy of (a) 120 nJ (b) 72 nJ and is processed sequentially using two scanning direction at 0° (bold arrow) and 300° (dotted arrow) [73].

Bert and Hans studied the formation of ripples on alloy 800H stainless steel using Ti:Sapphire femtosecond laser where the ripples are observed using a Helium ion microscope. The formation of pre-ripples is observed and they have a wavelength or spacing between 100–200 nm and an amplitude of 10 nm [74]. At

a fluence of  $13 \text{ mJ/cm}^2$ , small bubbles of diameter  $20 - 90 \text{ nm}$  are formed on the surface of the pre-ripples where the increase in fluence connects the bubbles to the pre-ripples. High fluence ( $4.1 \text{ J/cm}^2$ ) creates clustered particles of diameter  $250 \text{ nm}$  due to joining of several neighbouring bubbles [74]. The formation of bubbles and clustered particles is illustrated in Figure 2.10.

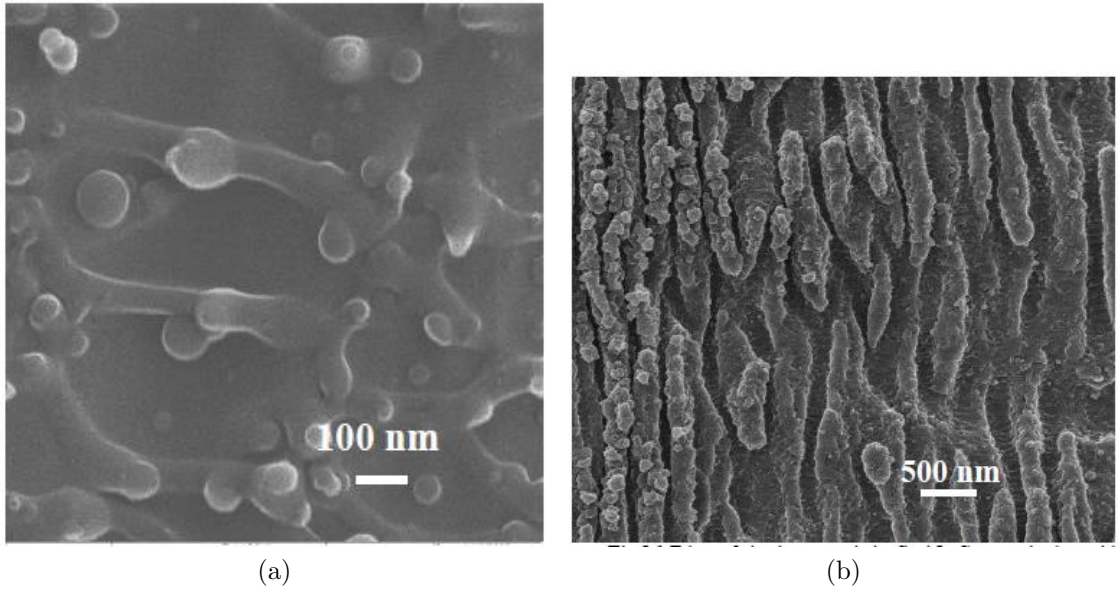


Figure 2.10: SHIM image (a) after 10 scans at  $800 \text{ mm/s}$  with fluence of  $13 \text{ mJ/cm}^2$ . (b) of coarse ripples with clustered particles with fluence of  $4.1 \text{ J/cm}^2$  [74].

Groenendijk and Meijer showed the formation of ripples on stainless steel 304 using a Ti:Sapphire femtosecond laser and observed that the surface of the stainless steel undergoes a surface morphology transition when the NOP, laser fluence and overlap changes [72]. A periodic ripple is first formed after the first incidence of the laser beam and the pits grows as the fluence and the NOP increases. The ripples are then transformed into a chaotic rough structure when the fluence and NOP is at a higher range [72].

## 2.3 Laser Surface Texturing

Laser surface texturing is a process that can generate periodic micro or nano or micro/nano structures involving very thin layer of material surface. LST is usually used to enhance the tribological properties of a mechanical component or to create functional surfaces for certain applications. The earliest commercial application of surface texturing was performed on cylinder honing in an I.C. engine. This process is very common and used to texture the surface of modern magnetic storage devices [75; 76; 77; 78]. In addition, the surface texturing process is also one of the solutions in overcoming the adhesion and stiction problem in MEMS devices [79]. Research in LST processes has been increasing rapidly over the last 15 years and many interesting results have been obtained and one of the examples is shown in Figure 2.11.

LST can be classified in many ways but is mostly classified based on the size of the textured features. In general, it can be classified into two main streams which are micro-surface texturing and nano-surface texturing where the former deals with micron size texture feature and the later deals with nano size texture feature. In the nano size feature, it can be further classified based on different laser texturing techniques as shown in Figure 2.12.

### 2.3.1 Micro-Surface Texturing

In the past 10 years, there are substantial amount of laser surface texturing research work originated in Germany and most of the journals are published in German language where only a few exception publications coming from the group lead by M. Geiger at the University of Erlangen-Nuremberg are in English [81; 82]. This research group used KrF excimer laser with a wavelength of 248 nm and a maximum fluence of  $6 \text{ J/cm}^2$  to perform texturing and they adopted a mask projection technique to produce square dents. The mask projection technique is done by producing mask of desired shape and allows the laser beam to pass through the mask before it is focused such that the geometrical information of the mask is projected onto the surface. Figure 2.13 illustrates the surface finishing of the texturing done on the silicon substrate.

In this research, the textured square sizes vary from  $1 - 1.5 \text{ mm}$  with a textured

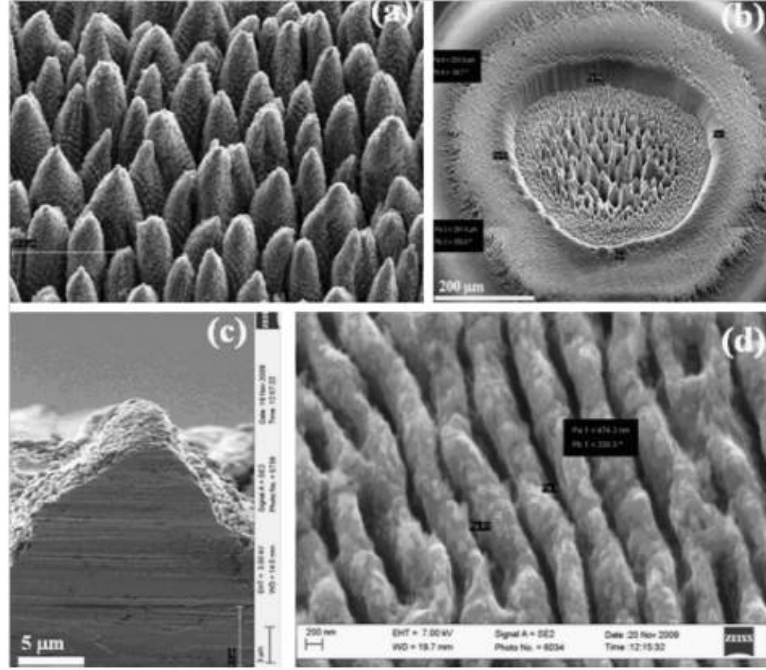


Figure 2.11: SEM image of: (a) laser treated surface showing the formation of micro/nano structures after exposing Ti surface with approximately 500 laser shots at fluence  $1.2 \text{ J/cm}^2$ . Inset is the photograph of a control (gray colour) and micro-structured titanium piece (black in colour), (b) laser-irradiated spot after being exposed with approximately 2000 shots showing the self-organized formation of micro/nanostructures, (c) cross-section of an individual conical microstructure and (d) nanoscale ripples formed on the conical microstructures [80].

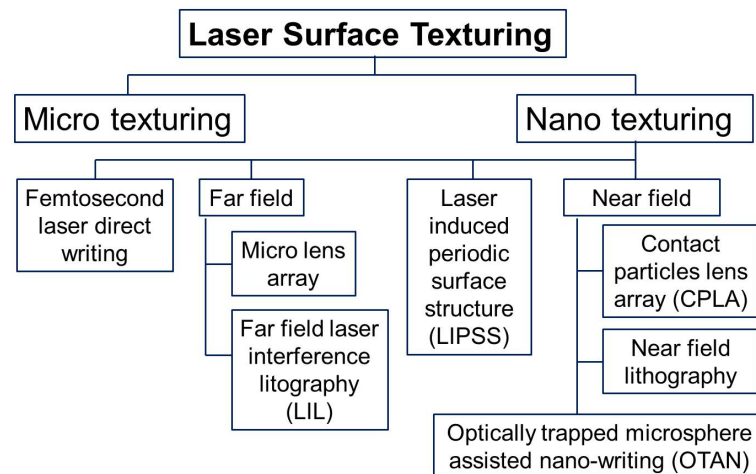


Figure 2.12: Classification of laser surface texturing.



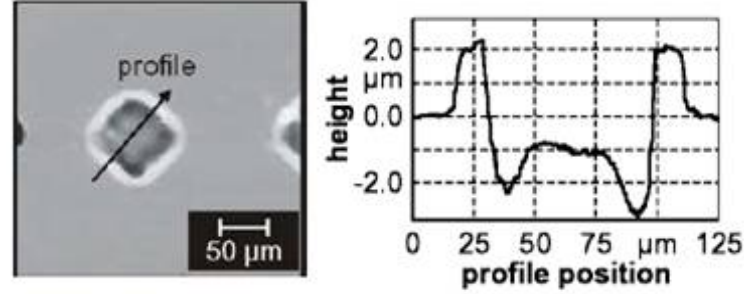


Figure 2.13: 3-dimensional topography measurement /profile of a single texture element [81].

area ratio of 10 % and 20 %. From the experiment, it was observed that tools with a textured area ratio of 10 % has a 145 % increase in the average tool life whereas the textured area ratio of 20 % gives an improvement of 169% in the average tool life [81]. In Tohoku University, Japan, a  $CO_2$  laser was used to study the effect of laser surface texturing on SiC surfaces. The effect of the texturing on transition from hydrodynamic to mixed lubrication regime was the main interest. The texturing done on the SiC surface was in the form of micro-pores with diameter of 100  $\mu m$ , 150  $\mu m$  and 200  $\mu m$  of about 8 – 10  $\mu m$  deep. The pores produced using the  $CO_2$  laser is illustrated in Figure 2.14.

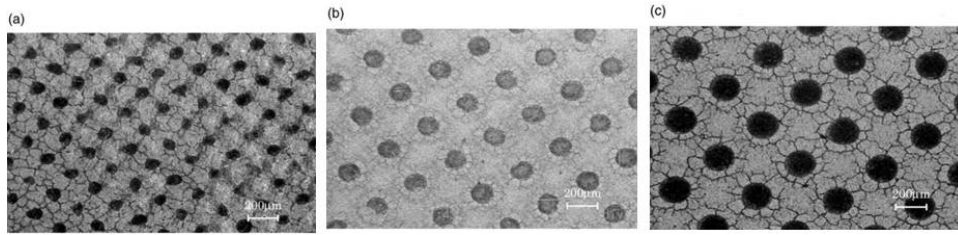


Figure 2.14: Optical images of pores on the disk surface produced by laser texturing. The pores with diameter of (a) 100  $\mu m$ ; (b) 150  $\mu m$ ; (c) 200  $\mu m$  [83].

It was observed that the holes produced by the  $CO_2$  laser has a significant heat affected zone that caused cracks around the holes. The crack definitely affects the performance of the materials as micro-cracks weaken the materials. This is illustrated in Figure 2.15.

It was found that for SiC material, the optimum pore area ratio was about 2.8% where having this pore area ratio, the critical load increased by 20 % as

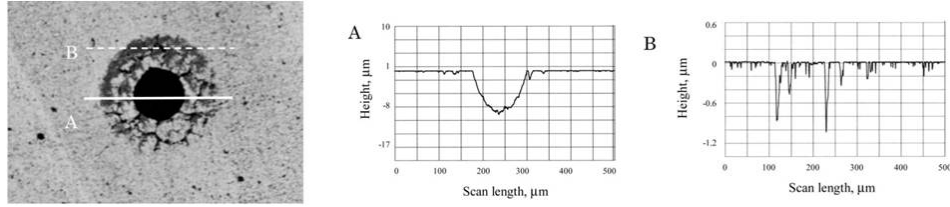


Figure 2.15: Profiles of the pore of diameter  $150\ \mu\text{m}$  and the heat affected zone: (a) at the pore centre, and (b) at the heat affected zone [83].

compared to un-textured surfaces [83].

At the Institute of Applied Physics of the University of Bern in Switzerland, extensive research on LST using Q-switch Nd:YAG laser had been done where most of the work used Ti:Sapphire femtosecond laser [84; 85; 86; 87; 88]. Most of the experiments conducted were mainly focus on the technique of producing surface texturing on different materials and only a small number of tribological tests were carried out to analyse the effect of the texture. G. Dumitru et al. published several papers on texturing different material surfaces such as steel [85], diamond-like carbon (DLC) films [86], diamond, titanium nitride [88] and tungsten carbide [87] where femtosecond laser were mainly used. Figure 2.16 shows the hole finishing on a steel surface using a nano pulsed Nd:YAG laser where the melted region along the circumference of the hole is concluded to be unavoidable.

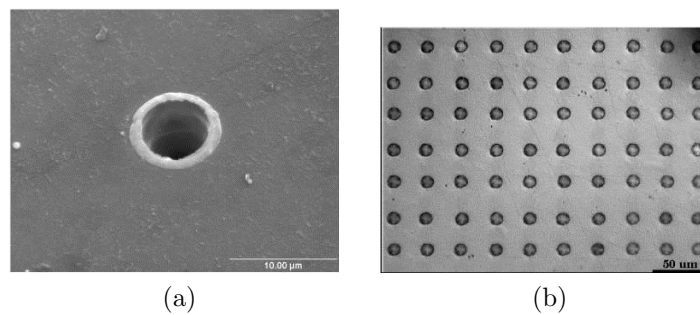


Figure 2.16: (a) “Satisfactory” micro-hole, induced with pulse energy of  $40\ \text{mJ}$  and a  $1/e^2$  beam radius of  $5\ \text{mm}$ . (b) Structure induced on a steel surface [85].

Texturing of tungsten carbide and diamond using femtosecond laser can be performed under normal air condition without any assisted gas or inert gas as



illustrated in Figures 2.17 and 2.18.

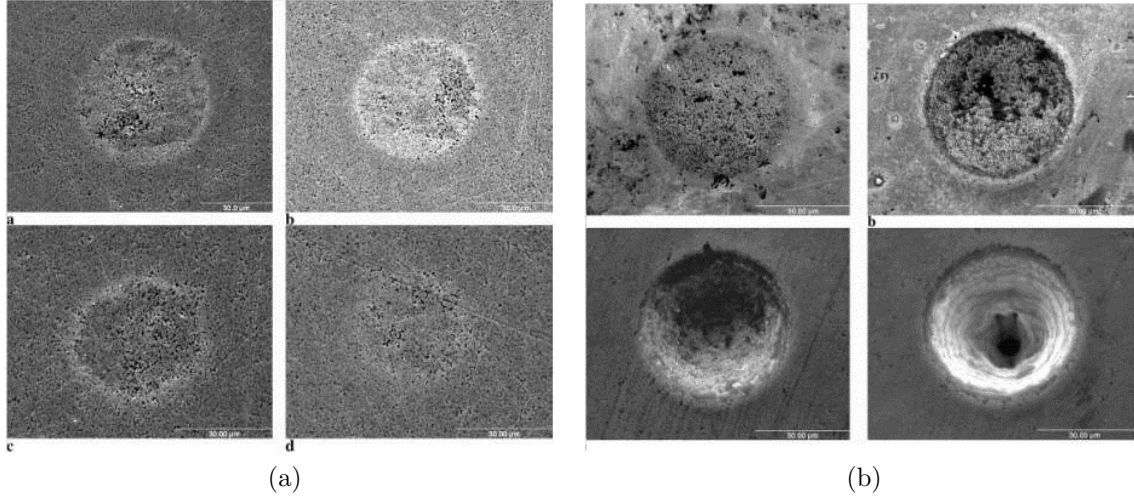


Figure 2.17: Left: Damage on cemented tungsten carbide induced with one laser pulse of 54 (a), 35 (b), 12 (c) and  $4.4 \mu J$  (d). Right: Craters on diamond after 10 (a), 50 (b), 250 (c) and 1000 (d) pulses ( $150 fs$ ,  $54 \mu J$ ) [88].

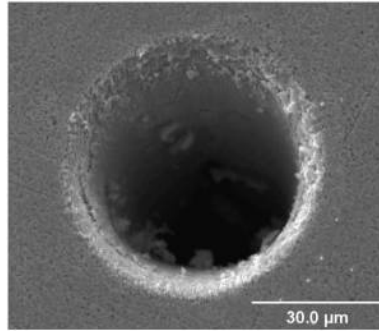


Figure 2.18: Crater in WC-Co produced with 10000 pulses ( $6.5 J/cm^2$ ) using a Ti:Sapphire femtosecond laser of  $100 fs$  pulse width and  $800 nm$  wavelength [87].

### 2.3.2 Laser Surface Cleaning

Lasers have been used for cleaning polymer surfaces, micro-fabricating of polymers by ablation and precise cutting. The geometry and dimensions of laser produced features are highly controllable using process parameters including laser fluence, pulse length and shape, scanning speed and laser shot superposition.

Laser treatment allows partially or complete removal of the superficial polymeric layer without affecting the fibre reinforcement [89; 90; 91; 92]. By selecting suitable laser parameters (laser fluence and NOP), a fully controlled ablation of the superficial polymer layer is obtained.

LST can be performed by individual laser shots or through a mask with a desired pattern. The intensity and interaction time of the laser beam determine the textured volume at the surface which usually ranges from a few nanometres to micrometers. Ultrashort pulsed lasers are mostly used, since they facilitate surface modification without changing the bulk properties of the base material. LST also offers competitive advantages over conventional sand-blasting and chemical treatments due to ease of automation, elimination of effluent, lack of contamination and ability for processing three-dimensional parts. Among various types of lasers, UV lasers are found more suitable for polymers as most organic materials adsorb UV radiation, creating photochemical reactions on the polymer surface of several molecular layers deep without damaging the bulk polymer [93]. The UV laser etching was thus used as a pre-adhesion surface treatment [89; 90; 91; 92; 94; 95; 96] with the advantages of chemical and morphological modification and cleaning of the polymer surface with minimal fibre damage.

The use of an excimer laser treatment to control the adhesion performances of glass/epoxy and carbon/epoxy composites were studied by Benard et al. [91]. After only one laser pulse, a complete cleaning of the surface was reached as evidenced by the complete removal of fluorine contamination shown in Table 2.2. Three different ablation stages were identified which are weak ablation ( $150 \text{ mJ/cm}^2$ , 40 NOP), medium ablation ( $150 \text{ mJ/cm}^2$ , 400 NOP) and total ablation ( $500 \text{ mJ/cm}^2$ , 500 NOP).

The weak ablation mode only provides a surface cleaning with no protrusion of fibre reinforcement or surface roughening as shown in Figure 2.19a. The medium ablation rate induced a rough surface which is composed of both fibre reinforcement and epoxy matrix (dark part on Figure 2.19b). Finally, the total ablation mode exhibits a complete removal of matrix; the residual surface is then composed only of the fibre reinforcement weaving. Laser treated composites showed improved adhesion performance in all the three cases evidenced by single lap shear tests. The use of the 400 NOPs treatment showed that the slight fibre

Table 2.2: Chemical composition (%) of epoxy matrix surface treated with KrF excimer laser of wavelength 248 nm and pulse width of 30 ns determined with ESCA analysis [91].

	C	O	N	F	Si	S	O/C
Bare surface	56.4	8.1	1.5	32.2	1.8	T 0.14	
$50mJ/cm^2 - 1pulse$	80.4	12.5	5.6 0.7	0.5	0.5	0.16	
$150mJ/cm^2 - 4pulses$	76.4 16.9	4.2 -	1.5	0.22			
$150mJ/cm^2 - 10pulses$	78.6	15..9	3.6	-	1.1	-	0.2
$150mJ/cm^2 - 40pulses$	77.8	16	5.4	T	-	0.8	0.21
$150mJ/cm^2 - 400pulses$	77.4	16.9	5	-	-	0.7	0.22
$500mJ/cm^2 - 40pulses$	75.3	15.7	5.8	-	1.9	1.1	0.21

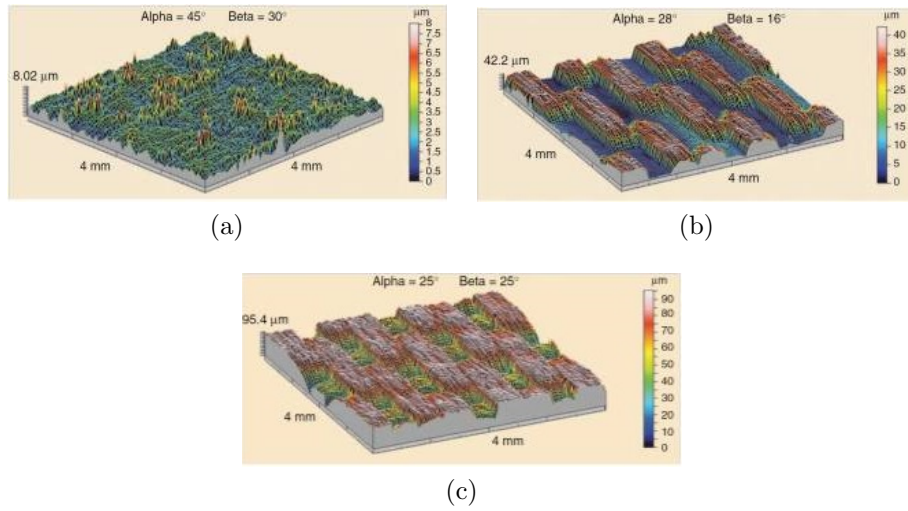


Figure 2.19: Surface profilometry and average roughness of glass/epoxy surfaces treated with different excimer laser beams conditions: (a) 150  $mJ/cm^2$ , 40 *NOP* ( $S_a$  0.6  $\mu m$ ). (b) 150  $mJ/cm^2$ , 400 *NOP* ( $S_a$  13.1  $\mu m$ ). (c) 500  $mJ/cm^2$ , 500 *NOP* ( $S_a$  17.2  $\mu m$ ) [91].

protruding lead to a great increase of lap shear value ( $\sim 30\%$  increase) providing a high performance quality of bonding. As for the totally ablated surfaces, only slight increase as compared to un-textured surface was observed. The decrease of this lap shear value on the extreme laser treatment was believed to be caused by the weak boundary layer between the superficial fibres exposed to laser beam as the SEM observations demonstrated completely ripped off of the reinforcing fibres. With the total superficial matrix ablation, the remaining fibres are not linked to the bulk material, thus explains the premature rupture for such totally ablated samples. The benefit of polymer matrix removal to get fibre protrusion to enhance adhesion performances of composite surface assemblies is consequently limited by the establishment of a weak boundary layer [91].

Rotel et al. investigated the application of an ArF excimer laser ( $193\text{ nm}$ ) for pre-adhesion surface treatment of various thermoplastic composites and some metallic materials as adherend [89; 90]. Laser treated samples were found to have chemical composition changes depending on the fluence identified by FTIR spectra and XPS analysis. The XPS analysis also showed various contaminants such as Mg and Si present on the un-treated surfaces but were absent on the laser treated surfaces. It was found that UV laser irradiation enhanced adhesion strength by  $250\%$  and  $450\%$  as compared to SiC abrasion treatment and un-treated surfaces respectively. The improved adhesion was correlated with the roughening of surfaces, surface chemical composition modification and removal of contaminants. The failure mode was also changed from adhesive to cohesive following laser treatment indicating interfacial adhesion improvement. The optimal laser treatment parameters were found for different polymers and metallic materials. Effectiveness of the treatment was reduced above optimum fluence and NOP due to ablation and carbonization of the surface. Mechanical properties of the laser treated substrates were maintained as the microstructural changes occurred only at superficial outer layers.

SEM images of the un-treated and SiC abraded PEEK composite adherend are shown in Figure 2.20 a and b. The surface of the abraded adherend is markedly damaged, cracked and the exposed fibres are broken. SEM images of the PEEK composite adherend after UV laser treatment at different conditions are shown in Figures 2.20 c - f. The ablation threshold for the PEEK composite was found

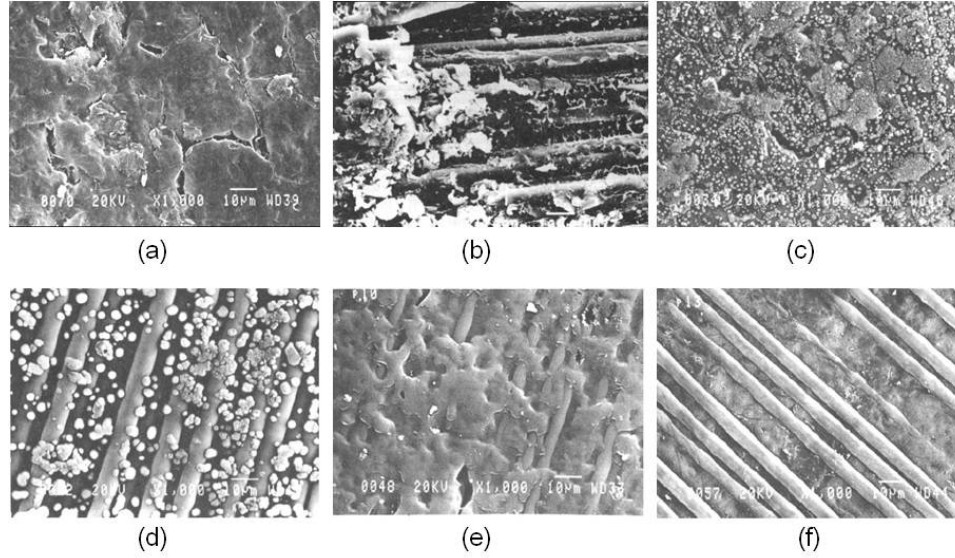


Figure 2.20: SEM images of PEEK composite surface after treatment at various parameters (a) un-treated. (b) SiC-abraded. (c) laser-treated:  $0.18 \text{ J/cm}^2$ , 50 *NOP*, (d)  $0.18 \text{ J/cm}^2$ , 100 *NOP*, (e)  $1 \text{ J/cm}^2$ , 10 *NOP*, (f)  $6 \text{ J/cm}^2$ , 10 *NOP* using a ArF excimer laser of  $193 \text{ nm}$  wavelength [89].

to be  $0.42 \text{ J/cm}^2$  [96]. Below this value, removal of the matrix on the surface region occurs and with high *NOP*, rounded granules are formed on the surface. The formation of granules was found significantly enlarging the surface area and contributed to better mechanical interlocking of the adhesive to the adherend [89]. Once the matrix is removed, the bare fibres are immune to etching. Above the ablation threshold the composite fibres are observed to etch smoothly. Micro-particles and debris redeposit onto the surface leaving a dust like texture. When the ablation threshold was greatly exceeded, fibres were thinned and buckled as shown in Figure 2.20.

Excimer laser surface treatment of glass fibre reinforced epoxy polymer composite done by Park et al. [92] has demonstrated an enhancement of adhesion. It was believed whilst the enhanced adhesion mechanism is contributed by changes in chemical composition through oxidation (from chain of hydrocarbon to polar groups such as carbonyl and hydroxyl group) for the treatment below ablation threshold; it is the increase in surface roughness from the ablation for the treatment above the ablation threshold. At high fluence, the ablation causes instant



fragmentation of polymeric chains, resulting in no oxidation of the surface [97]. Dependence of ablation rate of the epoxy matrix with NOP and laser fluence as shown in Figure 2.21 implies controllability of the selective epoxy matrix ablation process through optimised parameters.

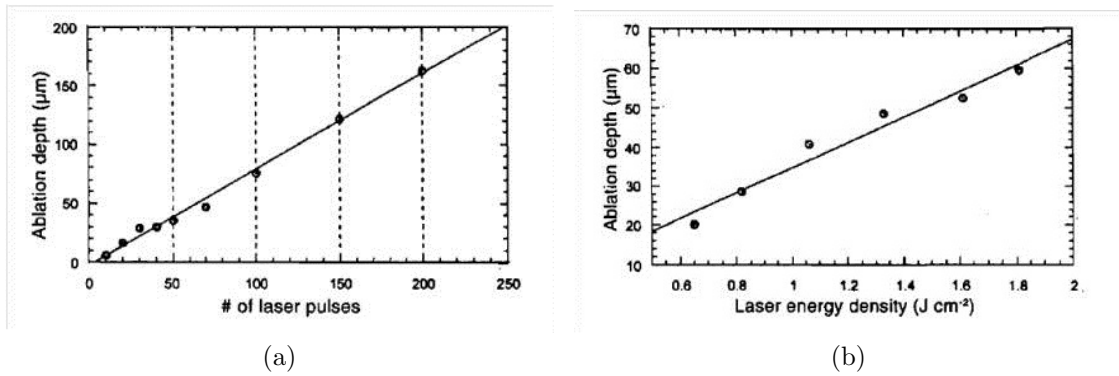


Figure 2.21: Depths of matrix ablation, (a) as a function of the number of pulses, fluence -  $1.01 \text{ J/cm}^2$ , pulse frequency -  $5 \text{ Hz}$  and (b) fluence, number of pulses - 50, pulse frequency -  $5 \text{ Hz}$ , showing linear relationship [92].

Surface modification of silicon and PTFE using 4th harmonic pulsed  $Nd : YAG$  laser ( $266 \text{ nm}$ ) was tested by Dong et al. to improve wettability and adhesion characteristics [98]. It was reported the surfaces treated by  $Nd : YAG$  laser irradiation were roughened and the hydrophobicity of silicon and PTFE surface was modified to hydrophilicity. The increased surface roughness proportional to the increase in wettability also improved adhesion strength of copper spray thin film deposited using  $\text{Ar}^+$  laser beam. The improved adhesion was also believed to be connected with the oxygen enrichment of the laser treated surfaces revealed by XPS analysis. The increased wettability and surface free energy and high percentage of oxygen functional groups through UV laser surface treatment of polymers were also observed by Gotoh et al. [95]. The increase in wettability and the acid-base component of the surface free energy is contributed by the increase in surface oxygen concentration rather than the topographical changes which is expected to cause an increase in adhesion of the polymers with other materials. Nevertheless surface roughness of UV laser treated PET samples was increased as compared to the un-treated sample.

LST is also used for pre-adhesive bonding surface treatment of metallic surfaces to enhance adhesion performance by producing microscopic wavy surface morphologies and nanoscopic surface roughness [99]. Similarly texturing of dental surfaces using lasers was reported to improve bond strength in composite bonding process to these surfaces [100].

## 2.4 Laser Surface Texturing Application

Due to the high reliability and flexibility of laser processing, it is widely adopted in many material surface engineering processes to produce required texture or surface patterns for different applications and is progressively popular in the aerospace and defence industries. In this part of the literature review, the effects of surface textures and surface modifications on adhesion and tribology performances are analysed. The applications involved are paint adhesion, dust attachment and tribological characteristics of moulding dies.

### 2.4.1 Effect of Surface Properties on Adhesion

Laser surface treatment on polymeric materials has been used for the modification of surface morphology and surface chemistry, which results in adhesion properties changes. Adhesion is the interaction between two surfaces at the interatomic level [101]. Adhesion is a complicated phenomenon where its strength is determined by a combination of different forces. Many theories and models that have been proposed over the years after this area of research was first recognised as an important aspect and as bearings to many branches of industry in 1992 [102]. To date, there is no universal model or theory that can be used to predict the adhesion between different materials or interface as it is such a complex system where each system is unique. Among the theories and models proposed, the fundamental of adhesion theory can be classified into four theories where in certain phenomenon, some theories are more influential than the others and it is depending on the type of adhesion and the material of the adherent and adhesive as well as the environment where the adhesion is taken place. The following subsections detail the relevant theories.

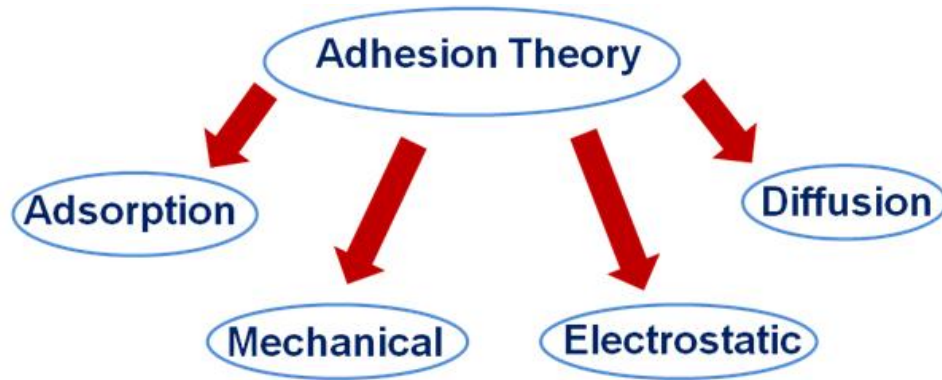


Figure 2.22: Classification of fundamental theories related to adhesion theory.

#### 2.4.1.1 Adhesion Theory

**Adsorption Theory** The adsorption theory is based on the bonding formation or force attractions between two surfaces when they come close together to adhere with each other. This theory is very closely related to the thermodynamic theory of wetting and spreading that has been well developed and understood. This theory deals with the measuring of the surface energy of a substrate surface using either a polar or a non- polar liquid or a combination of different types of liquid measured on the same surface. It relates the surface energy (or surface tension) of a material surface to the contact angle measured as well as the extent of the wetting property of the surface [103].

The adsorption theory states that the attraction force between two surfaces that adhere together is dependent on the chemical nature of the surfaces. To achieve a good adhesion, both surfaces should have strong attraction forces that attract each other such that they can be held together firmly. There are many different types of attraction forces discussed in the adsorption theory and they can be classified into two main categories: primary bond and secondary bond. There are five types of bonds that are associated with primary bond. They are metallic bond, covalent bond, hydrogen bond, ionic bond and ion-dipole interaction bond. For the secondary bond, the forces that associate with it are Keesom orientation force, London dispersion force and Debye induction force. These forces are generally referred to as van der Waals forces. The type of interaction and characteristic of the molecule/ particle involved in each type of secondary forces are



summarised in Table 2.3. The primary bond is used to describe the interaction between surfaces at a macro level, whereas the secondary bond is used in interaction at a micro or nano level. Although secondary forces exist in macro level adhesion interactions, the forces are insignificant compared to the primary bond as the primary bond is usually 10 times stronger than the secondary bond [103].

Table 2.3: Classification of secondary forces [103].

None-polar forces	London	Dispersion	Dipole Interaction	
			Transient/	Transient
Polar forces	Debye	Induction	Permanent/	Induced
	Keesom	Orientation	Permanent/	Permanent

In the case for polymer substrates, the types of bonds formed are strongly influenced by the functional group at the surface where different functional groups have different polarity, resulting in different reactivity due to the stability of the functional groups. In general, polymers have an inert surface as compared to metallic surfaces due to the polymeric chains and the covalent bonding within the bulk material as well as having functional groups that are inert such as alkyl group ( $CH_3$ ). In addition, the presence of contamination on the material surface which is deposited either chemically or as a layer of coating usually contains elements that are inert such as fluorine [91]. Polymer surface with oxygen rich functional groups promotes adhesion where Figure 2.23 shows possible bond formation with different oxygen functional groups on a PMMA surface. A carboxylate functional group ( $C = O$ ) forms hydrogen bond that is acidic where as a carboxylic functional group ( $O - C = O$ ) forms ion/dipole bond which is basic. In addition,  $O = C = O$  group forms ionic bond which is basic. The bond strength for the hydrogen and ion/dipole bond are stronger than the ionic bond.

In the case of metallic substrates, the bonding and adhesion are affected by the microstructure of the metal surface as well as the material properties of the metal itself such as thermal expansion coefficient etc. Most of the bonding is formed through some kind of polar or attraction forces of opposite charges. Such an interaction is very closely related to the acid-basic nature of the surface. Among the different theories of thermodynamic for wetting and spreading, the Lewis acid-base interaction theory has been recognised to be the most suitable theory for

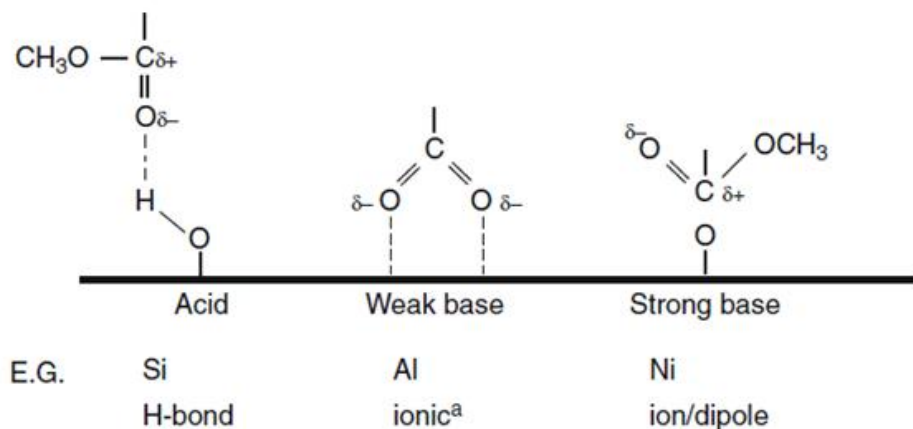


Figure 2.23: Interaction between PMMA surface and surfaces of different acidic and basic nature (After Leadley and Watts, 1997). <sup>a</sup> indicating hydrolysis of the ester and adsorption through the carboxylate anion [103; 104].

calculating surface energy using contact angle data. This is because the model of calculation used in this theory is purely based on the acid-base interaction between a surface and liquid. In addition, the surrounding environment also plays an important role in promoting adhesion as humid environment lower the surface energy of a material [103].

**Mechanical Theory** The mechanical theory also deals with surface energy of a material but in a more geometrical manner rather than chemical or bonding interactions. The theory states that a material with a rougher surface has higher surface energy at the asperity as it has less contact with the surrounding atoms and hence is more ‘reactive’. The argument is illustrated in Figure 2.24 where atom A has higher surface energy because it is only in contact with two atoms. As for atom S on a flat surface, it has lower surface energy than atom A but has higher energy than atom B because it is in contact with 4 atoms. Atom B has the lowest energy as it is in contact with the most number of atoms and is inside the bulk material. Hence, it is the most stable atom among the three atoms due to the geometrical arrangement and the contact surface between the atoms in the bulk material.

Such an argument is more suitable for a metallic substrates due to the atomic

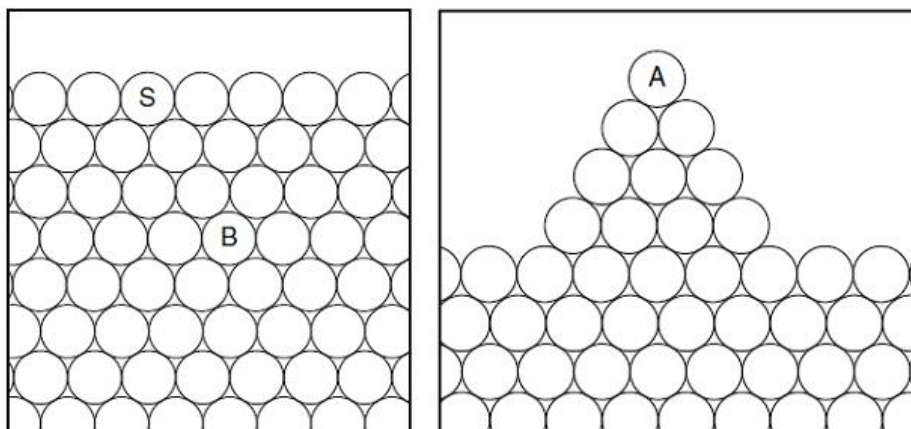


Figure 2.24: Schematic representation of a local environment for an atom in the bulk of a material (B), on a plane surface (S), and on an asperity on a rough surface (A) [103].

arrangement and packing pattern of metallic materials. As for polymeric materials, they consist of chain like structures with carbon backbones and therefore the effect of having less contact with neighbouring polymer chain is quite unlikely. Some researchers argued that the effect of surface roughness in a polymeric substrate surface is more towards providing a larger surface area for the two substrates to form chemical/ molecular bonding due to the existence of polar functional groups.

In general, this mechanism does not ultimately determine the adhesion strength as the strength of the bonding between the two substrates depends on the intimate contact between the substrates. If the contact between the two substrates has voids or vacancies due to the contaminants or inertness of one of the surfaces, it decreases the strength of the bonding between the two substrates.

**Electrostatic Theory** The electrostatic theory of adhesion is based on the fundamental theory of free charges that exist on all condensed materials in the universe. As all materials have electrons, there exists an electrochemical potential difference when two surfaces of different or similar material come close together as the electrochemical state of the two surfaces are different. Hence, free electrons or ionic charges then tend to move from a surface with higher electrochemical

potential to a surface with lower electrochemical potential such that equilibrium is established. The movement of the ionic charge and electrons creates an electrical double layer that act as a force to hold the two surfaces together. The formation of an electric double layer is illustrated in Figure 2.25.

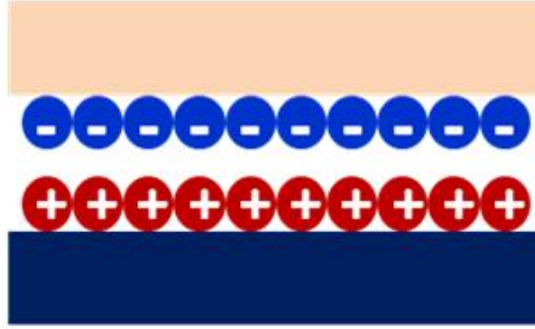


Figure 2.25: Illustration of an electric double layer formation.

This theory was first proposed by Deryagin in 1940s where the model proposed is similar to electron transfer between two plate surfaces which the two surfaces are adhered together [105]. A physical model was then introduced by Deryagin et al. in 1970s that describes the 3D electron double layer that exists between the interface of a solid and a polymer contact surface [106]. Deryagin showed that a correlation exists between the peel energy and the condenser discharge energy where the results are heavily criticised and debated [103]. Recently, Possart has used the potential contrast scanning electron microscopy to study the formation and existence of the electric double layer formed between polyethylene and aluminium surface [107]. He argues that such double layer exists and contributes to the adhesion between two surfaces in addition to other forces and mechanisms. Although most researchers deemed that the influence of the electrostatic mechanism/ force is very low in the mechanism of adhesion, it is still not universally accepted.

**Diffusion Theory** The diffusion theory was proposed by Voyutskii et al. who postulated that the molecules at the surface of two materials that adhere together had some form of interdiffusion process taking place. Due to the diffusion process, the adhesion interface disappears eventually [108]. Vassenin then quantifies the

diffusion process using Fickian diffusion theory [108; 109]. Such a diffusion process can be seen in metallic and polymeric systems although the diffusion process for the two systems is slightly different.

When the surface of a polymer is treated, a boundary layer which is usually in tens of nanometer to several hundred micrometer thickness is produced depending on the process parameters and treatment duration [110]. The cross-link and short polymeric chains affect the bonding capability and strength of the boundary layer and this has been observed in several publications [110; 111; 112; 113; 114; 115]. During surface treatments, the polymer chains undergoes a chain scission process where radical species are formed. The formation of radical species takes place and they react with surrounding media such as water vapour, nitrogen, oxygen or even radicals within the bulk materials. The radicals react with radicals or reactive functional groups within the bulk material to create cross-link whereas the reaction with elements in the surrounding media creates different functional groups depending on the elements available for reaction. The chain scission process forms short chain which weakens the boundary layer, whereas the formation of cross-link strengthen the boundary layer as it is attached to the bulk material more firmly. The phenomenon of cross-link formation also applies when two polymeric surfaces are adhered together. The fracture strength of polymers are dependent on the molecular weight as well as the chain length of the polymer where higher molecular weight and longer chain length results in higher fracture strength [103]. Hence, cross-link formation enhances the strength of the polymer and therefore increases the adhesion strength between two polymeric surfaces. Figure 2.26 shows the cross-link formation model for polymer film.

#### 2.4.1.2 Adhesion on CFRP

Painting, along with many other coating processes such as electrolytic and chemical plating, physical deposition and chemical vapour deposition require the substrate surface to be clean in addition to the existence of micro-textures which allow the deposit firmly held and adhered on the substrate. This is particularly critical for polymer matrix carbon fibre composites as many polymers suffer from low adhesion strength [116; 117]. Surface treatment not only provides favourable

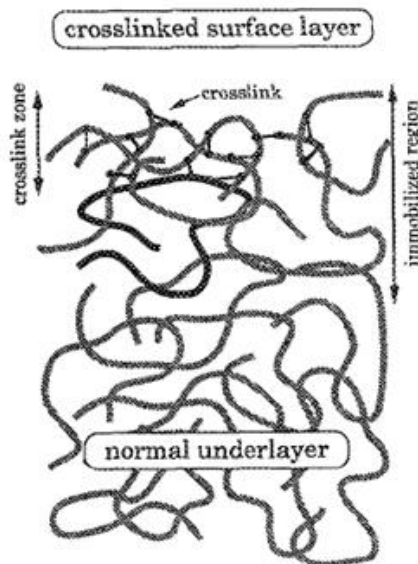


Figure 2.26: Model of polymer film in which cross-linking of the surface has occurred. Highlighted is a cross-link tracer chain [113].

topographical structure that increases surface area and a bond through mechanical interlocking mechanism, it also changes surface chemistry for paint adhesion without affecting the bulk properties.

A wide range of contaminants can be found on composite surfaces and by their nature may form weak boundary layer under the paint. Various techniques have been used to clean contaminants and provide a textured surface, including sand or grit blasting, chemical cleaning or treatment to etch the surface with acid and other corrosive type materials. Once the surface has been cleaned and structured, paint or other deposition materials, depending on applications, is normally applied to the surface by conventional methods such as brushing, spraying, dipping, roll coating, electrostatic coating or immersion. Many of these texturing processes are not commercially suitable due to high cost and severe environmental concerns owing to the use of dangerous chemical substances, which often require safe handling and safe disposal after use.

Laser texturing is a potential substitute to conventional surface modification techniques for some applications. Virtually any type of material can be textured using short pulsed lasers without damages to the bulk substrate. In a laser tex-

turing process, a focused laser beam is used to ablate a micro layer of the surface in a controlled manner in order to alter the surface morphology, or produce local melting and controlled surface waviness on micro-scale. The latter is particularly valuable since previous studies have demonstrated that controllable micro- or nano-roughness enhances the adhesion of subsequently applied layers. The following subsections review various texturing and cleaning techniques for polymers and composites surfaces for enhancing adhesion performance.

**Surface Preparation Methods for Improving Bonding** Various chemical, mechanical and energetic surface treatment methods have been evaluated and reported in the literature for the treatment of polymers and composites for bonding. These evaluations may also provide feasibility indication of their applications to the surface preparation of fibre reinforced composites for painting process. Some techniques are summarized in Table 2.4. Limited evaluation on some of the techniques including laser processing method has been reported in the literature.

Table 2.4: Surface pre-treatment methods.

Mechanical methods	Energetic methods	Chemical methods
Alumina grit blast	Corona discharge	Solvent Cleaning
Cryoblast	Plasma	Detergent Wash
Sodablast	Flame	Acid Ech
Peel ply	Excimer laser	Primer
Silicon Carbide abrasion		

A corona discharge technique was used by Kodokian and Kinloch to achieve chemical composition modification of the thermoplastic composite surfaces and increase wettability to improve interfacial contact and intrinsic adhesion for bonding [118]. Corona discharge technique uses energetic species in an electrical discharge produced from ionized air by applying high voltage between two electrodes above the treated surface. It was found that the surface energy level and consequently wettability of the electrical discharge treated thermoplastic composite increased (water contact angle decreased from 80° to 3°) giving improved adhesion. The improved bond performance was also related to chemical composition

modification of the surfaces by increased type and concentration of oxygen containing groups observed by X-ray photoelectron spectroscopy (XPS).

Plasma treatment has been increasingly used to modify the surface properties producing hydrophobic or hydrophilic surfaces on polymers and metals. Plasma is an ionised gas containing both charged and neutral particles, such as electrons, ions, atoms, molecules and radicals. The treatment of composite materials by means of cold plasma has shown to increase surface wetting properties as well as improving mechanical strength in terms of adhesion between fibres and matrix [119]. The method used for surface activation of polymers allowed the modification of surface characteristics to obtain improved bonding without affecting the bulk properties [120].

Plasma causes ablation of both molecular layers and organic residues from the polymer surfaces to increase surface roughness [121]. This phenomenon has been exploited for improving adhesion purposes through roughening the surface to increase the number of chemical links between the coating and substrate. Carrino et al. studied the cold plasma treatment of polypropylene surfaces to improve wettability and adhesion properties [122]. The water contact angle of the cold plasma treated samples using air gas was reduced by 30 % [122]. The dry and wet adhesion tests on samples painted using a primer have also shown a good adhesion of the paint film, independently of the process conditions. Also dry adhesion tests on samples painted with or without primer had shown a good adhesion of the paint film. Therefore, it represents an efficient, clean and economic alternative to activate polymeric surfaces.

Various other studies have shown formation of reactive energetic species in plasma such as ions and electrons interact with the surface causing chemical composition changes [94; 123]. Davies et al. used oxygen plasma treatment to improve adhesion bonding performance of the thermoplastic matrix composites and obtained much better bonding as compared to sand blasting using 150  $\mu m$  particles, but comparable to chromic/sulphuric acid etching [94]. Analysis of the plasma-treated surface by SEM and XPS showed that the main effects of the treatment was increased in surface roughness and carbonyl content. The plasma did not remove the silicone release agent. It was believed that the plasma treatment was more controllable than acid etching because the chromic acid used



was very aggressive result in rapid etching of the composite surface as shown in Figure 2.27 [94].

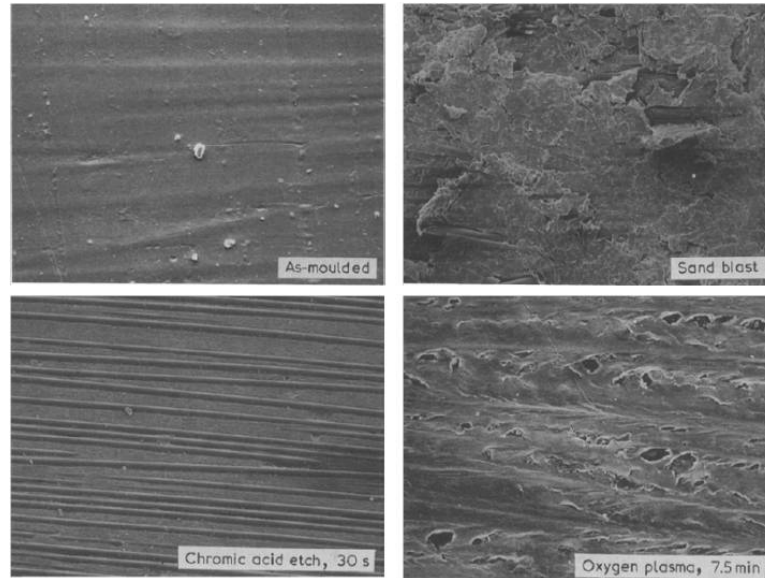


Figure 2.27: SEM images of the surface before and after surface pre-treatment [94].

Jung et al. studied surface modification of polyolefin automobile bumpers by using microwave technology with plasma treatment to enhance wettability and paint adhesion properties [124]. The surface is degreased in detergent solution followed by cleaning with propanol before oxygen plasma treatment and microwave power. Figure 2.28 demonstrates the oxygen plasma treatment induced hydrophilic effect where the water contact angle was decreased significantly (from  $70^\circ$  to  $30^\circ$ ) for the oxygen plasma treated polyolefin samples. The hydrophilic effect is attributed to the increased oxygen functional groups such as O-H and C-O-C on the polyolefin surface with microwave plasma treatment using oxygen gas. Adhesion tests of the plasma treated samples painted without the use of a primer showed improved adhesion.

Peel ply is one of the more common surface pre-treatments among the mechanical surface treatment methods for composite bonding [125; 126]. A peel ply is a layer of nylon or polyester fabric incorporated in the surface of a composite during its manufacturing process and is stripped off the surface immediately

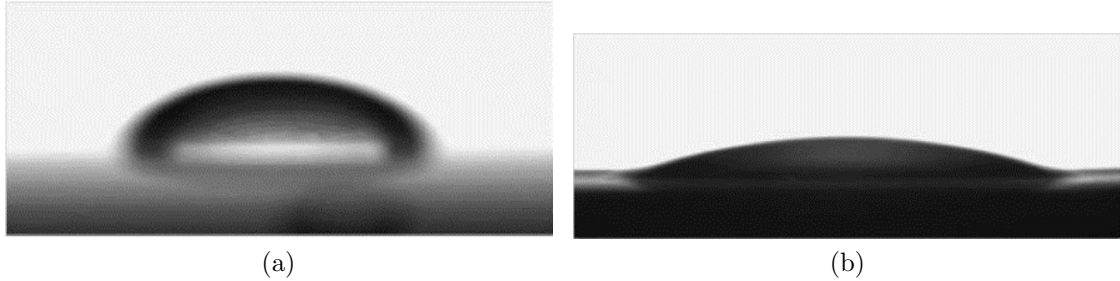


Figure 2.28: Contact angle of water droplet on (a) un-treated and (b) plasma treated polyolefin samples [124].

before bonding giving a rough and clean surface [126]. Several peel plies have allowed increase in surface roughness and surface cleaning efficiency in addition to surface chemical composition modification [127]. Contact angle values also exhibited a sharp decrease resulting from the use of peel ply corresponding to an increase of surface free energy, mostly due to the roughening of the composite surface as well as surface cleaning. Common surface contaminants like fluorinated or siliconed species are completely removed from the composite surface after peel ply treatment [127]. The surface cleaning and roughening lead to improved adhesion as evidenced by an increase of single lap shear values correlated with the increase in surface free energy.

Crane et al. studied the effect of a variety of mechanical surface treatments, including a peel ply, on the wetting and bonding behaviour of carbon/epoxy composite surfaces [125]. The treatments investigated included nylon and Nomex peel ply, and silicon carbide paper abrasion. It was found that the surface energy of the composite was approximately doubled from  $30 \times 10^{-5}$  to around  $60 \times 10^{-5} \text{ mJ/m}^2$  [125]. A 25 % improvement in lap shear strength over untreated carbon/epoxy was noted for the sanded samples, but no improvement in strength was shown for the peel ply treated composites indicating no direct correlation with surface energy. The main problem with peel ply is the cross-transfer of contamination or release agents on the ply to the composite. A regular weave fabric imprint surface morphology was obtained using a peel ply as shown in Figure 2.29a.

Alumina grit blasting has also been suggested as a good mechanical surface treatment for carbon/epoxy composite [128]. The effect of alumina grit blasting

is to modify the morphology of the surface and also to remove some surface contamination. The roughness introduced by the treatment also affects the wetting of the composite. The variables in grit blasting are the size of alumina grit, the blast pressure, the treatment time, the blast angle and the distance from the blast nozzle to the surface. It has been found that even at low blast pressures and short treatment times, fibre damage is evident with most carbon and glass reinforced composites as shown in Figure 2.29b [93]. Similarly silicon carbide abrasion also causes visible damages to carbon and glass fibres in the composite.

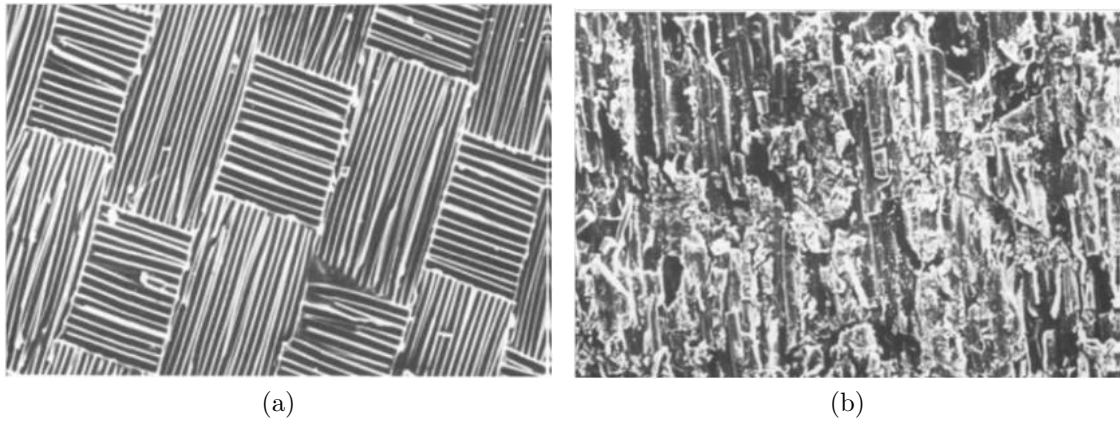


Figure 2.29: SEM images of (a) peel ply treated carbon/epoxy composite and (b) alumina grit blasted carbon epoxy composite [93].

Parker and Waghorne studied the effectiveness of mechanical treatments at removing chemical contaminants such as fluorocarbons and silicones from carbon/epoxy surfaces [129]. Alumina grit blasting and silicon carbide abrasion were found to be superior to Scotchbrite abrasion but none of these techniques removed all contaminants completely. The direct effect of the mechanical treatments on adhesion properties was confused by the detrimental effect of residual contamination, although the best joint strengths were obtained for grit blasted substrates.

**Paint Adhesion** Paint and surface coating are the two most commonly used terminology and are often used interchangeably. Generally, surface coating is referred to any materials that may be applied onto a surface as a continuous

thin layer. Paint on the other hand is used to describe pigmented materials that are used as surface coatings. Non-pigmented materials that form clear films are called lacquers or varnishes. Paint and surface coatings serve two purposes, they improve the aesthetic of the surface and serve as protective layers to the surface. As different types of paint have different properties for different purposes, it is recognised that it is difficult and nearly impossible to fulfil the requirement for painting by just a single coat of paint. Hence, a typical architectural paint system consists of a primer, undercoat and a topcoat. Each of the paints has different purpose, the primer is mainly designed to serve as a binder between the substrate and the undercoat so that the adhesion between the two can be improved. In addition, it also helps to seal the substrate and to make it more even. The undercoat on the other hand serves to provide a smooth surface and a complete coating before the application of the topcoat. All the different types of paints do still serves as protection and aesthetic purposes in addition to the properties mentioned.

In general, paint consists of four components; pigment, binder/film-former, solvent and paint additives [130]. Each of the different components has different functionalities. The pigment serves as a decorative as well as protective purpose in paint. Binder/film-former on the other hand serves as a basis for a continuous film formation on a surface where it holds the pigments together, as the pigment alone can be easily rubbed off a surface. The solvent serves as a solution that prevents the transformation of the binder from liquid state to a solid state through cross-link formation with each other. This is because it is easier to apply paint onto a surface when it is in a liquid state rather than a solid state. In addition, liquid state paint is more spreadable and capable of filling up crevices on a surface. Paint additives are added to enhance the performance of the paint through the addition of desirable properties such as resistant to UV light.

Pigments can be classified into primary pigments and supplementary pigments. Primary pigments are usually solid particulate material that is dispersed in the binder or film former and they are usually minerals. Supplementary pigments are usually other materials that are capable of achieving the properties of a primary pigments but cheaper in price. Hence supplementary pigments are usually used in conjunction with the primary pigments to achieve a specific type

of paint. Table 2.5 summarises some of the commonly used primary pigments in paint.

Table 2.5: Typical primary pigments used in paint [130].

Colour	Inorganic	Organic
Black	Carbon black	Aniline black
	Copper carbonate	
	Manganese dioxide	
Yellow	Lead, zink and barium	nickel azo yellow
	Chromates	
	Cadmium sulphide	
	Iron oxides	
Blue/violate	Ultramarine	Phthalocyanin blue
	Prussian blue	Indanthrone blue
	Cobalt blue	Carbazol violet
Green	Chromium oxide	Phthalocyanin green
Red	Red iron oxide	Toluidine red
	Cadmium selenide	Quinacridones
	Red lead	
	Chrome red	
White	Titanium dioxide	—
	Zinc oxide	
	Antimony oxide	
	Lead carbonate (basic)	

Binder/ film-former are classified according to their molecular weight, either in a low molecular weight or a high molecular weight binder. The selection of the type of binder depends on the area of application due to the different film formation mechanism of the two binders. The low molecular weight binder only forms a solid film when further chemical reaction takes place within the binder. The chemical reaction involved is cross-link formation to yield higher molecular weight molecules. On the contrary, a high molecular weight binder does not require such a reaction and it is usually suspended in aqueous medium where the solid film is formed once the suspension dries off. Table 2.6 summarises examples of the low molecular weight and high molecular weight binders used in paint.

Solvent in general is made of organic liquids and the type of solvent used is largely dependent on the type of binder/ film-former used. In some cases, solvent

Table 2.6: Examples of low molecular weight and high molecular weight binders used in paint [130].

Low molecular weight	High molecular weight
Oleoresinous binders	Nitrocellulose
Alkyds	Solution vinyls
Polyurethanes	Solution acrylics
Urethane oils	Non-aqueous dispersion polymers (NADs)
Amino resins	PVA
Phenolic resins	Acrylic
Epoxide resins	Styrene/ butadiene
Unsaturated polyesters	
Chlorinated rubber	

is also referred to as a diluent due to the functionality of the solvent as it serves as a liquid that does not dissolve polymeric binders. Common solvents used in paint include water, aliphatic hydrocarbon, terpenes, aromatic hydrocarbons, alcohols, ester, ketones, ethers and ether-alcohols, nitroparaffins and chloroparaffins [131]. Paint additives are chemicals added to overcome the defects that occur through painting in order to create a more uniform and better quality coating. The common defects that occur in painting are cissing, shrivelling, floating and flooding [130].

#### 2.4.1.3 Dust Adhesion on Polymer

Dust adhesion is a relatively uncommon topic of research where it is mainly of interest for researchers and engineers in the aerospace and astronomy fields. Dust adhesion involves the interaction of particles with a size smaller than  $10\ \mu m$  with other surfaces, which is very different from macro size particle systems. When such a small particle is adhered to a surface, the gravitational force effect is negligible [132]. The particle adhesion system is size dependent and is not material dependent as any material is capable of forming particles of such small size. For example, sand particles do not cause any real adhesion problems with any surface under normal room temperature and pressure as the gravitational force effect is not negligible due to the size of sand particles. Hence, sand particles can be removed from a surface through vibration. On the contrary, particles of

chalk created when writing on a blackboard adhere on the surface of the blackboard because the particles are smaller and easily trapped between the crevices of the blackboard surface.

J. Visser proposed an idealised geometry for a particle system and is shown in Figure 2.30 to simplify the explanation and modelling of the interaction of the forces involved [133]. In a real system, the shape of a particle can be of any geometry and the surface is not completely flat as compared to the idealised model where the particle is spherical and the adhered surface is flat. Hence when using any of the proposed models to estimate a real system, the difference in geometry has to be taken into account such that the estimation is not overestimated or underestimated.

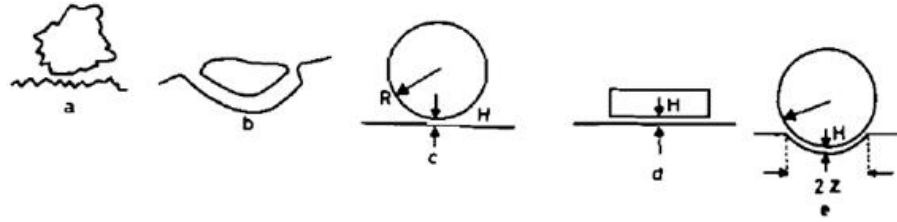


Figure 2.30: Possible particle geometries and surfaces for: (a,b) Real system. (c,d,e) Idealised models [133].

The force interaction of a particle adhering on a surface is illustrated in Figure 2.31. According to the Newton's third law of motion and equilibrium, for every force, there is always an opposite force of either similar magnitude or different magnitude where the resulting force direction and magnitude is the sum of the two forces. When a particle is adhered to a surface, there is a force,  $F_A$  that causes it to stick onto a surface and there is another force,  $F_C$  at the exact opposite direction from  $F_A$  where  $F_C$  is an external force. If  $F_C > F_A$ , the particle is removed from the surface. The force  $F_H$  on the other hand is a force in the perpendicular direction with respect to  $F_A$ , this can be considered to be a force from hydrodynamic movement of air or water.

Force  $F_A$  consists of several different forces. The main contribution is believed to be Van der Waals force, as this force is present in all systems. This force was first proposed by van der Waals in 1873 and was then quantified by London in

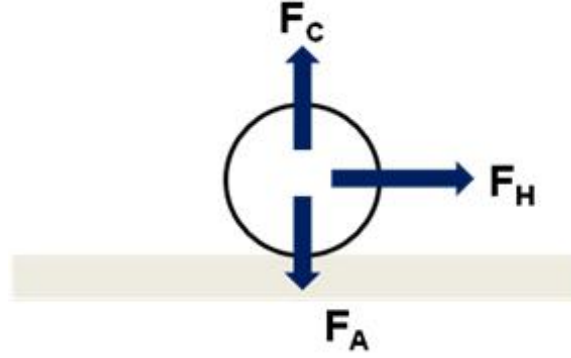


Figure 2.31: Diagram illustrating the force interaction to a particle when adhere on a surface.

1930 when quantum chemistry became available. Hamaker make used of London's idea and proposed a model to calculate such forces in 1937. This consists of two contact conditions where one deals with the interaction between two spherical particles and another deals with the interaction between two flat plates [134]. The equations are given as follow:

Two spherical particles

$$F_A = \frac{AR}{6H^2} \quad (2.20)$$

Two flat plates

$$P_A = \frac{A}{6\pi H^3} \quad (2.21)$$

where  $A$  is the material constant

For a system where a particle is adhering onto a flat surface, the adhesion force is deduced from the two equations above by taking into account of the contact area between the particle and the surface. The resulting equation is as follow [134]:

$$F_A = \frac{AR}{6H^2} + \frac{A}{6\pi H^3} \pi z^2 \quad (2.22)$$



where  $z$  is the radius of the contact area between the deformed particle and the surface

From equation 2.22, it is concluded that the magnitude of the force is dependent on the material constant,  $A$ , the size of the particle as well as the deformed contact area between the particle and the surface.

Electrostatic force is another form of force that can contribute to the adhesion force,  $F_A$ . In a gaseous environment containing airflow, electrostatic forces exist and are transferred between particles when there is a difference in work function. The transfer of charge is in the form of electrons where the particles with higher work function or Fermi-level transfer to the particles with lower work function [134]. The concept of work function is applicable to all materials from metals to semiconductors to glass and polymers [135; 136; 137]. The electrostatic force for sphere plate geometry is calculated using the following equation [134]:

$$F_{EL} = \pi\epsilon_o \frac{R(\Delta U)^2}{H} \quad (2.23)$$

where  $\epsilon_o$  is the permittivity of vacuum,

$\Delta U$  is the potential difference between the two particles

Electrostatic force can also be induced through polarization where a charged particle of a certain distance away from an uncharged surface induces a certain amount of charge of an opposite sign, which leads to an attractive force between the particle and the surface. The induced electrostatic force is given by the following equation [138]:

$$F_{CL} = \frac{q^2}{4R^2} \quad (2.24)$$

where  $q$  is the charge of the particle,

$2R$  is the distance between the particle and the surface

The effect of electrostatic force is non-permanent and can be nullified through charge leakage.

The final factor that contributes to the adhesion force of a particle is humidity. Although the presence of humidity can decrease the electrostatic forces of a particle due to the dipole nature of water molecule, it contributes to the adhesion of the particle to the substrate through capillary condensation. The effect of capillary condensation is shown in Figure 2.32 and the force contributed through this effect is calculated through the given equation [138]:

$$F_{CC} = 4\pi\gamma R \quad (2.25)$$

where  $\gamma$  is the surface tension of water

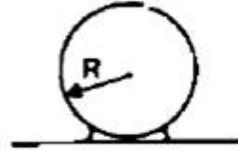


Figure 2.32: Illustration of capillary condensation effect between a spherical particle and a flat surface [133].

In conclusion, the forces that cause a particle to adhere to a surface are contributed by three main forces: van der Waals forces, electrostatic forces and capillary condensation forces. The adhesion forces of a particle are mainly contributed by van der Waals forces.

**Particle Removal Mechanism and Models** A particle can be removed or detached from a surface when a force larger than the adhesion force is applied to the particle. Hence, the particle can be detached through three different mechanisms which are lift-off, slide over or roll on the surface that the particle is adhered to. Tsai et al proposed a critical moment theory stated that the particle adhered to a surface can be detached if the external force moment acted on the particle is larger than the adhesion force [139]. Critical force ratio is used

to quantify the required external moment and is calculated using equation 2.26 where in most cases,  $\alpha_0$  is much smaller as compared to  $d/2$ . The annotation used in the equation is illustrated in Figure 2.33 [139].

$$\frac{F_t}{F_A} = \frac{2a}{2\frac{M_t}{F_t} + d + 2a\frac{F_L}{F_t}} \quad (2.26)$$

where  $F_A$  is the particle adhesion force,  
 $F_t$  is the tangential external force,  
 $M_t$  is the external moment,  
 $F_L$  is the lift force,  
 $d$  is the diameter of the particle,  
 $a$  is the radius of the deformed contact area

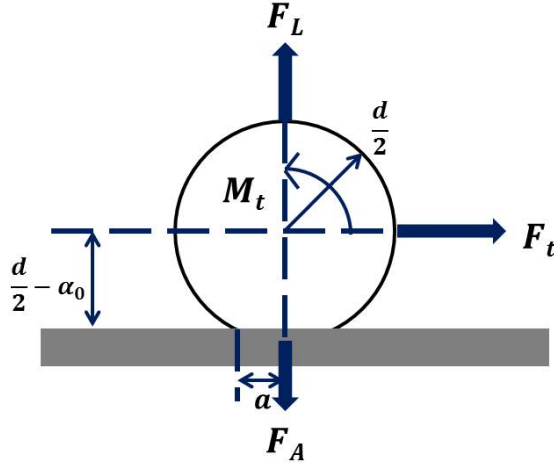


Figure 2.33: Geometry illustration of forces interaction of a spherical particle adheres on a smooth surface.

Wang proposed a calculation for sliding detachment in the study of inceptive motion on particle detachment and it is evaluated using the equation below [140]:

$$F_t \geq kF_A \quad (2.27)$$

where  $F_A$  is the particle adhesion force,  
 $F_t$  is the tangential external force,  
 $k$  is the static friction coefficient

A particle that adheres onto a surface can be re-suspended in air if the external force contributed through hydrodynamic or aerodynamic motion overcomes the adhesion force. The sliding and rolling detachment force required for a specific system can be evaluated using the three particle adhesion models proposed which are JKR model (proposed by Johnson, Kendal and Roberts) [141], DMT model (proposed by Derjaguin, Muller and Toporov) [142] and TPL model (proposed by Tsai, Pui and Liu) [143]. The DMT model is not suitable for such prediction because the model does not assume static equilibrium and it was not developed for particles under the combined normal and tangential force on a frictional surface [144]. Mehdi et al. proposed two models for the rolling and sliding detachment mechanism under turbulence burst/ inrush environment using the JKR and TPL model by calculating the critical sheer velocity needed for such a mechanism to take place. The following equation shows the critical sheer velocity calculation for the rolling detachment mechanism using TPL and JKR model [145].

$$u_{c,TPL}^* = [\{0.5exp[0.124(\Pi - 0.01)^{0.439}] + 0.2 \Pi\} \frac{0.32CW_A}{\rho} \times \sqrt{\frac{K_{20}z_0}{d^3}} (2.43 + 0.07 \frac{du_{c,TPL}^*}{\nu})^{-1}]^{1/2} \quad (2.28)$$

where  $u_{c,TPL}^*$  is the critical shear velocity using TPL model,

$\mathbf{\Pi}$  is the adhesion parameter,

$W_A$  is the thermodynamic work of adhesion,

$C$  is the Cunningham correction factor,

$\rho$  is the density,

$K_{20}$  is the deformation parameter at equilibrium condition,

$z_0$  is the minimum separation distance,

$d$  is the diameter of particle,

$\nu$  is the kinematic viscosity

$$u_{c,JKR}^* = 0.5 \left( \frac{C^{3/2} W_A^2 \pi^{1/2}}{\rho^{3/2} K^{1/3} d^2} \right)^{1/3} (2.43 + 0.07 \frac{du_{c,JKR}^*}{\nu})^{-1/2} \quad (2.29)$$

The critical shear velocity estimation for a sliding detachment mechanism using TPL and JKR model is shown in the equation below [145]:

$$u_{c,TPL}^* = [\{0.5 \exp[0.124(\mathbf{\Pi} - 0.01)^{0.439}] + 0.2 \mathbf{\Pi}\} \times \frac{0.55 C W_A}{\rho d} (2.43 + 0.07 \frac{du_{c,TPL}^*}{\nu})^{-1}]^{1/2} \quad (2.30)$$

$$u_{c,JKR}^* = 0.64 \left( \frac{0.55 C W_A}{\rho d} \right)^{1/2} (2.43 + 0.07 \frac{du_{c,JKR}^*}{\nu})^{-1/2} \quad (2.31)$$

In a turbulent flow situation, rolling detachment is the dominant re-suspension mechanism that occurs for a spherical particle. It is acknowledged that the dynamic torque acting on a particle that is adhered to a wall is significant which helps in particle re-suspension.

## 2.4.2 Surface Tribology

A change in material surface morphology can affect the tribology performance of the material as it affects the tribological responses such as friction and wear which then affect the material performance under certain environments such as rubbing, rolling and forming. In most engineering environments where two material surfaces are in contact, lubrication is generally involved to enhance the performance and also to protect the materials from wear and corrosion. The different classification of each tribological response as well as the different type of lubrications are summarised in the following section. This is then followed by a review on improving machining tool's life cycle where the main concentration is on the capability of laser surface texturing in improving material tribology performance as well as the geometry effect on tribology performance.

### 2.4.2.1 Friction, Wear and Lubrication

**Friction** Friction is referred to as the resistance relative to the motion of two contact bodies and is usually expressed in the form of a friction coefficient,  $\mu$ . Based on the earliest law of friction derived by Leonardo da Vinci, friction coefficient is the ratio of the minimum force,  $F_T$  required to initiate or sustain motion to the normal force,  $F_N$  on a surface. The relationship is shown in equation 2.32. The second law of friction states that the minimum force required to initiate or sustain motion,  $F_T$  is independent on the area of contact,  $A$ . Although the first two laws of friction obey over a large range of conditions, there are still some notable exceptions where the law does not hold.

$$F_T = \mu F_N \quad (2.32)$$

In general, friction can be classified into two categories: sliding friction and rolling friction. Sliding friction refers to the friction between two surfaces that slides between each other. Sliding friction is strongly dependent on several factors including the adhesion between the two surfaces, ploughing by wear particles and hard surface asperity and asperity deformation [146]. The contribution and effect of these factors are dependent on the material, properties and surface topography

of the sliding surface in addition to the sliding environment. Figure 2.34 illustrates different components that contribute to the sliding friction.

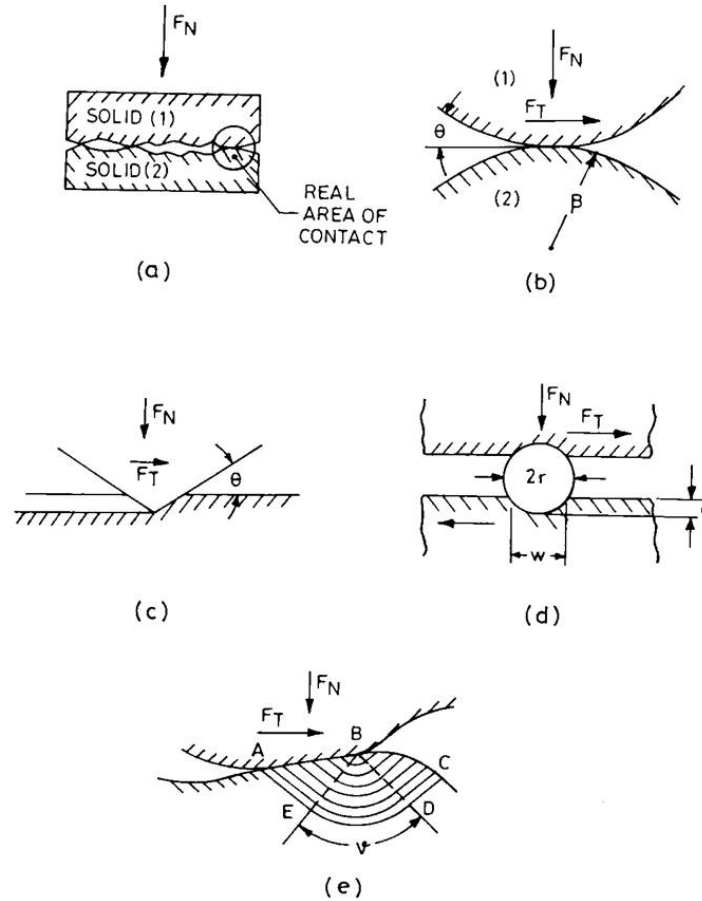


Figure 2.34: (a) Contact between two mating surfaces, (b) adhesion between contacting asperities, (c) ploughing of softer surface by an asperity of harder surface, (d) ploughing by foreign particle entrapped between moving surfaces and (e) slip line deformation model of friction [146].

In reality, material surfaces are not completely flat and are covered with asperities of certain height distribution that deforms elastically or plastically under a given force. Such deformation results in formation and breaking of interfacial bonds which contributes to the adhesion phenomenon of friction [147; 148]. The degree of influence depends on the material property and the degree of interpenetration of asperity as the friction force is dependent on the shear force needed

to shear the weakest tangential plane on the actual contact surface. Ploughing occurs when wear particles produced during the wear process is impacted by a force. Such occurrence is common when one of the sliding surfaces is harder than the other, where the harder material impacts the particle which is then ploughed into the soft material. In addition, the asperity of the harder material surface is ploughed onto the asperity of the softer material surface. Deformation occurs when two material surfaces slide into each other in an opposite direction in a way that the sum of the vertical component of the surface traction is equal to the normal force,  $F_N$ . Plastic deformation is the main contributor towards the friction between two sliding materials as this process is always accompanied by a loss of energy.

Rolling friction on the other hand is generally smaller in magnitude as compared to sliding friction as rolling friction has less occurrence of plastic deformation. It is also a very complex phenomenon as it is dependent on many factors such as the percentage of sliding friction (where it is more commonly known as slipping) taken place as well as energy losses during the deformation process. Classification of rolling friction falls into two categories: transmission of large tangential forces and transmission of small tangential forces. The former refers to a situation such as traction drives and driving wheels where the latter is more commonly known as free rolling. Four main factors are identified as the main contributor towards friction under a rolling contact and they are adhesion, micro-slip, elastic hysteresis and plastic deformation [146].

The contribution of the adhesion towards friction is deemed to be minor due to the interaction mechanism. Rolling contact is very different from sliding contact as the two materials approach and separate in a direction normal to the interface rather than tangential. Hence the main adhesion force between the two contact surfaces are merely van der Waals forces where short-range forces such as metallic bonds only occurs when within the micro-contacts in the micro-slip area. When bonding is formed, the separation is in tension rather than shear as compared to the sliding contact and therefore contributes very little to the friction resistance. Micro-slip occurs in all rolling contacts as a pure rolling action is not possible in reality. This is because when two surfaces are in contact, elastic deformation or plastic deformation occurs regardless of the contact area. Therefore, most



rolling contacts are a combination of rolling and a small degree of slipping. The elastic hysteresis is strongly related to the damping and relaxation property of the material. Hence, it is more common for viscoelastic materials. The occurrence of elastic hysteresis is mainly due to the difference in elastic energy consumed and the stress energy released before and after two surfaces are in contact at a different time as the rolling process is a continuous process. Deformation occurs when the contact pressure between the two surfaces exceeds a certain value and this value is called the maximum hertzian pressure. At the start of the first contact cycle, the surface is first compressed where the residual compressive stress reaches a steady state where further yielding is less likely. This process is called shakedown and the maximum load where this occurs is called the shakedown limit. If the rolling contact is subjected to an excessive load beyond the shakedown limit, the plastic deformation that occurs consists of a forward shearing of the surface. The deformation is accumulative in this case where an equal plastic strain increment is continuously added onto the system after each revolution. When a rolling contact is subjected to a load below the shakedown limit, no occurrence of plastic deformation is observed but occurrence of elastic deformation is visible.

**Wear** Wear is a process of material removal when two materials are in contact with each other through either sliding or rolling motion relative to each other. This process is a complicated process similar to friction where it is influenced by many factors and mechanisms. The wear process is generally a slow, continuous and steady process in a well-designed tribological system. The definition of wear process is ambiguous and imprecise where it is dependent on the practical wear problem and the emphasis intended. The commonly used wear classification is based on the wear mechanism involved where it is categorised into six different categories and they are adhesive wear, abrasive wear, fatigue wear, corrosive wear, erosive wear and electrical arc-induced wear. The wear process is quantified by the amount of material removal per unit sliding distance and is termed wear rate. It can be calculated using the equation below:

$$W = \frac{V}{L} \quad (2.33)$$

where  $W$  is the wear rate,  
 $V$  is the wear volume,  
 $L$  is the sliding distance

Adhesive wear is a process initiated through atomic level contact between two surfaces which forms interfacial adhesive junctions when a normal load is applied. The contact between two surfaces under a normal applied load causes cold welding of the junction and is a continuous process where the junction is sheared off and new junction is formed. During the adhesive wear process, wear particles are produced as well. Adhesive wear is also commonly known as galling or scuffing even though these two terms are used to describe other types of wear. The wear rate resulting from adhesive wear mechanism is described by the well-known Archard equation as described below [149; 150]:

$$W_{ad} = K \frac{F_N}{H} \quad (2.34)$$

where  $W_{ad}$  is the wear rate,  
 $K$  is the wear coefficient,  
 $F_N$  is the normal load,  
 $H$  is the hardness of the softer material

The Archard equation considers the material hardness as the only material properties that affect the wear rate of the material. This equation is suitable for wear rate calculation when the wear contact is an inelastic contact and is proven inappropriate for elastic contacts by Bhushan [151].

Abrasive wear is described as a process of surface damage by a harder material where wear particles are produced as a result of the wear process. It is also known as scratching, scoring or gouging depending of the severity of the wear process. The abrasive wear system in general can be classified into two types: two-body abrasion and three-body abrasion. In the two-body abrasion, it involves the rubbing or shearing contact of two surfaces where one of the surfaces is harder than the other where the softer material surface undergoes abrasive wear.

Example of such operation includes grinding, cutting and machining. In the three-body abrasion, the hard surface is the third body generally in a smaller particle form where it is between two other softer surfaces. In this system, the third body wears off either one of the two surfaces or both via the abrasive wear mechanism. The abrasive wear mechanism happens through pressing of the asperities of the harder surface onto the asperities of the softer material. As the two surfaces slide through each other in the opposite direction, the harder surface asperities removes the softer surface asperities through combining effect of micro-ploughing, micro-cutting and micro-cracking.

Fatigue wear is mainly due to prolong and continuous stress imposed onto the material surface results in micro-cracks (for metals) or delamination (for composites) within the material. There is no physical contact involved in this mechanism and is commonly seen under bearing or shaft environment where periodic and continuous stress is applied to the system.

Corrosive wear has a very different mechanism as compared to the other wear categories where this wear mechanism involves the interaction of the environment with the mating material. The corrosive wear mechanism is a two-step process where the reaction product is first formed on the surface of the material upon reacting with the environment. The reaction product then either result in the formation of cracks or abrasion between the contact of the materials. The process results in an increase in asperity reactivity due to the change in temperature and material properties of the asperities.

Erosive wear describes the wear caused by impingement of either solid particle, small drops of liquid or gas. It is a continuous process in most situations and it only occurs under erosive environment such as in acid or alkaline solution. Erosive wear is highly dependent on the material properties of the surface that is exposed as well as the erosive environment. The wear happens through spattering of material off the surface in a form of atom, molecules or gas when is impacted by either a solid particle, small drop of liquid or gas. This is illustrated in Figure 2.35.

Electrical arc-induced wear mechanism occurs when there is a high electrical potential being supplied across a thin air film between two surfaces in a sliding process. A dielectric breakdown occurs which leads to arcing where a high power

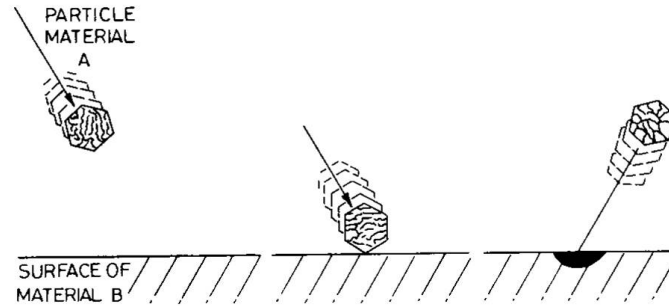


Figure 2.35: Illustration of the typical event of an erosive wear process [146].

density occurs in a very short time. The breakdown results in melting, corrosion and change in material properties such as hardness and phase change.

**Lubrication** Lubrication is a process used to reduce the friction and wear between two sliding or rolling surfaces in the opposite direction. This is achieved through the addition of lubricant between the two surfaces to reduce the contact area as well as reduce the resistance of the sliding motion. The lubricant can be in the form of solid, liquid or gas with certain material properties. In general, lubricant has a low friction coefficient.

Lubrication can be classified into four regimes and they are hydrodynamic lubrication, elastohydrodynamic lubrication, mixed lubrication and boundary lubrication. In the hydrodynamic lubrication system, the two surfaces have minimal contact as there is a thick layer of lubricant film formed between them which prevent deformation of material. The film formed has a maximum thickness at the leading edge and a minimum thickness at the trailing edge due to the pressure distribution of the system. The pressure distribution increases from the leading edge to the trailing edge due to the motion of the sliding as illustrated in Figure 2.36. The friction contribution is mainly from the friction between the lubricants itself. Elastohydrodynamic lubrication on the other hand has more surface contact between the two surfaces where some very little plastic deformation occurred on the sliding surface.

Mixed lubrication region is when the two surfaces experience hydrodynamic lubrication and boundary lubrication condition. In this region, there are sub-

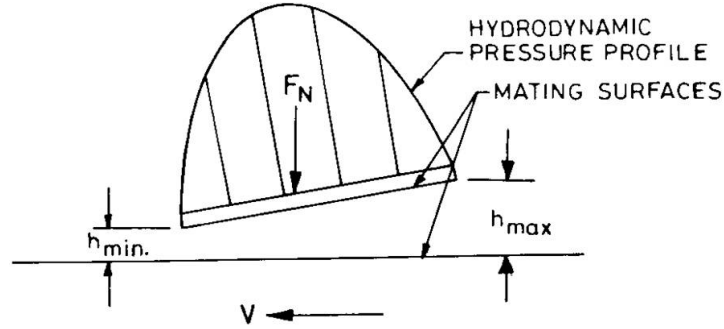


Figure 2.36: Pressure distribution of the lubricant film under hydrodynamic lubrication region [146].

stantial contacts between the asperities on the surface although the two surfaces are separated by a film of lubricant which is very thin in thickness. The friction contribution is mainly from the asperity contact between the two surfaces as well as the friction between the lubricants itself. Boundary lubrication occurs when the lubrication film is so thin that the asperity contact between the two surfaces is more than those in the mixed lubrication region. As the lubrication film is too thin, the friction and wear in the boundary lubrication becomes a very complex process as it is dependent on environmental factors. The classification of the lubrication region can be done by calculating the lubrication parameter which is related to the viscosity of the lubricant, the sliding velocity of the system and the contact pressure as shown in equation 2.35. A Stribeck curve is usually used to relate the lubrication parameter with the friction coefficient of a lubricated system as shown in Figure 2.37.

$$\text{Lubrication parameter} = \frac{\eta v}{P} \quad (2.35)$$

where  $\eta$  is the viscosity of the lubricant,  
 $v$  is the sliding velocity,  
 $P$  is the pressure exerted

By knowing the initial thickness of a film, the specific film thickness can be

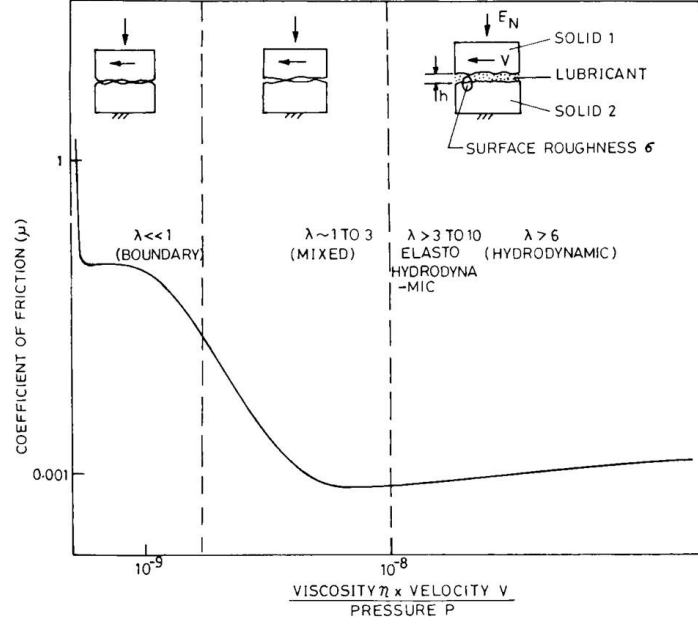


Figure 2.37: Stribeck curve that shows the relation between friction coefficient with the lubrication parameter [146].

calculated using equation 2.36. Table 2.7 summarises the typical lubricant film properties observed in a machine element application.

$$\lambda = \frac{h_{min}}{\sigma} \quad (2.36)$$

where  $\lambda$  is the specific film thickness,

$h_{min}$  is the minimum film thickness,

$\sigma$  is the rms surface roughness

#### 2.4.2.2 Improving Tool's Life Cycle

Many methods have been proposed and investigated to improve the tool life of the dies used in forming and moulding processes due to the significant tooling cost in such processes. Three main research areas that had been investigated in improving the tool wear of dies are:

Table 2.7: Typical lubricant film properties in a machine element application [146].

Lubrication Region	Lubricant Film Properties		
	Lubricant film thickness, $h_{min}$ ( $\mu m$ )	Specific film thickness, $\lambda$	Coefficient of friction, $\mu$
Boundary	0.005 – 0.1	$\ll 1$	0.03 – 1
Mixed	0.01 – 0.1	1 – 3	0.02 – 0.15
Elastohydrodynamic	0.01 – 10	3 – 10	0.01 – 0.1
Hydrodynamic	1 – 100	6 – 100	0.001 – 0.001

- Inventing new types of lubricant
- Perform surface coating with harder materials
- Surface modification to improve lubrication and coefficient of friction between the die surface and the forming sheet surface

Several researches have reported on different types of lubricants. K. Osada and K. Shirakawa have reported the effect of different composition of boron nitride and graphite mixture lubricants on the surface roughness of the formed parts [152]. They also reported the effect of the lubricant on the coefficient of friction between the die and the formed sheet. It was observed that certain types of graphite lubricant caused bad surface finishing with bumpy characteristics and all graphite or graphite rich mixtures showed thinning out behaviour [152]. On the other hand, K.P. Rao and J.J. Wei reported on the property and lubrication effect of newly formulated lubricants on aluminium alloy dies [153]. It was found that boric acid had comparable performance with the commonly used commercial lubricants and it is less toxic with easier and a safer post-cleaning process [153].

Research on the effect of applying different types of coatings such as TiN, CrN, and (Ti,Al)N to improve wear resistances has also been reported. B. Navinsek et al. reported on the improvement of die used for die casting process after coated with TiAlN and CrN coating using plasma vapour deposition (PVD) process [154]. The experiment claimed that the CrN coating improved the service life by 200 – 300 % as well as the cost per injection was lowered by 15 – 40 % [154]. C. Mitterer et al. reported on the effect of TiN, Ti(C,N), Ti(B,N) and

(Ti,Al)(C,N) coating using sputtering and plasma assisted chemical vapour deposition (PACVD) process on aluminium die [155]. It was observed that the TiN coating is capable of increasing the lifetime of the aluminium die whereas the TiN and Ti(C,N) coatings show an optimum combination of hardness, soldering behaviour, adhesion, oxidation resistance and stress state [155]. Similar observations had been found in the research done by Thomas Bjork et al. where multi-layered structure and aluminium content of (Ti,Al)N coating provides a superior chemical and mechanical resistance as compared to a single layered TiN coating [156].

The effect of surface morphology and structure on tool wear and lifetime had been studied as early as 1960's. In 1966, the effect of micro-surface structure in mechanical seal was studied by Hamilton et al. and consecutively by Anno et al. in 1968 and 1969 respectively [157; 158; 159]. It was discovered that the integration effect of the micro-asperities is useful in producing a separating force between parallel seal rings [160]. I. Etsion and L. Burstein also proposed a model to predict the performance of the micro-structured surface seals and found out that the optimum pore ratio is about 20 % where the optimum pore size is dependent on the viscosity of the lubricant, pressure and the pore ratio [160]. The model proposed was verified by experimental results and was shown that the model fits very well with the experimental data [161]. The reasoning behind the effectiveness of the micro-structured surface is as follow [81]:

- The surface has to transport sufficient amount of lubricant onto the forming zone
- The surface has to retain enough lubricant to sustain the formation of hydrostatic and hydrodynamic lubrication effects
- The surface has to have the ability to store wear particles

A micro-structured surface has the ability to achieve all three requirements mentioned above and is believed to act as a reservoir for the lubricant. These micro-structures are usually in the form of micro-dimples with diameter ranging from 50  $\mu m$  to about 200  $\mu m$  and depth ranged from as shallow as 1  $\mu m$  to



about  $10\ \mu\text{m}$ . Figure 2.38 illustrates an example surface morphology of a regular micro-dimple surface produced by laser.



Figure 2.38: Laser Surface texturing of regular micro-surface structure in the form of micro-dimples with diameter of  $100\ \mu\text{m}$ , depth of  $10\ \mu\text{m}$  and dimple density of 20 % [161].

Many techniques have been used to perform metal surface texturing and these techniques include:

- Grit-blasting [162]
- Chemical etching [163] [164]
- Electrochemical treatment [165]
- Abrasive jet machining [166]
- Laser treatment [75; 76; 77; 78]

However, laser surface treatment is still considered to be the best method in producing these micro-dimples because of the advantages of the process in terms of reproducibility and consistency [167]. In addition, laser processing is a non-contact process hence has zero tool wear as it does not have any mechanical interaction with the materials. Furthermore, the ability to produce beam size up to several tens of microns makes this process an attractive option to produce dimples which require small diameter hole sizes. The flexibility of this process in all three dimensions also makes it attractive in producing these dimples as it is

capable of producing these patterns on dies with different geometry and shapes. By properly selecting the machining parameters, dimples of zero edge burr, dross adhesion, minimal heat affected zone and good finishing can be achieved.

#### 2.4.2.3 Effect of Texturing Geometry on Wear

In the last 30 years, many studies have been conducted in analysing the effect of the texturing geometry on the surface tribology for different materials where the effect on the friction coefficient is of main interest. Two forms of contact conditions are investigated which are conformal contact and non-conformal contact. The texturing geometry of interest for circular shape are the diameter of the holes, the distance between the holes and the depth of the holes. The representation and relationship between the holes diameter and the distance between the holes is quantified by the following equation:

$$D_{area} = \pi \left( \frac{d}{2s} \right)^2 \times 100\% \quad (2.37)$$

where  $d$  is the dimple diameter,

$D_{area}$  is the dimple area ratio,

$s$  is the spacing between the dimples

A.A. Voevodin and J.S. Zabinski reported on the effect of different dimple area ratio on the wear cycle for Inconel 718 with TiCN coating under conformal contact condition [168]. The dimples were produced using a solid state  $Nd : VO_4$  laser with wavelength of 355 nm, pulse width of 35 ns, 150  $\mu J$  output power and 5 kHz repetition rate. Solid lubricant was used for the wear life cycle test and friction coefficient test. Three different types of lubricants were used which are  $MoS_2$  dry powder,  $MoS_2$  thin film and  $MoS_2$ /graphite/ $Sb_2O_3$  powder of 58/18/24 weight percentage composition. The dimple diameter was fixed at 10  $\mu m$  and 20  $\mu m$  with 3 – 5  $\mu m$  depth and the spacing between the dimples was fixed between 20 – 200  $\mu m$ . It was observed that an increase in dimples area ratio provides more ample supply for solid lubricant but at the same time increases the surface roughness which decreases the relative area of the hard coating which acts as a

support for contact stress that resist abrasive wear. It was also observed that smaller reservoir dimension could be more beneficial for solid lubricant storage and release [168]. 10 % dimple area ratio was concluded to be the optimum ratio for optimum performance where the separation distance was deemed to be  $50\ \mu m$  with dimple diameter of  $10\ \mu m$  and  $3 - 5\ \mu m$  depth where the optimal ratio is largely dependent on the geometry of the dimple.

H. Ogawa et al. reported on the effect of texturing size on the tribological properties of slideways [169]. The texturing was done using sand blasting process with diameter of  $50\ \mu m$  and  $1000\ \mu m$  of depth  $1 - 16\ \mu m$ . The distance between the dimples was  $100\ \mu m$  and  $1000\ \mu m$ . The effect of parallel and perpendicular groove patterning was also explored. The lubricant used in the experiment was a commercial oil lubricant with viscosity grade of ISO V G68. It was observed that the dimpled surface had a significant effect on reducing the friction in the mixed lubrication regime as compared to the flat surface and was believed to be caused by the difference in the pitch angle under the piling conditions [169]. As for the parallel groove surface, it showed an expansion of the hydrodynamic lubrication regime where it is believed to be due to the preservation of the oil film effect. It was also observed that the thickness of the oil film affects the friction value but was not considered in this experiment.

Andriy Kovalchenko et al. reported on the effect of textured H13 steel surfaces on the transition of lubrication regime from boundary to hydrodynamic under conformal contact condition [170]. The dimples were textured using laser with depth of  $4.5 - 6.5\ \mu m$  with diameter of  $58 - 140\ \mu m$ . The separation distance between dimples was set at  $100\ \mu m$  and  $200\ \mu m$ . Two types of lubricants were used in the experiment and they were low viscosity oil (Mobile - 10W 30) and high viscosity oil (Mobile - 115W50). It was observed that the textured surface had expanded the regime of the hydrodynamic lubrication in terms of load and sliding speed as described by the well-known Stribeck curve and the effect was more pronounce at higher speed and higher viscosity lubricants [170]. It was also observed that the removal of the bulges at the edges of the dimples through lapping after laser texturing was essential as to have a positive impact on the increase in hydrodynamic lubrication regime. The friction coefficient of the textured surface was relatively smaller than the non-textured surface. Another

publication by Andriy Kovalchenko et al. also reported similar observation on the effect of laser surface texturing on transitions in lubrication regimes during unidirectional sliding contact [171].

Andriy Kovalchenko et al. also reported results of laser surface dimpled H13 steel on the friction and wear behaviour under non-conformal contact condition [172]. The steel surface was textured with dimples of  $5.8\ \mu\text{m}$  and  $7.8\ \mu\text{m}$  diameter,  $5-5.5\ \mu\text{m}$  deep and a dimple separation distance of  $80-200\ \mu\text{m}$ . The lubrication used was a poly-alpha-olefin oil (Mobil-1) with different kinetic viscosities and the wear test was done under a normal load of  $10\ \text{N}$  with variable sliding speed. An increase in wear rate was observed for all laser surface textured steel surfaces as compared to the un-textured surface where the increase is due to the reduction in lubrication film thickness.

Chouquet et al. reported results for dimpled diamond-like carbon (DLC) coating on steel on the friction and wear behaviour using laser lithography technique under non-conformal contact condition [173]. The textured dimple had a geometry of  $7\ \mu\text{m}$  and  $65\ \mu\text{m}$  in diameter,  $1.3\ \mu\text{m}$  and  $0.3\ \mu\text{m}$  depth and a dimple area ratio of 14 % and 22 %. The lubricant used had a viscosity of  $0.12\ \text{Pas}$  at  $25^\circ\text{C}$  and the wear test was done under a Hertzian pressure of  $1.1\ \text{GPa}$  and a sliding speed of  $5.5-6.5\ \text{cm/s}$ . A reduction in wear rate was observed for all textured surfaces as compared to the un-textured surface where it contradicts with the results reported by Kovalchenko et al..

Haiwu Yu et al. reported on the effect of geometrical shape of surface texture on the generation of hydrodynamic pressure between conformal contacting surfaces [174]. Three shapes were considered in this research and they are circle, ellipse and triangle and Figure 2.39 illustrates the texture of these shapes was done using a laser process.

An analytical model has been proposed to solve the resultant hydrodynamic pressure induced on each of the shape to see the distribution of the pressure over time. In this model, the orientation of the shape on the direction where the sliding force was applied is crucial and it was found that the shape and orientation of dimples had an obvious influence on the load carrying capacity [174]. It was found that for triangular shape dimples, the load carrying capacity is higher when the point of the triangle is pointing along the direction of the applied force and is

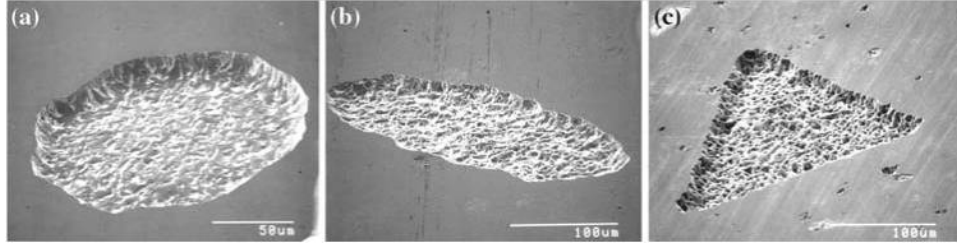


Figure 2.39: Surface texture of different shapes: (a) circle, (b) ellipse, (c) triangle [175].

opposite otherwise. As for the eclipse shape dimple, the load carrying capacity is higher when the main axis is perpendicular to the direction of the force applied and is opposite otherwise. As for the circle shape dimple, it is not affected due to the symmetry of the shape. Figure 2.40 shows the pressure distribution for different shapes and orientations.

## 2.5 Summary

The laser surface texturing process uses an ablation mechanism to achieve material surface structural and chemical composition modification. The ablation mechanisms rely on the interaction of the laser beam with materials and as such interaction is closely related to the electronic and lattice dynamic and absorption of the laser beam by the material. Polymeric materials are found to have high absorptivity in the UV range wavelength whereas for metallic material, the laser beam absorptivity ranged from UV to IR wavelength depending on the properties of the materials.

The efficiency and governing mechanism of ablation is influenced by laser beam wavelength, laser pulse width, laser frequency, number of pulses and material properties where they determine whether the ablation process is thermal or non-thermal. Generally, thermal ablation process is achieved through shorter laser beam wavelength for metallic materials in addition to longer pulse width, higher frequency and NOP. On the contrary, non-thermal ablation process is achieved through shorter laser beam wavelength for polymeric materials and longer laser beam wavelength for metallic materials in addition to shorter pulse width, lower

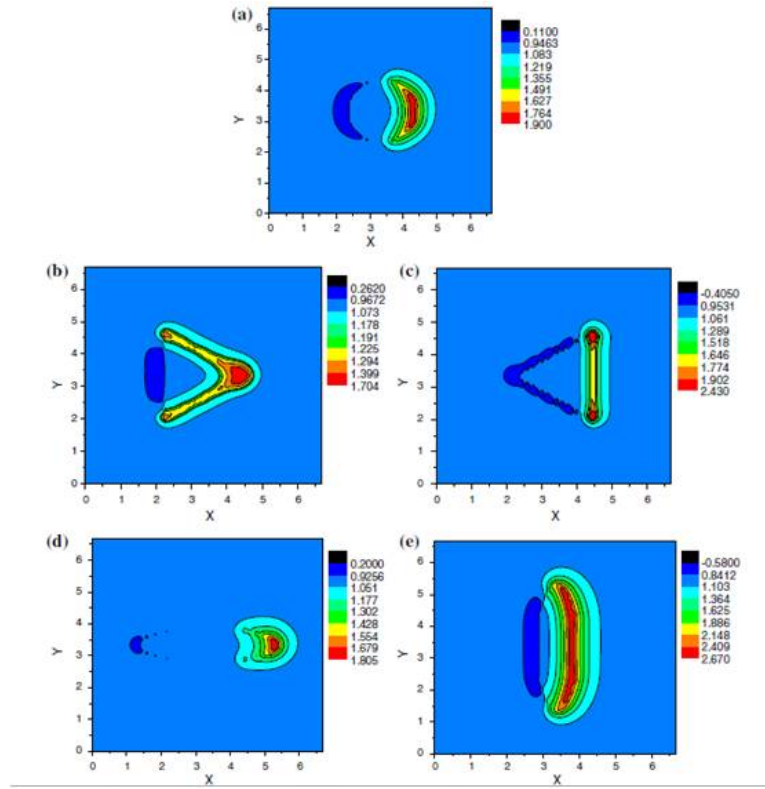


Figure 2.40: Dimensionless pressure distribution of different textural shapes and orientations. (a) Circle, (b) Triangle $\triangle \uparrow$ , (c) Triangle $\triangle \downarrow$ , (d) Ellipse $\parallel$ , (e) Ellipse $\perp$  [174].

frequency and NOP.

The efficiency of laser ablation is quantified using a term known as ablation threshold where it represents the minimum laser fluence required to initiate ablation on a material. The ablation threshold is affected by similar factor as mentioned above and the threshold is found to be dependent on the number of pulses which is known as the incubation effect where the dependency is govern by the incubation factor. The ablation rate is also found to be strongly dependent on the laser fluence used. Under ultrashort pulsed laser ablation for metallic materials, two ablation rates are observed (low fluence regime and high fluence regime) which is described by the two temperature model. As for polymeric materials ablated using short and ultrashort pulsed lasers and metallic materials ablated using short pulsed lasers, only one ablation rate is observed. In addition to surface structural and chemical composition changes, laser ablation might result in plasma phenomena and laser induced periodic structure.

LST has been used in producing nano- and micro-surface texture of different geometry and shapes on different materials for various applications. The two aspect of laser material processing discussed in this literature review are the effects on surface adhesion and tribological performance which is linked to three applications: paint adhesion, dust attachment and tribological characteristics of moulding dies.

Paint is formed through oxidation of binder/ film-former within the solution with oxygen in air which then forms a continuous film on a substrate. During the film formation process, the paint interacts and adheres onto the surface through forces that can be explained using one or a combination of the four different theories which are adsorption, mechanical, electrostatic and diffusion theory where none of the theories can be used to explain all possible adhesion phenomena. Surface treatment for improvement of adhesion for composite has been reported for several surface treatment techniques including corona discharge, plasma treatment, peel ply, alumina grit blasting and laser surface treatment. All reported results shows an increase in adhesion improvement as a result of increase in surface roughness, removal of surface contamination and increase in oxygen and nitrogen rich functional groups on the surface of the polymers The most commonly used laser for surface treatment to improve composite adhesion is the excimer

laser where all published results show an increase in the adhesion strength of the composite surfaces without damaging the fibre and modifying the bulk materials. None of the publications involved any discussion on the effect of laser surface treated composites on paint adhesion improvement.

Dust attachment on the other hand is a relatively uncommon research topic where very little literature is being published in this area. Most published literatures are on particle adhesion where the research and discussion is on building theoretical model for calculating particle adhesion forces. The main forces that cause particles to adhere onto the surface are Van der Waals forces, electrostatic forces, capillary condensation forces and gravity force if the particle size is  $> 10\mu m$ . Particle removal mechanism and model has been proposed in some literature where there exist three types of removal mechanisms: lift-off, slide over and roll on. Theoretical models such as JKR, DMT and TPL model are proposed for calculating critical shear velocity for rolling and sliding detachment mechanism. None of the publications involved extensive experimentation on the effect of laser treated surface on dust attachment.

Micro-dimpled surfaces have been shown to improve tribological performance of moulding die surface in terms of reduction in friction coefficient and wear rate. Dimples of different geometry can be textured onto moulding die materials using different techniques including grit blasting, chemical etching, electrochemical treatment, abrasive jet machining and laser texturing where laser texturing is the most promising technique as it is capable of producing micro or nano size dimples.

Friction coefficient is influenced by the sliding speed, viscosity of the lubricant and the contact pressure of the two surfaces where it is classified into four main regions which are boundary, mixed, elastohydrodynamic and hydrodynamic lubrication according to the Stribeck curve. Each lubrication region indicates different levels of wear and friction coefficient. Micro-dimpled surface shifted the lubrication region from boundary to hydrodynamic lubrication which reduced the asperity contact result in lower wear rate where such improvement is highly related to the geometry of the dimples.

The reduction of wear rate for micro-dimpled surfaces is achieved through increased lubricant thickness where the dimples act as a reservoir to store lubri-



cants as well as wear particle produced during the wear process. The increase in lubricant thickness reduces the contact between asperities of both surfaces causing a reduction in abrasive wear and adhesive wear. The wear rate of a surface is dependent on the density, the size and the depth of the dimple under both conformal and non-conformal contact condition.

Most publications concentrate on wear phenomenon under oil lubrication and conformal contact conditions as such very little literature is found on wear phenomenon under solid lubrication and non-conformal contact condition. There are some contradictions between some published literature on non-conformal contact condition where further clarification and experimentation is required to further understand the effect of dimpled surfaces on friction coefficient and wear rate performance.

## **Chapter 3**

# **MATERIALS AND EQUIPMENT**

### **3.1 Introduction**

This chapter introduces the materials that were investigated, the laser equipment and surface analysis instruments used. Four main materials were investigated, these are CFRP, epoxy resin, HR4 nickel alloy and ABS polymer. Two different lasers were used, excimer laser and Ti:Sapphire femtosecond laser. The surface morphology analysis instruments used in the research included optical microscope, SEM and white light interferometer. The surface chemical composition analysis and surface hardness analysis instrument used in the research included XPS and a microhardness tester. There are other material surface performance instruments used in the research which are introduced in specific chapters where the instruments were used.

### **3.2 Materials**

#### **3.2.1 Carbon Fibre Reinforced Polymer Composite**

Composites are materials consisting of two or more materials with different physical and chemical properties. Composites conserve and combine the desirable

properties of individual materials creating a more superior properties than the individual components. In general, a composite consists of a matrix and fibre material where the matrix acts as a protective layer for the fibres from corrosion and environmental damages. As for the fibres, they act as the stress and load carrier for the composites by which they determine the strength of the materials. The fibres can be woven in different directions and multiple layers such that the strength of the material is multidirectional rather than unidirectional. Carbon and glass are the most commonly used fibre in a composite.

The composite material used in the research was CFRP supplied by BAe Systems. The CFRPs have a dimension of  $4\text{ cm} \times 4.5\text{ cm}$  and a thickness of  $4\text{ mm}$ . The fibre orientation of the CFRPs were  $[0^\circ, 90^\circ]$ . The CFRPs come in two different surface conditions which are smooth surface and rough surface with an underlying imprinted pattern. Figure 3.1 shows the top view of the different CFRPs surface conditions.

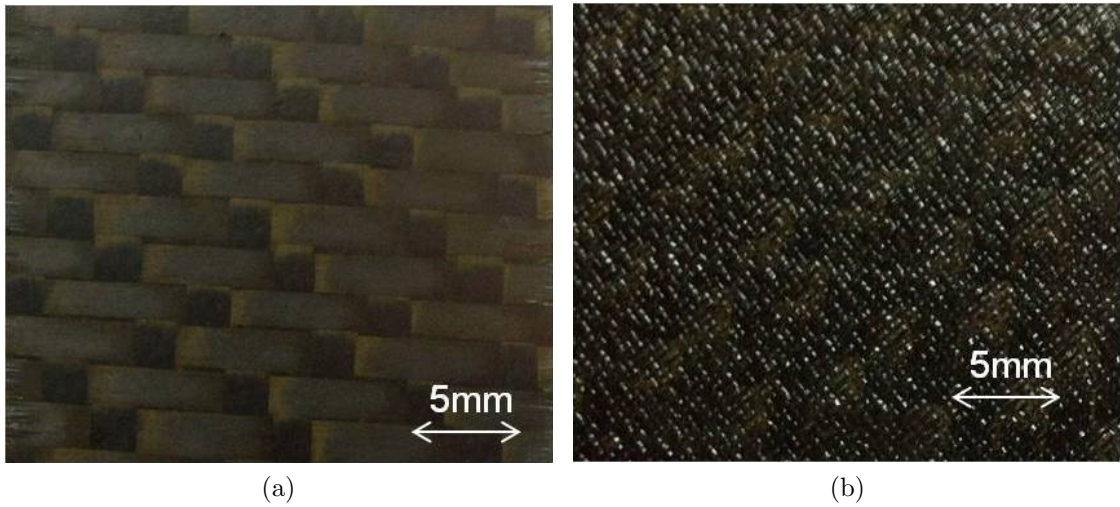


Figure 3.1: Optical images of surface view of (a) smooth surface and (b) rough surface of the CFRP.

### 3.2.2 Epoxy resin

Epoxy polymers are the most commonly used matrix material for composites. There are different types of epoxy resins of which different formulations have spe-

cific desired properties. The epoxy polymer used in the research was an Araldite bisphenol A epoxy resin manufactured by Huntsman Advance Materials. This epoxy is a commonly used in carbon composite manufacturing and it consists of two parts, the resin and the hardener. The epoxy sample was made in house by mixing the resin and the hardener in a ratio of 10 : 1 where the solution was stirred prior to achieving a uniform mixture. The solution was then left in a container to cure for a day. The samples produced were transparent in colour.

### 3.2.3 Nickel Alloy

Metal alloy is a class of material that consists of two or more metals or a metal and a non-metal that exhibits a more superior material properties than the individual components. Nickel alloy exists in a variety of cast and wrought form depending on the manufacturing processes. Nickel alloys are normally classified into two main groups based on the chemical composition. Nickel alloys containing heavy metals are usually grouped together due to the high strength at high temperatures whereas nickel alloys with elements such as Cr, Co, Mn and Fe are usually grouped together [27]. The material used in this research was the nickel cast alloy of british standard grade HR4 supplied by BAe Systems which is mainly used in aerospace application. The elemental composition of the HR4 nickel alloy used in the research is summarised in Table 3.1.

Table 3.1: Elemental composition of the HR4 nickel alloy (weight %).

	C	Mn	Si	Cr	Ni	Nb	Other
Composition (%)	0.6	1.2	1.8	17.5	51	1	W add

### 3.2.4 Acrylonitrile Butadiene Styrene Polymer

ABS is a commonly used thermoplastic due to its high impact resistance and toughness. ABS is a terpolymer consists of three main monomers which are styrene, acrylonitrile and polybutadiene. The chemical formula for ABS is  $(C_8H_8)_x (C_4H_6)_y (C_3H_3N)_z$  where the composition of the three monomers varies. ABS is an amorphous material and hence does not have a true melting point. The ABS

used in the research was supplied by Dyson Ltd where the material is manufactured by Perrite. It comes in size of  $90\text{ mm} \times 55\text{ mm}$  with a thickness of  $2\text{ mm}$ . The material is white in colour and has a density of  $1.04\text{ g/cm}^3$  [176].

## 3.3 Equipment

### 3.3.1 Laser Equipment

#### 3.3.1.1 Excimer Laser

Excimer lasers are one of the commonly used industrial gas laser other than the  $CO_2$  laser. The laser beam of an excimer laser is produced through mixing one of the krypton (Kr), Argon (Ar) or Xenon (Xe) gas with either Fluorine (F) or Chlorine (Cl) gas. The typical gas mixture is  $4 - 5\text{ mbar}$  halogen gas and  $30 - 500\text{ mbar}$  Ar, Kr, or Xe gas with the remaining  $4 - 5\text{ bar}$  filled with He or Ne gas [2]. The laser beam is produced through excitation of  $50 - 100\text{ ns}$  duration of  $35 - 50\text{ kV}$  pulse across the electrodes with a peak current density of  $1\text{ kA/cm}^2$ . Pre-ionisation is also required to avoid electron sparking in the cavity and this is achieved by flooding the cavity with UV light.

The output wavelength of excimer lasers is dependent on the gas composition where different compositions produce a laser beam of different wavelengths in the UV spectrum as summarised in Table 3.2. The output laser beam is usually rectangular in shape with a ratio of  $2 - 3\text{ cm} : 1\text{ cm}$  with a high divergence of  $2 - 10\text{ mrad}$  due to the nature of the system where it is superradiant as well as the high Fersnel number of the cavity. The optics of the laser are typically made from fused silica, crystalline  $CaF_2$  or  $MgF_2$  where one of the cavity mirrors has aluminium coating on the rear surface to prevent corrosion by the halogen gas.

The laser used in the research was a KrF excimer laser model IMPEX 848 from LUMONICS IMPACT equipped with an Aerotech x-y translation stage as shown in Figure 3.2. The laser beam at the excimer laser system output was controlled using an electromechanical shutter and the beam was passed through a focusing lens of  $200\text{ mm}$  focus length before reaching the sample. The specification of the laser is as follow:

Table 3.2: Range of wavelength for excimer laser with different gas mixtures [2].

Gas mixture	Wavelength ( $nm$ )
KrF	248
ArF	193
XeF	354
KrCl	222
XeCl	308

- Wavelength ,  $\lambda$ : 248  $nm$
- Pulse Width: 15  $ns$
- Beam Mode:  $TEM_{00}$
- Output Power, P: 80  $W$
- Frequency: 200  $Hz$
- Peak Pulse Power: 45  $kW$
- Resulting Pulse Energy: 550  $mJ$

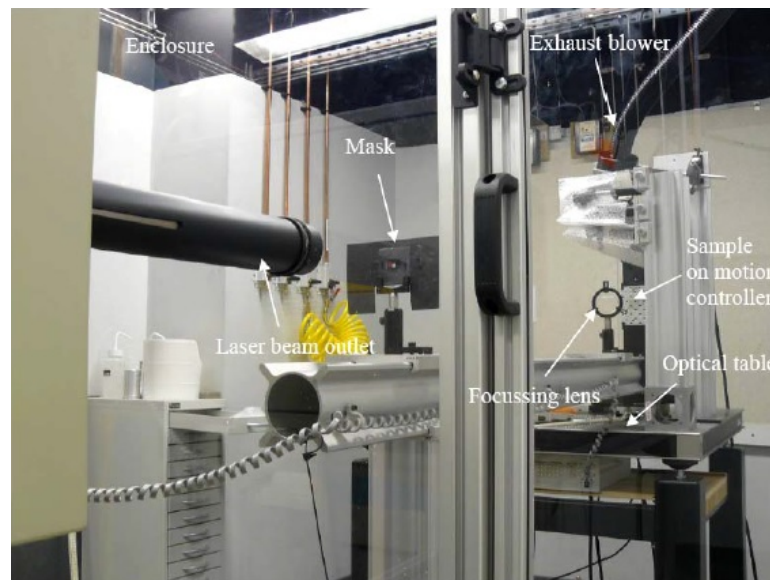


Figure 3.2: Image of the excimer laser layout.

### 3.3.1.2 Femtosecond Laser

Ti:Sapphire laser is a type of diode pump laser where the lasing medium consist of a titanium ion doped sapphire crystal ( $Al_2O_3$ ). The Ti:Sapphire laser produces a laser beam of IR wavelength with an optimum operating condition at a wavelength close to 800  $nm$ . Due to the mode-locked oscillator used in the laser, the capability of producing an ultrashort pulsed laser beam with a pulse width as short as 10 femtoseconds or a few picoseconds is achievable. The oscillator is usually pumped with a continuous-wave laser beam from an argon or  $Nd : YO_4$  laser. This produces laser beam of low average power, 1 – 10 *watt* but high peak power. Hence, such a laser is normally used in laboratory for research purposes due to the efficiency of the instrument even though high machining quality can be achieved.

The laser used in this research was a Ti:Sapphire femtosecond laser (Coherent Libra) equipped with a Galvo head and an Aerotech x-y-z translation stage with the layout illustrated in Figure 3.3 and Figure 3.4. The laser beam at the Ti-Sapphire femtosecond laser system output was controlled using an electromechanical shutter. The beam was then passed through 2 mirrors at an angle of  $45^\circ$  before passing through two attenuators. The beam was directed onto the Galvo head using two more mirrors and a periscope which consisted of two mirrors. The laser beam was then focused through a 97.6 – 99.1  $mm$  focus length f-theta lens within the Galvo head. The focused spot size of the laser beam was measured to be 60  $\mu m$  in diameter through spot diameter measurement of ablated region by varying the focal position. The specification of the laser is summarised as follow:

- Wavelength,  $\lambda$  : 800  $nm$
- Pulse Width : < 100  $fs$
- Beam Mode :  $TEM_{00}$
- Output Power, P : 1  $W$
- Frequency : 1  $kHz$
- Peak Pulse Power : 10  $GW$
- Resulting Pulse Energy : 1  $mJ$

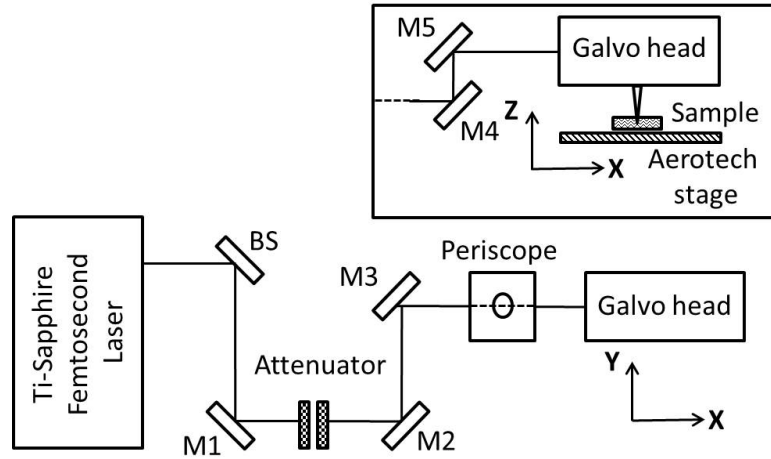


Figure 3.3: Schematic diagram of the femtosecond laser layout (M1, M2, M3, M4, M5, M6: mirror).

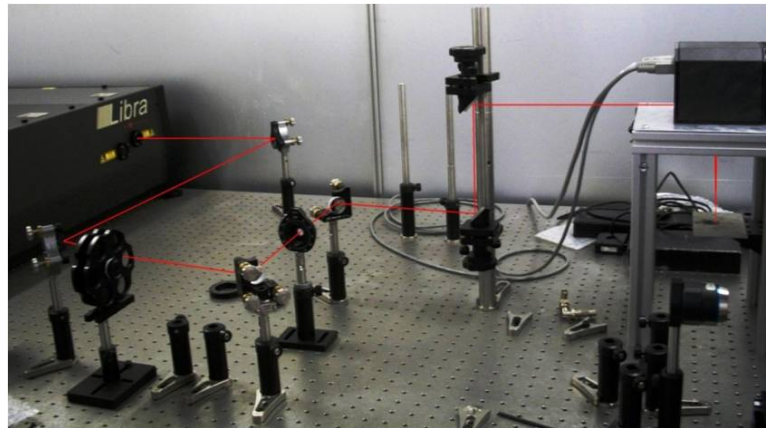


Figure 3.4: Image of the femtosecond laser layout.



### 3.3.2 Surface Characterisation Equipment

#### 3.3.2.1 Scanning Electron Microscope

A scanning electron microscope works by collecting signals produced when a high energy beam of electron hits the surface of the material as shown in Figure 3.5. Typical signals such as back scattered electrons, secondary electrons, characteristic x-rays and light are collected. The primary mode of SEM is the secondary electron mode whereby a high-resolution image of the surface morphology can be obtained with a large depth of focus. The magnification of the image can go from about 40 times to a few ten thousand times depending on the resolution required. Materials have to be electrically conductive to be analysed with a SEM. Non-conductive materials need to be coated with a layer of carbon or gold before it is placed in the sample chamber for analysis. Coating of non-conductive materials can be avoided by using a variable pressure SEM resulting in minimisation of the charging effect. The SEM used in the research to examine the surface of the samples was Evo 50 manufactured by Carl Zeiss AG.

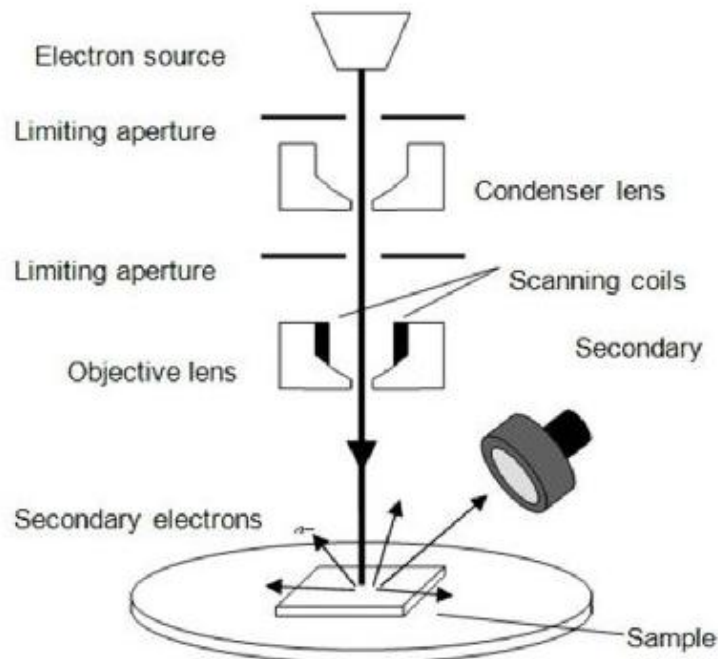


Figure 3.5: Schematic diagram of SEM setup [177].

### 3.3.2.2 White Light Interferometer

A white light interferometer uses light interference theory to image and capture 3D surface topography characteristics of any material surfaces that reflects visible lights. This instrument provides easy, fast and reliable measurement for topography characterisation as no material preparation is required before imaging. The 3D surface topography is obtained through matching the fringes obtained from the surface with the reference fringe set through splitting the light source with a beam splitter as shown in Figure 3.6. The fringes obtained from the surface changes according to the height relative to the objective lens when it moves from the top to the bottom which creates the 3D topography through a computer algorithm.

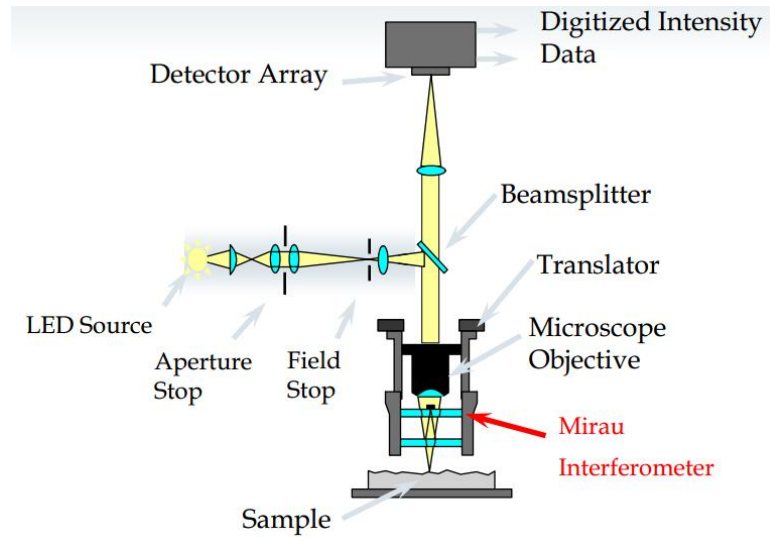


Figure 3.6: Schematic diagram of white light interferometer setup [178].

The white light interferometer used in the research was the ContourGT - K13D optical microscope manufactured by Bruker Corporation. The instrument is capable of measuring surface roughness down to nanometer range for a relatively flat and reflective surface. The image is captured through a CCD camera and is then fed to a computer system with a software that is capable of performing surface analysis such as surface roughness calculation, S-parameter and V-parameter evaluation.

The measurements were taken at 6 random points on the surface and the average of the measurements were taken as the representative surface roughness value. This method was adopted as to avoid having a localised measurement as the measured area for each scan was limited to the maximum size of  $2.5\text{ mm} \times 3\text{ mm}$ . Hence to increase the reliability and better representation of the measurement, the measurement could either be an average of several localized measurements or by obtaining one measurement that covered a sufficiently large area. The later was deemed to be less effective and more prone to error as stitching through a large area using this instrument is relatively difficult and less controllable due to the sensitivity nature of the instrument. In addition, it is time consuming to perform a stitching operation. Although both methods averages across a certain area, the later method is less accurate and less efficient because the first method applied human intervention to the process of averaging hence the error is controllable.

### 3.3.2.3 X-ray Photoelectron Spectroscope

XPS is a surface sensitive quantitative instrument for measuring elemental composition of a material. The measurement is obtained from the top  $10\text{nm}$  depth of the material through irradiation with an x-ray source where the kinetic energy of the electrons that escape from the surface is measured and analysed. The x-ray source interacts with atoms on the surface region through photoelectric effect, causing electrons to be emitted [179]. The emitted electrons have kinetic energies (KE) given by

$$KE = h\nu - BE - \phi \quad (3.1)$$

where  $h\nu$  is the energy of emitted photons,

$BE$  is the binding energy of the atomic orbital from which the electron originate,

$\phi$  is the machine work function

The electrons leaving the sample are detected by an electron spectrometer

according to their kinetic energy. The analyser normally operates using an energy “window”, accepting electrons having energy within the range of this fixed window which referred to as the pass energy. Scanning for different energies is accomplished by applying a variable electrostatic field on the electrons before reaching the analyser. This retardation voltage may be varied from zero up to the photon energy. Electrons are detected as discrete events and the number of electrons for a given detection time and energy is stored digitally or recorded using analogue circuitry [179]. The measurement resolution is dependent on the incident angle of the x-ray source.

The XPS instrument used in the research was a Kratos Axis Ultra equipped with an aluminium/magnesium dual anode and a monochromated aluminium X-ray source. The spectrum was obtained using Al  $K\alpha$  ( $h\nu = 1486.6\text{ eV}$ ) radiation through a scanning area of  $700 \times 300\text{ }\mu\text{m}$  [180]. The binding energy scale was calibrated by setting the C 1s signal at  $285\text{ eV}$ . Wide scan spectrum and high resolution scan spectrum for C 1s, O 1s and N 1s were obtained from each sample.

#### 3.3.2.4 Microhardness Tester

The microhardness tester is an instrument that measures the hardness of the material surface through indentation using a micro-indenter by applying a force perpendicular to the surface of the material. The hardness of a material is estimated through size measurement of the indent formed on the surface using an optical microscope. The microhardness tester used in the research was an Instron Tukon 2100 microhardness tester. The instrument measured Vickers hardness (HV) with a sensitivity of  $0.1\text{ HV}$ . An indentation force of  $0.2\text{ kg}$  was applied for  $3\text{ s}$  with a dwell time of  $10\text{ s}$ .

#### 3.3.2.5 Optical Microscope

An optical microscope uses a system of lenses to magnify sample images through the aid of visible light. Optical microscope are generally connected to a computer system for visualisation and the images are captured using a CCD camera and shown on a computer screen for further analysis such as size measurement. Two optical microscope systems were used in the research and they are  $VHX - 500F$

digital microscope manufactured by Keyence and *DM2500M* microscope manufactured by Leica. The *VHX – 500F* digital microscope was equipped with a 2.11 million pixel handheld camera which enabled clear and crisp observations to be made [181]. The *DM2500M* microscope manufactured by Leica was equipped with a 100 *W* illumination stage as well as having the capability of producing high quality optical images.

## Chapter 4

# LASER BEAM INTERACTION WITH MATERIALS

### 4.1 Introduction

Ablation is an important material removal mechanism in laser surface micro/nano texturing. Hence the understanding of the ablation mechanisms and phenomenon on different materials is crucial for laser texturing parameter selection and optimisation and for the understanding of material property changes. Laser ablation of a material is achieved through initially the absorption of photon energy from the laser beam. Hence, the laser beam absorption characteristics are important. Laser material interaction parameters such as ablation threshold ( $F_{th}$ ), optical penetration depth ( $\alpha^{-1}$ ), thermal penetration depth ( $\ell$ ), and incubation factor ( $\xi$ ) are among the factors to be investigated. The commonly used method in evaluating the laser material interaction parameters are through measuring the diameter [27; 34; 182; 183] or depth [27; 33; 35; 182; 183; 184] of the ablated site using a spot ablation process.

Generally, polymers are laser processed using a UV wavelength laser due to the high absorptivity and photo-chemical reactions [89; 90; 98; 185]. Laser beam interaction with polymers at UV wavelengths has been reported for many years where excimer lasers are mainly used. In the published literature, polymers that had been investigated include polyimide [26; 43; 186], PMMA [26; 43], PTFE

[98; 185; 186], thermoplastic composite [89; 90], ABS [187; 188; 189; 190] and PEEK [186].

In recent years, the introduction of femtosecond lasers with ultrashort pulse widths in the range of  $10^{-14} - 10^{-13}$  s overcomes many of the undesirable thermal defects in machining caused by nanosecond lasers. Femtosecond laser interaction with materials has three main features: rapid energy deposition; creation of a vapour and plasma phase, and ablation of materials without producing molten phase, and having low heat-affected zones which is commonly known as cold machining [35]. Compared with conventional nanosecond laser processing, femtosecond laser processing requires much lower laser fluences to achieve an ablation for metals [33; 184; 191; 192; 193] and is capable of producing sharper contours [35; 194].

Since ultrashort pulse laser processing is a relatively new technology in laser manufacturing, there are limited publications on systematic investigation of femtosecond laser ablation characteristics, although there are a few reports on similar topics [27; 34; 35; 182; 183; 195]. For nickel alloy materials, investigations on femtosecond laser ablation of *CMSX - 4* [34] and *C263* [27] nickel alloys have been published. As for polymeric materials, only investigations on femtosecond laser interactions with polyimide [196; 197], PMMA [197; 198; 199; 200] and polyethylene terephthalate film [201] have been published.

This chapter explores the interaction of a Ti:Sapphire femtosecond laser with HR4 nickel alloy and ABS polymer and KrF excimer laser interactions with epoxy resin polymer and ABS polymer.

## 4.2 Experimental Procedures

The laser beam interaction with materials was investigated through the understanding of laser ablation thresholds and an analysis of the changes in surface chemical composition and morphology after laser treatment. The laser ablation threshold experiment involved irradiating the laser beam on a single spot at different laser fluences and number of pulses to investigate the ablation crater geometry of the materials. The depth of each spot was measured using a white light interferometer. The surface chemical composition changes of the material

after laser ablation was analysed using XPS.

The range of fluences used in the investigation of femtosecond laser beam interaction with nickel HR4 alloy ranged within  $0.5 - 32 \text{ J/cm}^2$  with a pulse repetition rate of  $1 \text{ kHz}$ . The NOP used for the experiment ranged within  $1 - 100$ . The nickel alloy surface was ground with various grades of grinding paper of up to 4000 grit size to achieve a surface roughness of around  $0.1 \text{ }\mu\text{m}$ .

The range of fluences used in the investigation of excimer laser beam interaction with epoxy resin polymer ranged within  $0.05 - 1.5 \text{ J/cm}^2$  with a pulse repetition rate of  $10 \text{ Hz}$ . The NOP used for the experiment ranged within  $50 - 500$ . Three different laser parameters were used to irradiate on both smooth and rough surface of the CFRP for surface chemical composition changes analysis summarised in Table 4.1.

Table 4.1: Excimer laser surface treatment parameters for CFRP.

CFRP surface	Fluence ( $mJ/cm^2$ )	NOP
Smooth	90	3
	175	3
	200	3
Rough	50	20
	250	20
	275	20

The fluence used in the investigation of excimer laser beam interaction with ABS ranged within  $0.05 - 1.5 \text{ J/cm}^2$ , a pulse repetition rate of  $10 \text{ Hz}$  and NOP of 100. The fluence used in the investigation of the femtosecond laser interaction with ABS ranged within  $0.5 - 32 \text{ J/cm}^2$ , a pulse repetition rate of  $1 \text{ kHz}$  and NOP range within  $1 - 100$ . Eight different laser parameters were used for each laser to irradiate the ABS polymer for surface chemical composition changes analysis summarised in Tables 4.2 and Table 4.3.

Table 4.2: Excimer laser surface treatment parameters for ABS polymer.

Fluence ( $mJ/cm^2$ )	50	100	200	400	50	100	200	400
NOP	10				50			



Table 4.3: Femtosecond laser surface treatment parameters for ABS polymer.

Fluence ( $J/cm^2$ )	7.43				3.71			
NOP	1	2	4	8	1	2	4	8

## 4.3 Results and Discussion

### 4.3.1 Femtosecond Laser Beam Interaction with HR4 Nickel Alloy

#### 4.3.1.1 Ablation Morphology

Figure 4.1 shows the optical images of the craters produced on the nickel surface using different femtosecond laser fluences and NOPs. One ablation morphology region was observed at the lowest fluence and NOP with no discolouration of the material surface. Formation of periodic ripple structure was observed after the laser irradiation at a low fluence and NOP ( $9.55 J/cm^2$ , 10 NOP), which is commonly known as laser induced periodic surface structure (LIPPS) and is caused by the interference between the incident and surface wave scattered on sub-wavelength imperfections such as corrugations [71]. Polarization, wavelength, NOP, angle of incident and fluence of the laser beam are the factors that affect the orientation and wavelength of the ripples formed [72]. Such formation is commonly found in materials containing transition metals (Co, Cr, Mo, W, Fe) [27] [182] [202] ablated with a femtosecond laser and is absent in materials containing noble metals (Cu, Au)[195]. This is due to the higher electron heat diffusion length in transition metals as compared to noble metals, which enables transition metals to transfer energy from electrons to the lattice faster due to stronger electron-phonon coupling. As the laser fluence and NOP increases, two ablation morphology regions were observed and marked as ‘A’ and ‘B’ in Figure 4.1b, 4.1c and 4.1d. Discolouration was observed in ablation morphology region ‘B’ but there was no sign of melting or solidification. It was also observed that as the laser fluence and NOP further increased, the area of the ablation morphology region ‘A’ increases whereas the area of the ablation morphology region ‘B’ remains unchanged.

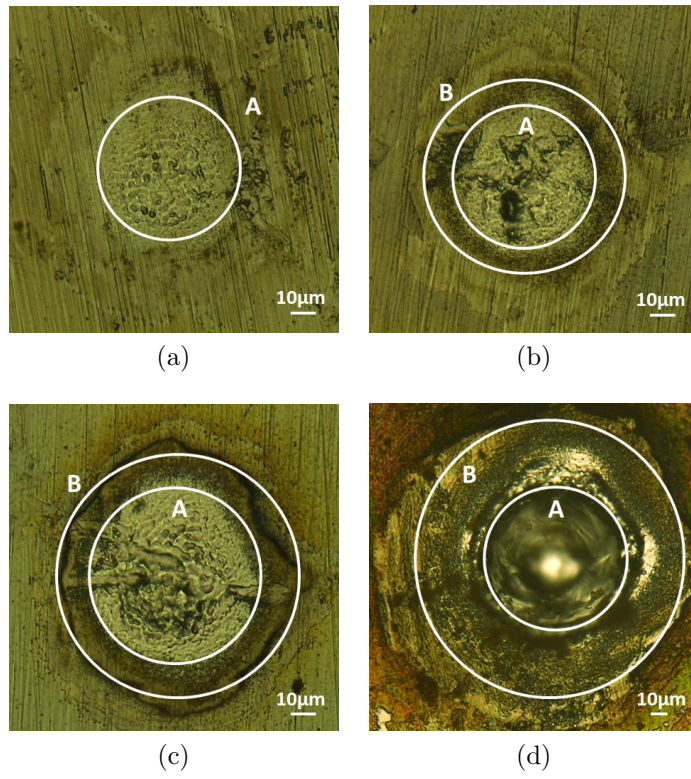


Figure 4.1: Optical images of the craters produced at (a)  $9.55 \text{ J/cm}^2$ , 10 *NOP*, (b)  $10.61 \text{ J/cm}^2$ , 30 *NOP*, (c)  $15.21 \text{ J/cm}^2$ , 100 *NOP* and (d)  $31.12 \text{ J/cm}^2$ , 200 *NOP*.

The above observation on the ablation morphology corresponds to the Gaussian nature of the laser beam. The intensity of the beam decreases radially outwards due to the normal distribution nature of the Gaussian spatial distribution with a peak in the middle. The formation of the two different ablation morphology regions indicates the existence of two ablation threshold regions due to the Gaussian distribution of the laser beam as illustrated in Figure 4.2. The laser fluence is sufficiently low at a certain distance off the centre of the laser beam, which then creates another ablation region with a lower ablation threshold that creates two ablation morphology regions on the surface of the alloy. The shape of the ablated crater resembling the shape of the laser beam was also observed when the laser fluence and NOP are increased as shown in Figure 4.1 and melting becomes obvious and the molten area becomes larger. The shape of the ablated spots are not completely symmetric and circular and this is believed to be caused by non-idealised Gaussian beam profile of the laser beam.

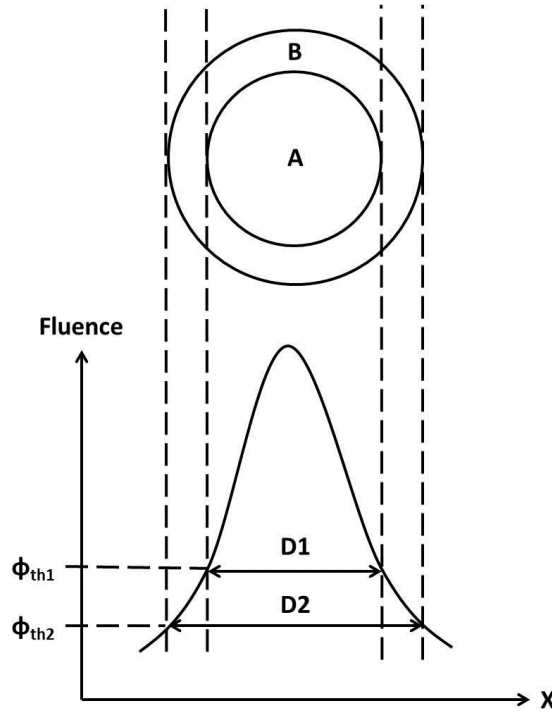


Figure 4.2: Schematic diagram illustrating the correlation between the Gaussian spatial distributions of the laser fluence with the resultant ablation morphology region.

#### 4.3.1.2 Ablation Characteristic

**Spot Ablation** The ablation depth under different laser fluence and NOP was measured and plotted in Figure 4.3. The ablation depth increased with laser fluence and NOP in a linear fashion at different rates where the ablation rate also increased with laser fluence and NOP.

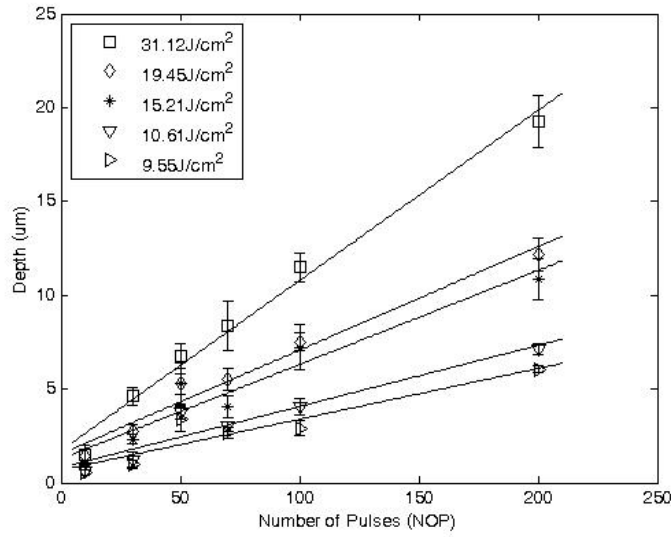


Figure 4.3: Plot of ablation depth versus NOP for different laser fluence.

The ablation threshold can be determined through either measuring the diameter or the depth of the ablated region. The fluence distribution of a Gaussian spatial beam profile,  $F(r)$  with a laser beam spatial radius,  $\omega_0$  can be described using [203]:

$$F(r) = F_0^{pk} \exp \left( -\frac{2r^2}{\omega_0^2} \right) \quad (4.1)$$

where  $r$  is the radial distance from the centre of the Gaussian spatial beam profile,  $F_0^{pk}$  is the peak laser fluence when  $r = 0$

The square of the diameter of the ablated crater is governed by the equation:

$$D^2 = 2\omega_0^2 \ln \frac{F_0^{pk}}{F_{th}} = 2\omega_0^2 \ln \frac{E_p}{E_{th}} \quad (4.2)$$

where  $D$  is the crater diameter,  
 $E_{th}$  is the pulse energy,  
 $E_p$  is the threshold pulse energy

The peak pulse energy is related to the peak laser fluence with the following equation:

$$F_0^{pk} = \frac{2E_p}{\pi\omega_0^2} \quad (4.3)$$

The square of the diameter ( $D^2$ ) measured was plotted against  $\ln(E_p)$  as shown in Figure 4.4 to evaluate the laser beam spatial radius,  $\omega_0$  on the material surface using equation 4.2. The value of  $\omega_0$  was evaluated to be  $32.3 \pm 0.65 \mu m$ , which is close to the spot size of the laser beam which was then used to calculate the peak laser fluence using equation 4.3. A plot of  $D^2$  vs  $\ln(F_0^{pk})$  was plotted which was then used to evaluate the ablation threshold through extrapolating the linear fit to obtain the x-axis interception value as shown in Figure 4.5. The ablation threshold for a NOP of 1 was estimated to be  $0.408 J/cm^2$ .

From Figure 4.5, it can be seen that the ablation threshold decreased with NOP which was also shown on a different plot in Figure 4.6a. The dependence of ablation threshold on NOP is known as an incubation effect and is govern by equation 4.4. Such an effect is caused by the formation of plastic stress-strain induced by heat accumulated from laser radiation that is not completely dissipated resulting in a local plastic deformation in metals. The material is able to be ablated at a lower threshold due to the degradation of the material properties as a result of the plastic stress-strain formation. The ablation threshold was lowered drastically at the first 25 NOP and then gradually decreased with further increase in NOP. The ablation threshold decrease asymptotically where the ablation threshold reached a constant value,  $F_{th}^\infty$  when NOP tends to infinity. This implies that when the surface is irradiated by a laser fluence below  $F_{th}^\infty$ , it

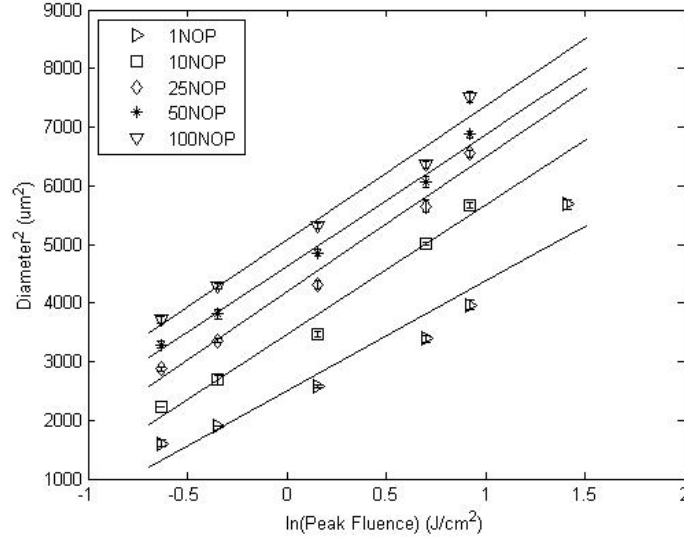


Figure 4.4: Plot of  $D^2$  versus  $\ln(E_p)$  for different NOP on femtosecond laser spot ablation on nickel alloy.

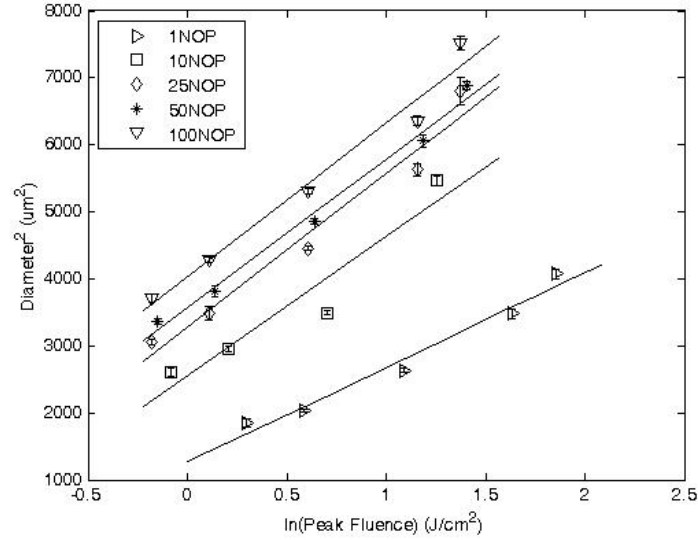


Figure 4.5: Plot of  $D^2$  versus logarithmic of peak laser fluence from which the ablation threshold for different NOP were determined for femtosecond laser spot ablation on nickel alloy.

requires an infinite NOP to initiate any ablation on the surface. The incubation effect can be described using a factor termed the incubation factor,  $\xi$  which is the slope of the linear plot from Figure 4.6b.

$$F_{th}^N = F_{th}^1 \times N^{\xi-1} \quad (4.4)$$

where  $N$  is the number of pulses,

$\xi$  is the incubation factor,

$F_{th}$  is the threshold fluence

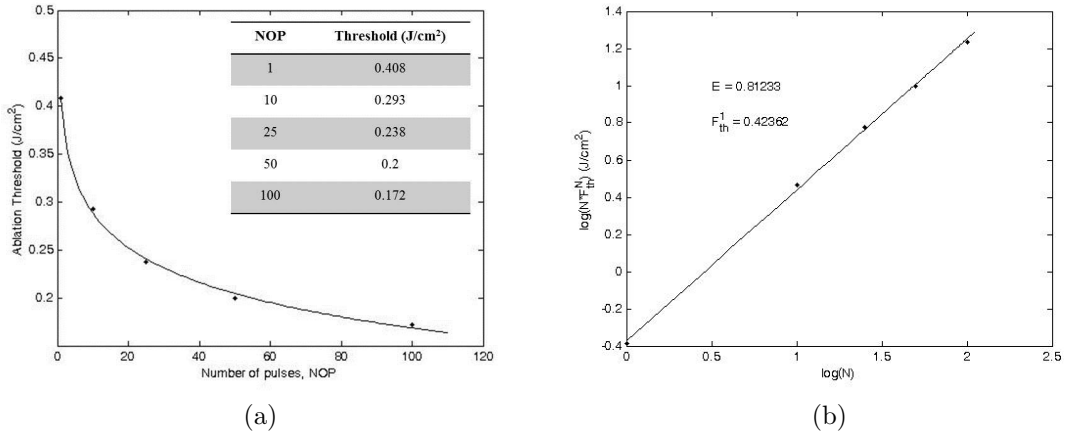


Figure 4.6: Plot of (a) ablation threshold versus NOP and (b)  $\log(N * F_{th}^N)$  versus  $\log(N)$  for femtosecond laser spot ablation on nickel alloy using diameter measurement.

The incubation factor,  $\xi$  was deduced to be 0.81 through the linear fit of the plot  $\log(N * F_{th}^N)$  versus  $\log(N)$  with ablation threshold,  $F_{th}^1$  being evaluated as  $0.423 J/cm^2$ .

The ablation threshold was also evaluated using the depth measurement in addition to the diameter measurement in which the depth of the ablated spot was measured and normalised to per pulse depth by dividing the depth with the NOP assuming that the contribution of each pulse on the amount of ablated

material was equal. A plot of laser fluence in logarithmic scale versus ablation depth per pulse is presented in Figure 4.7 where the data was fitted with several linear fits. The ablation threshold is given by the intersection between the linear fit equations with the x-axis through extrapolation.

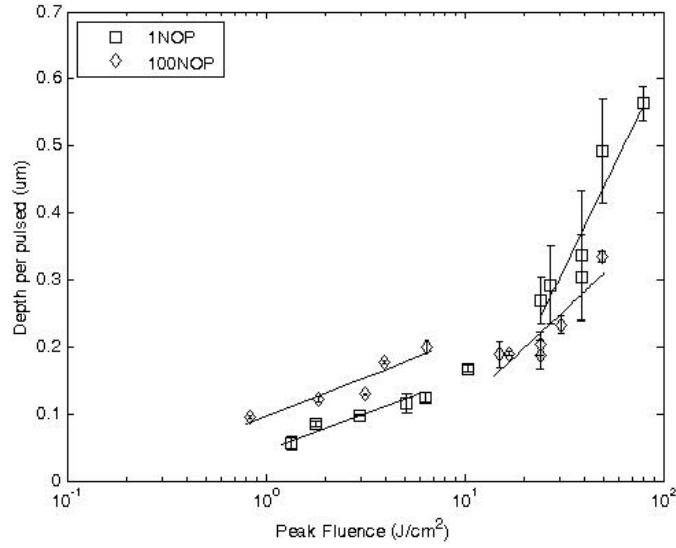


Figure 4.7: Plot of laser fluence in logarithmic scale versus ablation depth per pulse at a frequency of 1  $kHz$  for femtosecond laser ( $\lambda = 800\text{ nm}$ ,  $pulse\ width = 100\text{ fs}$ ) spot ablation on nickel alloy using depth measurement.

Two distinct ablation regimes were presented as shown in Figure 4.7 which is in agreement with most of the ablation threshold plot for metals using ultrashort pulsed laser (laser pulse width  $< 5ps$ ) [27; 32; 33; 34]. The two ablation regimes are known as the low fluence regime with low ablation rate and the high fluence regime with high ablation rate. The high fluence regime is governed by thermal ablation process similar to most lasers. The low fluence regime however is governed by a different ablation mechanism in which material is ablated through transfer of photon energy from the laser beam into the material which is absorbed by the electrons in the atom due to its higher heat capacity as compared to the lattice [35].

Based on the ablation mechanism for the material removal using ultrashort pulsed laser, the low fluence ablation regime ( $F_a = 0.92 - 2.7\text{ J/cm}^2$ ) is dependent on the optical penetration depth,  $\alpha^{-1}$  of the electron which is related to the



ablation rate,  $d_l$  using the well-known two-temperature model [27; 34; 35]:

$$D_\alpha = \frac{1}{\alpha} \ln \frac{F_\alpha}{F_{th}^\alpha} \quad (4.5)$$

where  $D_\alpha$  is the ablation depth per pulse,  
 $\alpha^{-1}$  is the optical penetration depth

The optical penetration depth,  $\alpha^{-1}$  was  $47.3nm$  for the ablation threshold,  $F_{th}^\alpha$  of  $0.377 J/cm^2$  in the low fluence ablation regime. It was also observed that the average depth per pulse contribution at the low fluence ablation regime increased with NOP as shown in Figure 4.7. This aligns with the incubation effect explained earlier where the material removal rate increases due to the reduction of ablation threshold when the NOP increases at a fixed laser fluence. In addition, the ablation rate (the slope of the curve) for different NOP was nearly constant which implied that the optical penetration depth for different NOP is constant.

The high fluence ablation regime was observed for laser fluence higher than  $5 J/cm^2$  as shown in Figure 4.7. At this ablation regime, the ablation mechanism is dependent on the energy penetration depth,  $l$  which is characterised as the length over which the heat has been transferred into the material by the electrons. In some previous publications, this is also known as heat penetration depth and is related to ablation rate,  $d_l$  at the high fluence regime ( $F_l = 6.8 - 13.5 J/cm^2$ ) with the relationship [27; 35]:

$$D_l = \frac{1}{l} \ln \frac{F_l}{F_{th}^l} \quad (4.6)$$

where  $D_l$  is the ablation depth per pulse,  
 $l$  is the energy penetration depth

(4.7)

The energy penetration depth,  $l$  obtained for the high fluence ablation regime was  $264.8 nm$  for the ablation threshold,  $F_{th}^l$  of  $9.561 J/cm^2$ . Cold machining

occurs at the fluence close to the ablation threshold and good quality finishing is obtained when working close to that regime. As the fluence regime is shifted away from the ablation threshold value, more heat is produced causing melt and poor finishing.

The NOP effect on the ablation threshold using this method was also examined as shown in Figure 4.8. The ablation threshold for NOP of 1,  $F_{th}^1$  was evaluated to be  $0.38 \text{ J/cm}^2$  with the incubation factor,  $\xi = 0.78$ . The ablation threshold and incubation factor evaluated using the depth measurement was close to the value evaluated using the diameter measurement.

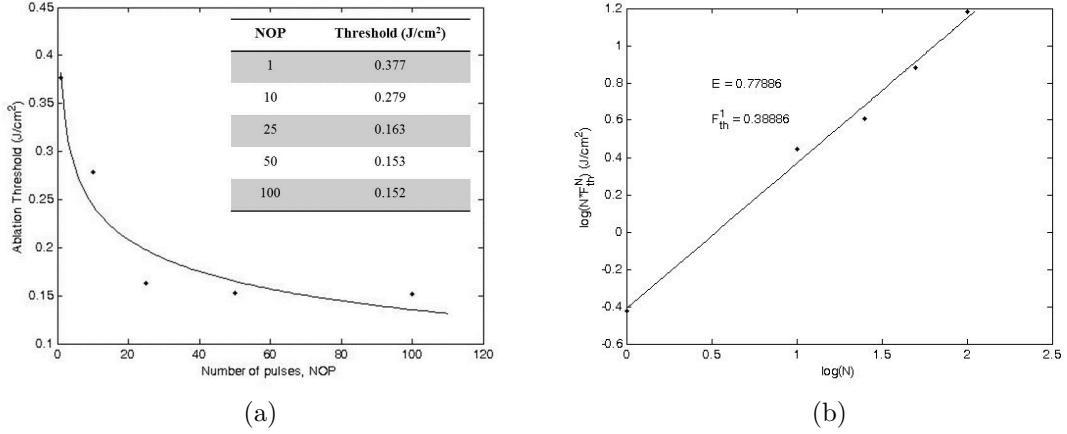


Figure 4.8: Plot of (a) ablation threshold versus NOP and (b)  $\log(N * F_{th}^N)$  versus  $\log(N)$  for femtosecond laser spot ablation on nickel alloy using depth measurement.

**Line ablation** A series of line ablation on the nickel alloy material were performed with NOP from 1 – 100 at a frequency of  $1 \text{ kHz}$  and scanning speed of  $60 \text{ mm/s}$  such that there is no overlapping between the laser pulses. Variation of laser fluence was used for a comparison of laser material interaction parameters obtained using a different ablation process. The laser beam spatial radius,  $\omega_0$  at the surface using equation 4.2 was found to be  $36.96 \pm 2.24 \mu\text{m}$  which is close to the spot size of the actual laser beam. Then  $D^2$  was plotted with  $\ln(F_o^{pk})$  where the ablation threshold was obtained through extrapolating the linear fit as shown in Figure 4.9.

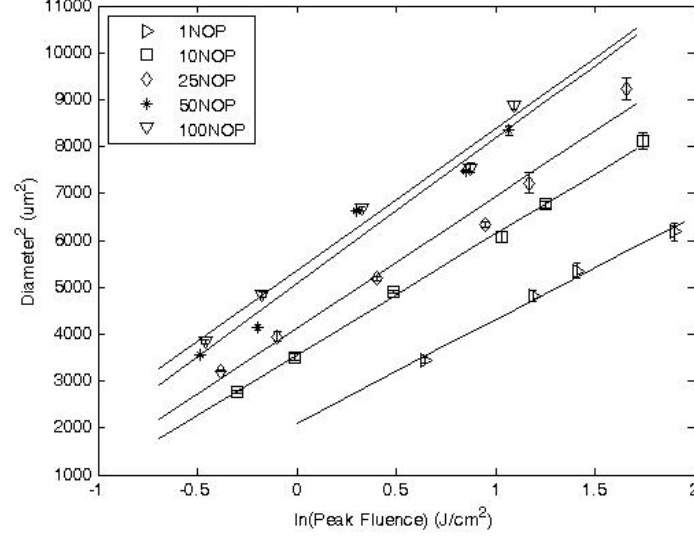


Figure 4.9: Plot of  $D^2$  versus logarithmic of peak laser fluence from which the ablation threshold for different NOP were determined for femtosecond laser ( $\lambda = 800 \text{ nm}$ ,  $pulse \ width = 100 \text{ fs}$ ) line ablation on nickel alloy.

The ablation threshold for the NOP of 1 was estimated to be  $0.385 \text{ J/cm}^2$ . Incubation effect was also observed as shown in Figure 4.9. This is similar to the observation described earlier using the diameter measurement. The main characteristic is the decrease of ablation threshold, i.e. increases in ablation rate, as the NOP increases. The incubation factor,  $\xi$  was deduced to be 0.83 through the linear fit of the plot  $\log(N * F_{th}^N)$  versus  $\log(N)$  shown in Figure 4.10 with ablation threshold,  $F_{th}^1$  evaluated to be  $0.385 \text{ J/cm}^2$ .

Figure 4.11 shows the change of ablation depth with the variation of laser fluence and NOP for the line ablation process. Similar curves with similar characteristics were observed. The optical penetration depth,  $\alpha^{-1}$  was evaluated to be  $49.9 \text{ nm}$  for the ablation threshold,  $F_{th}^\alpha$  of  $0.455 \text{ J/cm}^2$  in the low fluence ablation regime. It was also observed that the average depth per pulse contribution at the low fluence ablation regime decreased with NOP. In addition, the ablation rate decreased with increase in NOP. This is in contradiction to the incubation effect found in the spot ablation process explained earlier and a possible reason for this observation is described in the following section. The energy penetration depth,  $\alpha$  obtained for the high fluence ablation regime was  $169.6 \text{ nm}$  for the ablation

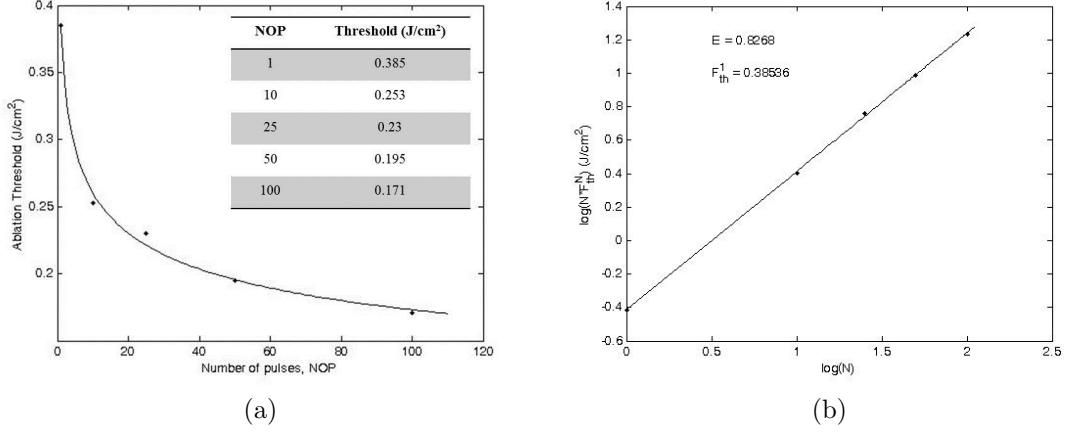


Figure 4.10: Plot of (a) ablation threshold versus NOP and (b)  $\log(N * F_{th}^N)$  versus  $\log(N)$  for femtosecond laser line ablation on nickel alloy using diameter measurement.

threshold,  $F_{th}^\alpha$  of  $5.317 J/cm^2$ .

The pulse effect on the ablation threshold using this method was also examined and displayed in Figure 4.12. The ablation threshold for the NOP of 1,  $F_{th}^1$  was evaluated to be  $0.495 J/cm^2$  with the incubation factor,  $\xi = 0.85$ . The  $F_{th}^1$  obtained was larger compared to the value evaluated using the diameter measurement ( $0.385 J/cm^2$ ).

#### 4.3.1.3 Comparison of Ablation Methods

The laser material interaction parameters obtained through diameter and depth measurements are summarized in Table 4.4 and the values obtained were found to be similar. Compared with those reported for C263 ( $0.25 J/cm^2$ ) [27] and CMSX-4 ( $0.3 J/cm^2$ ) [34], these values are larger, suggesting that the HR4 nickel alloy requires higher energy to initiate material removal. The optical penetration depth ( $47.3 nm$ ) is larger compared to Ni ( $15 nm$ ) [204] and CMSX-4 ( $18 nm$ ) [34] but has a similar magnitude to C263 ( $37.2 nm$ ) [27]. As the optical penetration depth is affected by the thermalisation of the electronic sub-system which is dependent on the density of state at Fermi level [183; 195], the larger value observed might be due to the nickel content in the HR4 nickel alloy as it

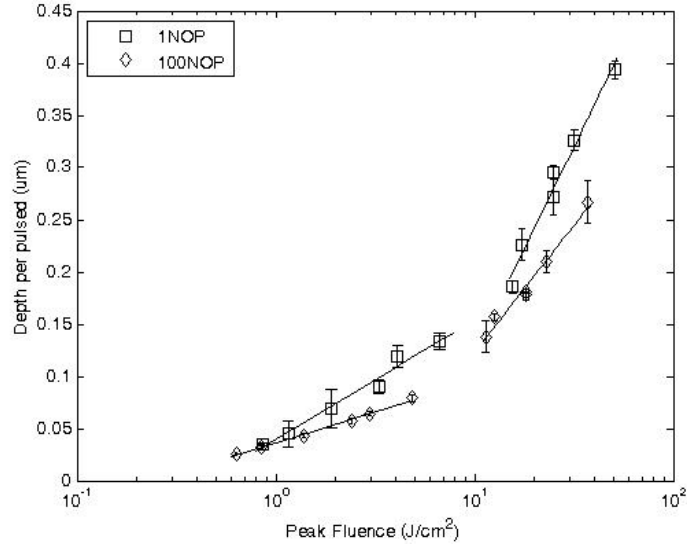


Figure 4.11: Plot of laser fluence in logarithmic scale versus ablation depth per pulse at a frequency of 1  $\text{kHz}$  for femtosecond laser line ablation on nickel alloy using depth measurement.

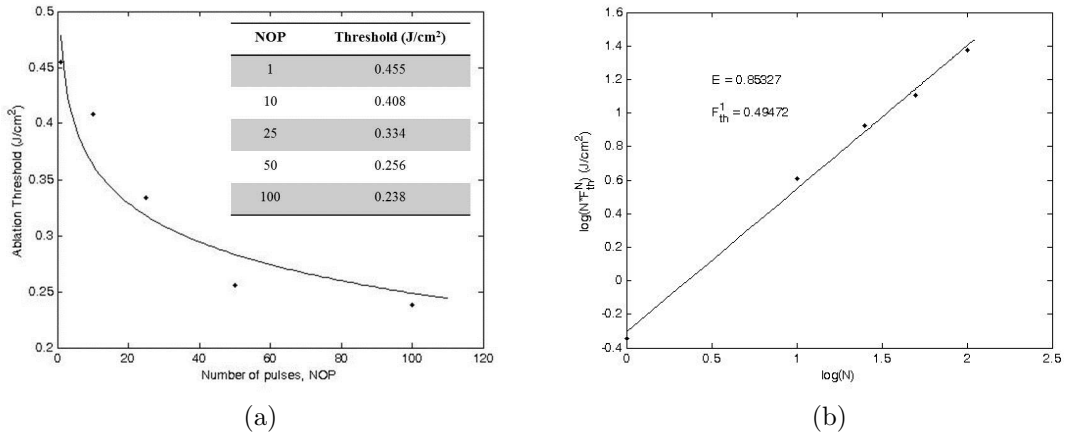


Figure 4.12: Plot of (a) ablation threshold versus NOP and (b)  $\log(N * F_{th}^N)$  versus  $\log(N)$  for femtosecond laser line ablation on nickel alloy using depth measurement.

has a lower nickel percentage in the alloy and also having a substantial amount of chromium and tungsten. The incubation factor estimated based on different geometry measurements were close, but larger than those reported for *C263* (0.72) [27], implying that the effect of NOP on the ablation thresholds for the HR4 nickel alloy is less pronounced as compared to the *C263* nickel alloy.

Table 4.4: Summary of ablation characteristics obtained using different geometry measurements for nickel alloy.

Ablation Process Geometry measurement	Spot		Line	
	Diameter	Depth	Diameter	Depth
Laser beam spatial radius, $\omega_0(\mu m)$	32.3	—	36.96	—
Ablation threshold ( $J/cm^2$ )	Measured	0.408	0.377	0.385
	Evaluated	0.423	0.389	0.385
$\alpha^{-1}$ (nm)	—	47.3	—	49.9
Incubation factor, $\xi$	0.81	0.78	0.83	0.85

For the line ablation process, the ablation threshold and incubation factor through the diameter measurement, as well as the optical penetration depth via the depth measurement were close to the values obtained from the spot ablation. On the contrary, the ablation threshold and incubation factor obtained through the depth measurement were higher than the values obtained through the depth measurement for spot ablation. Such differences might be attributed to the ablation mechanism involved in the spot and line ablation in which the line ablation consists of a series of spots aligning to each other. During the scanning process, it was difficult for the laser beam spot to coincide onto the same spot ablated by the previous scan. Therefore, the surface area irradiated by the laser beam is variable. Consequently, the ablation rate varies and it is more likely that the ablation depth becomes smaller. Therefore, the ablation thresholds based on the measurement of depth were less than the actual values. However, the diameters of the ablated tracks were not affected as the optically induced phase transformation on the material is constant as long as the focusing distance between the lens and the material surface is constant. Therefore, the parameters estimated using the diameter measurement in the line ablation process was consistent with the values obtained through spot ablation. As for the optical penetration depth

evaluated using the depth measurement in line ablation, the value was comparable because it was evaluated on a single line ablation which is equivalent to the single spot ablation.

By comparing the data obtained using different geometry measurements, it was found that the data obtained through the diameter measurement had smaller variation and thus considered to be more reliable. As for depth measurement, special care is required for sample preparation as it affects the measurement and hence affects the evaluation of the parameters. Samples have to be flat and even for increase reliability.

## 4.3.2 Excimer Laser Beam Interaction with CFRP

### 4.3.2.1 Ablation Characteristics

Only one ablation morphology region of a rectangular crater shape was observed when the epoxy resin was ablated using different laser parameters as shown in Figure 4.13. The ablation depth seemed to increase with laser fluence and the relationship is governed by the Beer-Lambert law that holds for light absorption of moderate intensity given by:

$$d = \frac{1}{\alpha} \ln \frac{F}{F_{th}} \quad (4.8)$$

where  $d$  is the ablation depth,

$\alpha$  is the optical penetration depth,

$F$  is the fluence,

$F_{th}$  is the threshold fluence

The relationship between ablation depth and laser fluence was shown by measuring the depth of the ablated spot and normalised to per pulse depth by dividing the depth with the NOP assuming equal contribution of each pulse on the amount of ablated material. A plot of laser fluence in logarithmic scale versus ablation depth per pulse was plotted as shown in Figure 4.14 where the data was



Figure 4.13: Optical images of square crater produced by excimer laser on epoxy using  $1.5 \text{ J/cm}^2$  laser fluence, (a)100 NOP and (b)200 NOP.

fitted with several linear fits. The ablation threshold is given by the intersection between the linear fit equations with the x-axis through extrapolation.

Figure 4.14 clearly indicated one ablation regime which agrees with most of the ablation threshold plot for short pulsed laser (pulse width  $> \text{ns}$ ) [44]. The ablation mechanism involved in polymer material removal can be achieved through either photoablation or thermal ablation where photoablation is the primary ablation mechanism involved when using UV wavelength laser beam. This was further confirmed in the surface chemical composition analysis results presented in the following section where chain scission phenomenon was observed after laser ablation. The ablation threshold,  $F_{th}$  for 50 NOP was estimated to be  $0.432 \text{ J/cm}^2$  with the associated optical penetration depth,  $\alpha^{-1}$  of  $282 \text{ nm}$ .

In addition, it was also observed that the average depth per pulse contribution increased with NOP as shown in Figure 4.14. In other words, the ablation threshold value decreased with increasing NOP which is known as the incubation effect as shown in Figure 4.15a. In polymer, such effect is not discussed and elaborated much but is believed to be caused by the weakening of the polymer chain through change in the structure of the polymer rather than the removal of materials [29]. The side-chain of the polymer that undergoes changes in orientation is termed the chromophoric group that increases the absorptivity to light [29]. Such phe-



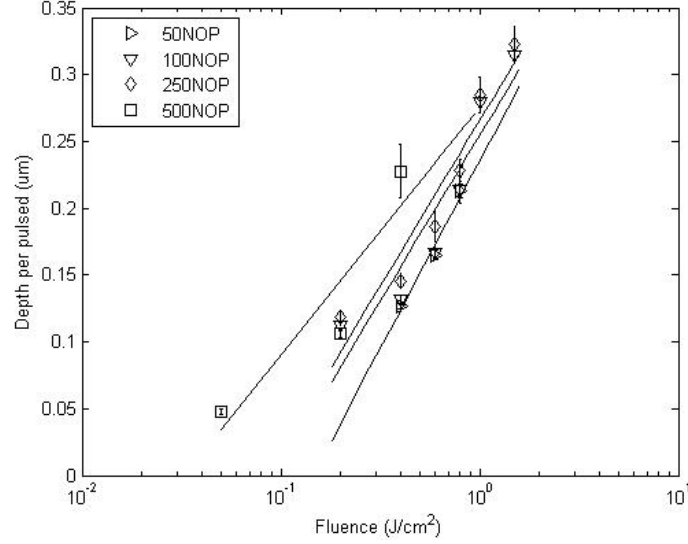


Figure 4.14: Plot of laser fluence in logarithmic scale versus ablation depth per pulse with excimer laser at a frequency of 10  $Hz$  for epoxy resin.

nomenon degrades the material properties, allowing the material to be ablated at a lower threshold. The ablation threshold was lowered drastically at the first 100  $NOP$  and then gradually decreased with further increase in  $NOP$ . The ablation threshold seemed to decrease asymptotically where the ablation threshold reached a constant value,  $F_{th}^{\infty}$  when  $NOP$  tends to infinite. The incubation factor was determined by equation 4.4 where the incubation factor is the slope of the linear plot from Figure 4.15b. The incubation factor,  $\xi$  was deduced to be 0.75 through the linear fit of the plot  $\log(N * F_{th}^N)$  versus  $\log(N)$  with ablation threshold,  $F_{th}^1$  being evaluated as  $1.169 J/cm^2$ . In addition, the ablation rate (the slope of the curve) for different  $NOP$  was nearly constant.

#### 4.3.2.2 Surface Chemical Composition Analysis

The XPS spectrum was curve fitted to obtain the chemical composition of the CFRP surfaces that were investigated. The curve fitting was performed through identifying the peaks of the spectrum and then was automatically matched with the database where elements with matching peaks were listed and the composition was calculated. Before the spectrum was curve-fitted, the spectrum was calibrated

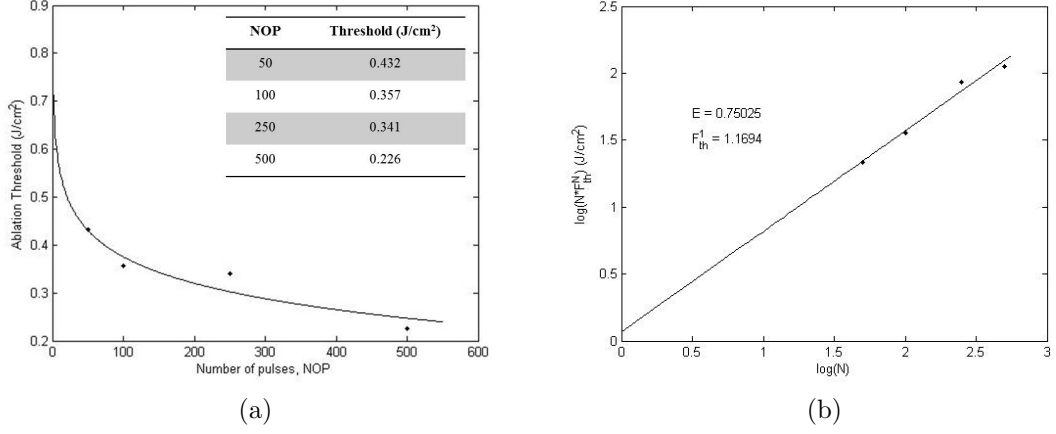


Figure 4.15: Plot of (a) ablation threshold versus NOP and (b)  $\log(N * F_{th}^N)$  versus  $\log(N)$  for epoxy resin using depth measurement.

using the carbon high resolution spectrum. Several peaks were fitted to form a spectrum similar to the high resolution spectrum using a Gaussian-Lorentzian peak shape curve. The calibration was done by fixing the first peak in the fitting spectrum at 285 eV and was then checked with the wide scan spectrum fitting result [205; 206]. Figure 4.16 shows two examples of the spectrum obtained from the XPS machine on different surface treated CFRP. The chemical composition for different surface treated CFRPs are summarised in Table 4.5.

Table 4.5: Elemental composition of the CFRP surface measured by XPS before and after various excimer laser treatment conditions.

Pre-surface condition	Surface Treatment	Atomic Percentage (%)							
		O	C	N	F	Ca	S	O/C	N/C
Smooth	None treated	12.2	82.5	0.9	—	1.9	2.2	0.15	0.01
	90mJ/cm <sup>2</sup> , 3NOP	17	76.1	4.6	—	—	2.3	0.22	0.06
	175mJ/cm <sup>2</sup> , 3NOP	14.4	79	5.1	—	—	1.5	0.18	0.065
	200mJ/cm <sup>2</sup> , 3NOP	13.8	82.8	1.7	—	1.7	—	0.17	0.021
Rough	None treated	9.4	57.3	1.1	30.1	0.9	1.3	0.16	0.02
	50mJ/cm <sup>2</sup> , 20NOP	16	73.6	4.2	6.3	—	—	0.22	0.06
	250mJ/cm <sup>2</sup> , 20NOP	14.7	80.3	4.2	—	—	0.8	0.18	0.05
	275mJ/cm <sup>2</sup> , 20NOP	13.5	81.7	2.1	—	1.4	1.3	0.17	0.026

A different method was used for fitting the high resolution scan spectrum for

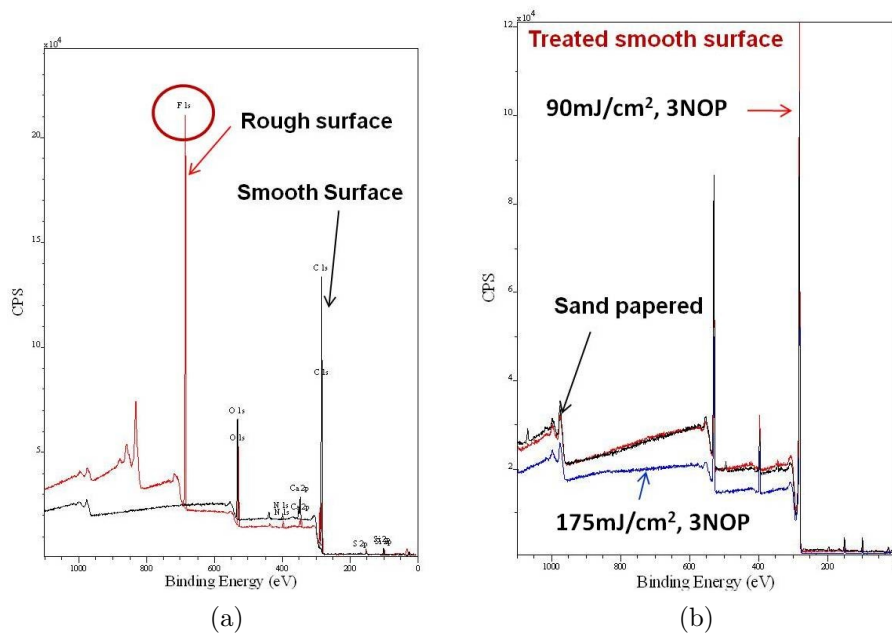


Figure 4.16: Wide scan XPS spectrum for (a) as received smooth and rough CFRP surface and (b) different excimer laser surface treatment conditions for the smooth CFRP surface.

carbon, oxygen and nitrogen. A constraint was fixed to individual carbon and oxygen peaks before the curve was fitted to the spectrum. The constraint was set based on the separation of the bonding energy between different carbon functional groups and the corresponding oxygen functional group where the difference in binding energy for carbon are summarised in Table 4.6. Figure 4.17 shows two examples of the carbon high resolution scan spectrum obtained through XPS on different surface treated CFRPs. The relative area percentage of different carbon bonding states is summarised in Table 4.7 where the oxygen and nitrogen bonding states is summarised in Table 4.8.

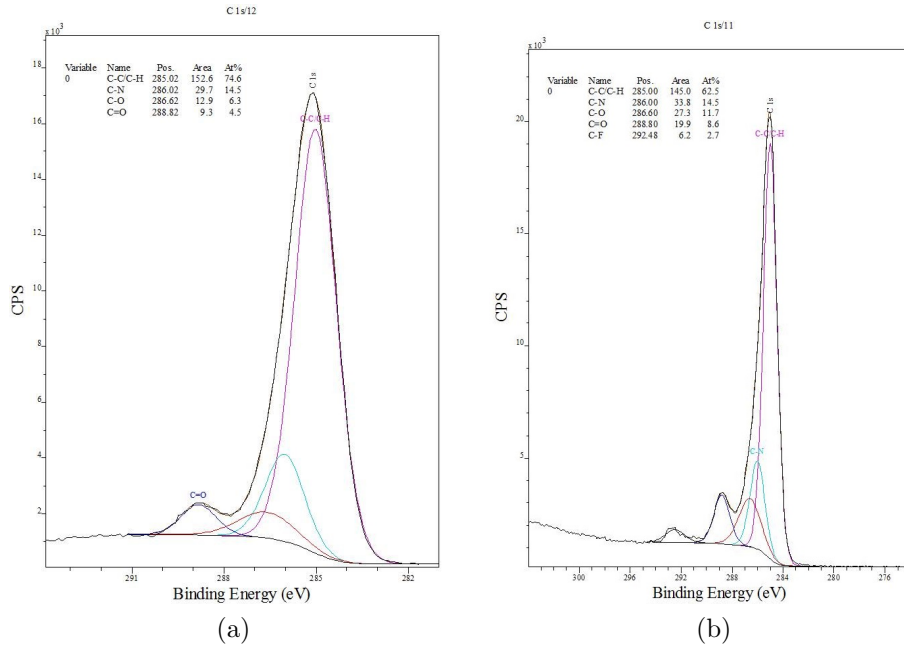


Figure 4.17: High resolution carbon scan XPS spectrum for excimer laser treated (a) smooth CFRP with 90  $mJ/cm^2$ , 3 NOP and (b) rough CFRP with 50  $mJ/cm^2$ , 20 NOP.

In the high resolution carbon spectrum, four main carbon bonds were identified and they are the C-C/C-H bond, C-N bond, C-O bond and C=O bond. The C-O bond has three possible chain formation which are C-O-C, C-O-C=O and C-O-H. The C=O has two possible chain formation which are C=O and O-C=O. In the high resolution oxygen spectrum, three main oxygen bonds were identified and they are O-C bond, O=C bond and C-OH bond. The change in composition

Table 4.6: XPS chemical shifts of carbon 1s electrons for carbon-nitrogen and carbon-oxygen functional group and the relevant binding energy published [205; 207; 208; 209; 210; 211].

Functional Group	Separation (eV)	Binding Energy (eV)
C-C/C-H	0	284.6 – 285
C-N	1	–
C-O	1.6	285.7 – 286.7
C=O	3.8	288.5 – 289.3

Table 4.7: Surface chemical composition changes of the CFRP surface measured by XPS carbon high resolution scan before and after various excimer laser treatment conditions.

Pre-surface condition	Surface Treatment	Relative Area Percentage (%)				
		285 ± 0.1 C-C/C-H	286 ± 0.1 C-N	286.6 ± 0.1 C-O	288.8 ± 0.1 -C=O	292.2 ± 0.1 C-F
Smooth	None treated	87.67	1.95	5.92	4.46	–
	90mJ/cm <sup>2</sup> , 3NOP	74.65	14.52	6.29	4.54	–
	175mJ/cm <sup>2</sup> , 3NOP	73.5	16.97	6.09	4.54	–
	200mJ/cm <sup>2</sup> , 3NOP	86.8	3.8	5.2	4.2	–
Rough	None treated	70.15	3.22	7.66	4.76	14.2
	50mJ/cm <sup>2</sup> , 20NOP	62.5	14.5	11.7	8.6	2.7
	250mJ/cm <sup>2</sup> , 20NOP	60.7	11.6	19.2	8.5	–
	275mJ/cm <sup>2</sup> , 20NOP	85.6	3.1	6.7	4.6	–

Table 4.8: Surface chemical composition changes of the CFRP surface measured by XPS oxygen and nitrogen high resolution scan before and after various excimer laser treatment conditions.

Pre-surface condition	Surface Treatment	Relative Area Percentage (%)			
		532.1	533.3	532.9	400
		$\pm 0.1$	$\pm 0.1$	$\pm 0.1$	$\pm 0.1$
		O*-C=O	O-C=O*	C-OH	N-C
Smooth	None treated	67.9	32.1	—	100
	90mJ/cm <sup>2</sup> , 3NOP	58.28	41.72	—	100
	175mJ/cm <sup>2</sup> , 3NOP	58	42	—	100
	200mJ/cm <sup>2</sup> , 3NOP	62.3	37.7	—	100
Rough	None treated	58.74	41.26	—	100
	50mJ/cm <sup>2</sup> , 20NOP	57.8	42.2	—	100
	250mJ/cm <sup>2</sup> , 20NOP	54.2	45.8	—	100
	275mJ/cm <sup>2</sup> , 20NOP	60.8	39.2	—	100

on the composite surface for the carbon spectrum was corresponded with the respective oxygen bond in the oxygen spectrum as shown in Table 4.7 and Table 4.8.

In the high resolution carbon scan spectrum for the un-treated rough CFRP surface, a peak at 292.2 eV was observed and this is the characteristic peak for C-F functional group [205]. This aligned with the wide scan of the un-treated rough CFRP surface as it had fluorine element on the surface of the composite indicating the existence of contaminant from the release films or other ancillary consumable during the manufacturing process. Correspond with the high resolution scan for the carbon C 1s, the fluorine seemed to react with the polymer during the manufacturing process forming C-F bond. When the surface of the CFRP was treated with the laser, the fluorine content was reduced or even removed if the laser fluence used was sufficiently high. The result for the smooth CFRP surface did not indicate any contaminant for the un-treated surface.

The surface chemical composition of the laser treated CFRP surfaces showed changes and was indicated both in the wide scan and carbon high resolution XPS spectrum. From the wide scan spectrum, the increase in N/C ratio and O/C ratio indicated changes in chemical composition of the CFRP surfaces and this was further confirmed by the high resolution carbon spectrum. In the high

resolution carbon spectrum, there was a decrease in C-C/C-H bond percentage and an increase in oxygen and nitrogen rich carbon functional group percentage for the laser treated CFRP surfaces at lower fluence as compared to the untreated surface. This indicated that chain scission occurs in both treatments which aligns with most literatures as the photon energy of the laser beam is high enough to break the C-C bond in polymers [212; 213; 214]. Higher fluence used in the abrading process promotes more chain scission. Chain scission creates free radical carbons on the top polymer surface layer which then react with oxygen, nitrogen and water in air to form C-N, carbonyl group (C=O) or carboxyl group (COO-) [212; 213; 214; 215]. Hence, an increase in nitrogen and oxygen rich functional groups could be seen in both laser surface treated and sand-papered CFRP surface. This process is known as photo-oxidation.

The interaction between the free radical carbons in the polymer chain with air molecules is possible through either direct reaction or with ionised air molecules. As free radical carbons within a polymeric chain is very unstable, they react with oxygen, nitrogen or water in air to form bonding which helps stabilise the polymeric chain [216]. During the laser ablation process, laser-induced breakdown phenomenon occurs in parallel with the process. This phenomenon gives rise to the ionisation of the air molecules which reacts with the free radical carbons in the polymer. The ionisation of air molecules can be observed through a glow or flash or even spark if there is sufficient air molecules being ionised [217]. The ionisation process of air molecules happens when a laser beam is focused onto a spot in small spatial domain which result in sudden rise in temperature where the electric field of the radiation is higher than the binding energy of the electron of the molecules to their nuclei [218]. This causes a breakdown of the bonds between the atoms in the molecules itself and produces ionised gas. Adelgren et al. described the deposition of energy from a focus laser beam into a gas by four progressives and they are [219]:

1. Initial release of electrons by multi-photon effects.
2. Ionisation of the gas in the focal region by producing electron through collision cascade ionisation.
3. Absorption and reflection of laser energy by gaseous plasma.

4. Formation and propagation of a deformation shock wave into the surrounding and relaxation of the focal region plasma.

There are two main mechanisms used to explain the occurrence of gas ionisation through laser beam and they are multi-photon ionisation [217; 220; 221] and inverse bremsstrahlung absorption or cascade ionisation [222; 223]. The two mechanisms are fundamentally different and are described by different theories. In simple explanation, the multi-photon ionisation occurs when a neutral atom manage to absorb enough energy within a quantum lifetime of the excited state which is usually within  $< 10^{-16}$  s. The photon energy absorbed is sufficient to raise the electron of the atom from the ground state to the ionisation level which results in ionisation of the gas molecules [217]. As for cascade ionisation process, a few initial electrons within the breakdown region is required for the process to occur. These electrons in the breakdown region can be created through either multi-photon ionisation process or with the presence of dust or electrons created at ambient gas temperature [224]. The ionisation of gas molecules occurs through inelastic collisions by electrons that accumulate enough energy through absorbing energy from the laser beam to produce two electrons of a lower energy. The process is then repeats like a chain like reaction [223]. The two mechanisms are illustrated in Figure 4.18.

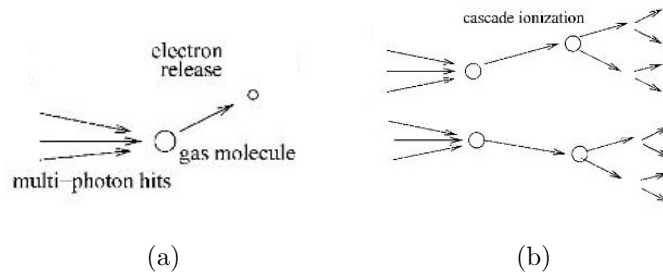


Figure 4.18: Illustration of (a) multi-photon ionisation mechanism and (b) cascade ionization mechanism [225].

The ionisation energy of air is  $15.6 \text{ eV}$  and the photon energy of the KrF excimer laser is  $5 \text{ eV}$ . Hence, in order to ionize the gas molecules in air, only four photons are required to be absorbed within a short quantum excitation lifetime



[217]. Since the number of photons required is very small, the main mechanism for the process is deemed to be multi-photon ionisation with cascade ionisation mechanism being involved at a later stage in the laser induced breakdown process [224]. As for other lasers with the laser beam wavelength in the infrared or visible region, the photon energy are much smaller and it requires 10 – 300 photons to be absorbed within a quantum lifetime of the excited state ( $< 10^{-14}$  s) in order to ionise the gas molecules in air. Hence, it is highly unlikely that the gas molecules in air are ionised with laser beam having wavelength in these regions [217; 223].

On the other hand, although there was no evidence of an increase in the C-C/C-H bond from the carbon high resolution scan for low fluence laser surface treated CFRP, cross-link formation might still be possible as the reaction of the free radicals from the chain scission process is random. However, based on the data obtained, most of the free radicals formed on the CFRP surface from the chain scission process seemed to react with the oxygen and nitrogen in air and form less cross-link within the modified layer. On the contrary, there was an increase in the C-C/C-H bond percentage and a decrease in the oxygen and nitrogen rich carbon functional group percentage when the CFRP surface was treated with higher laser fluence. The increase in the C-C/C-H bond indicated the expose of carbon fibre within the composite as using higher laser fluence to treat the CFRP surface removed an extensive amount of the polymer layer resulted in carbon fibre exposure.

The increase in oxygen rich functional group for the rough CFRP surface was higher as compared to the smooth CFRP surface. This is because the rough surface has more contact area with the surrounding hence is more reactive with the elements in air and therefore more prone to polar functional groups formation through interaction with the elements in air.

### 4.3.3 Excimer Laser and Femtosecond Laser Beam Interaction with ABS

#### 4.3.3.1 Ablation Morphology

Figure 4.19 shows the optical images of the ablated region on ABS using excimer laser of different laser flences at 100 *NOP*. As the laser beam is rectangular in

shape and has a top-hat beam profile, a uniform single ablation morphology region was observed on all the ablated regions shown in the optical images. At low laser fluence, bubbles and line shape structures were observed on the ablated region and the density of such structures increased as the fluence increases. These structures were believed to be caused by thermodynamic effect where the polymer surface undergoes rapid phase transformation or rapid thermal-plastic expansion and rupture due to the sudden increase in surface temperature up to 1000  $K$  during laser irradiation [43]. On the contrary, some ablated regions were observed to have the same surface morphology as the un-treated surface as shown in Figure 4.20. At higher fluence, polymer melting was clearly observed where resolidification of molten polymer could be seen at the edge of the ablated region as shown in Figure 4.19d. Cracks and surface defects were also observed on the ablated region at high fluence.

Figure 4.21 shows the SEM images of the ablated craters on ABS using the femtosecond laser at different laser flences and NOPs. Only a single ablation morphology region was observed on all the ablated craters as shown in the SEM images. At low fluence and NOP(4.1  $J/cm^2$ , 1 NOP), the ablated crater was not well define and only part of the laser irradiated area was ablated producing a porous coral like structure as shown in Figure 4.21a. As the fluence and NOP increases, the diameter and depth of the ablated crater increased where the increase in diameter was more apparent with the increase in NOP while the increase in depth was more apparent with the increase in fluence. At higher fluence and NOPs, resolidification of molten polymer in the form of small droplets was observed along the wall of the ablated craters as shown in Figure 4.21c and 4.21d. The ablated crater had a ‘V’ shape as shown in Figure 4.22 and the shape was more apparent with higher fluence and NOPs. This was mainly due to the Gaussian nature of the laser beam used where the beam followed a normal distribution curve with a sharp peak in the middle with decreasing intensity radially outwards. The edge of the ablated craters were more pronounce at higher NOPs and fluence which is agreed in most publications [226; 227; 228]. It is also observed that the laser beam profile is not an idealised Gaussian distribution and is asymmetrical in shape.

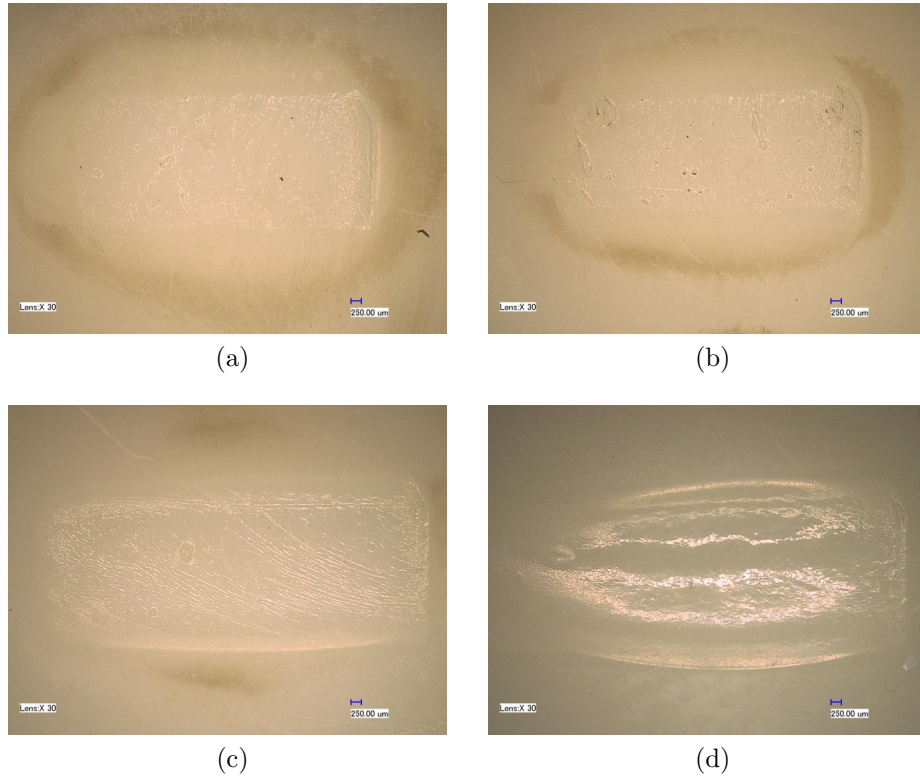


Figure 4.19: Optical images of the ablated region produced at (a)  $0.05 \text{ J/cm}^2$ , (b)  $0.4 \text{ J/cm}^2$ , (c)  $0.8 \text{ J/cm}^2$  and (d)  $1.5 \text{ J/cm}^2$  at 100 *NOP* using excimer laser ( $\lambda = 248 \text{ nm}$ , *pulse width* = 15 *ns*).

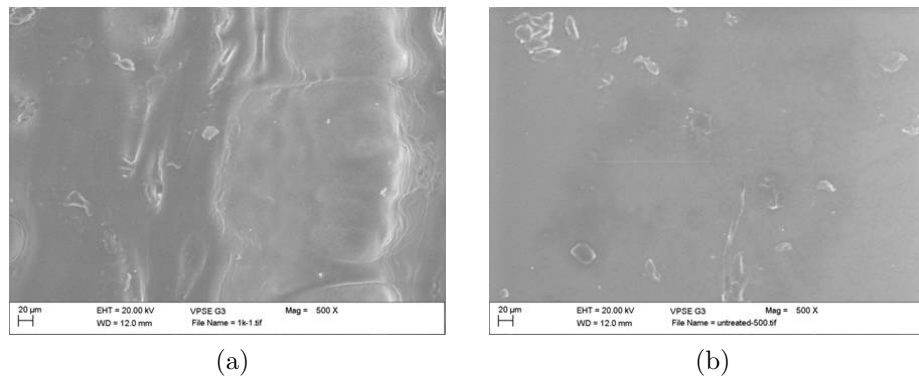


Figure 4.20: SEM images of the (a) ablation region produced at  $0.05 \text{ J/cm}^2$ , 100 *NOP* using excimer laser ( $\lambda = 248 \text{ nm}$ , *pulse width* = 15 *ns*) and (b) un-treated ABS surface.

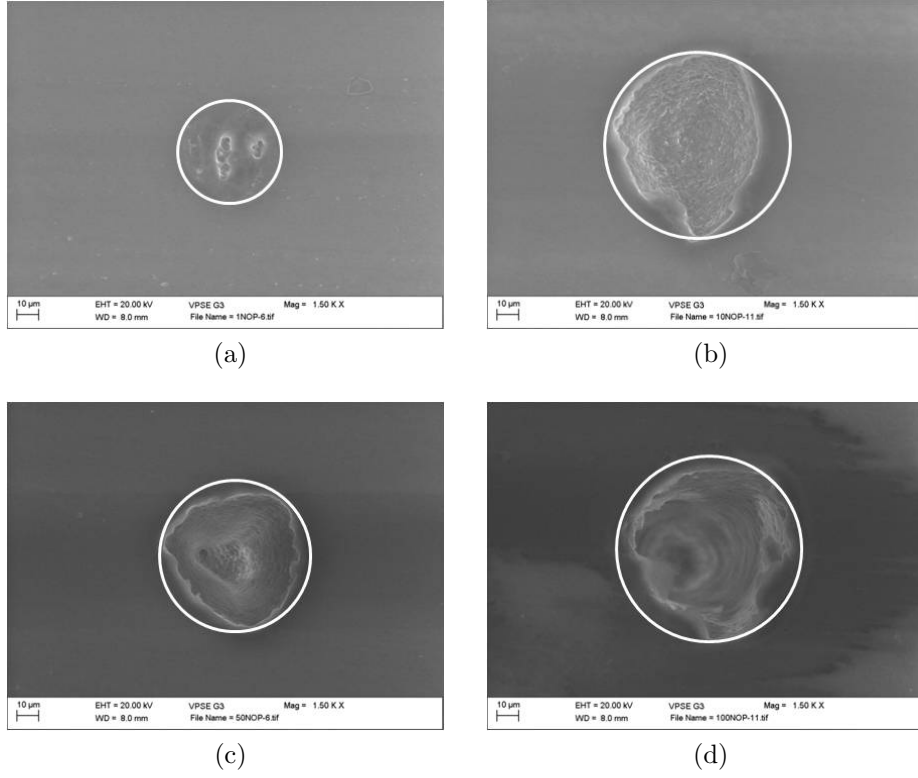


Figure 4.21: SEM images of the craters produced at (a)  $4.1 \text{ J/cm}^2$ , 1 *NOP*, (b)  $19.45 \text{ J/cm}^2$ , 10 *NOP*, (c)  $4.1 \text{ J/cm}^2$ , 50 *NOP* and (d)  $19.45 \text{ J/cm}^2$ , 100 *NOP* using femtosecond laser ( $\lambda = 800 \text{ nm}$ , *pulse width* = 100 *fs*).

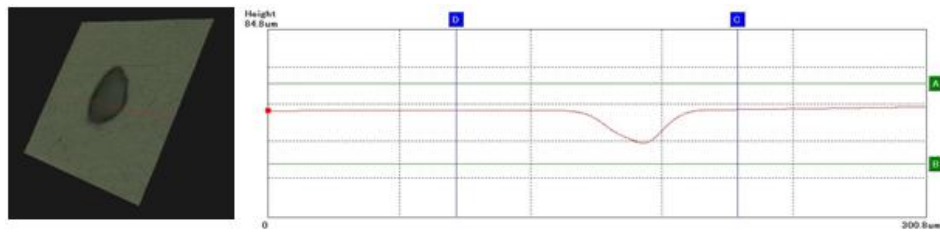


Figure 4.22: 3D optical microscope image with ablated crater profile produced at  $4.1 \text{ J/cm}^2$ , 50 *NOP* using femtosecond laser.

#### 4.3.3.2 Ablation Characteristics

A series of spot ablation on the ABS polymer were performed with 100 *NOP* and varying laser fluence ( $0.5 - 1.5 \text{ J/cm}^2$ ) at a frequency of 10 *Hz* using the KrF excimer laser. There was no plasma formation during ablation as the peak power density used was less than  $10^{10} \text{ W/cm}^2$  ( $7.5 \times 10^7 \text{ W/cm}^2$ ) [69]. The ablation threshold was determined through measuring the depth of the ablated region using the optical white light interferometer. A plot of ablation depth per pulse versus laser fluence in logarithmic scale is presented in Figure 4.23 where the data were fitted with a linear fit. The ablation threshold is given by the intersection between the linear fit line with the x-axis through extrapolation.

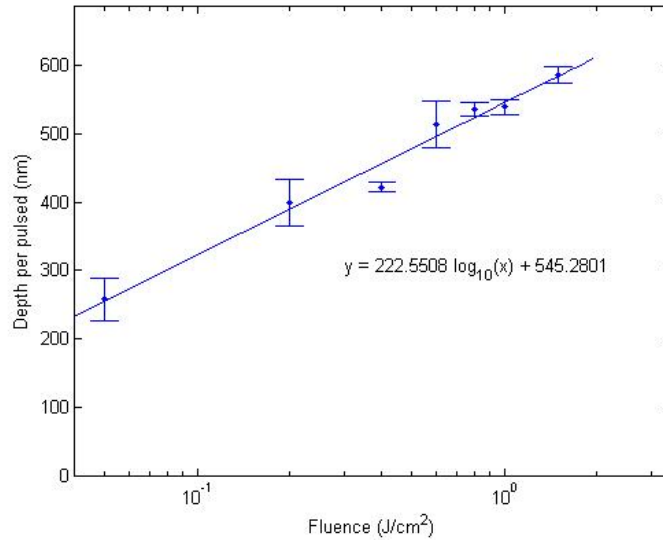


Figure 4.23: Plot of laser fluence in logarithmic scale versus ablation depth per pulse at a frequency of 10 *Hz* for ABS polymer using excimer laser.

Figure 4.23 clearly presents one distinct ablation regime that is commonly seen in most ablation threshold plots for polymers [186; 198]. The ablation depth per pulse varied logarithmically with the laser fluence and satisfies equation 4.8 as predicted by Beer's law where the ablation rate is dependent on the optical penetration depth,  $\alpha^{-1}$  of the chromophoric group within the polymers [229; 230; 231; 232]. The ablation threshold,  $F_{th}$  for 100 *NOP* is estimated to be  $0.087 \text{ J/cm}^2$  with the associated optical penetration depth,  $\alpha^{-1}$  of 223 *nm*.

A series of spot ablation on the ABS polymer were performed with varying NOP (1 – 100) and laser fluences ( $0.92 - 13.5 \text{ J/cm}^2$ ) at a frequency of  $1 \text{ kHz}$  using the Ti:Sapphire femtosecond laser. There was some plasma formation during the ablation as the peak power density used is higher than  $10^{10} \text{ W/cm}^2$  ( $1.35 \times 10^{14} \text{ W/cm}^2$ ) [69]. Similar analysis was performed on the ABS material where the ablation threshold was determined through measuring the diameter and depth of the ablated region. The square of the diameter ( $D^2$ ) measured was plotted against  $\ln(E_p)$  to evaluate the laser beam spatial radius,  $\omega_0$  on the material surface using equation 4.2. The value of  $\omega_0$  was evaluated to be  $19.5 \pm 1.02 \mu\text{m}$ , which was smaller than the spot size of the laser beam which was then used to calculate the peak laser fluence using equation 4.3. A plot of  $D^2$  vs  $\ln(F_0^{pk})$  was plotted which was then used to evaluate the ablation threshold through extrapolating the linear fit to obtain the interception on the x-axis as shown in Figure 4.24. The ablation threshold for 1 *NOP* is estimated to be  $1.648 \text{ J/cm}^2$ .

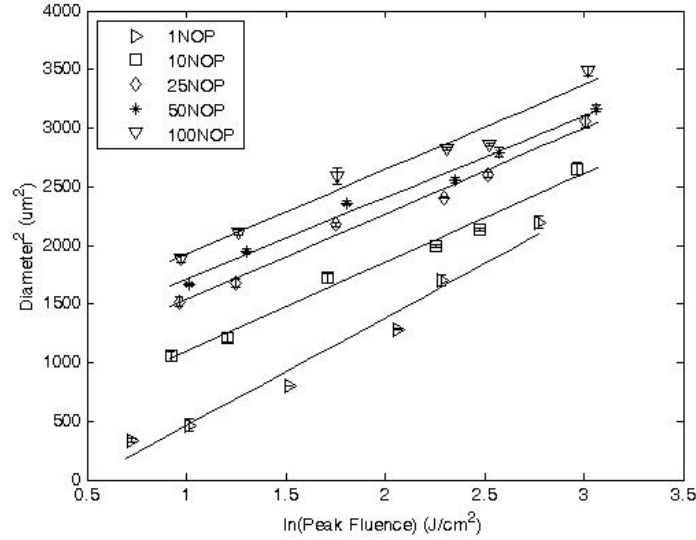


Figure 4.24: Plot of  $D^2$  versus logarithmic of peak laser fluence from which the ablation threshold for different NOP were determined for spot ablation on ABS using femtosecond laser.

From Figure 4.24, it could be seen that the ablation threshold decreased with the NOP which was also shown on a different plot in Figure 4.25a. The dependence of ablation threshold on NOP is known as the incubation effect and is

observed by other researchers [196]. The ablation threshold was lowered drastically at the first 25 NOP and then gradually decreased with further increase in NOP. The ablation threshold seemed to decrease asymptotically where the ablation threshold reaches a constant value,  $F_{th}^\infty$  when NOP tends to infinite. The incubation effect can be described using a factor termed the incubation factor,  $\xi$  which is the slope of the linear plot from Figure 4.25b.

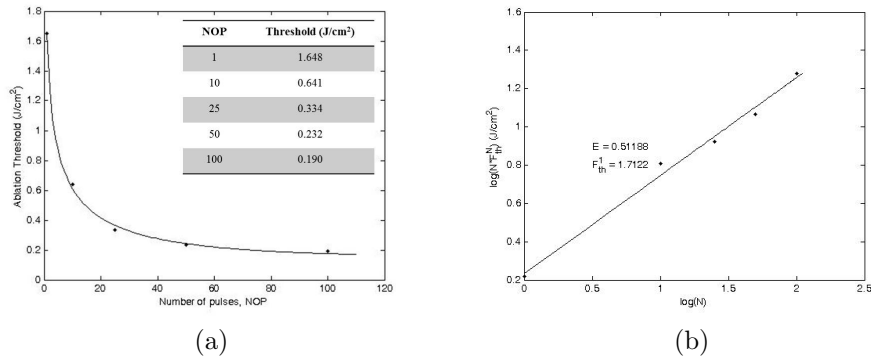


Figure 4.25: Plot of (a) ablation threshold versus NOP and (b)  $\log(N * F_{th}^N)$  versus  $\log(N)$  for femtosecond laser spot ablation on ABS polymer using diameter measurement.

The incubation factor,  $\xi$  was deduced to be 0.51 through the linear fit of the plot  $\log(N * F_{th}^N)$  versus  $\log(N)$  with ablation threshold,  $F_{th}^1$  being evaluated as  $1.712 J/cm^2$ .

In addition to the diameter measurement, the ablation threshold was also evaluated based on the depth measurement, in which the depth of the ablated spot were measured and normalised to per pulse depth by dividing the depth with the NOP assuming equal contribution of each pulse on the amount of ablated material. A plot of laser fluence in logarithmic scale versus ablation depth per pulse is presented in Figure 4.26 where the data was fitted with several linear fits. The ablation threshold is given by the intersection between the linear fit lines with the x-axis through extrapolation.

Figure 4.26 clearly presented two distinct ablation regimes, which is commonly seen in most ablation threshold plot for metals using ultrashort pulsed laser (laser pulse width  $< 5 ps$ ) [27; 32; 34; 191]. Such observation is not com-



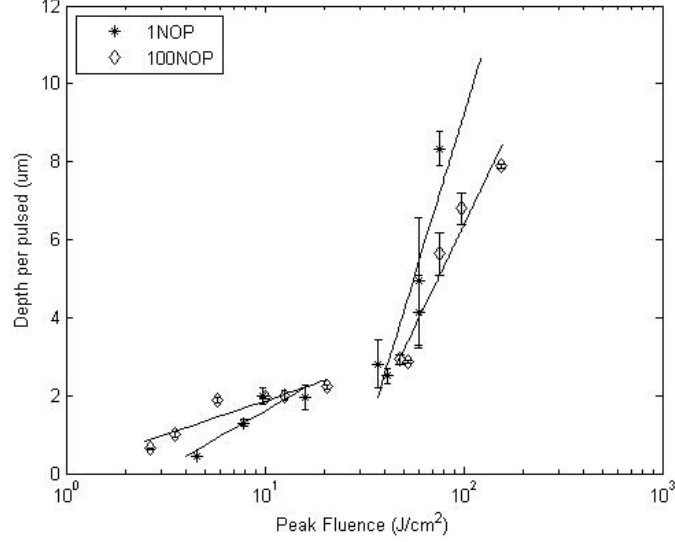


Figure 4.26: Plot of laser fluence in logarithmic scale versus ablation depth per pulse with a femtosecond laser ( $\lambda = 800 \text{ nm}$ ,  $pulse \ width = 100 \text{ fs}$ ) at a frequency of  $1 \text{ kHz}$  for ABS using depth measurement.

mon in femtosecond ablation of polymer where only one ablation regime has been observed in all the published results [196; 200; 233]. The observed trend is explained in detail in the following subsection. Both ablation regimes had a linear relationship between laser fluence in logarithmic scale and ablation depth per pulse which obey Beer's law. The two ablation regimes are differentiated as low fluence ablation regime ( $F_\alpha = 0.92 - 2.7 \text{ J/cm}^2$ ) and high fluence ablation regime ( $F_\alpha = 6.8 - 13.5 \text{ J/cm}^2$ ).

The optical penetration depth,  $\alpha^{-1}$  was  $2.917 \text{ nm}$  for the ablation threshold,  $F_{th}^\alpha$  of  $1.567 \text{ J/cm}^2$  in the low fluence ablation regime ( $F_\alpha = 0.92 - 2.7 \text{ J/cm}^2$ ). In the high fluence ablation regime ( $F_\alpha = 6.8 - 13.5 \text{ J/cm}^2$ ), the optical penetration depth,  $\alpha^{-1}$  was  $16.78 \text{ nm}$  for the ablation threshold,  $F_{th}^\alpha$  of  $4.267 \text{ J/cm}^2$ . It was also observed that the average depth per pulse contribution at the low fluence ablation regime increased with NOP as shown in Figure 4.7. This aligned with the incubation effect explained earlier where the material removal rate increases due to the reduction of ablation threshold when the NOP increases at a fixed laser fluence.



#### 4.3.3.3 Surface Chemical Composition Analysis

Figure 4.27 and figure 4.28 shows two examples of the fitted high resolution carbon spectrum before and after laser treated ABS surface using excimer laser and femtosecond laser.

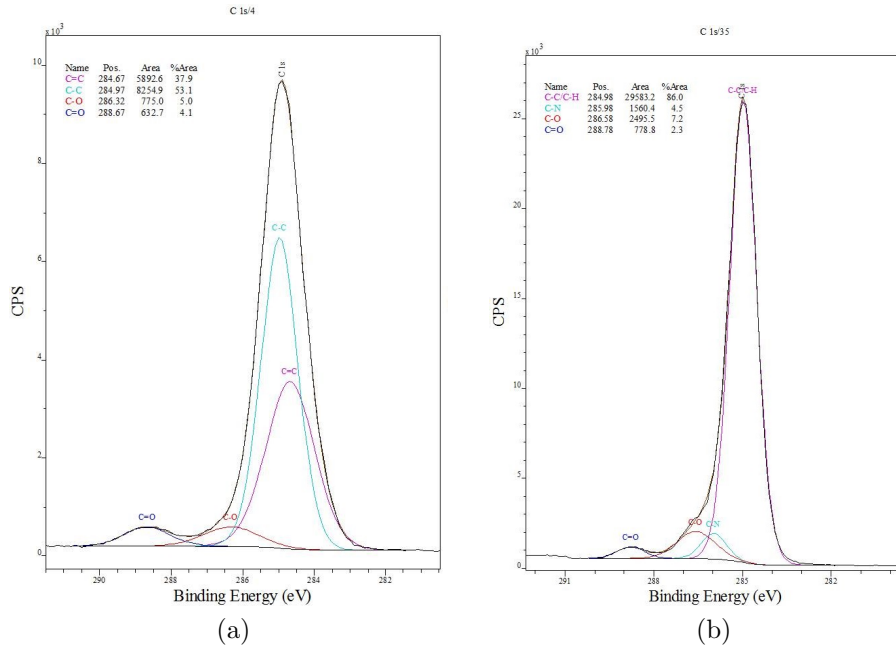


Figure 4.27: High resolution carbon scan XPS spectrum for (a) non-treated ABS and (b) excimer laser ( $\lambda = 248 \text{ nm}$ ,  $\text{pulse width} = 15 \text{ ns}$ ) treated ABS with  $200 \text{ mJ/cm}^2$ , 50 *NOP*.

The wide scan result for excimer laser and femtosecond laser is summarised in Table 4.9 and 4.10. From the XPS surface analysis, only oxygen, carbon, silicon and sulphur were identified on the un-treated ABS where the silicon and sulphur were deemed as contaminants on the surface. Nitrogen element was observed in all the excimer and femtosecond laser treated ABS surface indicating the addition of nitrogen functional group in the polymer. The absent of the nitrogen element on the as-received ABS might be due to the small quantity of the element within the monomer and the possibility of the nitrile group sidechain being embedded within the bulk material staying away from the surface [234; 235]. For the excimer laser ablated ABS, there was an increase in the N/C ratio as the fluence increases with 10 *NOP* and a similar observation was made at 50 *NOP* except for the highest

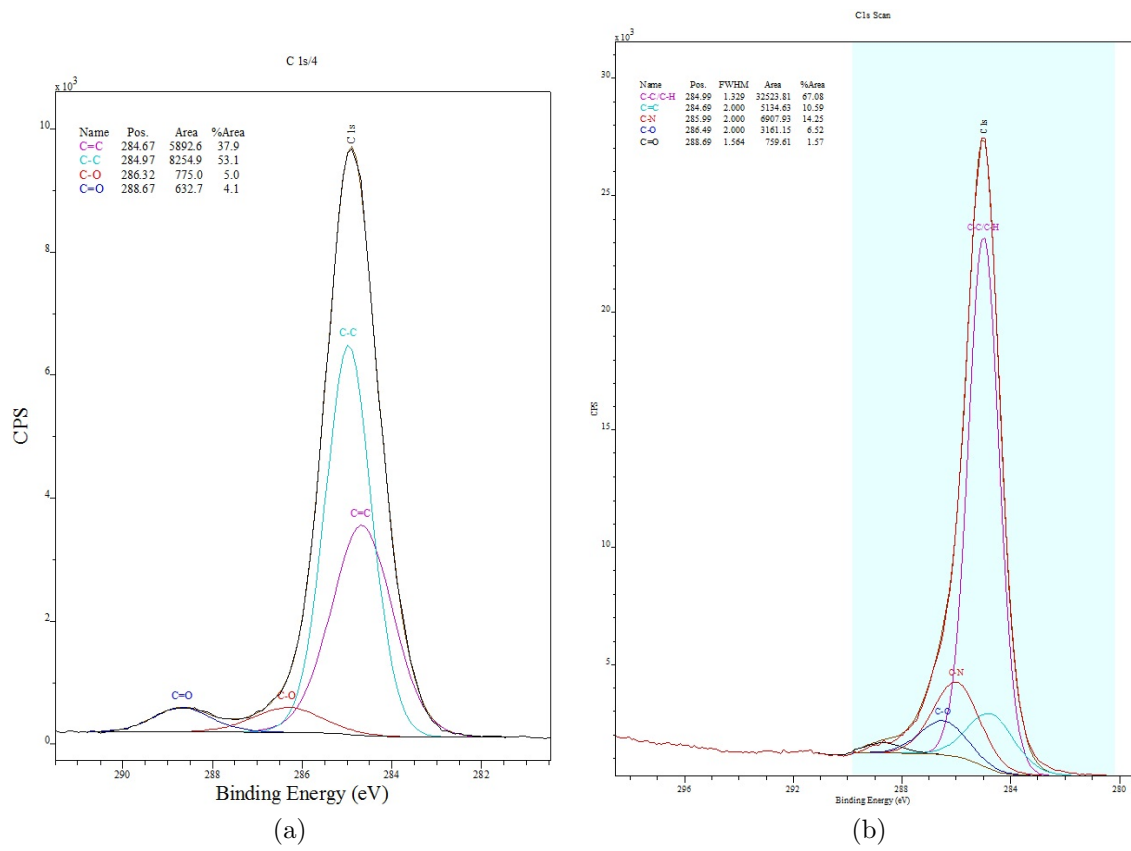


Figure 4.28: High resolution carbon scan XPS spectrum for (a) non-treated ABS and (b) femtosecond laser ( $\lambda = 800 \text{ nm}$ , *pulse width* = 100 fs) treated ABS with  $7.43 \text{ J/cm}^2$ , 8 NOP.

fluence where the ratio reduces. The O/C ratio was found to have decreased as the fluence increased with fixed NOP. As for the femtosecond laser ablated ABS, there was no particular trend in the N/C ratio variation relative to the laser fluence and NOP. However, there was a general decrease in the O/C ratio for all laser treated ABS surfaces relative to the un-treated surface. The ratio increased with NOP. From the data, it suggests that the ABS surface chemically reacted with other elements such as oxygen, nitrogen and water in air during those processes and this can be further confirmed by analysing the high-resolution scans of the carbon element as follows.

Table 4.9: Elemental composition of the ABS surface measured by XPS before and after various excimer laser treatment conditions.

Surface Treatment	Atomic Percentage (%)					
	O	C	N	Si	O/C	N/C
None treated	12.5	86.3	—	1.3	0.145	—
$50\text{mJ}/\text{cm}^2$ , 10NOP	12.4	86.9	0.7	—	0.143	0.008
$50\text{mJ}/\text{cm}^2$ , 50NOP	12.4	86.2	0.5	0.9	0.144	0.006
$100\text{mJ}/\text{cm}^2$ , 10NOP	12.4	86.8	0.8	—	0.143	0.009
$100\text{mJ}/\text{cm}^2$ , 50NOP	13	83.9	1.1	1.9	0.155	0.013
$200\text{mJ}/\text{cm}^2$ , 10NOP	12.3	85	0.8	1.9	0.145	0.009
$200\text{mJ}/\text{cm}^2$ , 50NOP	11.4	86.1	1.5	1	0.132	0.017
$400\text{mJ}/\text{cm}^2$ , 10NOP	11.6	86.1	1.2	1.1	0.135	0.014
$400\text{mJ}/\text{cm}^2$ , 50NOP	10.1	89.1	0.8	—	0.113	0.009

In the high resolution carbon spectrum, four main carbon bonds were identified on laser ablated surface and they are C-C/C-H bond, C-N bond, C-O bond and C=O bond. In the high resolution oxygen spectrum, two main oxygen bonds were identified and they are O-C bond and O=C bond. The identification of C=C bond indicated that the ABS polymer had unsaturated polymer chains within the material which agreed with the chemical formula of the ABS polymer. The double bond (C=C) undergoes chain scission and was converted into C-C/C-H bond or other carbon functional groups after excimer laser treatment as shown in Table 4.11. On the contrary, only 1/3 of the double bond undergone chain scission after femtosecond laser treatment as shown in Table 4.12. This is mainly due to the difference in the photon absorption mechanism of the ABS material as a result of

Table 4.10: Elemental composition of the ABS surface measured by XPS before and after various femtosecond laser treatment conditions.

Surface Treatment	Atomic Percentage (%)						
	O	C	N	Si	S	O/C	N/C
None treated	12.5	86.3	—	1.3	—	0.145	—
$7.43J/cm^2$ , 1NOP	6.03	91.05	2.13	0.6	0.18	0.066	0.023
$7.43J/cm^2$ , 2NOP	6.55	90.79	1.96	0.42	0.28	0.072	0.022
$7.43J/cm^2$ , 4NOP	7.12	89.95	2.15	0.53	0.26	0.079	0.024
$7.43J/cm^2$ , 8NOP	6.76	90.47	1.9	0.54	0.33	0.075	0.021
$3.71J/cm^2$ , 1NOP	7.04	90.41	1.97	0.43	0.16	0.078	0.022
$3.71J/cm^2$ , 2NOP	6.91	90.88	1.79	0.43	—	0.076	0.020
$3.71J/cm^2$ , 4NOP	8.01	89.81	1.47	0.71	—	0.089	0.016
$3.71J/cm^2$ , 8NOP	8.14	88.89	1.66	1.09	0.22	0.092	0.019

the difference in photon energy of the two lasers. Since excimer laser beam has a higher photon energy than the femtosecond laser beam, the excimer laser beam is able to initiate chain scission process through single-photon absorption. Hence, the C=C bond chain scission rate was higher and results in a thicker modified polymer layer.

In comparison to the un-treated ABS surface, there was an increase in the oxygen and nitrogen rich functional group percentage after both laser treatments. For the excimer laser treatment, this was partially aided by the ionisation of air molecules around the focal point of the laser beam through laser induced breakdown by adsorbing photon energy of the laser [224]. These active groups react with ionised oxygen and nitrogen molecules in air to form C-N, carbonyl group (C=O), carboxyl group (COO-) or hydroxyl group (C-OH) [212; 213; 214; 236]. The addition of nitrogen functional group might also be possible through chain scission of the nitrile group within the polymer chain creating free radical carbon and nitrogen who then recombine and form C-N group. The free radical carbon produced through chain scission process seemed to favour the formation of cross-link within the polymer rather than combining with the air molecules such as nitrogen, oxygen and water in air. This was observed through the increase in the C-C/C-H bond shown in Table 4.11 and Table 4.12.

There is a variation of the C-C/C-H bond percentage with different laser flu-

ence at fixed NOP for the excimer laser treated ABS but no significant trend that can be observed. A similar observation was seen with the oxygen rich functional groups. On the contrary, there was an increase in the nitrogen rich functional group percentage with the fluence at fixed NOP. This indicated that the free radical carbons were in favour of forming nitrogen rich functional groups than the oxygen rich functional groups.

On the other hand, it is observed that the nitrogen rich functional group increased with NOP at fixed fluence after femtosecond laser treatment as shown in Table 4.12. There is a decrease in the oxygen rich functional group (C-O and C=O bond) with increasing NOP at fixed laser fluence for femtosecond laser treatment. As the photon energy of the femtosecond laser is relatively low, the chances of air molecules ionisation around the focal point of the laser beam through laser induced breakdown is relatively low. This implied that the affinity of the carbon free radical produced during the chain scission process towards nitrogen molecule is higher than oxygen molecule.

Table 4.11: Surface chemical composition changes of the ABS surface measured by XPS carbon high resolution scan before and after various excimer laser treatment conditions.

Surface Treatment	Relative Area Percentage (%)				
	284.7	285	286	286.6	288.8
	$\pm 0.1$	$\pm 0.1$	$\pm 0.1$	$\pm 0.1$	$\pm 0.1$
	C=C	C-C/C-H	C-N	C-O	-C=O
None treated	37.9	53.1	—	5	4.1
$50\text{mJ}/\text{cm}^2$ , 10NOP	—	87.5	1.5	6.3	4.7
$50\text{mJ}/\text{cm}^2$ , 50NOP	—	87.9	1.9	6.1	4.1
$100\text{mJ}/\text{cm}^2$ , 10NOP	—	85.6	2.2	6.8	5.5
$100\text{mJ}/\text{cm}^2$ , 50NOP	—	83.3	4.9	7	4.8
$200\text{mJ}/\text{cm}^2$ , 10NOP	—	84.2	5.1	5.4	5.3
$200\text{mJ}/\text{cm}^2$ , 50NOP	—	86	4.5	7.2	2.3
$400\text{mJ}/\text{cm}^2$ , 10NOP	—	86.3	4.6	6.1	3
$400\text{mJ}/\text{cm}^2$ , 50NOP	—	88.6	4.2	4.7	2.5

Table 4.12: Surface chemical composition changes of the ABS surface measured by XPS carbon high resolution scan before and after various femtosecond laser treatment conditions.

Surface Treatment	Relative Area Percentage (%)				
	284.7	285	286	286.6	288.8
	$\pm 0.1$	$\pm 0.1$	$\pm 0.1$	$\pm 0.1$	$\pm 0.1$
	C=C	C-C/C-H	C-N	C-O	-C=O
None treated	37.9	53.1	—	5	4.1
$7.43J/cm^2, 1NOP$	10.27	70.47	9.41	8.92	0.94
$7.43J/cm^2, 2NOP$	15.19	65.53	9.66	7.69	1.92
$7.43J/cm^2, 4NOP$	13.16	67.85	11.22	5.96	1.81
$7.43J/cm^2, 8NOP$	10.59	67.08	14.25	6.52	1.57
$3.71J/cm^2, 1NOP$	10.83	68.34	5.77	12.94	2.11
$3.71J/cm^2, 2NOP$	10.01	69.8	3.3	15.35	1.54
$3.71J/cm^2, 4NOP$	10.84	69.6	8.56	9.72	1.28
$3.71J/cm^2, 8NOP$	11	68.87	10.44	9.02	0.67

Table 4.13: Surface chemical composition changes of the ABS surface measured by XPS oxygen and nitrogen high resolution scan before and after various excimer laser treatment conditions.

Surface Treatment	Relative Area Percentage (%)		
	532.1	533.3	400
	$\pm 0.1$	$\pm 0.1$	$\pm 0.1$
	O*-C=O	O-C=O*	N-C
None treated	55	45	100
$50mJ/cm^2, 10NOP$	79.2	20.8	100
$50mJ/cm^2, 50NOP$	74.3	25.7	100
$100mJ/cm^2, 10NOP$	83.2	16.8	100
$100mJ/cm^2, 50NOP$	79.3	20.7	100
$200mJ/cm^2, 10NOP$	80.1	19.9	100
$200mJ/cm^2, 50NOP$	72.9	27.1	100
$400mJ/cm^2, 10NOP$	72.7	27.3	100
$400mJ/cm^2, 50NOP$	70	30	100

Table 4.14: Surface chemical composition changes of the ABS surface measured by XPS oxygen and nitrogen high resolution scan before and after various femtosecond laser treatment conditions.

Surface Treatment	Relative Area Percentage (%)		
	532.1	533.3	400
	$\pm 0.1$	$\pm 0.1$	$\pm 0.1$
	O*-C=O	O-C=O*	N-C
None treated	55	45	100
$7.43J/cm^2, 1NOP$	53.7	46.3	100
$7.43J/cm^2, 2NOP$	42.25	54.75	100
$7.43J/cm^2, 4NOP$	52.09	47.91	100
$3.71J/cm^2, 8NOP$	51.22	48.78	100
$3.71J/cm^2, 1NOP$	44.5	55.5	100
$3.71J/cm^2, 2NOP$	38.08	61.92	100
$3.71J/cm^2, 4NOP$	43.38	56.62	100
$3.71J/cm^2, 8NOP$	51.56	48.44	100

#### 4.3.3.4 Comparison of Ablation Characteristic

Table 4.15 summarises the laser material interaction parameters for the ABS material with excimer laser and femtosecond laser. From the table, it was clearly observed that the interaction parameters of the material with the two lasers are different. The ABS requires lower ablation threshold to initiate ablation with excimer laser as compared to the femtosecond laser. This is mainly due to the difference in photon energy (wavelength) and pulse width of the two lasers. The excimer laser having a shorter wavelength (248 nm) has higher photon energy (5 eV) than the femtosecond laser (800 nm, 1.55 eV). Hence, the main mechanism of ablation for the excimer laser is a combination of photoablation and thermal ablation through single-photon absorption as the photon energy of the KrF excimer laser is greater than the gap energy of most polymeric bonds (3–5 eV) and the pulse width of the laser is longer as compared to the femtosecond laser [43; 46; 212; 213; 214; 236]. Such ablation mechanism is also known as thermal-photochemical ablation [46] or photophysical ablation [41]. The photons are absorbed by the chromophoric group at different electronic states and are converted into vibrational energy which leads to thermal decomposition and

ablation [41; 43].

Table 4.15: Summary of ablation characteristics obtained using different geometry measurement for ABS polymer.

<b>Laser</b>	<b>Excimer</b>	<b>Femtosecond</b>	
Geometry measurement	Depth	Diameter	Depth
Ablation threshold ( $J/cm^2$ )	0.87	1.648	1.567
$\alpha^{-1}$ (nm)	223	—	2.19
Incubation factor, $\xi$	—	0.51	—

On the contrary, due to the lower photon energy and shorter pulse duration of the femtosecond laser, the governing ablation mechanism is photoablation at low fluence and thermal ablation at high fluence through multi-photon absorption which is similar to the two temperature model proposed for metallic materials. The relationship between the ablation depth per pulse and photon density under a saturated multiphoton absorption process is given by [237; 238]:

$$d_n \approx \frac{2(S_o - S_{th})}{nl_o} \quad (4.9)$$

where  $S_{th}$  is the threshold photon density,

$S_o$  is the photon density at ground state for n-photon ablation respectively,

$l_o$  is the chromophores density constant in the ground state

As the photon density,  $S = F(h\nu)^{-1}$ , the linear fitting relationship between the depth per pulse and laser fluence (photon density) support the hypothesis that a multi-photon absorption mechanism is dominant under femtosecond laser ablation process [237; 238]. Such a model has been proposed by N.M. Bityurin et al. and is known as the photophysical model whereby it uses a four level model to relate between the ground state, electronic excited state and vibrational state of the chromophores after laser irradiation [41; 68]. There exist multiple electronic excited states,  $S$  to accommodate the excited electron in the vibrational state when it relaxes. The excited electrons in the vibrational state are able



to relax directly into the ground state by emission of photons or relax to one of the electronic excited states emitting fluorescence, phosphorescence or photon depending on the difference in band energy difference [66]. The relaxation time can be as short as  $10^{-11}$  s and as long as  $10^{-4}$  s depending on the energy band transition [239]. As the femtosecond laser has a much lower photon energy and shorter pulse width, at low fluence region, the chances of ablation occurring is much lower as compared to the excimer laser. Hence, the ablation of material is governed by photoablation through multi-photon absorption where electronic-to-vibrational energy transfer does not occur in this region as the pulse width is much shorter than the shortest possible electron relaxation time ( $10^{-11}$  s). As the laser fluence increases, thermal ablation is involved in the ablation process similar to the mechanism between the excimer laser and polymer. Hence, two distinct ablation regimes are observed for femtosecond laser ablation plot.

On the contrary, the optical penetration depth for the excimer laser beam on ABS is higher as compared to the femtosecond laser beam and this observation oppose to the theoretical optical penetration depth value for the IR wavelength laser beam as a higher value is expected ( $>$  tens of micrometers) as compared to the UV wavelength laser beam due to lower absorptivity of the IR wavelength laser beam [240]. The optical penetration depth value measured through ablation depth measurement method is highly dependent on the applied laser fluence as well as the lifetime of the molecule which is highly dependent on the complexity of the polymeric molecules [241]. Based on the photophysical ablation model, the ablation of a polymer in the low fluence regime is due to the change in the chromophores group density that significantly changes the complexity of the molecules in addition to the nature of the ablation (photochemical). Hence, the estimated optical penetration depth is lower than the theoretical value where the reported values took into consideration of the effect of material changes during laser irradiation such as bleaching and decomposition of absorbing chromophores [230; 242; 243]. It is believed that this is due to the difference in photon energy of the laser beam. As optical penetration depth is defined as the distance from the surface of the material where the intensity of the laser beam drops to  $1/e$  ( 37 %) of the initial intensity at the surface, the femtosecond laser beam, having a lower photon energy, has a lower optical penetration depth than the excimer

laser beam. This is further supported through the XPS analysis where there exist partial chain scission of C=C bond at low laser fluence and NOP using femtosecond laser where none was observed with the excimer laser.

## 4.4 Summary

1. The laser fluence versus ablation depth per pulse plot for HR4 nickel alloy material with femtosecond laser clearly indicates two ablation regimes and this is explained using the two temperature model. The ablation threshold is dependent on the NOP where the dependency is governed by the incubation factor.
2. The laser material interaction parameters evaluated using the diameter measurement on line ablation agreed with the spot ablation.
3. The ablation threshold and incubation factor evaluated using the depth measurement on line ablation is larger compared with spot ablation.
4. The diameter measurement shows a smaller measurement variation than the depth measurement, thus considered to be more reliable.
5. The ablation threshold (low fluence ablation region) for the HR4 nickel alloy was evaluated to be  $F_{th1} = 0.39 \text{ J/cm}^2$  with the incubation factor,  $\xi = 0.8$  and optical penetration depth of  $47.3 \text{ nm}$ .
6. The laser fluence versus ablation depth per pulse plot for the epoxy material with the excimer laser clearly indicates one ablation regime.
7. The ablation threshold of the epoxy material with the excimer laser is dependent on the NOP due to the change in the molecular structure of the polymer resulting in an increase in material absorptivity where the dependency is governed by the incubation factor.
8. The ablation threshold,  $F_{th}^1$  for epoxy was evaluated to be  $1.169 \text{ J/cm}^2$ . The incubation factor,  $\xi$  was deduced to be 0.75 where the optical penetration depth,  $\alpha^{-1}$  was evaluated to be  $282 \text{ nm}$ .

9. Excimer laser treated epoxy surfaces undergo chain scission through photolytic process. The chain scission process reduces the polymeric chain size and increases the oxygen rich (C-O and C=O) and nitrogen rich (C-N) functional groups through reaction between the free radical carbons with oxygen, nitrogen and water vapour in air. The increase in laser fluence and NOPs increases the oxygen and nitrogen rich functional groups on the epoxy resin surface when is treated with the excimer laser.
10. Fluorine contaminants are identified on the rough CFRP surface but not on the smooth CFRP surface. The fluorine contaminants are removed by laser surface treatment using suitable laser parameters.
11. The ablation threshold value is lower for ABS interaction with the excimer laser ( $F_{th} = 0.87 \text{ J/cm}^2$ ) as compared to the interaction with the femtosecond laser ( $F_{th} = 1.642 \text{ J/cm}^2$ ). This is due to the different in the ablation mechanism where the former is governed by thermal ablation with single-photon absorption and the latter is governed by photoablation (at low fluence regime) and thermal ablation (at high fluence regime) with multi-photon absorption.
12. The optical penetration depth value is higher for ABS interaction with the excimer laser ( $\alpha^{-1} = 223 \text{ nm}$ ) as compared to the interaction with the femtosecond laser ( $\alpha^{-1} = 2.917 \text{ nm}$ ). This is due to the difference in photon energy of the laser beam of different wavelength.
13. The ablation threshold is dependent on the NOP where the ablation threshold decreases with increasing NOP due to the change in the molecular structure of the polymer resulting in an increase in material absorptivity where the dependency is governed by the incubation factor.
14. Chain scission process occurs when ABS is treated with the excimer and femtosecond lasers causing a reduction in C=C bond creating free radical carbons which then either form cross-link with another free radical carbon or react with oxygen, nitrogen and water in air producing oxygen rich (C-O and C=O bond) and nitrogen rich (C-N) functional groups.

15. There is a decrease in oxygen rich functional groups for all laser treated ABS surfaces with increase fluence and NOPs. On the contrary, there is an increase in nitrogen rich functional group for all laser treated ABS surfaces with increase NOPs at fixed fluence.
16. Free radical carbons produced through chain scission process after laser treatment has a higher affinity towards nitrogen molecules than oxygen molecules.

## Chapter 5

# LASER CLEANING AND ABRADING OF CFRP FOR IMPROVED PAINT ADHESION

### 5.1 Introduction

Pre-surface treatment is very important for materials with low surface energy as the process enhances the adhesion property of the material surface. The purpose of surface pre-treatment for painting or other deposition processes are:

- Removal of surface contaminants
- Increase surface free energy for improved wettability
- Increase surface roughness for improved mechanical interlocking or bondable surface area

Contaminants can be found on the composite surfaces from various manufacturing processes, and by their nature form a weak boundary layer on the surface. These contaminants include silicones from release agents and bagging materials, fluorocarbon release sprays and films, machining oils, fingerprints and components in the composite itself which have migrated to the surface, such as calcium

separate from self-releasing formulations, water and plasticizers. Table 5.1 gives evidence of chemical contamination by fluorine species (30 %) for CFRP surface [127].

Table 5.1: Chemical composition (%) of CFRP surface [127].

	C	O	N	F	Si	S	O/C
Carbon/Epoxy	56.4	8.1	1.5	32.2	1.8	-	0.14

Table 5.2: Roughness and surface free energy of bare composite surfaces [127].

	<b>Roughness, Ra</b> ( $\mu m$ )	$\gamma^{LW}$ ( $mJ/m^2$ )	$\gamma^{AB}$ ( $mJ/m^2$ )	$\gamma^{TOT}$ ( $mJ/m^2$ )
Glass/Epoxy	0.79( $\pm 0.08$ )	31.6( $\pm 1.11$ )	2.36( $\pm 0.42$ )	33.96( $\pm 1.51$ )
Carbon/Epoxy	0.81( $\pm 0.17$ )	38.54( $\pm 0.9$ )	1.13( $\pm 0.17$ )	39.67( $\pm 1$ )

Composites usually present smooth and glossy moulded surfaces as shown in Table 5.2 due to the usage of fluorinated film as mould release agent during manufacturing [127]. Surface energy of composites tend to be low, especially for the thermoplastic matrices that makes wetting of the surfaces difficult. To achieve durable painting, the composite surface needs pre-treatment to modify the surface wettability and morphology and remove surface contaminants for better paint adhesion.

Various surface pre-treatment methods to improve adhesion performance of composite materials have been detailed in the literature review chapter. Surface contaminations originating from the manufacturing process, smooth surfaces, lower surface energy and lower wettability impair the adhesive behaviour the composites. The surface pre-treatment of composite materials is important for painting. It is necessary to limit the changes to a thin surface layer to preserve the bulk material properties whilst achieving the above objectives. Particularly composite materials require special considerations when treating their surfaces. There is a danger that some treatments may cause delamination defects just below the surface or damage to the relatively brittle fibres. These defects may result in poorer mechanical properties of the composites.

The bulk mechanical properties of the composite can be affected by abrasive surface treatments like alumina grit blasting and silicon carbide abrasion. Corona discharge and plasma treatments cause chemical composition changes and roughening of the composite surfaces. These methods also introduce oxygen functional groups onto the composite surface, resulting in improved wetting of the surface.

The use of UV laser ablation as surface pre-treatment is effective and has advantages compared to other conventional pre-treatments such as chemical etching, abrasive blasting and plasma treatments. Laser pre-treatment allows partial or complete removing of the superficial polymeric layer without affecting the fibre reinforcement. Excimer laser pre-treatment has been used for composite surfaces to improve adhesion performances. The laser parameters (laser fluence and NOP) have to be carefully selected to achieve suitable surface characteristics. The general phenomena observed due to laser pre-treatment are surface cleaning by removal of contaminants and weak boundary layers through evaporation, modification of surface chemical composition by imposing oxide derivatives and hydroxides, and change of surface morphology by introduction of uniform roughness. Consequently important considerations such as cleanliness, mechanical interlocking, chemical attraction and wettability affecting the adhesion performance can all be satisfied through laser pre-treatment method.

This research aims to utilize laser pre-treatment, in terms of cleaning and abrading, of CFRP for enhancement of paint adhesion, without damaging the carbon fibres, i.e. avoiding exposure of carbon fibre after laser pre-treatment. The specific objectives are:

- To determine the best-suited laser parameters for the pre-treatment process.
- To characterise the surface structures created after laser pre-treatment, including removal depth and surface roughness using optical microscope and optical white light interferometer.
- To characterise surface chemical composition changes after laser pre-treatment, including elemental composition and change in chemical bonding using XPS.
- To evaluate the surface wettability of laser pre-treated surfaces by contact

angle test.

- To evaluate the paint adhesion of various surfaces by pull-off adhesion test.

## 5.2 Methodology

### 5.2.1 Material Preparation

The composite material used in this project was CFRP supplied by BAe System. The CFRP had a dimension of  $4\text{ cm} \times 4.5\text{ cm}$  and a thickness of  $4\text{ mm}$ .

### 5.2.2 Surface Pre-treatment Methods

Two types of surface pre-treatment methods were considered in this experiment to be used as a comparison and they are sand papering pre-treatment and laser surface pre-treatment. Sand paper pre-treatment method is commonly used in the industry to perform cleaning and abrading on the CFRP surface before painting. Hence, this method was used as a benchmark to determine which method produced a better surface for paint adhesion. The following subsection details each of the surface pre-treatment methods used.

#### 5.2.2.1 Sand-paper Grinding Pre-treatment Method

The sand-paper pre-treatment method used in the experiment followed the procedure used in industry. The type of sand paper used in the pre-treatment process was a water resistant sand paper of grit size 240. The surface was sanded and tested using the water break test by dipping the sample into deionised water. If the ground surface was capable of holding a thin layer of water film for more than  $25\text{ s}$  without breaking, the sample passes the water break test. If not, the sample was re-sanded until it passed the test. Once the sample surface passed the water break test, it was rinsed by deionised water and then air dried.



### 5.2.2.2 Laser Surface Pre-treatment Method

A mask projection method was used to perform laser surface pre-treatment on the CFRP surface where the laser beam is passed through a mask with machined patterns where the patterns is then projected onto the material surface by partially blocking the laser beam. Different mask and laser parameters were used to abrade different sides of the CFRP as the initial surface finishing of the composite was different. The range of laser fluence used in the laser pre-treatment method ranged from  $50 - 300 \text{ mJ/cm}^2$  and the NOP used ranged from  $5 - 50$ . The overlap between the scanning track was  $50 \%$  with a frequency of  $10 \text{ Hz}$  when treating the smooth CFRP surface and  $30 \text{ Hz}$  when treating the rough CFRP surface. The laser pre-treatment for rough CFRP surface used higher frequency because the NOP needed to treat the rough surface was higher. Therefore, using a higher frequency speed up the pre-treatment process. The layout of the experiment is shown in Figure 5.1.

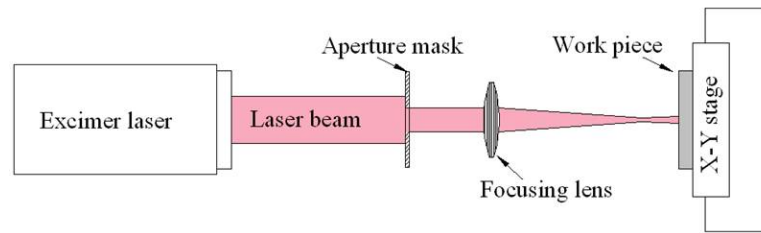


Figure 5.1: Illustration of the mask projection technique using a “hole array” mask.

### 5.2.3 Material Characterisation

Material characterisation had been carried out using optical microscopy, XPS and optical white light interferometer.

#### 5.2.3.1 Paint Adhesion Tester

The paint adhesion test was carried out using a PosiTest manufactured by De-Felsko Corporation. This machine conforms to international standards including ASTM *D4541/D7234* and ISO 4624/16276–1 [244]. The machine uses aluminium

test dollies of 20 mm diameter for the adhesion test where the dolly was stuck to the coating using the epoxy resin provided. The dolly was then applied with an upward pressure using a heavy-duty hydraulic pump manually. The pressure value was recorded by a digital monitor with a resolution of 1 *psi* or 0.01 *MPa* [244]. Figure 5.2 shows the PosiTest used in the adhesion test.



Figure 5.2: PosiTest AT-M Manual model [244]

Before the adhesion test, the samples were first coated with a layer of 2K acrylic primer manufactured by Fisher Motor Factors Ltd using a paint brush. The primer used was an oil based coating with a light gray colour and had a dry film thickness of 75  $\mu m$ . The process was done manually and the coating was always applied from the left direction to the right. After the application of the primer layer, they were left to cure (dry) for about half an hour to an hour. Then, the resin and hardener were mixed on a piece of cupboard with a ratio of one to one using a wooden stick and was stirred until an even creamy colour was observed. A thin layer of epoxy resin mixture was applied to the dolly. The dolly was then placed on the sample vertically and a uniform pressure was applied vertically where excessive resin mixture was removed using a pop stick. The sample was then placed in a furnace at 66°C for 2 hours for the resin to cure.

When the resin was cured, the sample was left to cool for about 15 minutes. Once the sample had cooled down, a cutter was used to make a circular cut around the dolly. Then, the pressure cylinder was placed firmly on the dolly. Once ready, pressure was continuously applied to the dolly until the dolly was lifted from the surface of the sample. A schematic diagram of the actual test samples before the pull off test is shown in Figure 5.3.

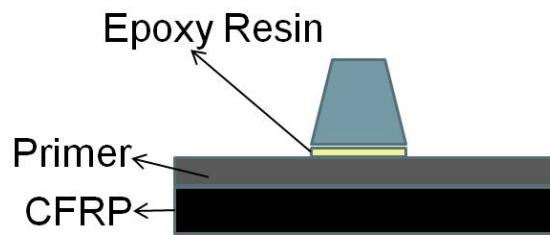


Figure 5.3: Pull-off test used for evaluating the adhesion of primer coating on CFRP.

## 5.3 Results and Discussion

### 5.3.1 Basic Material Characterisation of the CFRP

Three pieces of information was obtained from examining the CFRP material provided and they are:

- The thickness of the composite polymeric layer above the first fibre layer that is closest to the surface
- The size of the fibre used in the CFRP
- Surface chemical composition of the CFRP

The CFRP material used comes in two different finishing where one surface was rough and the other was smooth. The CFRP was cut into smaller pieces where the cross section of the material was moulded, ground and polished until the use of  $0.6\ \mu m$  size polishing cloth. The polished sample was then examined under the optical microscope. From the images shown in Figure 5.4, it was

observed that the thickness of the polymeric layer above the first fibre layer closest to the top smooth CFRP surface was  $\sim 10 \mu m$  and  $\sim 25 \mu m$  for the rough CFRP surface. The diameter of the fibre used in the CFRP was  $5 \mu m$  as shown in Figure 5.5. Figure 5.6 shows a contour plot of the polymeric layer thickness of CFRP obtained using the optical white light interferometer.

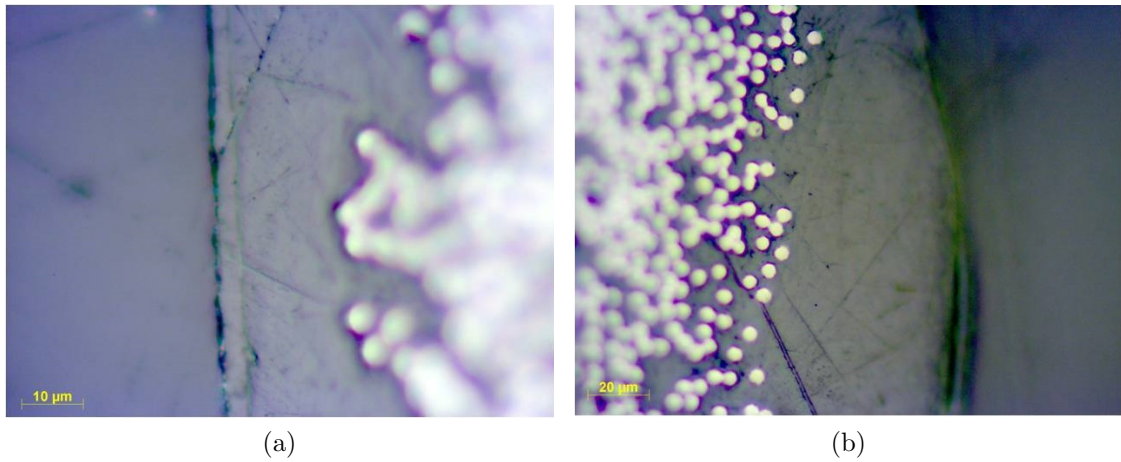


Figure 5.4: Optical microscope images of cross section showing polymeric layer thickness for (a) smooth surface and (b) rough surface of CFRP.

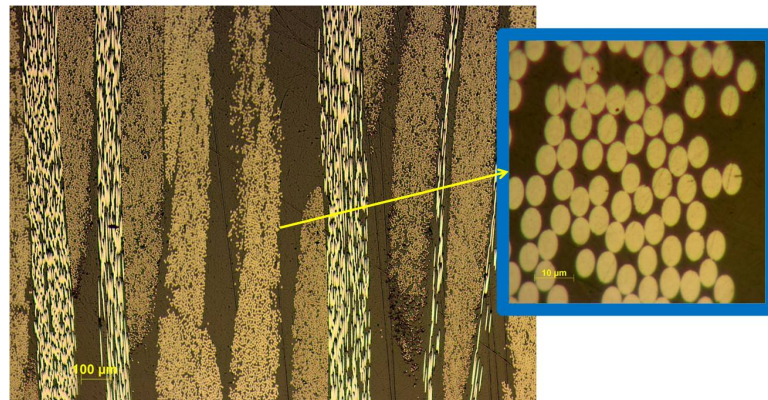


Figure 5.5: Optical images of the CFRP cross section showing the fibre diameter used in the composite.

The surface chemical composition analysis for both sides of the CFRP samples are summarised in Chapter 4. Fluorine element was identified on the rough CFRP surface sample indicating the existence of contaminants from the release films or

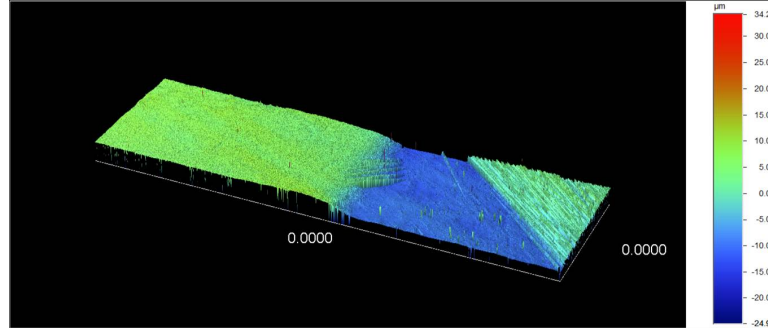


Figure 5.6: 3D optical profile of CFRC showing the thickness of the total polymer layer above the fibres around  $10\ \mu\text{m}$ .

other ancillary consumable during the manufacturing process. On the contrary, the XPS analysis result indicated that the smooth CFRP surface were free from contaminant contributed from the manufacturing process.

### 5.3.2 Investigation of Laser Surface Pre-treatment on Paint Adhesion Strength

An understanding of the factors that influence the adhesion of paint on composite is crucial before optimising the laser parameters for the laser surface pre-treatment method. Hence, three different laser parameters were chosen to pre-treat each CFRP surfaces and the surface property changes such as surface roughness, wettability, surface chemical composition and paint adhesion was investigated and compared to the as-received and sand-papered CFRP. A hole-array mask was used to pre-treat the smooth CFRP surface as shown in Figure 5.7 where the hole-array mask is believed to have the capability of roughening the surface of the CFRP. The mask consists of 36 holes arranged in a  $6 \times 6$  array with a diameter of  $1.2\ \text{mm}$  and a separation distance of  $0.6\ \text{mm}$ . On the other hand, a square mask of  $5\ \text{mm} \times 5\ \text{mm}$  was used to pre-treat the rough CFRP surface as the surface do not require further roughening. Three laser parameters representing low, medium and high laser fluence are selected and summarised in Table 5.3.

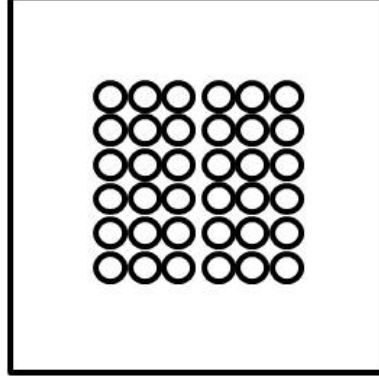


Figure 5.7: Illustration of the hole-array mask used in the experiment.

Table 5.3: Laser parameters used for CFRP surface pre-treatment experiment.

Pre-surface Condition	Smooth Surface			Rough Surface		
Laser Parameters	75	150	175	50	150	250
	$mJ/cm^2$	$mJ/cm^2$	$mJ/cm^2$	$mJ/cm^2$	$mJ/cm^2$	$mJ/cm^2$
	6 <i>NOP</i>	5 <i>NOP</i>	3 <i>NOP</i>	20 <i>NOP</i>	40 <i>NOP</i>	20 <i>NOP</i>

#### 5.3.2.1 Morphological and Chemical Characteristics of the surface

The surface morphology changes for laser surface pre-treated and sand-papered CFRP are shown in Figure 5.8 and Figure 5.9 where all the laser surface pre-treated CFRP did not expose any fibres. The underlying pattern of the rough CFRP surface remained after laser surface pre-treatment process as shown in Figure 5.9. The change in roughness between different pre-treatment method is shown in Figure 5.10. From Figure 5.10, the surface roughness increased across the laser parameters used for the rough CFRP surface. At the laser fluence of  $50 \text{ mJ/cm}^2$  and 20 *NOP*, the laser treatment smoothened the surface compared to the as-received surface. At the laser fluence of  $250 \text{ mJ/cm}^2$  and 20 *NOP*, the surface roughness increased and formation of small ripples on top of the underlying features was observed as shown in Figure 5.8d. The surface roughness for the smooth CFRP surface treated with the selected laser parameters did not show significant differences between each other but was smoothened slightly as compared to the as-received surface, as shown in Figure 5.10. The sand-papered smooth CFRP surface roughened the surface relative to the as-received smooth



surface whereas the sand-papered rough CFRP surface smoothened the surface relative to the as-received rough surface by removing the underlying patterns. Both sand-papered CFRP surfaces had similar morphology and similar surface roughness as shown in Figure 5.8b, Figure 5.9b and Figure 5.10.

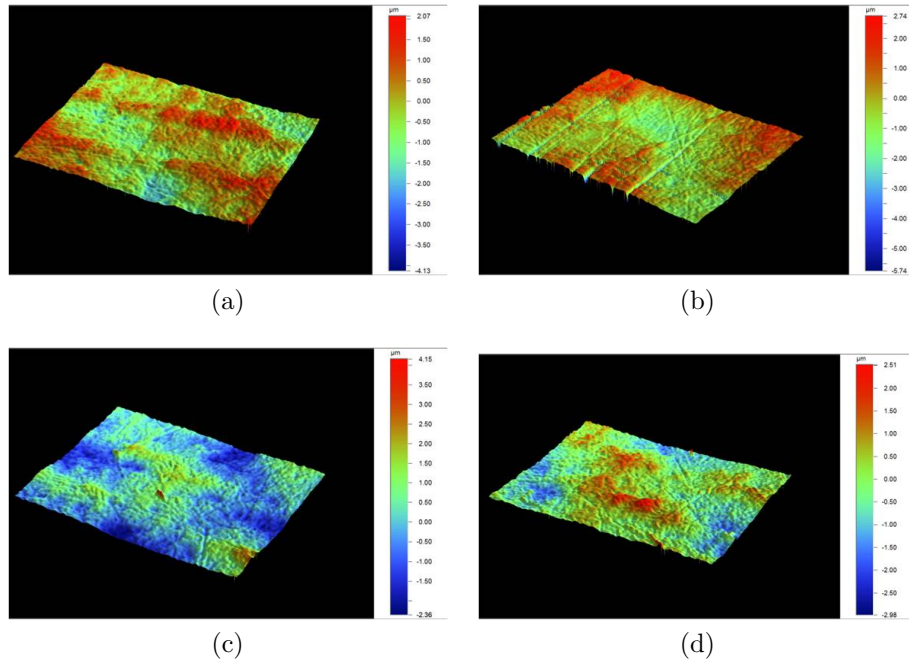


Figure 5.8: Surface morphology of the CFRP smooth surface before and after various treatments. (a) as-received, (b) sand-papered, (c) excimer laser treated with 50  $mJ/cm^2$ , 20 NOP and (d) excimer laser treated with 250  $mJ/cm^2$ , 20 NOP.

The surface chemical compositional changes of laser pre-treated CFRP is summarised in Chapter 4. In general, the laser pre-treated CFRP surface showed chain scission between the C-C bond and an increase in the nitrogen and oxygen functional groups within the polymer. The surface chemical composition changes of the sand-papered CFRP is summarised in Table 5.4, Table 5.5 and Table 5.6. From the wide scan results, it could be observed that the contamination on the rough CFRP surface had been removed as there was no indication of fluorine element present on the surface. This indicated that sand-papering was capable of removing contaminant on the CFRP surface.

By comparing the nitrogen-carbon ratio and the oxygen-carbon ratio of the

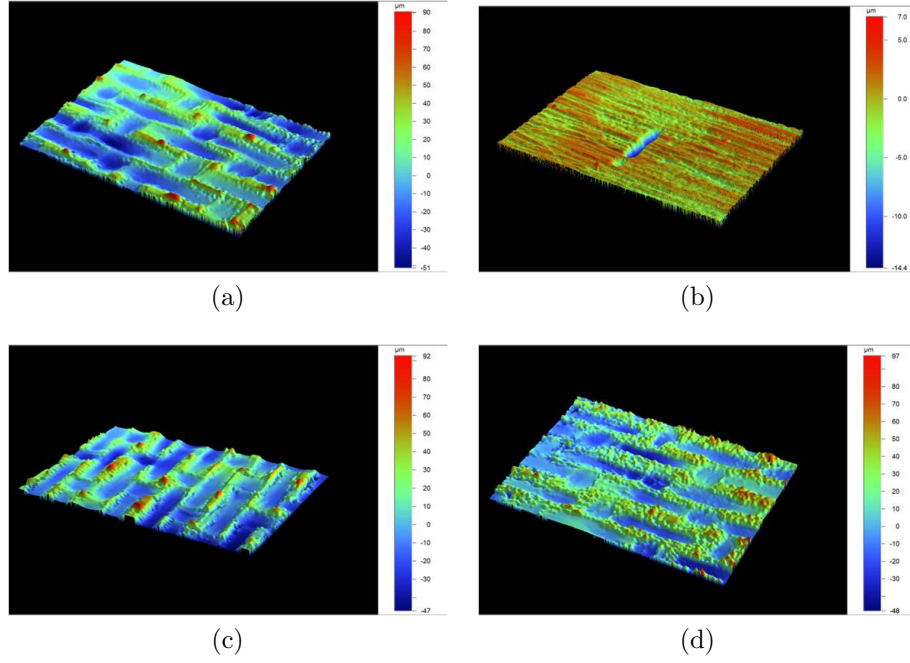


Figure 5.9: Surface morphology of the CFRP rough surface before and after various treatments. (a) as-received, (b) sand-papered, (c) excimer laser treated with  $75 \text{ mJ/cm}^2$ , 6 NOP and (d) excimer laser treated with  $175 \text{ mJ/cm}^2$ , 3 NOP.

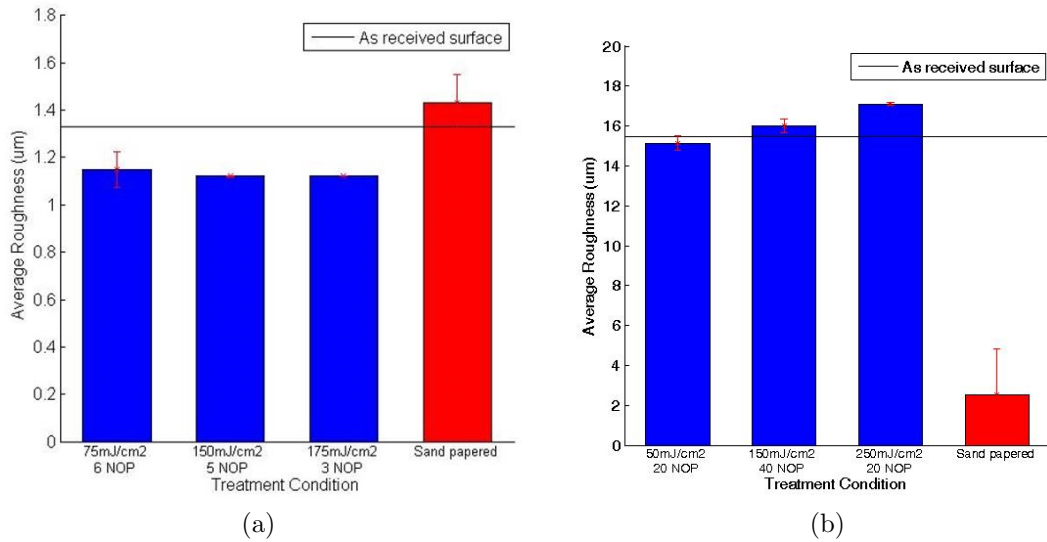


Figure 5.10: Surface roughness for excimer laser treated and sand-papered CFRP surface in comparison with the as-received CFRP surface on (a) smooth surface and (b) rough surface.



Table 5.4: Elemental composition of the CFRP surface measured by XPS after abrasion by sand paper.

Pre-surface condition	Atomic Percentage (%)							
	O	C	N	F	Ca	S	O/C	N/C
Smooth	17.6	76.1	3.5	—	—	2.8	0.23	0.05
Rough	18.8	74	3.4	—	—	3.8	0.25	0.05

Table 5.5: Surface chemical composition changes of the CFRP surface measured by XPS carbon high resolution scan after abrasion using sand paper.

Pre-surface condition	Relative Area Percentage (%)				
	$285 \pm 0.1$ C-C/C-H	$286 \pm 0.1$ C-N	$286.6 \pm 0.1$ C-O	$288.8 \pm 0.1$ -C=O	$292.2 \pm 0.1$ C-F
Smooth	47.64	24.81	19.11	8.44	—
Rough	58.3	19.6	14.9	7.2	—

Table 5.6: Surface chemical composition changes of the CFRP surface measured by XPS oxygen and nitrogen high resolution scan after abrasion using sand paper.

Pre-surface condition	Relative Area Percentage (%)			
	$532.1 \pm 0.1$ O*-C=O	$533.3 \pm 0.1$ O-C=O*	$532.9 \pm 0.1$ C-OH	$400 \pm 0.1$ N-C
Smooth	35.4	20.6	44	100
Rough	46.6	30.6	22.28	100

sand-papered CFRP surface to the as-received CFRP surface, the surface chemistry had changed where there was more oxygen and nitrogen functional groups in the polymeric chain. This was further confirmed by looking at the carbon high resolution scan. This indicated that the sand-papered CFRP surface interact with oxygen, nitrogen and water in air to form new functional groups within the polymeric chain. This process is not possible without having free radical carbons within the polymer chain. Homolytic cleavage process can be achieved through three mechanisms which are photolithic process, thermal process or mechanochemical process. Photolithic process uses photon energy that is equivalent to bond energy of the covalent bond to cause homolytic cleavage which produces free radicals. On the other hand, thermal process uses thermal energy to achieve this and as for mechanochemical process, it uses stress and strain imposed onto the material surface to achieve homolytic cleavage [245]. Sand-papering process created free radical carbons within the polymeric chain at the surface through mechanochemical process which then allowed the free radical carbons to react with oxygen, nitrogen and water in air, resulting in a more stable polymeric chain [216].

Hydroxyl functional group was identified in the high resolution carbon and oxygen spectrum for the sand-papered CFRP surface. The existence of the hydroxyl functional group is believed to be caused by the water break test process which takes place after the sanding process. As the sand-papering process also caused chain scission on the surface of the polymer, the free radical carbons reacted with the water molecules when in contact thus forming hydroxyl group on the surface of the polymer [215]. The amount of chain scission caused by the sand-papering process was higher than those caused by the laser surface pre-treatment process.

### 5.3.2.2 Wettability of the surface

The change in contact angle for all the different pre-treated CFRP surfaces are shown in Figure 5.11. The rough CFRP surface was hydrophobic (contact angle  $> 90^\circ$ ) whereas the smooth CFRP surface was hydrophilic (contact angle  $< 90^\circ$ ). The change in contact angle between different surface pre-treatments on different

CFRP surfaces showed different trends. For the rough CFRP surface, the laser pre-treated surface showed reduction in contact angle as compared to the as-received surface. On the other hand, the laser pre-treated surface at the laser fluence of  $75 \text{ mJ/cm}^2$  and 6 *NOP* for the smooth CFRP surface showed a slight increase in contact angle but the laser fluence of  $175 \text{ mJ/cm}^2$  and 3 *NOP* reduced the contact angles as compared to the as-received surface. The sand-papered CFRP surface showed reduction in contact angle for both smooth and rough CFRP surface where the sand-papered rough CFRP surface resulted in a lower contact angle as compared to the sand-papered smooth CFRP surface.

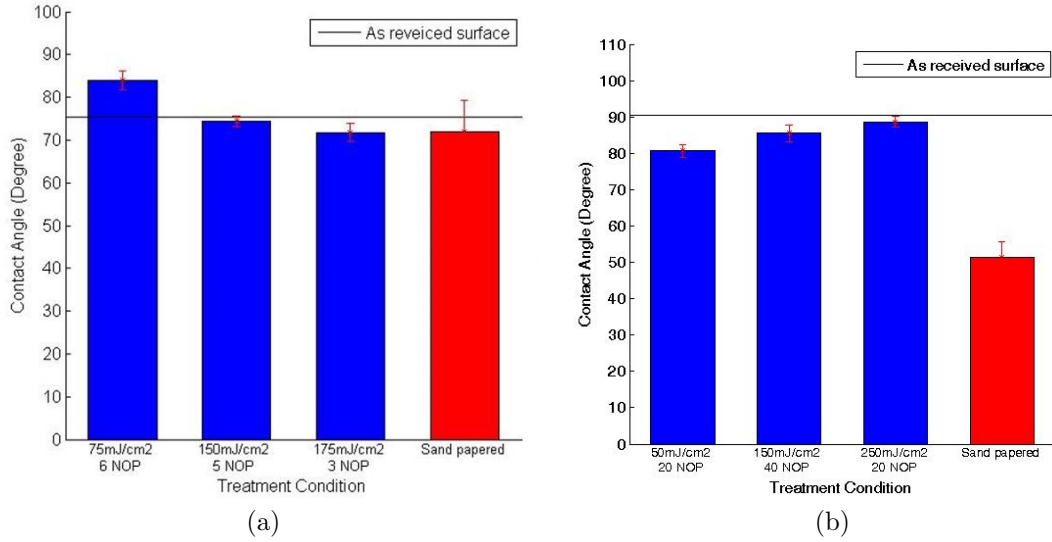


Figure 5.11: Contact angle for excimer laser treated and sand-papered CFRP surfaces in comparison with the as-received CFRP surface on (a) smooth surface and (b) rough surface.

The change in contact angle is affected by several factors and they are surface roughness, surface chemical composition and surface contaminants [246]. In general, removal of surface contaminants like fluorine results in lower contact angle. Change in surface roughness affect contact angle in a way where it act as an amplifier to the nature of the surface itself according to Wenzel model [247]. For example if the surface is hydrophilic (contact angle  $< 90^\circ$ ), increase in surface roughness decreases the contact angle of the surface, i.e. increase hydrophilicity. If the surface is hydrophobic (contact angle  $> 90^\circ$ ), the increase in surface

roughness increases the contact angle, i.e. increase hydrophobicity.

In addition, for polymer materials, the functional groups on the polymer surface also significantly affect its wettability. The presence of fluorine contamination on the rough CFRP surface identified through XPS analysis caused the surface to be hydrophobic. For the laser pre-treated surface, the reduction (for laser parameter of  $50 \text{ mJ/cm}^2$  and 20 *NOP*)/ removal (for laser parameter of  $200 \text{ mJ/cm}^2$  and 20 *NOP*) of the fluorine contaminant and increased in polar functional group decreases hydrophobicity. On the contrary, the roughening of the surface except for that pre-treated with  $50 \text{ mJ/cm}^2$  and 20 *NOP*, increases hydrophobicity as the initial surface was hydrophobic in nature. Hence, the resultant contact angle was slightly lower than the as-received CFRP contact angle as the two factors have a counter effect on each other.

The laser pre-treated smooth CFRP with  $75 \text{ mJ/cm}^2$  and 6 *NOP* had a higher contact angle as compared to the as-received surface. This is due to the decrease in surface roughness after laser pre-treatment as the smooth CFRP surface was hydrophilic in nature. Hence, the decrease in surface roughness decreased the hydrophilicity of the surface. All laser pre-treated smooth CFRP surfaces had a similar and lower surface roughness as compared to the as-received smooth CFRP surface but the polar functional groups on the surface were increased as shown in the XPS analysis. Hence, the contact angle for the three surfaces decreased. Similar argument is applied to the sand-papered CFRP surfaces.

### 5.3.2.3 Paint Adhesion Performance

The paint adhesion performance for different pre-treated CFRP surfaces were investigated through measuring the strength between the primer and the CFRP surface interface as shown in Figure 5.12. From figure 5.12, it was observed that the breaking point between the primer and the rough CFRR surface happened at the peak of the rough surface (tip). This is because the tip point is asserted with a higher pressure and contains a thinner coating. The CFRP paint adhesion performance for different pre-treated surfaces are shown in Figure 5.13. Improvement on paint adhesion strength was observed on all laser pre-treated CFRP on both smooth and rough surfaces. The degree of improvement was dependent on

the laser fluence and NOP where the combination of high fluence and low NOP achieved the highest improvement. This combination avoided the exposure of fibres and achieved favourable surface property changes that improved paint adhesion of CFRP. Sand-papered CFRP surface also showed improvement in paint adhesion strength as expected.

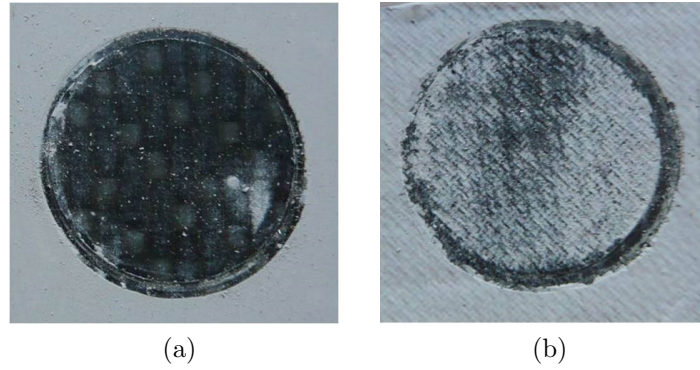


Figure 5.12: Top surface view of the composite after paint adhesion test. (a) smooth surface and (b) rough surface of the CFRP.

Paint adhesion is affected by several factors and in order to have a clear understanding of such improvement, all the factors should be looked into as well as the mechanism of paint adhering onto the surface. Some of the important factors include surface contaminants, surface roughness and surface chemical composition. Surfaces that are free from contamination are always required to promote good adhesion between two materials. Increase in surface roughness promotes more bonding between the surfaces through mechanical interlocking due to larger surface area of contact. This is particularly critical for CFRP as many polymers exhibit low adhesion characteristics due to low surface energy [116; 117].

As the primer used in the investigation was an oil based primer coating, the adhesion mechanism of the primer is through chemical reaction between the primer and air. Oxidative drying between the oil solvent and the oxygen or water vapour in air through attacking the double bonds in the solvent via direct addition creates free radical carbons within the polymer chain. The free radical carbons promote cross-link between the polymer compounds within the primer [131]. In addition, the free radical carbons also promote cross-link between the primer

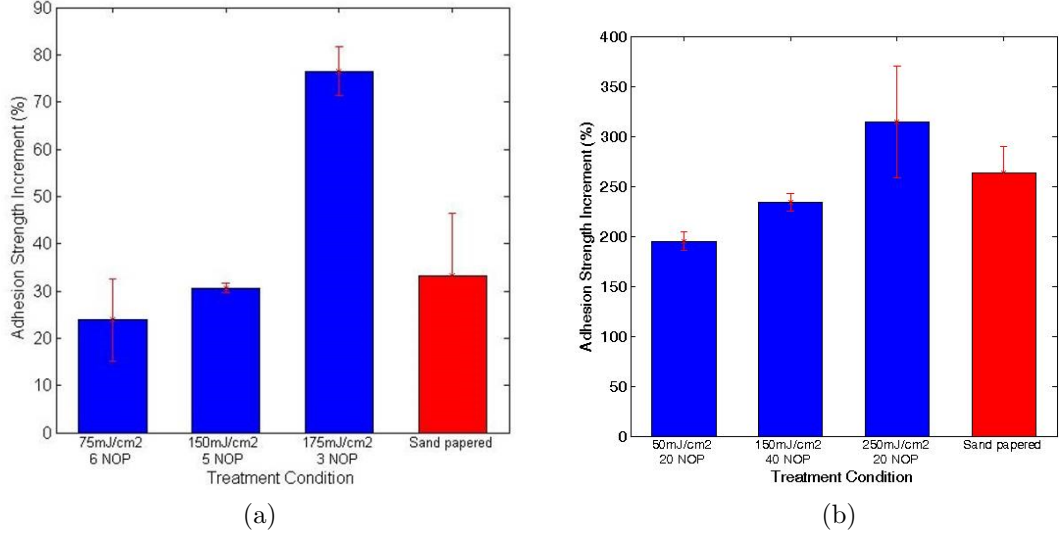


Figure 5.13: Paint adhesion improvement after excimer laser treatment in comparison with the sand-papered surface for (a) smooth surface and (b) rough surface of the CFRP.

layer and the CFRP surface which strengthen the bond between the interface. Hence, the existence of polar groups on the CFRP surface improves paint adhesion strength as they are more reactive than other inert functional groups of carbon such as C-C, C-H and C-F towards free radical carbons [212; 236].

The laser pre-treated rough CFRP surface using 50  $mJ/cm^2$  and 150  $mJ/cm^2$  with 90 *NOP* and 40 *NOP* showed lower adhesion improvement than the sand-papered CFRP surface. This was due to the fluorine contaminant remaining on the surface after laser pre-treatment as shown from the XPS analysis. As for the rough CFRP laser treated with 250  $mJ/cm^2$  and 20 *NOP*, The paint adhesion improvement was better as compared to the sand-papered CFRP surface because the surface was completely free from fluorine contamination. In addition, the surface had higher concentrations of polar function groups and surface roughness as compared to the sand-papered CFRP surface. From the paint adhesion strength, it was observed that surface contaminants particularly the presence of fluorine played a determining role in this case.

The smooth CFRP laser pre-treated surfaces with laser fluences of 75  $mJ/cm^2$  and 150  $mJ/cm^2$  with 6 *NOP* and 5 *NOP* showed less adhesion improvement

than the sand-papered CFRP surface. This might be associated with the amount of polar functional groups formed where the laser pre-treated CFRP with these parameters had less polar functional groups as compared to the sand-papered CFRP. However, when the CFRP surface was treated with laser fluence of  $175 \text{ mJ/cm}^2$  and 3 *NOP*, although the amount of polar functional groups was slightly less than the sand-papered CFRP, the laser modified layer was stronger. This is because the chain scission process was less when the surface is laser pre-treated as compared to sand-papered surface. This implies that the laser modified layer through using high fluence and low *NOP* is capable of holding the layers together firmly resulting in better improvement in paint adhesion strength. On the contrary, although the sand-papered and laser pre-treated surfaces changed the CFRP surface roughness slightly as compared with the as-received CFRP surface as shown in Figure 5.10, it did not seem to affect the paint adhesion significantly. Hence, the surface chemical composition in terms of polar functional groups formation and the amount of chain scission occurrence play a more important role.

The surface pre-treated rough CFRP surfaces showed higher paint adhesion strength improvement as compared to the smooth CFRP surfaces. This is mainly due to the higher surface contamination on the rough CFRP surface before laser pre-treatment as well as higher surface roughness as compared to the smooth CFRP surface. From the analysis of the various surface properties of different surface pre-treatment conditions, it is believe that the surface roughness and surface chemical composition plays an important role in determining the adhesion strength of the CFRP with paint.

On the contrary, the contact angle does not seem to have any relation or indication in determining the adhesion property of CFRP with paint as shown in Figure 5.11. The contact angle theory is based on the equilibrium interaction between three mediums which are solid, liquid and gas where the main interaction is the solid-liquid and liquid-liquid interaction. When the contact angle is zero, the solid surface is considered to have perfect wetting (hydrophilic) and has a stronger solid-liquid interaction as opposed to the liquid-liquid interaction. When the angle is between zero and  $90^\circ$ , it is considered as high wettability having solid-liquid interaction more or less equal to the liquid-liquid interaction but does not always imply strong interaction strength. When the angle is more than  $90^\circ$ ,

the solid-liquid interaction strength is weaker than the liquid-liquid interaction strength as summarised in table 5.7. Hence, having a low contact angle does not imply strong adhesion force between the solid-liquid inter face.

Table 5.7: Solid-liquid and liquid-liquid interaction strength of different contact angle values [248].

Contact angle	Degree of wetting	Interaction strength	
		Solid-liquid	Liquid-liquid
$\theta = 0$	perfect wetting	strong	weak
$0 < \theta < 90^\circ$	high wettability	strong	strong
		weak	weak
$90^\circ \leq \theta < 180^\circ$	low wettability	weak	strong
$\theta = 180^\circ$	perfectly non-wetting	weak	strong

There are many publications indicate the relationship between contact angle and adhesion where low contact angle results in higher adhesion. This case is true from the point of view where having a wettable surface increases the contact area between the liquid and the surface due to the strong interaction force at the solid-liquid interface. But in the case of painting, it is a process where the liquid is spread on the surface mechanically, hence the liquid spreadability of the surface does not have much influence on the paint adhesion strength of CFRP. In addition, the adhesion strength between the primer and the CFRP surface is determined by the amount of covalent bond formed between the primer film and the CFRP surface through oxidative drying process. Hence the main influence of paint adhesion is the density of the polar functional groups on the surface of the CFRP. As mentioned in the previous section under wettability, contact angle measurement is influenced by several factors including surface roughness, surface chemistry and environmental conditions, therefore the contact angle value does not reflect or match against the paint adhesion results completely.

### 5.3.3 Operating Window for Smooth CFRP Surface

The hole-array mask shown in Figure 5.7 was used to establish the operating window for the smooth CFRP surface. The operating window for the smooth CFRP surface was separated into three different regions marked with different



colours: red, yellow and blue. Laser parameters in the red region indicating carbon fibre exposure after laser surface pre-treatment. On the other hand, yellow and blue region indicating non-exposure of carbon fibre after laser surface pre-treatment. This data was obtained through a series of experiments done using a square mask with varying fluence and NOPs where the samples were then examined under the optical microscope and optical white light interferometer for any visible exposed fibre. Figures 5.14 presents the 3D optical profiles of the CFRP surface after laser surface pre-treatment under various laser parameters. Figure 5.15 shows the variation of removal depth by laser surface pre-treatment with different laser parameters. It was observed that the removal depth could be well controlled, without exposure of carbon fibres. Table 5.8 summarised the results observed where Figure 5.16 shows the optical images of the three surface condition classified. As the paint adhesion of the laser treated surface is compared with the sand-papered surface, the paint adhesion strength of the sand-papered surface was used as a bench mark. From the experiment, it was found that the sand-papered CFRP surface had a  $35 \pm 13$  % increase in paint adhesion strength relative to the as-received CFRP surface. Hence, this value was used to mark the line between the blue and yellow region where the blue region indicates insufficient increase in paint adhesion strength or in similar term has an increase of less than 35 % relative to the as-received CFRP surface. The green region indicated the allowable fluence and NOP shift from the optimal laser parameter to obtain a reasonably close paint adhesion strength relative to the optimal value.

Table 5.8: Observation of the smooth CFRP surfaces after laser pre-treatment using different laser parameters.

NOP	Fluence (mJ/cm <sup>2</sup> )					
	25	50	75	100	150	200
10	No Damage	No Damage	No Damage	No Damage	No Damage	Threshold
20	No Damage	No Damage	No Damage	No Damage	Threshold	Fibre exposed
40	No Damage	No Damage	Threshold	Threshold	Fibre exposed	Fibre exposed
100	No Damage	No Damage	Fibres exposed	Fibre exposed	Fibre exposed	Fibre exposed
200	No Damage	Threshold	Fibre exposure	Fibre exposed	Fibre exposed	Fibre exposed

Through a series of tests, the optimal laser parameter was concluded to be

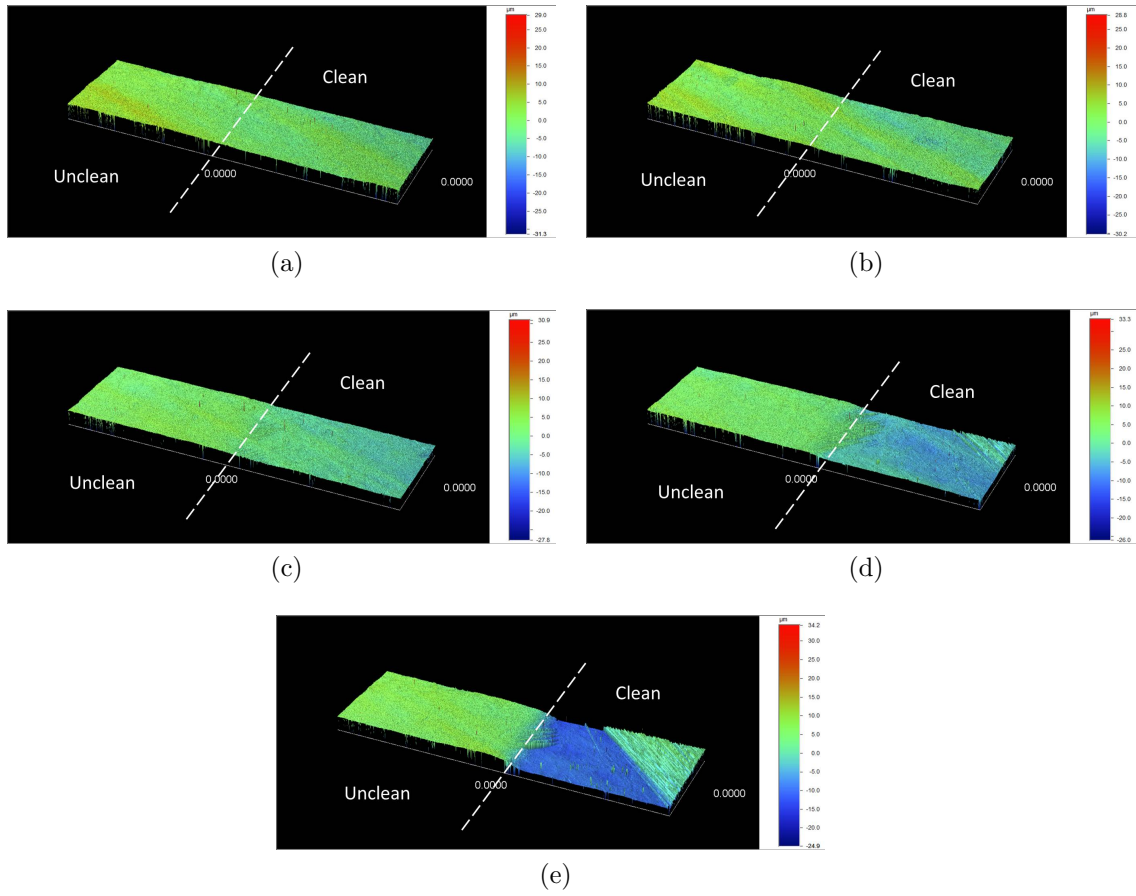


Figure 5.14: 3D optical profiles of the surface after excimer laser ( $\lambda = 248 \text{ nm}$ , *pulse width* =  $15 \text{ ns}$ ) cleaning at laser fluence of  $200 \text{ mJ/cm}^2$  and NOP of (a) 10 (b) 20 (c) 40 (d) 100 and (e) 200.

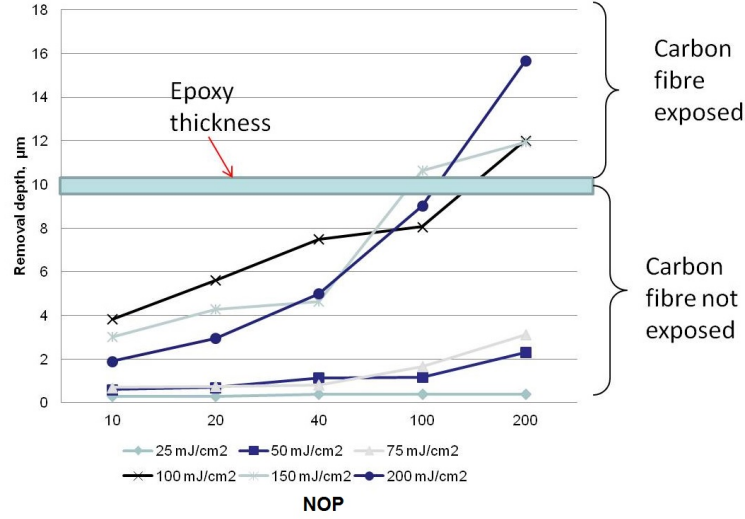


Figure 5.15: Variation of removal depth with different laser pre-treatment parameters.

$175 \pm 10 \text{ mJ/cm}^2$  with  $3 \pm 1 \text{ NOP}$  at a frequency of  $10 \text{ Hz}$  and with  $0 \%$  overlap. The operating window diagram is shown in Figure 5.17.

The laser pre-treatment coverage using the hole-array mask on the smooth CFRP surface is partial as there are areas in between the hole-array that had not been treated by the laser beam. Without the use of the hole-array mask, the roughness of the surface is deemed to be insufficient for improving paint adhesion strength. Hence an investigation on the effect of laser pre-treatment using different mask combinations (hole-array, square and hole-array + square mask) on paint adhesion strength was carried out. The NOP used during the hole-array + square mask was equally split between the two masks. The experiment was performed on the smooth CFRP surface and the laser parameters used are as follow:

- Fluence ( $\text{mJ/cm}^2$ ): 100
- NOP: 7
- Overlap (%): 0 (For hole-array mask), 50 (For square mask)
- Frequency ( $\text{Hz}$ ): 10

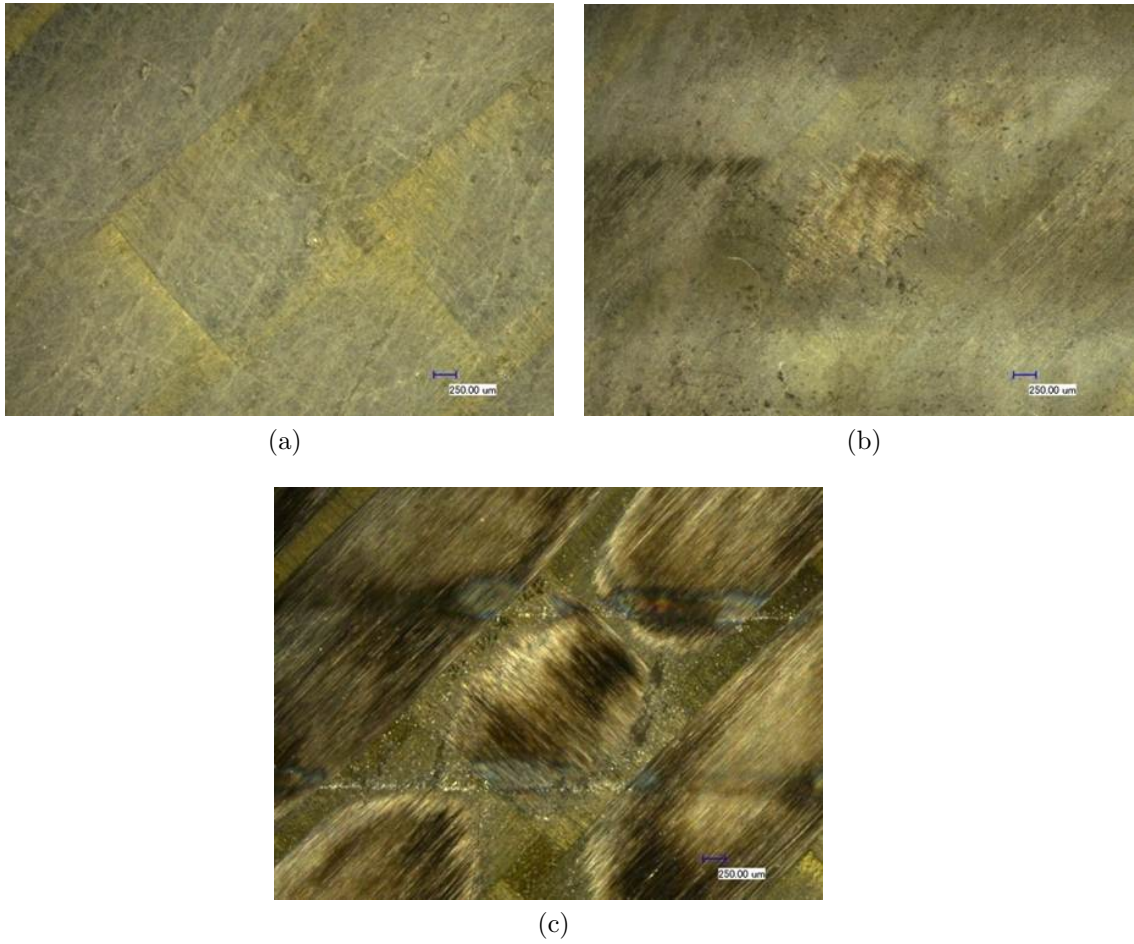


Figure 5.16: Optical images of the surface after excimer laser ( $\lambda = 248 \text{ nm}$ , *pulse width* = 15 ns) cleaning at laser fluence of (a) 25 mJ/cm<sup>2</sup>, 100 NOP (No damage), (b) 50 mJ/cm<sup>2</sup>, 200 NOP (Threshold) and (c) 200 mJ/cm<sup>2</sup>, 200 NOP (Fibre exposed).

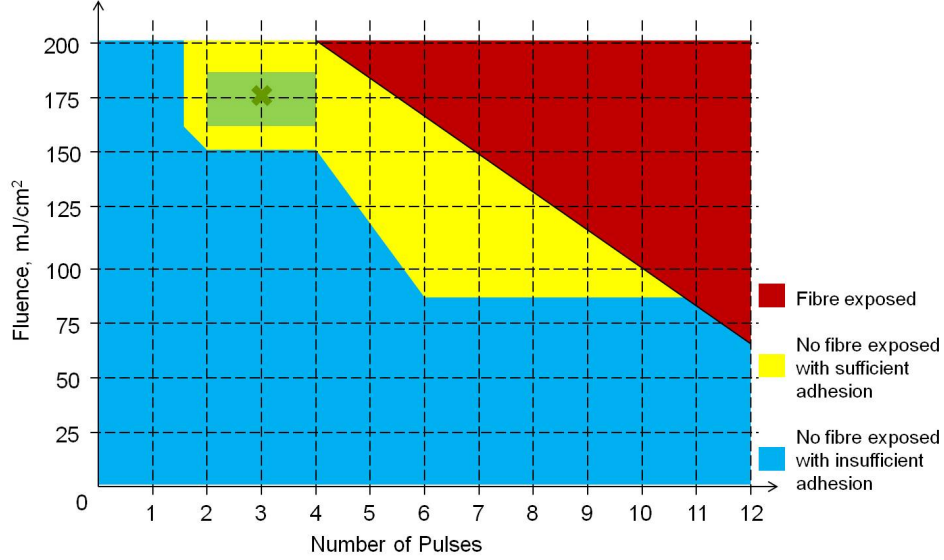


Figure 5.17: Operating window diagram for the smooth CFRP surface using hole-array mask.

The paint adhesion strength increment plot for the experiment is shown in Figure 5.18 and it strongly indicated that the laser pre-treatment process using hole-array + square mask had the highest paint adhesion strength increment. The surface pre-treated with either square mask or hole-array mask alone showed similar adhesion strength increment. This is because the square mask pre-treated the CFRP surface completely where the polar functional groups of the CFRP surface increased throughout the surface as shown in the XPS analysis results. On the contrary, due to the top-hat shape of the incident laser beam, the surface roughness was reduced and therefore reduced the paint adhesion strength relative to the surface pre-treated with hole-array + square mask. As for the CFRP surface pre-treated with the hole-array mask, although the surface was roughened, the change on surface chemical composition was not even where area that are not treated by the laser beam contained lower polar functional groups which weakened the paint adhesion strength. The surface pre-treated using hole-array + square mask showed the best paint adhesion strength due to the increase in polar functional groups throughout the surface in addition to the increase in surface roughness. Although the surface roughness was lower compared to the surface pre-treated with hole-array mask, the paint adhesion strength was higher as the

increase in polar functional groups on the CFRP surface had a more significant influence on the paint adhesion strength.

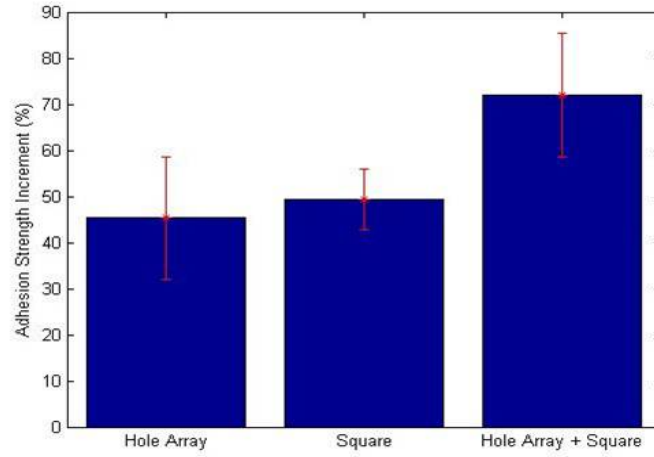


Figure 5.18: Bar plot of adhesion strength increment vs different mask used at fluence of  $100 \text{ mJ/cm}^2$  and 7 NOP for the smooth CFRP surface.

A new mask was designed to incorporate the square mask and the hole-array mask effect into a single mask so that the pre-treatment process could be done through a single pass. The new mask is named hybrid mask where it consists of two parallel slots at both ends and an array of 24 holes in the form of  $6 \times 4$  array as illustrated in Figure 5.19. The design of the hybrid mask has to be symmetrical due to the laser pre-treatment process as it moves in a serpentine motion. The mask is designed in such a way as the square mask and the hole-array mask effect is equally distributed. During the cleaning process, there was a 50 % overlap as to make sure that the rectangular slot fully covers the treated area. Hence, the hole-array only covers half of the mask as to avoid the overlapping whereas the rectangular slot covers the full 10 mm length. Therefore, the ratio of the total width of the slot to the holes is 1 : 2 due to the overlapping of the slot as it was calculated based on the NOP contributed by each section of the mask which is related to the width of the shape. The hybrid mask was manufactured using the Ti:Sapphire femtosecond laser which has the following dimension and is illustrated in Figure 5.20.

- Rectangular slot: 10 mm (height)  $\times$  0.9 mm (width)

- Hole: 0.6 *mm* (diameter) and 0.6 *mm* separation (between two holes)
- Separation distance between the slot and the hole-array: 0.8 *mm*

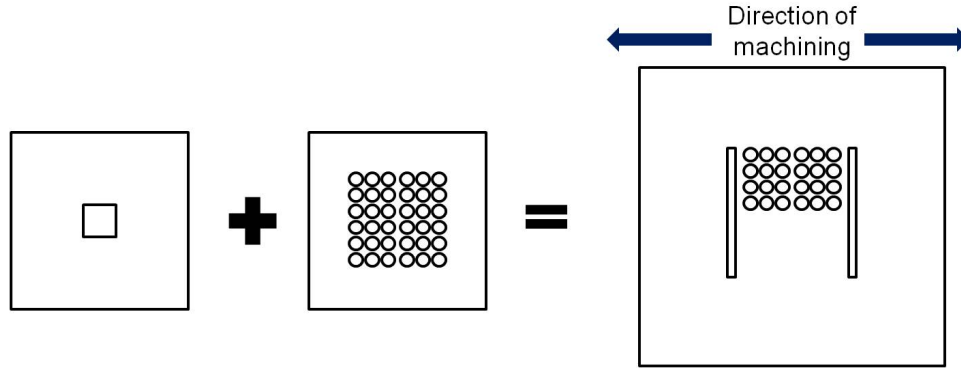


Figure 5.19: Illustration of the hybrid mask concept.

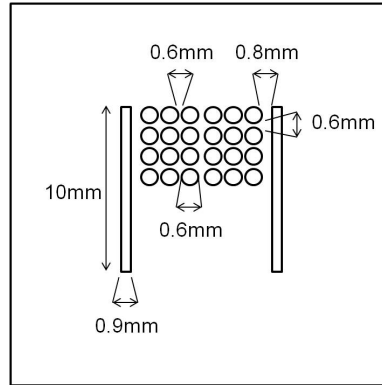


Figure 5.20: Dimension of the hybrid mask.

The hybrid mask was then tested using the laser parameters around the optimal operating window for the smooth CFRP surface. The test result is summarised in Figure 5.21. From the test results, the surface pre-treatment using the hybrid mask had a higher paint adhesion strength as compared to the surface pre-treatment using the hole-array mask alone which agreed with the previous investigation results using three different masks.

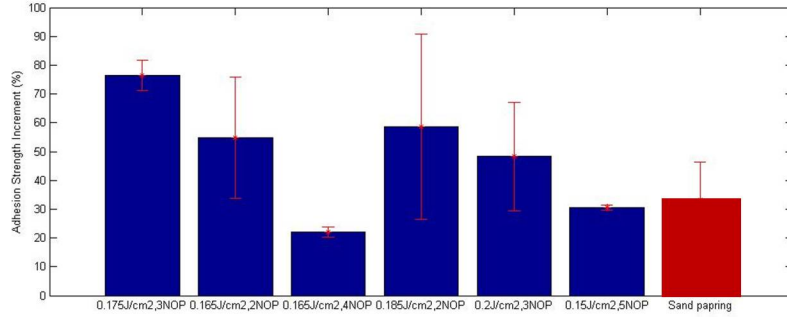


Figure 5.21: Bar plot of adhesion strength increment vs different laser parameters using the hybrid mask for the smooth CFRP surface.

#### 5.3.4 Operating Window for Rough CFRP Surface

A square mask was used to establish the operating window for the rough CFRP as shown in Figure 5.22. The square mask had a dimension of  $5\text{ mm} \times 5\text{ mm}$ . The square mask was used for the rough CFRP surface due to the underlying imprinted rough pattern finishing. Therefore, no further roughening was needed but the removal of surface contaminants and the increase in surface polar functional groups was required for paint adhesion strength improvement.

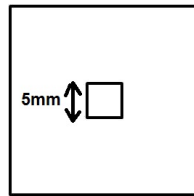


Figure 5.22: Illustration of the square mask used in the experiment.

The operating window for the rough CFRP surface was separated into three different regions similar to the colour code used for the smooth CFRP surface operating window. This data was obtained using a similar experimental procedure. Figure 5.23 shows the 3D surface profile of the laser pre-treated CFRP of different laser parameters using the optical white light interferometer and it could be seen that there was an underlying imprinted pattern on all the surfaces. These imprinted patterns might be due to the manufacturing process of the CFRP sheets. The threshold was identified through observing any visible fibre exposed in all the



laser pre-treated surfaces as shown in Figure 5.24 and the results are summarised in Table 5.9.

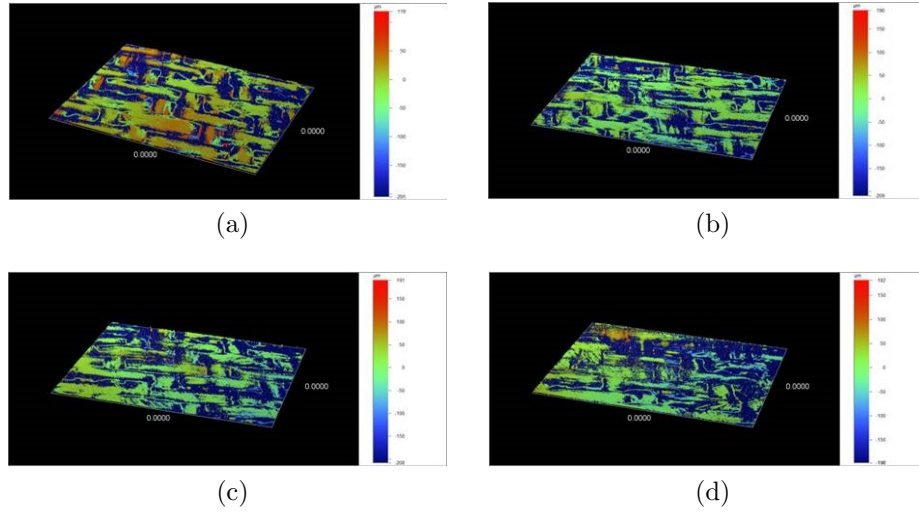


Figure 5.23: 3D optical profiles of the surfaces with excimer laser ( $\lambda = 248 \text{ nm}$ , *pulse width* = 15 ns) cleaning parameter (a) 50  $\text{mJ}/\text{cm}^2$  and 20 *NOP*, (b) 100  $\text{mJ}/\text{cm}^2$  and 50 *NOP*, (c) 200  $\text{mJ}/\text{cm}^2$  and 100 *NOP*, (d) 400  $\text{mJ}/\text{cm}^2$  and 100 *NOP*.

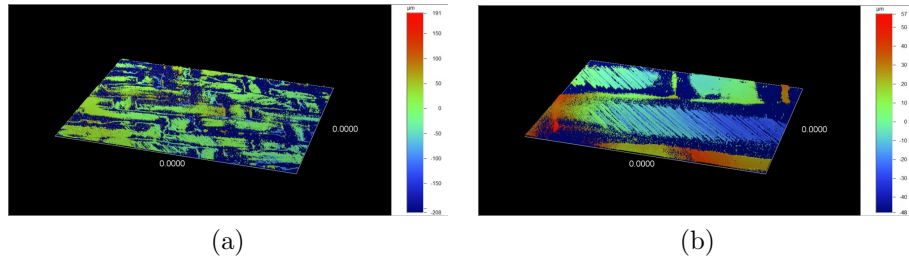


Figure 5.24: 3D optical profile of the laser cleaned surface with 200  $\text{mJ}/\text{cm}^2$  and 100 *NOP* with different magnifications.

The paint adhesion strength of the sand-papered CFRP surface was used as a bench mark for paint adhesion improvement. From the experiment, it was found that the sand-papered CFRP surface had a  $263 \pm 27 \%$  increase in paint adhesion strength relative to the as-received rough CFRP surface. The increase in paint adhesion strength of the rough CFRP surface in general had higher

Table 5.9: Observation of the rough CFRP surfaces after laser pre-treatment using different laser parameters.

NOP \ Fluence (mJ/cm <sup>2</sup> )	50	100	200	300	400
20	ND	ND	ND	ND	T
50	ND	ND	ND	T	E
100	ND	ND	T	E	E

ND = No damage  
 T = Threshold  
 E = Expose

values because the as-received rough CFRP surface had very poor paint adhesion strength due to the fluorine contamination on the surface. Hence, a value of 220 % in paint adhesion strength increment (85 % of sand-papered surface paint adhesion strength) was used as a bench mark to indicate sufficient paint adhesion strength that marked the line between the blue and yellow region. Through a series of tests, the optimal laser parameter was deemed to be  $225 \pm 25 \text{ mJ/cm}^2$  with  $20 \pm 5 \text{ NOP}$  at a frequency of  $30 \text{ Hz}$  with a 50 % overlap. The operating window diagram is shown in Figure 5.25.

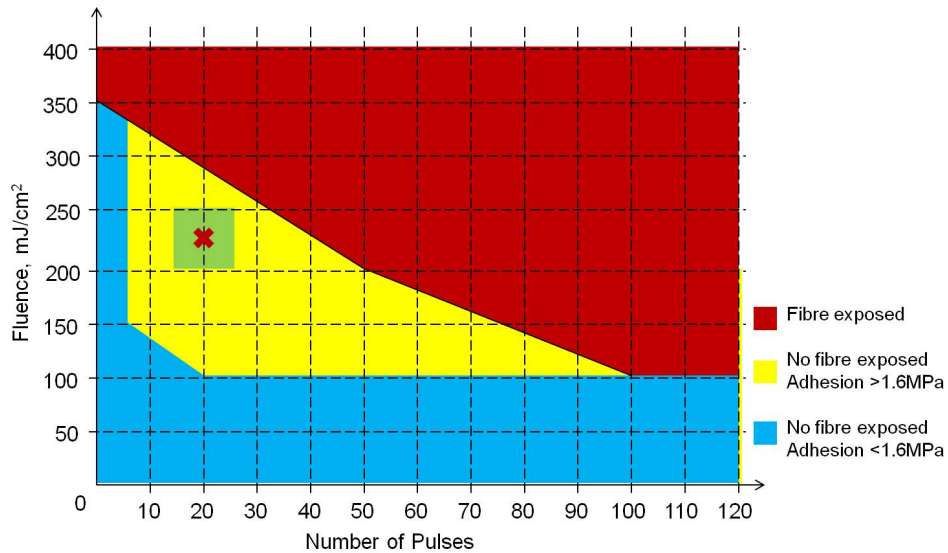


Figure 5.25: Operating window diagram for the rough CFRP surface using a square mask.

### 5.3.5 3D component cleaning

The capability of the laser system to perform pre-treatment on a 3D CFRP component was investigated. In order to establish the capability of 3D laser pre-treatment method, the effect of angled laser pre-treatment on the paint adhesion strength was investigated. The angle of the sample surface was measured relative to the laser beam as illustrated in Figure 5.26. The four angles tested are  $90^\circ$ ,  $60^\circ$ ,  $45^\circ$  and  $30^\circ$  using the following laser parameter:

- Fluence ( $mJ/cm^2$ ): 175
- NOP: 3
- Overlap (%): 50
- Frequency ( $Hz$ ): 10
- Mask: Hybrid mask (50 % cleaning operation and 50 % abrading operation)

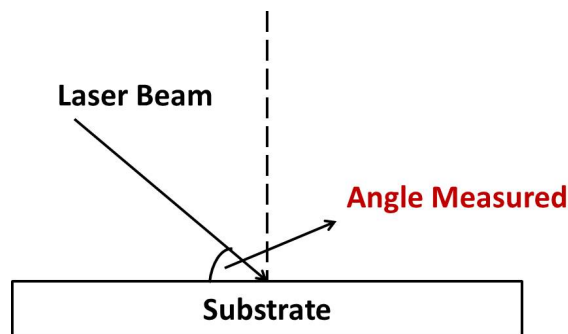


Figure 5.26: Schematic diagram illustrating the measured beam angle relative to the sample.

The results were plotted on an adhesion strength increment versus plane angle plot shown in Figure 5.27. From the results, it was observed that the decrease in laser beam angle relative to the sample plane resulted in a decrease in paint adhesion strength. The critical plane angle was deemed to be at  $55^\circ$  where laser pre-treatment process carried out below this angle will result in a drastic decrease in paint adhesion strength. From the plot, it was observed that the adhesion

strength increment for the angled plane was more than the sand-papered CFRP surface if the difference in angle between the plane of the sample and the laser beam was less than  $30^\circ$ . By considering the measurement error, the maximum allowable angle for surface pre-treatment was concluded to be  $60^\circ$ .

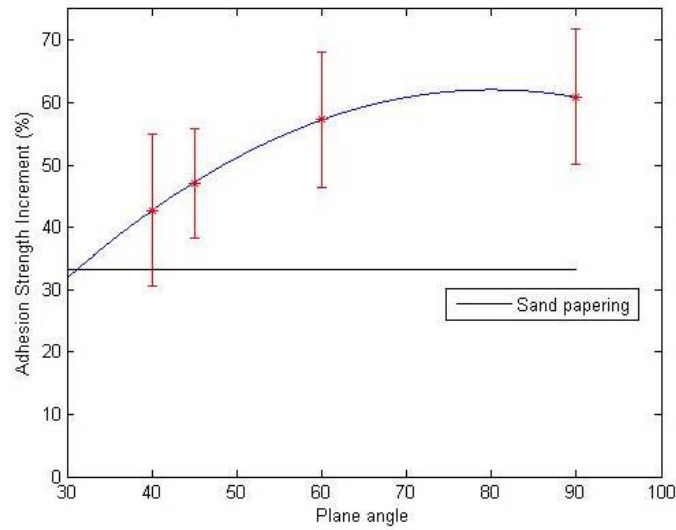


Figure 5.27: Plot of adhesion strength increment vs plane angle relative to the laser beam.

A 3D component was made to test the performance of the laser pre-treatment process using the optimal laser parameter with the hybrid mask. The 3D component consists of two flat surface of different height and a tilted surface of  $45^\circ$  relative to the laser beam. The 3D component used in the experiment was made using the smooth CFRP surface and is illustrated in Figure 5.28. A beam collimator is used to create a collimated laser beam where the beam size does not change with distance. The excimer laser setup used is shown in Figure 5.29.

The paint adhesion test was carried out on three area of the 3D component surfaces labelled top, side and bottom as shown in Figure 5.30a. The result of the increment in paint adhesion strength for different 3D components is shown in Figure 5.30b where the top and bottom surface showed similar paint adhesion strength increment value and the side surface showed slightly smaller paint adhesion strength increment value which agreed in the previous experimental results.

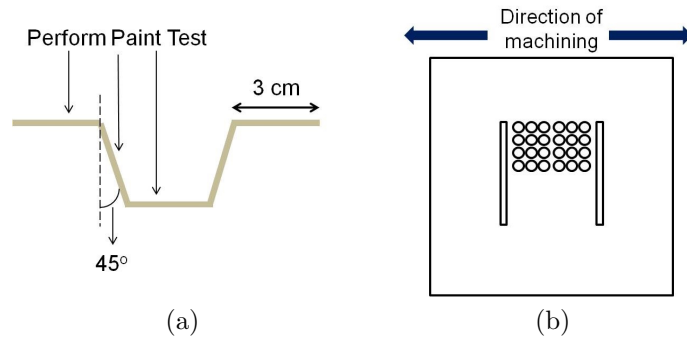


Figure 5.28: (a) 3D component of the CFRP used for testing. (b) Hybrid mask used in the 3D component testing experiment.

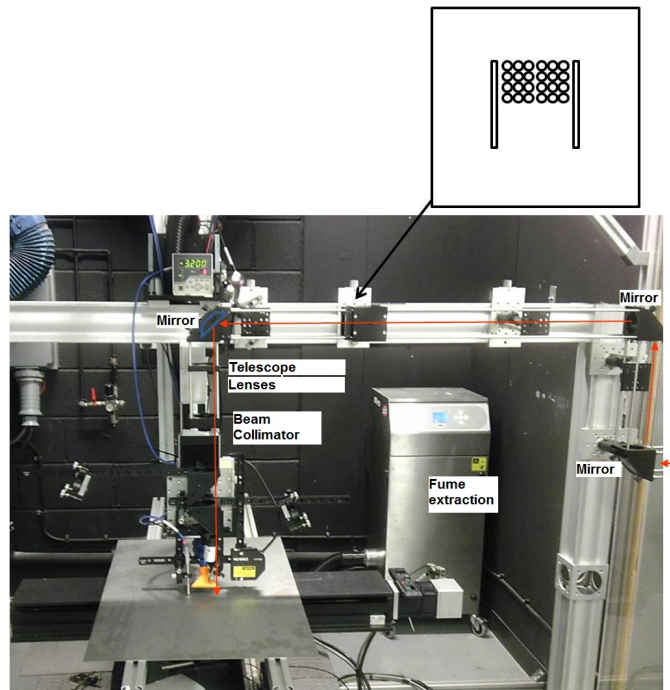


Figure 5.29: Excimer laser layout used for the pre-treatment of the 3D CFRP component.

This is mainly due to the enlargement of the laser beam spot size when pre-treated at the tilted surface of the 3D component. The increase in laser beam spot size decreased the laser fluence and hence decreased the paint adhesion strength performance of the CFRP surface.

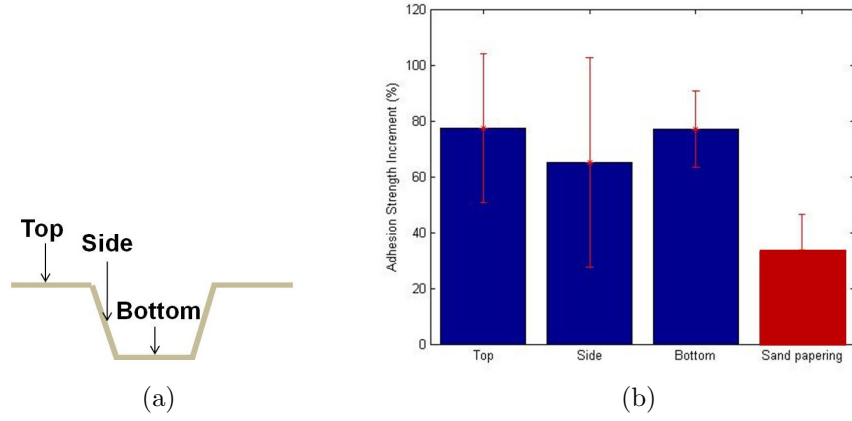


Figure 5.30: (a) Surface labeling of the 3D component used. (b) Bar plot of adhesion strength increment vs different 3D component surface with the fluence of  $175 \text{ mJ/cm}^2$  and 3 NOP for the smooth CFRP surface.

## 5.4 Summary

1. The polymeric layer thickness above the first fibre layer closest to the top smooth and rough CFRP surfaces are  $\sim 10 \mu\text{m}$  and  $\sim 25 \mu\text{m}$  respectively. The diameter of the fibre used in the CFRP is  $5 \mu\text{m}$ .
2. Excimer laser pre-treatment is capable of improving CFRP paint adhesion strength in a controllable manner where exposure of fibre can be avoided. In addition, the surface property changes on the CFRP surface such as surface roughness and surface chemical composition can be controlled with different laser fluence and NOPs.
3. The increase in polar functional groups on the CFRP surface improve paint adhesion as they form chemical bonds with the oil solvent within the primer during film formation process (drying process).

4. The three main influential factors on CFRP paint adhesion strength with primer are surface contamination, surface chemical composition and surface roughness. The desirable surface property for strong paint adhesion strength is having a surface that is contamination free, high content of polar functional groups and high surface roughness where the degree of influence is in respective order.
5. Paint adhesion strength improvement is better for laser pre-treated CFRP surfaces than sand-papered CFRP surfaces when appropriate laser parameter is used. The operating window diagram is designed for both rough and smooth CFRP surface indicating the set of laser parameters suitable for treating CFRP for better paint adhesion improvement without exposure of carbon fibre after surface pre-treatment.
6. The optimal laser parameter for the smooth CFRP surface is deemed to be  $175 \pm 10 \text{ mJ/cm}^2$  with  $3 \pm 1 \text{ NOP}$  at a frequency of  $10 \text{ Hz}$  and  $0 \%$  overlap using the hybrid mask. As for the rough CFRP surface, the optimal laser parameter is deemed to be  $225 \pm 25 \text{ mJ/cm}^2$  with  $20 \pm 5 \text{ NOP}$  at a frequency of  $30 \text{ Hz}$  and  $50 \%$  overlap using the square mask. The critical plane angle relative to the incident laser beam for 3D component pre-treatment is deemed to be  $60^\circ$ .

## Chapter 6

# LASER SURFACE TEXTURING OF NICKEL ALLOY AND TRIBOLOGY BEHAVIOUR

### 6.1 Introduction

The term superplasticity is used to describe the ductility characteristic of certain metals when it is deformed under specific strain rate and temperature conditions and these metals usually have a tensile ductility of 200 % to 1000 % elongation [249]. The superplastic forming process (SPF) is a process that takes advantage of the superplasticity property of a material where it is typically accomplished by blow forming. This process is done by clamping a sheet blank in a die where gas pressure is applied from one side which plastically deform the sheet towards the die thus forms the sheet to the shape of the die [250]. The process is illustrated in Figure. 6.1.

SPF process is quite similar to the conventional stamping process and is very popular in industries that has low production volumes such as aerospace, rail and architecture which has now been considered as the standard manufacturing process [250]. The reasons behind the popularity of this process in these industries



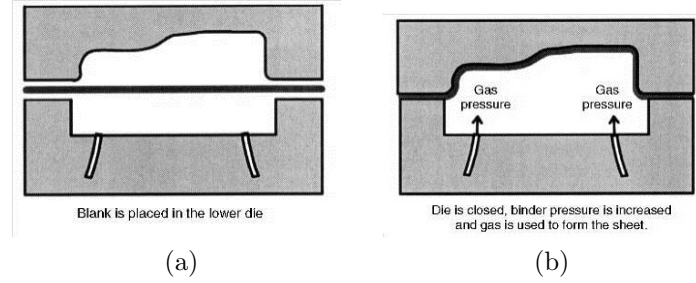


Figure 6.1: Schematic of a single-sided SPF tool shown (a) before and (b) after gas pressure forming [250].

are mainly due to the low investment and inexpensive tool cost as this process only requires one die for each design as compared to stamping which needs a pair of dies. Nonetheless, this process requires low force to plastically deform the materials as the process is done under high pressure and temperature. Furthermore, this process is capable of eliminating spring-back effect, part consolidation and most importantly increase the freedom of design [250].

On the contrary, conventional SPF has several drawbacks due to the nature of the process. SPF is a slow process as it is rate sensitive where the process cycle is mainly dependent on the deformation rate of the materials. The formed parts using SPF might result in tears, wears or non-uniform wall thickness if is not properly controlled as SPF is a stretch forming process which does not draw in any additional materials during the process [249]. This drawback then limits the ability of SPF in forming complicated components. Despite these limitations, several new SPF processes have been developed over the years such as two stage gas forming (TSGF) process and hot draw mechanical pre-forming (HDMP) process where these new processes enables the production of complex shape design panels [249].

Lubrication is an important element in any forming process as the friction between the sheet material and the die surface determines the quality of the formed parts. The primary role of lubricant in mechanical processing such as parts forming process is to reduce the friction coefficient between the material and the die surface which then allows the material to slide across the die surface, thereby avoiding tear and wear [251]. In addition, the lubricant protects the die surface

from oxidation and wear. Furthermore, proper lubrication eases the release of the formed parts from the die after the forming process. Oil-based or waxy lubricants are commonly used in stamping operations but are not suitable for the SPF process due to the high temperature ( $> 400\text{ }^{\circ}\text{C}$ ) and pressure environment of the process [250]. Solid lubricants on the other hand such as boron nitride or graphite are more commonly used where boron nitride is more favourable over graphite as it produces parts with better surface quality even though it is more expensive [152].

Lubrication is very important in SPF process as it determines the quality of the final formed parts. The main issue with the solid lubricant - boron nitride used in industry is the lubricant adheres to the formed parts rather than the die surface after each forming cycle. This poses a problem where application of solid lubricant to the die is required after a few cycles to maintain a constant lubricant thickness. This significantly slows down the forming process as well as increase the usage of the solid lubricant. In addition, post processing is needed to remove the lubricant from the formed part surface before the parts can be further processed. The post-cleaning process can sometimes be difficult and costly [252; 253; 254].

Material surface texturing of dies improves tool wear life cycle and friction coefficient between the contact surfaces under conformal contact configuration such as mechanical seal and bearings components. On the other hand, under non-conformal contact configuration, there has been contradicting publications where micro-dimpled surfaces are reported to either significantly increase the wear of the counter-face [172] or significantly reduce the wear of the counter-face [173]. Laser surface texturing is deemed one of the best methods to produce these textures due to the advantages of the process and has spark interest among researchers over the last 20 years. In most of the research published, the optimum dimple area ratio for several different metallic materials is reported to be between 10 % – 20 % with dimple diameter of size between  $50\text{ }\mu\text{m}$  –  $200\text{ }\mu\text{m}$ . Although some of the researches published does consider different dimple depth which range from as shallow as  $1\text{ }\mu\text{m}$  –  $10\text{ }\mu\text{m}$ . As for the texture shape, circular is still the best option due to the ease of production as well as the symmetrical property of the shape. Other shapes such as triangular and eclipse might be good for certain applications where directionality is of importance.

The research aims to utilize laser surface texturing to produce dimple texture on HR4 nickel alloy and investigate the effect of dimple texture on tribology performance in terms of friction coefficient changes and wear rate performance under non-conformal contact configuration (dry and oil lubricant lubricated conditions). The specific objectives are:

- To determine the best-suited laser parameter for the texturing process.
- To characterise the dimples created by laser texturing, including dimple depth, diameter, separation distance and surface finish, using optical microscope, SEM and optical white light interferometer.
- To evaluate the surface friction coefficient changes of laser textured surfaces of different dimple area ratio and depth under dry and lubricated conditions.
- To evaluate the laser textured surfaces wear rate of different dimple area ratio and depth under dry and lubricated conditions.

## 6.2 Methodology

### 6.2.1 Material Preparation

The nickel alloy sample used was sliced into size of  $30\text{ mm} \times 20\text{ mm} \times 4\text{ mm}$  using a water jet machine. The samples were then ground using the MECAPOL P255U metallographic polishing machine manufactured by PRESI with grinding paper up to grit size of 600, achieving a surface roughness,  $R_a$  of  $0.1\text{ }\mu\text{m}$  measured using the optical white light interferometer.

### 6.2.2 Laser Surface Texturing

The Ti:Sapphire femtosecond laser ( $\lambda = 800\text{ nm}$ , *pulse width* =  $100\text{ fs}$ ) was used to produce the dimples on the nickel alloy surface. The dimples were produced through scanning two concentric circles with diameter of  $80\text{ }\mu\text{m}$  and  $10\text{ }\mu\text{m}$  using different laser parameters as summarised in Table 6.1. The processing time is dependent on the dimple dimension, depth, dimple density, laser fluence, NOP as

well as scanning speed. For this set of experiment, the processing time required to produce 1  $cm^2$  dimple of 50 % density requires 20 *min*.

Table 6.1: Laser parameters used to produce the dimples.

	Fluence ( $J/cm^2$ )	NOP	Speed (mm/s)	Frequency (kHz)
outer hole	4.2	1 – 20	30	1
inner hole	4.2	3	120	1

### 6.2.3 Material Characterisation

Materials characterisation was carried out using optical microscopy, SEM, optical white light interferometer and microhardness tester.

### 6.2.4 Friction and Wear Test

The friction coefficient and wear property of the textured nickel alloy surface was examined with a POD-2 Pin on Disc wear tester manufactured by Teer Coatings Ltd under room temperature condition. This machine used a 5 *mm* diameter WC-Co ball (Hertzian contact pressure of  $\sim 0.15$  *GPa*) to perform the friction coefficient measurement test with a reading accuracy of  $\pm 0.1$  %. Figure 6.2 shows the wear tester machine used in the experiment. In addition to the normal point contact test, the ball was manually ground and polished such that a flat area of diameter 3 *mm* and 4 *mm* were produced in order to perform an area contact test. The experimental condition for the room temperature wear test experiment is summarised as follow:

- Test Duration: 900 *s*
- Load: 10 *N*
- Rotational Speed: 500 *rpm*
- Track Diameter: 70 *mm*
- Temperature: 22°C

- Humidity: 45 %RH



Figure 6.2: POD-2 pin on disc wear tester [255].

The test was done in two conditions which are dry (with no lubricant) and lubricated (oil lubricant) condition under room temperature environment. The oil lubricant used was a 3-in-1 multipurpose oil with PTFE manufactured by WD-40 Company Ltd.

The wear rate was calculated using the famous Archard equation as shown below [149; 150]:

$$\text{Wear rate} = \frac{\text{volume loss per unit sliding distance}}{\text{load}} \quad (6.1)$$

A more specific equation was derived for the POD-2 Pin on Disc wear tester for wear rate and wear volume calculation as shown below. The annotation used in the equations are illustrated in Figure 6.3.

$$\text{Wear rate} = \frac{wt}{2 \times \text{load} \times \text{No. of rev.}} \quad (6.2)$$

$$\text{Wear volume} = \frac{wt}{2} \times \pi d \quad (6.3)$$

where No. of rev. = rpm  $\times$  test duration  
 $w$  = track width  
 $t$  = wear depth

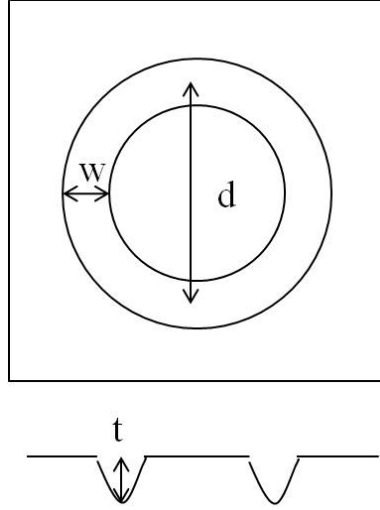


Figure 6.3: Schematic illustration of the parameters used in wear rate and wear volume calculation.

### 6.2.5 Characteristic of Dimple

The dimple machined had a diameter of  $100\ \mu m$  with varying dimple depth of  $0.15\ \mu m - 10\ \mu m$  and dimple area ratio of  $5\ \% - 50\ \%$ . The dimple area ratio was calculated based on the percentage coverage of the dimple area to the overall area coverage using equation 6.4. The separation distance between dimples for different dimple area ratio is summarised in Table 6.2. The SEM image of the dimple produced is shown in Figure 6.4. The surface hardness at the circumference of the dimple ( $202.7 \pm 13.5\ HV$ ) was found to be similar as compared to the non-textured surface ( $210.7 \pm 20.4\ HV$ ).

$$D_{area} = \pi \left( \frac{d}{2s} \right)^2 \times 100\% \quad (6.4)$$

where  $d$  = dimple diameter

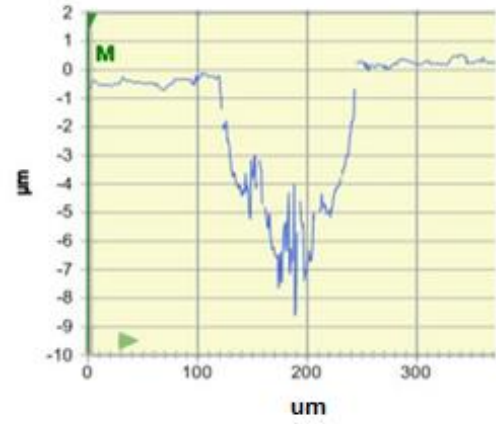
$s$  = spacing between the dimples

Table 6.2: Spacing between dimples for different dimple area ratio.

Dimple area ratio (%)	5	10	15	20	25	30	50
Spacing ( $\mu m$ )	396	280	229	198	177	162	125



(a)



(b)

Figure 6.4: (a) SEM image of a dimple taken at  $45^\circ$  incline plane and (b) optical white light interferometer profile of the dimples produced at  $4.2 J/cm^2$  fluence and 15 NOP.

## 6.2.6 Wear Characteristics

### 6.2.6.1 In the Dry Environment (No Lubrication) at Room Temperature

Figure 6.5 shows the wear rate and friction coefficient for textured nickel alloy surface with different dimple area ratio of depth  $2.5\ \mu\text{m}$  under dry environment using a standard wear tester ball. All textured surfaces showed better wear rate than the un-textured surface. The wear rate decreased for surfaces having dimple area ratio of 5 % to 20 % and reached an asymptotical value with a reduction of 64 % in wear rate as compared to the un-textured surface.

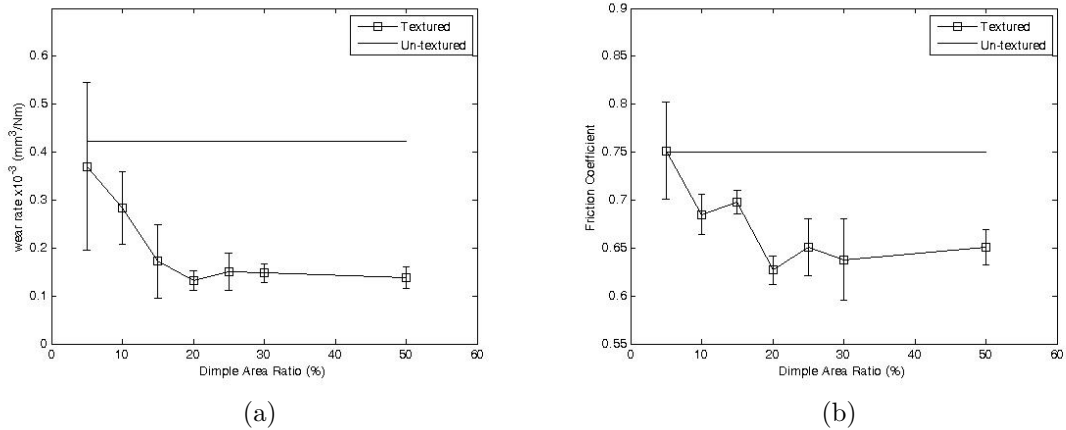


Figure 6.5: (a) The wear rate and (b) average steady state friction coefficient of textured surfaces with different dimple area ratio of depth  $2.5\ \mu\text{m}$  under dry environment and room temperature condition.

The wear mechanism involved in the dry environment under room temperature is abrasive wear and this was clearly observed on the SEM images shown in Figure 6.6. New scratches align with the direction of the ball movement along the wear track could be observed. When the ball was in contact with the asperity on the surface of the substrate, wear particles were produced. These wear particles were mobile under the non-lubricated environment with high possibility of depositing into the wear track which accelerated the wear rate of the substrate through the abrasive wear mechanism. Hence, the dimples act as reservoir to trap wear particles which prevent them from depositing into the wear track. The quantity of



wear particles produced was limited by the test duration which set the maximum possible wear rate of the surface. Theoretically, a lower wear rate would be observed for higher dimple area ratio surfaces if the test duration is prolonged. In addition, the wear rate variation (error bar) for a lower dimple area ratio was much higher as compared to those with a higher dimple area ratio. This is mainly due to the different initial surface condition in contact with the wear tester ball at the beginning of the test as well as the duration needed to achieve equilibrium. According to the Hertzian contact theory, the resultant contact radius of two contact body with a given applied force,  $F_n$  is given by:

$$r = \sqrt[3]{\frac{3 F_n R}{4E^*}} \quad (6.5)$$

where  $R$  = radius of the ball

$E^*$  = effective young modulus

The contact radius,  $r$  was calculated to be  $180 \mu m$ . As the contact radius is smaller than the separation distance between dimples for the low dimple area ratio, the possibility of the wear tester ball starting on a different surface condition is higher. The friction coefficient trend matches with the wear rate trend where it decreased with increasing dimple area ratio from 5 % to 20 % and reached an asymptotical value with a 62 % reduction in the friction coefficient as compared to the un-textured surface. This indicated that the friction coefficient value was influenced by the quantity of wear particles between the two wear surfaces.

#### **6.2.6.2 In the Oil Lubricated Environment at Room Temperature**

The influence of sliding speed and contact pressure on the friction coefficient of the un-textured nickel surface under an oil lubricated environment was investigated. The study involved an area contact test using the modified WC-Co ball with a contact diameter of 3 mm (Maximum pressure achieved with 40 N weight = 5.66 MPa) and 4 mm (Maximum pressure achieved with 40 N weight

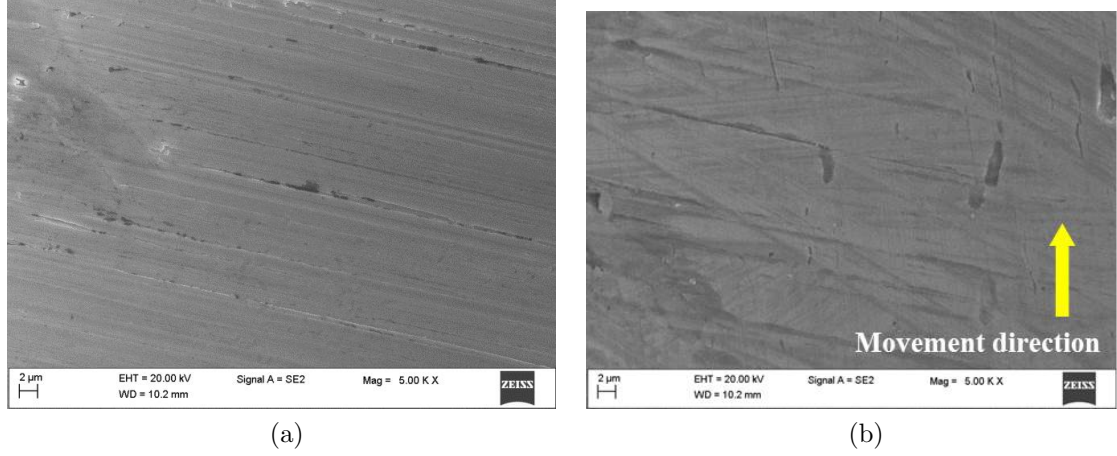


Figure 6.6: SEM images of the grinded nickel alloy surface (a) before wear test and (b) after wear test.

$= 3.18 \text{ MPa}$ ) where the speed varied from  $10 \text{ rpm}$  ( $0.0042 \text{ m/s}$ ) to  $1000 \text{ rpm}$  ( $0.42 \text{ m/s}$ ). Under very low speed ( $< 100 \text{ rpm}$ ) and high pressure ( $5.66 \text{ MPa}$ ), the friction coefficient response followed a sinusoidal curve shape where the friction coefficient value fluctuated between two values at a certain frequency as shown in Figure 6.7a. Such phenomenon was observed for sliding speed of  $< 80 \text{ rpm}$  ( $0.035 \text{ m/s}$ ) indicating variable hydrodynamic pressure with time with a reduction in peak to peak value as the speed increased as shown in Figure 6.7b. Hence, two lubrication regimes existed: low friction coefficient (thicker oil film) and high friction coefficient (thinner oil film). The period of the curve indicates the time required to gain enough pressure to form a thicker film between the two contact surfaces. As the sliding speed increased, the thickness of the base film increased resulted in a decrease in peak to peak value indicating a more constant hydrodynamic pressure between the two surfaces. This is in agreement with the Stribeck's work where the friction coefficient is dependent on the sliding speed, pressure and viscosity of the lubricant [146].

Under high sliding speed, the friction coefficients for both contact pressures decreased with increased sliding speed as shown in Figure 6.8. In addition, the friction coefficient was lower when the contact pressure decreased from  $1.415 \text{ MPa}$  to  $0.796 \text{ MPa}$  under similar sliding speeds. This agrees with the Stribeck's curve theory where the friction coefficient is inversely proportional to the contact pres-

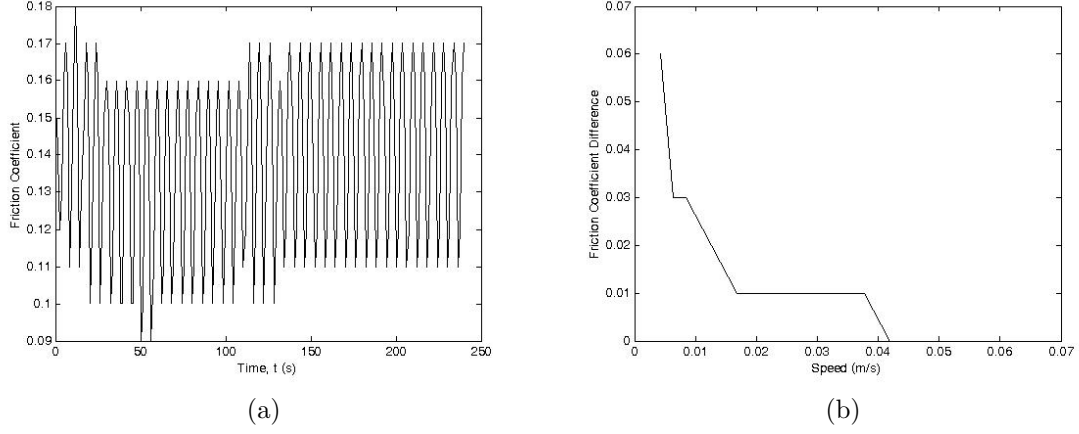


Figure 6.7: (a) Plot of friction coefficient respond with sliding speed of  $0.0042 \text{ m/s}$  and (b) Peak to peak friction coefficient difference with different sliding speed for un-textured nickel surface in oil lubrication environment under the pressure of  $5.66 \text{ MPa}$ .

sure and is directly proportional to the sliding speed. Under the lower contact pressure, the friction coefficient value increased when the sliding speed exceeded  $0.33 \text{ m/s}$ . This is mainly due to the thickness of the oil film formed. When the lubrication regime between the two surfaces changes from boundary to hydrodynamic, it indicates an increase in the oil film thickness which then helps in reducing the friction coefficient by minimising the contact of the asperities between the two surfaces. However, a further increase in film thickness results in an increase in drag force between the oil films thus increases the friction coefficient. Hence a slight increase in friction coefficient was observed when the sliding speed was further increased under hydrodynamic lubrication region.

The friction coefficient for textured nickel surface with dimple area ratio of 20 % and dimple depth of  $2.5 \mu\text{m}$  was investigated and compared to the un-textured surface as shown in Figure 6.9. It was observed that the friction coefficient value decreased for the textured nickel alloy surface when the sliding speed was lower than  $0.2 \text{ m/s}$  but was higher when the sliding speed exceeded  $0.2 \text{ m/s}$ . This showed that the dimpled surface shifted the lubrication regime to a lower sliding speed, indicating expansion of the hydrodynamic lubrication regime, achievable at a lower sliding speed. This agreed with results published

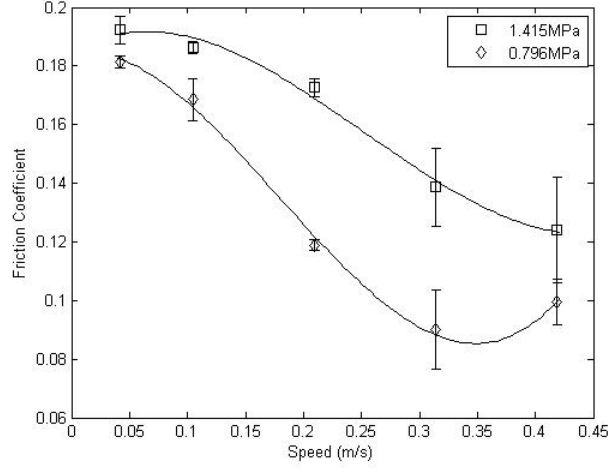


Figure 6.8: Plot of friction coefficient versus sliding speed under different contact pressure in oil lubrication environment.

by other researchers [170; 171; 256]. The increase in friction coefficient when the sliding speed exceeded  $0.2\text{m/s}$  was due to the film thickness effect as explained earlier.

Figure 6.10 shows the wear rate and friction coefficient for textured nickel alloy surface with different dimple area ratio of depth  $2.5\text{ }\mu\text{m}$  under oil lubricated environment. All dimpled surface showed an increase in wear rate excluding the surface with 20 % dimple area ratio where a reduction of 35 % in wear rate as compared to the un-textured surface was observed. The wear rate decreased with increasing dimple area ratio up to the optimal dimple area ratio of 20 % where the wear rate then increased with dimple area ratio as shown in Figure 6.10.

The wear rate is dependent on the contact pressure and the number of dimples available for trapping wear particles as well as storing lubricant. The contact pressure is directly proportional to the wear rate whereas the number of dimples is inversely proportional to the wear rate. Hence there exists a trade-off between the contact pressure of the surface and the availability of dimples for trapping wear particle and storing lubricant where 20 % was the optimal combination between the two parameters for the test duration of 900 s. Under conformal contact configuration, the contact pressure between the wear tester ball and the surface is much higher as compared to the non-conformal contact configuration

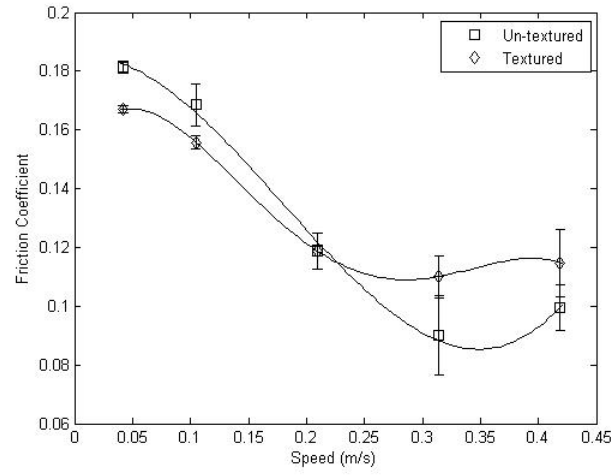


Figure 6.9: Plot of friction coefficient versus sliding speed for textured (20 % dimple area ratio with  $2.5 \mu\text{m}$  depth) and un-textured nickel surface in oil lubrication environment.

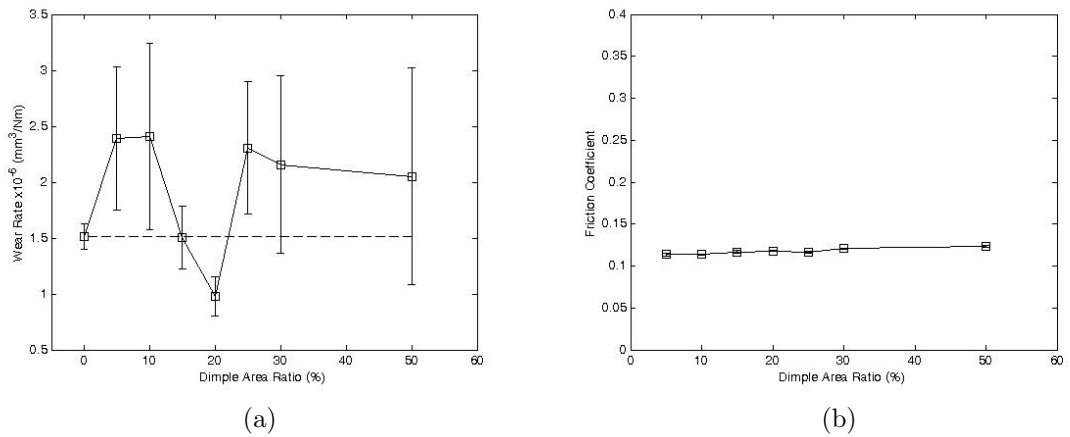


Figure 6.10: (a) The wear rate and (b) average steady state friction coefficient of textured surfaces with different dimple area ratio of depth  $2.5 \mu\text{m}$  under oil lubricated condition.

resulting in wear phenomena under boundary lubrication region [172]. Hence, the asperity contact between two surfaces increases, causing rapid abrasive wear especially on the edges of the dimple as these are stress concentration area. In addition, the dimple diameter to contact area diameter ratio affect the wear rate. If the ratio is low (dimple diameter  $\ll$  contact area diameter) as in the case reported by C. Chouquet et. al., the oil reservoir effect by the dimple is more significant through removal of lubricant from the cavity via tangential shear stress which increased the local lubricant film thickness leading to a reduction of abrasive [173; 257]. On the contrary, if the ratio is high as in the case reported by Andriy Kovalchenko et. al., the wear rate increased for all dimpled surfaces as compared to the un-textured surface [172]. Since the ratio used in this experiment is in between the ones reported in [172] and [173], some of the dimpled surfaces show an increase in wear rate whereas some show a decrease in wear rate. Under lubricated environments, the friction coefficient response reduces tremendously as compared to the dry environment. The friction coefficients for different dimple area ratio were constant which implied similar lubrication condition (boundary lubrication region) [146].

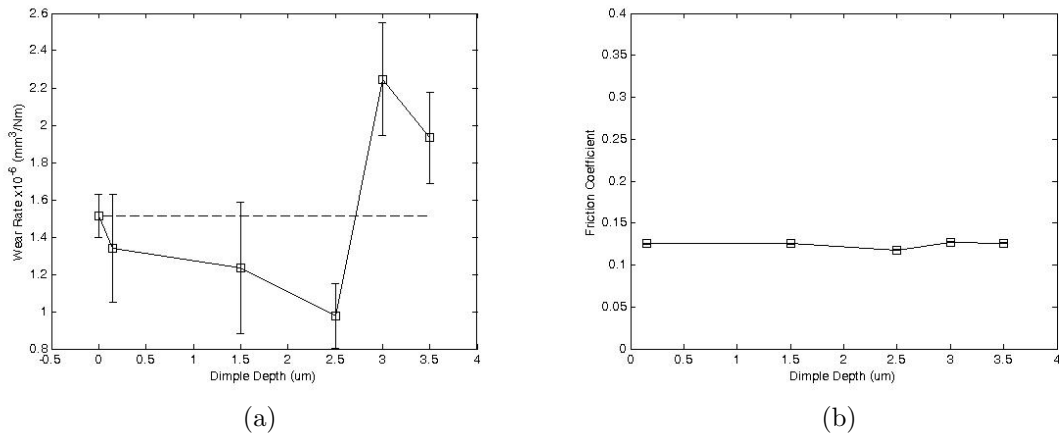


Figure 6.11: (a) The wear rate and (b) average steady state friction coefficient of textured surfaces with different dimple depth of 20 % dimple area ratio under oil lubricated environment.

Figure 6.11 shows the wear rate and friction coefficient for textured nickel alloy with different dimple depth of 20 % dimple area ratio under oil lubricated envi-

ronment. A similar lubrication condition (boundary lubrication) was achieved for different dimple depth as shown from the friction coefficient response [146]. The wear rates, on the other hand, were similar with  $< 2.5 \mu m$  depth and increased after. This is due to the decrease of lubricant film thickness as the depth increases where the increase in depth causes lubricant film breakdown [258]. Although the reservoir capacity increases with depth, the reduction in the lubricant film results in a more severe wear due to increase contact between the asperities of the two surfaces.

### 6.3 Summary

1. Laser surface micro-dimpled nickel alloy of  $100 \mu m$  diameter shows reduction in wear rate under dry and oil lubricated environments.
2. Under dry environment and non-conformal contact condition, an increase in dimple area ratio reduces the wear rate of the nickel surface. For the test duration of  $900 s$ , the optimal dimple area ratio is 20 % with a wear rate reduction of 64 % relative to the un-textured surface.
3. Under oil lubricated environment, the friction coefficient is dependent on the surface contact pressure, sliding speed and the viscosity of the lubricant. The textured surface shifted the hydrodynamic lubrication region to a lower sliding speed.
4. Under oil lubricated environment and non-conformal contact condition, The optimal dimple parameter is at dimple area ratio of 20 % and dimple depth of  $2.5 \mu m$  with a reduction of 35 % relative to the un-textured surface.
5. The wear rate of a dimpled surface is dependent on three factors which are the dimple diameter to contact area diameter ratio, dimple depth and dimple area ratio. The increase in the dimple area ratio increases the contact pressure of the surface which increases the wear rate performance of the surface. On the contrary, it also increases the reservoir capacity which decreases the wear rate of the surface. The increase in dimple depth decreases

the thickness of the lubricant film under oil-lubricated condition which results in an increased wear rate. The effect of dimple as lubricant reservoir is dependent on the dimple diameter to contact area diameter ratio where the effect decrease with increasing ratio. The wear mechanism under room temperature environment is governed by abrasive wear.



## Chapter 7

# LASER SURFACE TEXTURING OF ABS AND DUST ADHESION BEHAVIOUR

### 7.1 Introduction

A vacuum cleaner is a machine that cleans dust and dirt through an air suction technique. Conventional vacuum cleaners use a dust bag to collect dust and dirt which is made out of paper and is disposed off and cannot be recycled when the dust bag is filled. Such design is not environmental friendly and is inefficient as more power is needed to maintain the pressure difference between the dust bag and the surrounding to produce sufficient suction power after prolonged usage. Thus, bagless vacuum cleaners were invented using cyclone separation system where the paper dust bag is replaced by a plastic container. The container can be washed and reused. A separation system air flow for Dyson DC37 bagless vacuum cleaner and its components are shown in Figure 7.1 and Figure 7.2.

The drawback of such design is the blockages of the separation system due to dust adhesion especially on the cyclone wall and cone tip after prolonged usage. The blockage reduces the suction power of the vacuum machine and hence

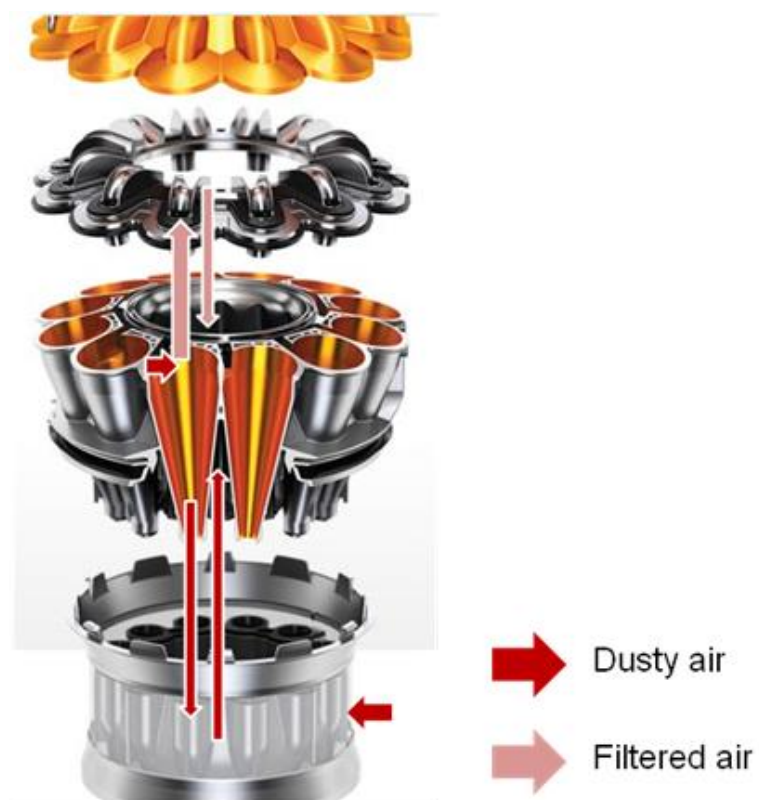


Figure 7.1: Illustration of the air flow in the separation system of Dyson DC37 bagless vacuum cleaner.



Figure 7.2: Separation system components of the of Dyson DC37 bagless vacuum cleaner.

reduces the efficiency of the cleaning. Part of the components need to be changed or dismantled for cleaning which makes things difficult and tedious. Hence, to improve the longevity and efficiency of the machine, having an anti-dust surface is crucial.

### 7.1.1 Factors Causing Dust Adhesion

The main force that contributes to the adhesion force for a particle system smaller than  $10\text{ }\mu\text{m}$  in size is the van der Waals force as described in the literature review chapter. The magnitude of the van der Waals force is directly proportional to the size of the particle and the constant  $A$  which is dependent on the material properties. Since the particle size is constant, the constant  $A$  needs to be reduced in order to reduce the adhesion force. The constant  $A$  is dependent on the surface energy of the materials where metallic materials have a higher  $A$  value as compared to polymers [133]. In addition, the electrostatic force also contributes to the particle adhesion force. Hence, having materials with anti-static property reduces the strength of the electrostatic forces induced by the charged particles onto the surface which then reduce the adhesion force of the particles. Nonetheless,

water causes capillary condensation effect which increases the adhesion force of the particles. Hence to avoid the effect of capillary condensation effect, it is best to keep the environment dry so that there is no condensation of water molecules onto the surface.

As van der Waals force is present in all the systems on earth, it is impossible to eliminate the adhesion force completely. Hence, external forces such as aerodynamic force and hydrodynamic force larger than the particle adhesion force are required to achieve particle removal. The application of hydrodynamic force is not practical because it induces a capillary condensation effect which increases the adhesion force afterwards although it decreases the electrostatic force and van der Waals force of the particles. As for the aerodynamic force,  $F_H$ , the amount of force needed to remove a particle that is adhered on a surface with a force  $F_A$  is given by the following equation [134][145]:

$$F_H = \gamma F_A \quad (7.0)$$

where  $\gamma$  is the static coefficient of friction

The breakdown of the removal mechanisms involved in a particle adhesion system is shown in Figure 7.3.

Based on the literature review, several factors have been identified that potentially influence the dust adhesion on a surface, they are surface roughness, anti-static charge surface property, surface chemical composition, humidity and dust particle size as summarised in Figure 7.4.

This research aims to investigate the effect of laser surface engineering (surface texturing and surface chemical composition modification) of ABS polymer surface on dust adhesion behaviour. The specific objectives are:

- To determine suitable laser parameters for laser surface engineering process.
- To characterise surface textures created by laser, including feature depth and finishing using an optical microscope, SEM and optical white light interferometer.
- To evaluate the surface chemical composition changes of ABS polymer after laser surface treatment.

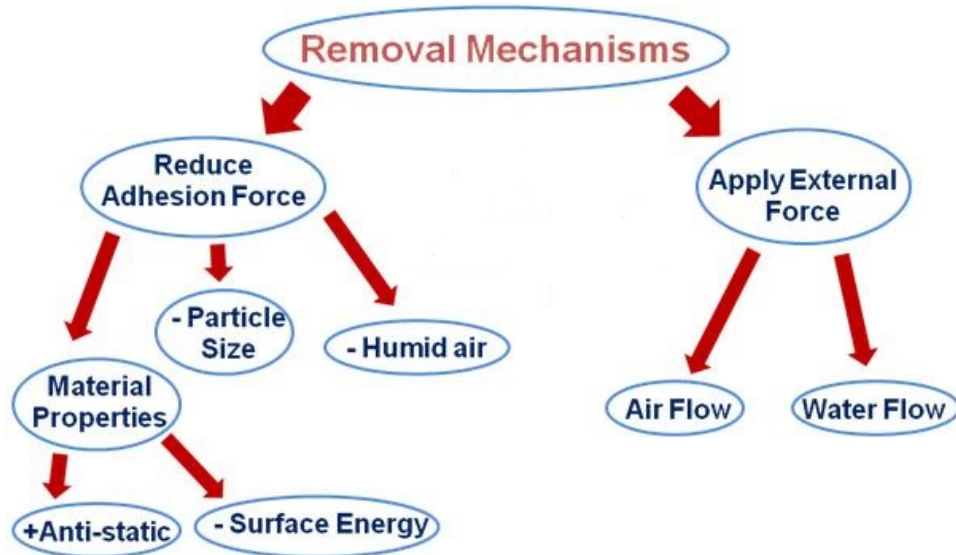


Figure 7.3: Removal mechanisms involved in a particle adhesion system.

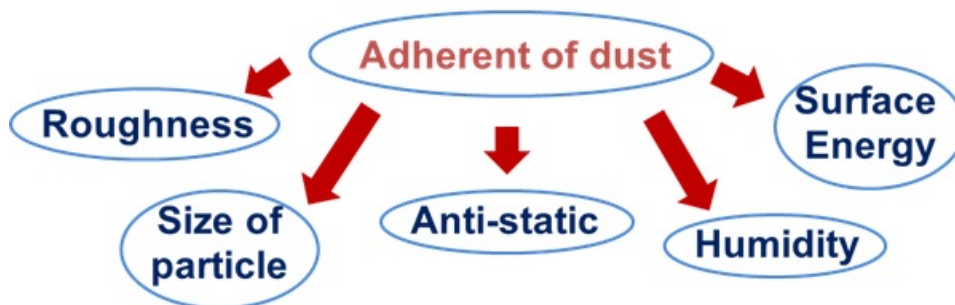


Figure 7.4: Factors influencing dust particle adhesion on a surface.

- To evaluate the dust attachment/ adhesion for different laser treated ABS surfaces under cyclone airflow environment.

## 7.2 Methodology

### 7.2.1 Material Preparation

The ABS samples used in the experiment were cut into size of  $15\text{ mm} \times 15\text{ mm}$ . The surface roughness was  $R_a = 0.06 \pm 0.015\text{ }\mu\text{m}$ . A thistle multi-finish plaster manufactured by British Gypsum was used as dust particles in the experiment. The plaster has a mean aerodynamic dust particle size of  $1.13\text{ }\mu\text{m}$  measured using an aerodynamic particle sizer (APS) model 3321 manufactured by TSI with a measurement resolution of  $0.02\text{ }\mu\text{m}$ . The particle distribution plot is shown in Figure 7.5.

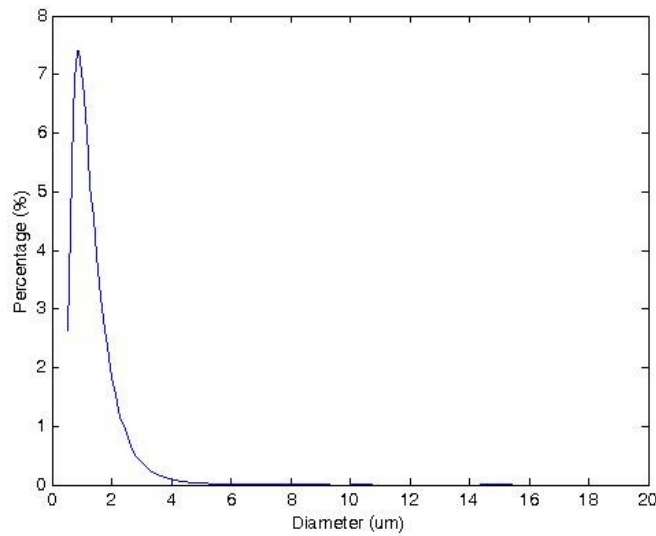


Figure 7.5: Aerodynamic particle size distribution plot for Thistle multi-finish plaster measured using APS.

## 7.2.2 Laser Surface

Two factors that affect dust adhesion forces were investigated which are the effect of surface energy and the effect of surface roughness. Both modifications were done through laser surface engineering as summarised in the following sub-section.

### 7.2.2.1 Surface Energy Modification

The surface energy modification of ABS was done using the KrF excimer laser through a mask projection technique utilising a square mask to obtain a more uniform laser beam profile. The laser parameters used to treat the ABS surface are summarised as follow:

- Fluence ( $mJ/cm^2$ ): 50, 100, 200, 400
- Number of Pulses: 10, 25, 50
- Frequency ( $Hz$ ): 10

### 7.2.2.2 Surface Texturing Modification

The surface texturing of ABS was done using the Ti:Sapphire femtosecond laser by scanning three different texturing patterns which are line, hatch and circle as illustrated in Figure 7.6. The laser parameters used to texture the ABS surface are summarised as follow:

- Power ( $mW$ ): 100, 250
- Frequency ( $kHz$ ): 1
- Number of passes: 6
- Speed ( $mm/s$ ): 60
- Spot size ( $\mu m$ ): 60
- Pattern separation ( $\mu m$ ): 100, 200, 300, 400
- Hole diameter for circular pattern ( $\mu m$ ): 100

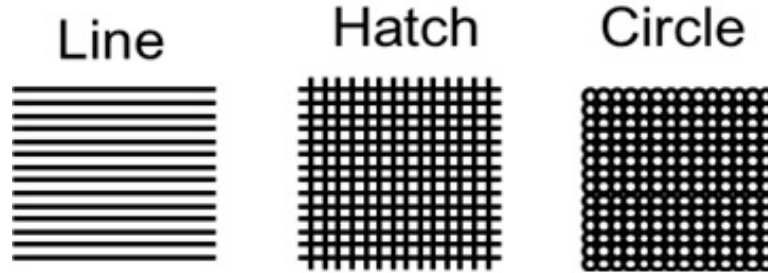


Figure 7.6: Patterns used for ABS surface texturing.

### 7.2.3 Material Characterisation

The morphology of the laser engineered surfaces was examined using the SEM and optical white light interferometer. The chemical composition of the ABS was analysed using the XPS.

### 7.2.4 Dust Adhesion Test

The dust adhesion test was done using a test rig consisted of a *DC37* vacuum cleaner, mechanical shaker, coulombmeter, pitot tube, data logger and a PC with the layout shown in Figure 7.7. The laser surface engineered samples were firmly mounted at the inlet of the vacuum cleaner. A constant air flow rate of 2100 – 2200 LPM was used and monitored through a pitot tube connected to the NI PCI-6221 data logger and PC. The dust particles were loaded into the system at a rate of 5 *g/min* using a V20/PA100 mechanical shaker by Gearing & Watson at a frequency of 100 *Hz*. The static electric charge of the dust particles were measured using the IPC-1964-M coulombmeter. The change in dust adhesion for different laser surface engineered ABS was quantified through weight measurements using the Sartorius 2024MP model manufactured by Data Weighing Systems Inc. as shown in Figure 7.8. The weighing machine uses a cubic modular system where a cubic transparent cover is used to stabilize the system from surrounding environment interference. The system is capable of reading down to 0.00001 *g* accuracy with a maximum capacity of 15 *g*.



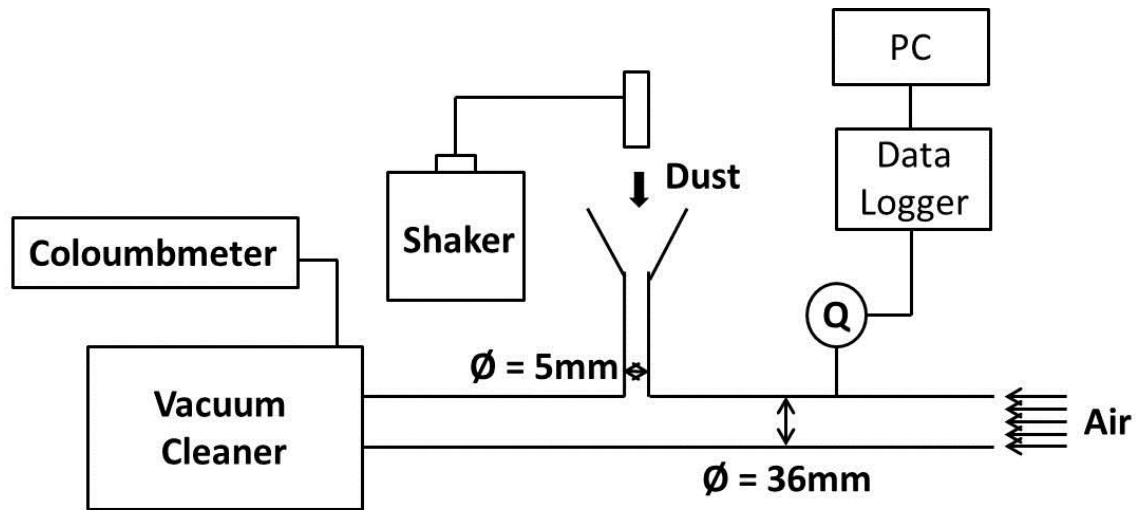


Figure 7.7: Schematic diagram of the dust adhesion test rig used in the experiment.



Figure 7.8: The Sartorius 2024MP digital weighing machine manufactured by Data Weighing Systems Inc.

## 7.3 Results and Discussion

### 7.3.1 Surface Morphology of the Textured Surface

#### 7.3.1.1 Surface Energy Modification

Figure 7.9 shows the surface morphology images of different excimer laser treated ABS surfaces obtained using optical white light interferometer. It is observed that all excimer laser surface treated ABS had a rougher surface as compared to the un-treated surface. The roughness of the surface increased with laser fluence and NOP as shown in Figure 7.10.

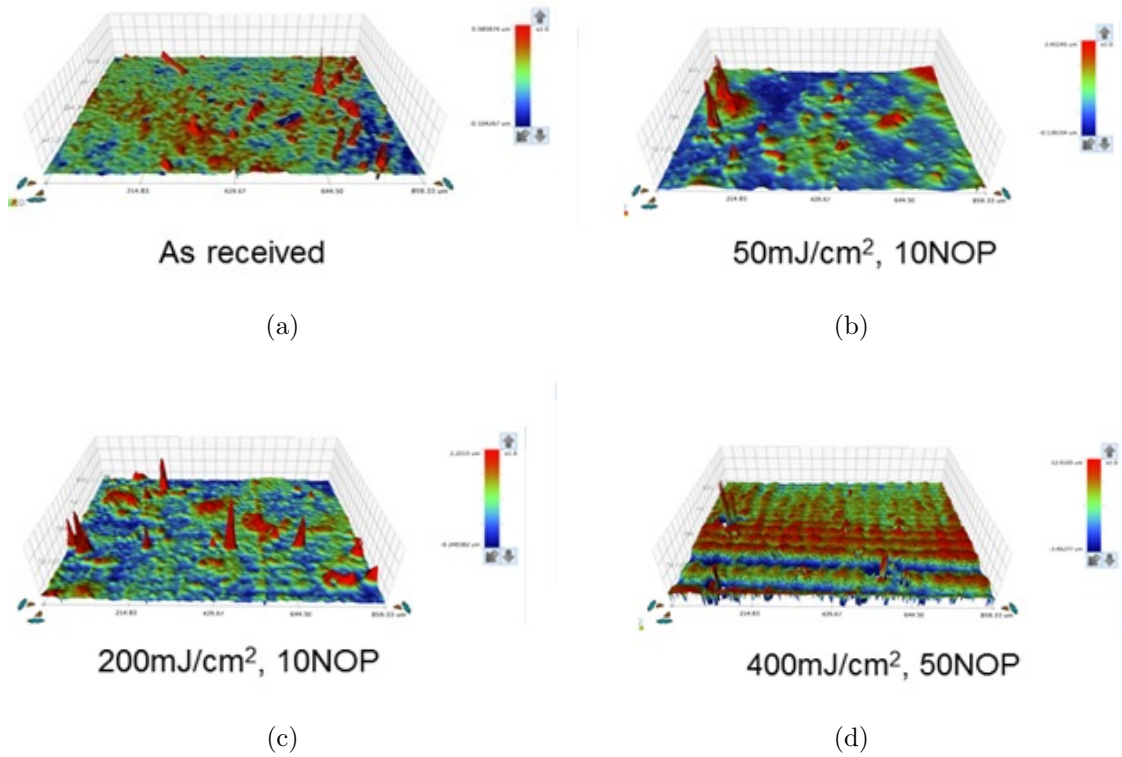


Figure 7.9: Optical white light interferometer contour plot illustrating surface morphology of different excimer laser ( $\lambda = 248 \text{ nm}$ ,  $pulse \ width = 15 \text{ ns}$ ) surface treatment conditions: (a) as-received, (b)  $50 \text{ mJ/cm}^2$ , 10 NOP, (c)  $200 \text{ mJ/cm}^2$ , 10 NOP and (d)  $400 \text{ mJ/cm}^2$ , 50 NOP for ABS surface.

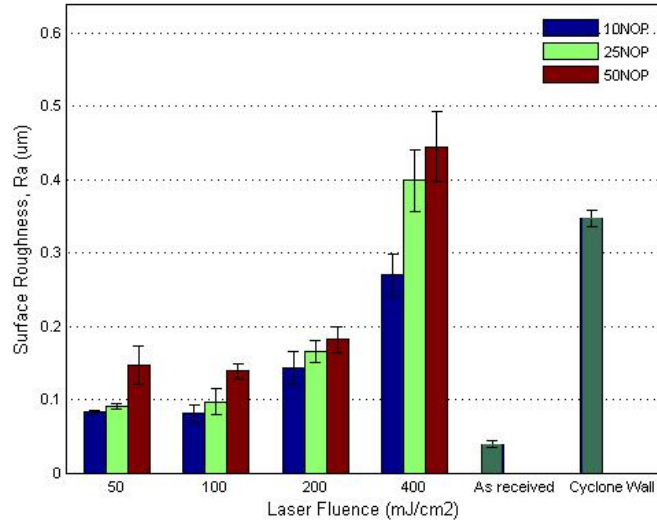


Figure 7.10: Surface roughness plot for different excimer laser surface treatment conditions for ABS surface.

### 7.3.1.2 Surface Texturing

Five different surface textures were produced using the three different scanning patterns through femtosecond laser by varying the separation distance between each scan. The structures produced include dimple, line, hatch, needle shape and fin shape as shown in Figure 7.11. Table 7.1 summarises the height of the structures produced using different scanning patterns and separation distances.

Table 7.1: Summary of the feature height for different ABS textured surfaces.

	Scanning pattern	Separation distance ( $\mu m$ )	
		100	200, 300, 400
Feature Height ( $\mu m$ )	Circle	15	25
	Hatch	15	15
	Line	15	

Figure 7.12 shows the plot of the surface roughness of different textured surface using the femtosecond laser. It is observed that the surface roughness of the femtosecond laser textured surface is much higher as compared to the un-textured surfaces. The surface roughness reduces with increasing separation distance (de-

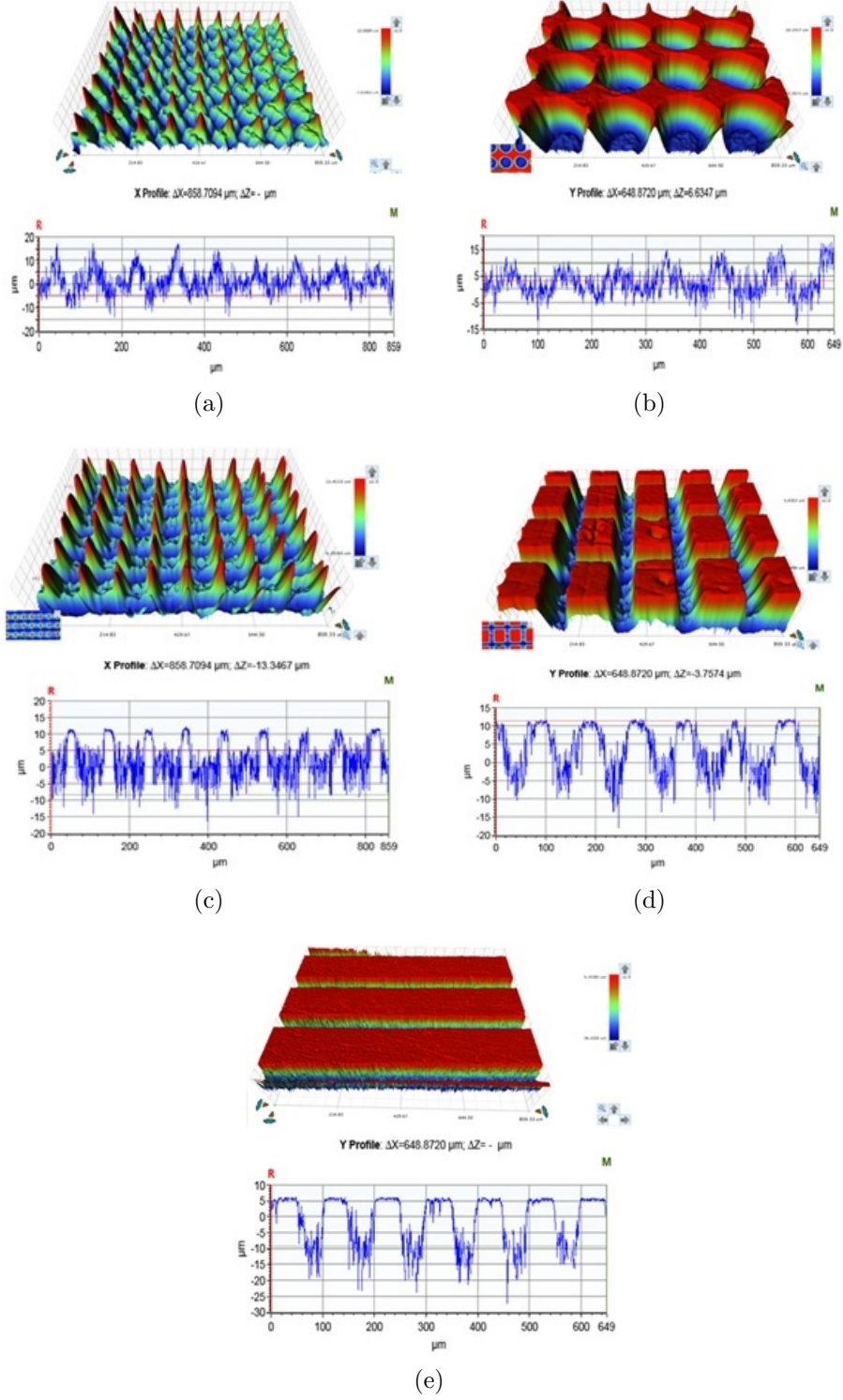


Figure 7.11: Optical white light interferometer surface morphology profile for femtosecond laser textured ABS with (a) circular pattern with separation distance of  $100\ \mu\text{m}$  (needle shape) and (b)  $200\ \mu\text{m}$  (dimple shape), (c) hatch pattern with separation distance of  $100\ \mu\text{m}$  (fin shape) and (d)  $200\ \mu\text{m}$  (hatch shape) and (e) line pattern with separation distance of  $200\ \mu\text{m}$  (line shape).

creasing pattern density). The needle shape texture had lower surface roughness as compared to the dimpled surface with separation distance of  $200\ \mu\text{m}$  and  $300\ \mu\text{m}$ . Similar characteristics were seen for the fin shape texture surface.

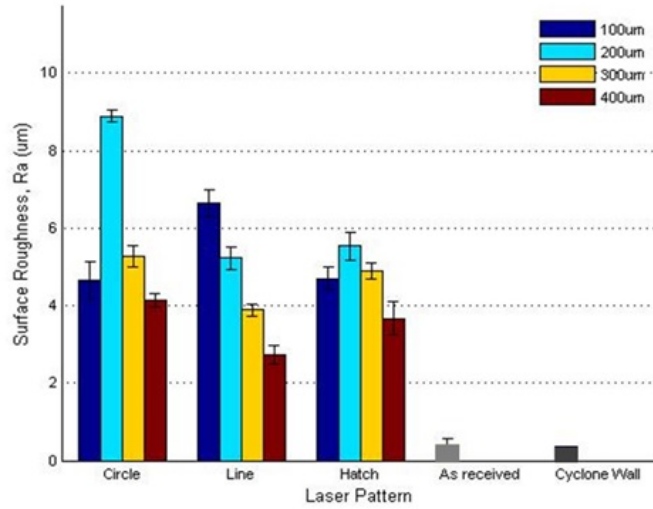


Figure 7.12: Surface roughness plot for different femtosecond laser surface texturing conditions for ABS polymer.

### 7.3.2 Particle Charge Property

The particles used had a broad range of sizes ranging from sub-micron to a few microns as shown in Figure 7.13. The electrostatic charge of the particles running through the test rig were measured using a coulombmeter. The coulombmeter was first calibrated to determine the accuracy of the measurement by charging capacitors of different capacitance ( $10\ \text{nF}$ ,  $22\ \text{nF}$ ,  $33\ \text{nF}$ ,  $47\ \text{nF}$  and  $68\ \text{nF}$ ) using a DC voltage supply ( $1 - 6\ \text{V}$ ). Two types of calibrations were carried out with different DC voltage supply and capacitors with different capacitance. The calibration plot is shown in Figure 7.14.

The coulombmeter was then used to measure the charge distribution of the particles feed into the system by connecting the probe to the inner chamber of the test rig through a wire where the inner chamber was made conductive through applying a layer of silver paint manufactured by Agar Scientific. The charge of the

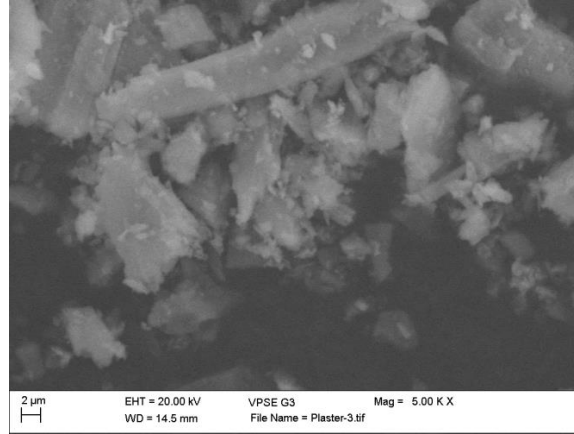


Figure 7.13: SEM image of the dust particles used in the experiment.

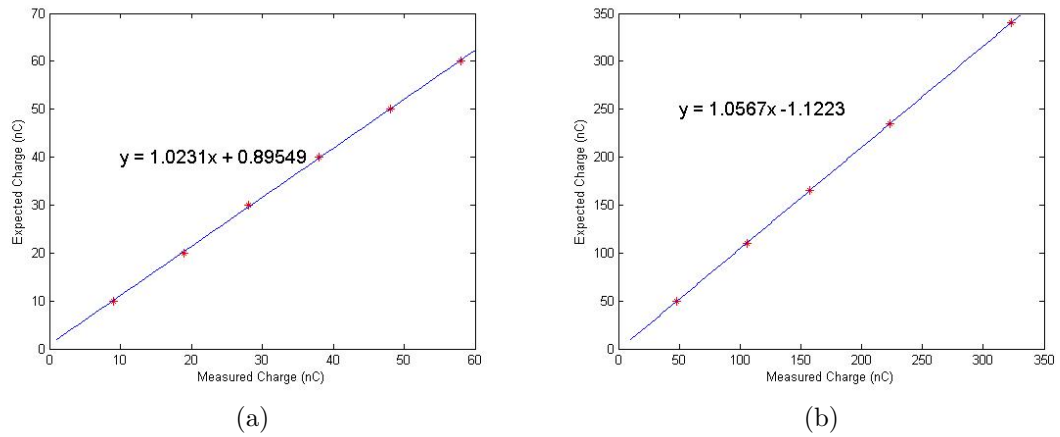


Figure 7.14: Calibration plot for (a) capacitor of 10 nF with varying voltage. (b) Capacitor of different capacitance charged with a constant 5 V supply.

particle over time was measured and shown in Figure 7.15 where the contribution of charged particle was constant at a value of  $5 \text{ nC/s}$ .

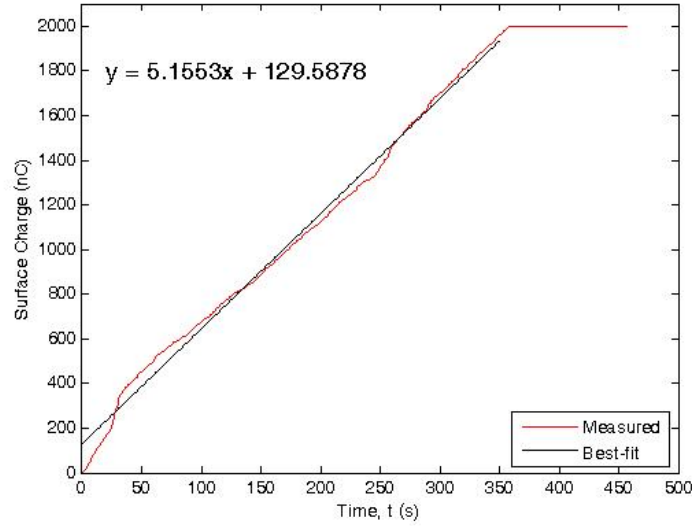


Figure 7.15: Plot of particle charge accumulation versus time.

### 7.3.3 Dust Adhesion Test

**Surface Energy Modification** The dust adhesion test results for the laser engineered ABS surfaces using the excimer laser are summarised in Figure 7.16. The dust adhesion performance is presented in percentage increase relative to the un-treated ABS surface. At 10 *NOP*, the excimer laser treated surface showed a drastic decrease of dust accumulation from  $50 \text{ mJ/cm}^2$  to  $100 \text{ mJ/cm}^2$  and increased after with fluence. As for 25 *NOP*, the dust accumulation remained constant with a slight decrease at  $400 \text{ mJ/cm}^2$ . The dust adhesion for 50 *NOP* increased with fluence with the lower fluence ( $50 \text{ mJ/cm}^2$  and  $100 \text{ mJ/cm}^2$ ) showing lower dust adhesion as compared to the un-treated ABS surface.

The observed dust accumulation trend on excimer laser treated surface is believed to be influenced by two factors: surface roughness and surface energy. As the laser fluence increased, the surface roughness increased as shown in the previous section. The increase in surface roughness increased the surface area available for dust to adhere to causing an increase in dust adhesion.



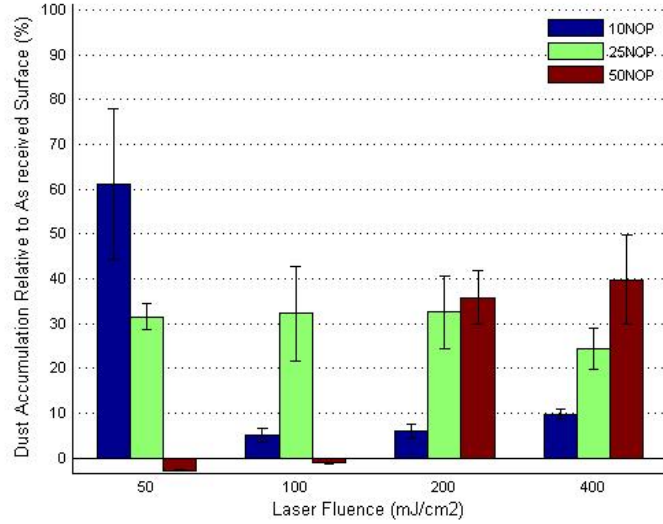


Figure 7.16: Dust adhesion performance for different excimer laser ( $\lambda = 248 \text{ nm}$ ,  $\text{pulse width} = 15 \text{ ns}$ ) surface treatment conditions under air flow dust test.

The increase in laser fluence increased the surface energy of the polymer through increase in polar function groups (C-O, C=O, C-N) on the surface as shown in the XPS analysis in chapter 4. As the particle fed into the test rig was charged as shown from the coulombmeter measurement as shown in Figure 7.14, the increase in polar functional groups on the polymer surface resulted in an increase in dust accumulation. This is because the laser treated ABS surfaces have higher tendency of inducing polar charges of opposite polarity relative to the dust particles due to the increase in polar functional group. Hence, secondary force formed between the dust particles and the polymer surface are stronger according to the adsorption adhesion theory and electrostatic adhesion theory.

On the contrary, the change in surface roughness is believed to affect the drag coefficient of the air flow which then reduces the amount of dust adhering onto the surface. The increase in surface roughness decreases the critical Reynolds number but increases the minimum drag coefficient [259; 260]. Reynold number is defined as the ratio of the inertial force to the viscous force where low Reynold number implies laminar flow and high Reynold number implies turbulent flow. At a low Reynold number, the viscous force is more dominant in the flow whereas at high



Reynold number, the inertial force is more dominant in the flow. Hence, having a lower Reynold number implies a decrease in the drag coefficient and vice versa. Therefore, an increase in surface roughness increases the drag coefficient between the air flow and the surface. This resulted in an increase in the external force exerted onto the particles and hence increased the removal rate of the particles that adhered onto the surface. Hence the increase in surface roughness had a counter effect on the dust accumulation under dynamic condition. Therefore at low fluences and NOPs under cyclone airflow condition, the laser treated surface accumulated a higher amount of dust on the surface.

**Surface Texturing Modification** The dust adhesion test results for the laser engineered ABS surfaces using the femtosecond laser are summarised in Figure 7.17. All textured surfaces showed increased dust accumulation as compared to the un-textured surface except for the line texture where it showed similar dust accumulation as compared to un-textured surface. On the other hand, the hatch and dimple texture showed a decrease in dust accumulation with an increased separation distance where the accumulated dust is higher for dimple texture as compared to the hatch texture. In addition, the fin and needle texture showed an increase in dust accumulation with needle texture showing a higher increase than the fin texture.

The dust accumulation of femtosecond laser textured ABS surfaces showed similar variation trend to the surface roughness changes. As all the femtosecond laser textured surfaces had a much higher roughness as compared to the excimer laser treated surface, the increase in dust accumulation is relatively higher for all the textured surface with the exception of the line texture. The observed variation of the dust accumulation for dimple and hatch texture with separation distance is mainly due to the reduction in surface area as well as the nature of the texture as these texture trap dust particles easily and is hard to be removed. This is clearly observed in the SEM images of the surface after dust adhesion test shown in Figure 7.18 where the dust particles partially filled up the textured area. In addition to the macro-surface roughness, the micro-surface roughness of the textured area also increased. The textured area produces a porous structure that may be a result of re-solidification of the melted polymer as shown in Figure

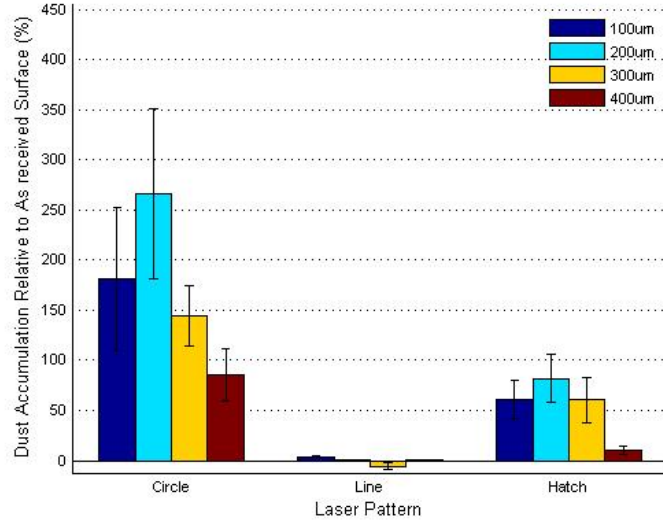


Figure 7.17: Dust adhesion performance for different femtosecond laser ( $\lambda = 800 \text{ nm}$ ,  $\text{pulse width} = 100 \text{ fs}$ ) surface texturing conditions under air flow dust test.

7.19. Such surface structure is prone to trapping dust as the size of the porous structure is in the micro scale level which is bigger as compared to the size of the dust particles.

The fin and needle texture has slightly lower dust adhesion as compared to the dimple and hatch texture with smallest separation distance because these two textures had a lower surface roughness than the dimple and hatch texture with smallest separation distance. As for the line patterned ABS surface, the dust adhesion is close to the un-textured surface. This observation is believed to be caused by the changes in aerodynamic due to the texture effect as the line patterned was placed parallel to the air flow. This observation is also seen on the difference in dust accumulation between the dimple texture and the hatch texture where the hatch texture has a relatively low dust adhesion as compared to the dimple texture. In addition, the femtosecond textured surface resulted in surface chemical composition changes where the surface energy is increased as shown in the XPS analysis in chapter 4 which then increases the tendency of the surface to attract dust particles to adhere onto the surface.

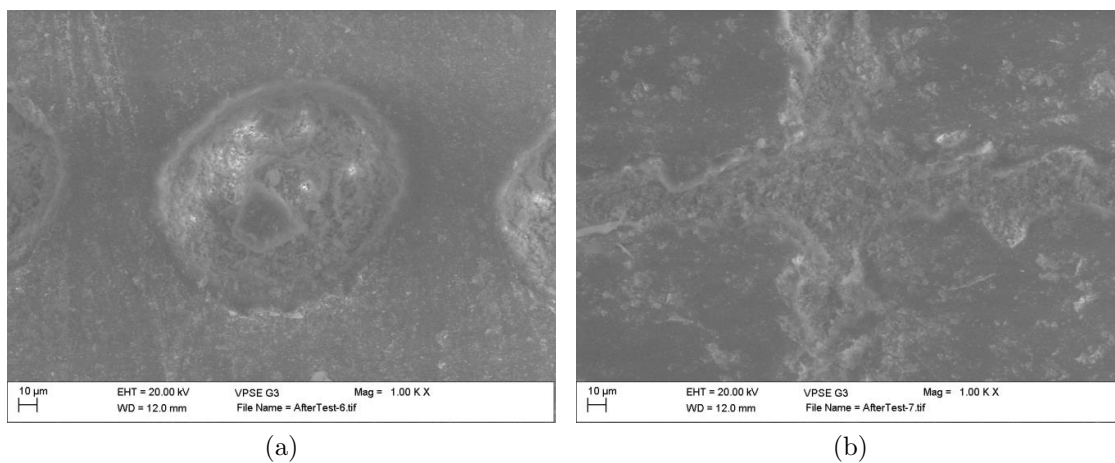


Figure 7.18: SEM images of (a) dimple and (b) hatch texture on ABS after dust adhesion test.

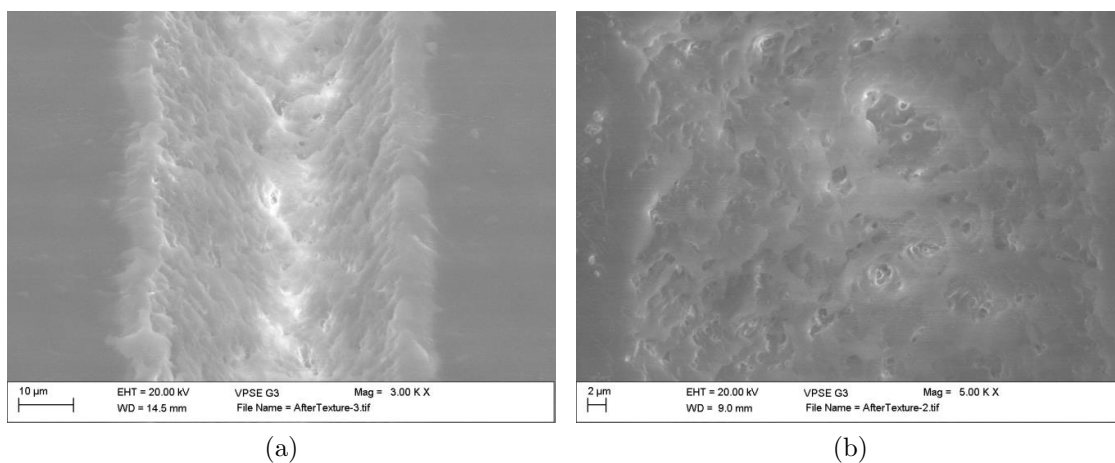


Figure 7.19: SEM images of line pattern at an angle of (a)  $45^\circ$  and (b)  $0^\circ$ .

## 7.4 Summary

1. Under cyclone airflow environment, the laser surface engineered ABS shows an increase in dust accumulation as compared to the un-treated surface with the exception of line textured surface where similar dust accumulation was observed.
2. The main factors that affect the changes in dust adhesion performance of the ABS surface are changes in surface roughness and surface chemical composition which can be explained through adsorption and electrostatic adhesion theory.
3. The increase in surface roughness increased the available surface area for dust particles to adhere onto the surface resulting in better adhesion. Nonetheless, the femtosecond laser textured ABS produced porous micro-scale structures on the textured area which acts as a repository area for the dust particles to adhere.
4. The increase in surface roughness increased the drag coefficient of the air flow result in higher removal force exerted by the air flow onto the dust particles. In addition, the localised aerodynamic flow on the surface changes with different surface textures which seemed to increase the particle removal force through a decrease in dust accumulation result.
5. The excimer laser and femtosecond laser surface treatment changed the surface chemical composition of the ABS through chain scission process by which cross-link formation and addition of polar functional groups into the polymeric chain were observed. As the dust particles were charged, the increase in polar functional groups increased the adhesion of the dust particles onto the surface due to induce dipole moment.

# Chapter 8

## Conclusions

This thesis reported an investigation on the understanding of the interactions between excimer and femtosecond laser beams and CFRP, ABS polymer and HR4 nickel alloy in laser surface micro/nano texturing of these materials, and their applications for improved paint adhesion, control of dust attachment to surfaces and tribology performances in a SPF moulding process. These applications required the modification of material surface properties. Hence, the effect of interactions between the laser beam on material surface morphological characteristics, chemical and crystallographic changes were crucial in understanding the behaviour of the surface engineered materials under different application environments.

Surface adhesion is one of the research topics in this thesis whereby the applications involve paint adhesion on CFRP and dust adhesion on ABS polymer. Laser surface treatment using excimer laser had been proven to be an effective pre-treatment method for paint adhesion improvement of CFRP as it is controllable, reliable and having the possibility of being automated. In addition, laser surface treated ABS using the excimer and femtosecond laser also showed an improvement in dust adhesion.

The main factors that cause improvement of adhesion for both situations are changes in surface morphology and surface chemical composition through the laser ablation process. For the excimer laser beam (pulse width in the ns regime) ablation of materials, the ablation depth per pulse shows a single ablation regime that obeys Beer-Lambert's logarithmic law. For the femtosecond laser ablation of materials, two ablation regimes are observed where the dependency of

the ablation rate at the low fluence ablation regime is dependent on the optical penetration depth and at high fluence ablation regime, it is dependent on the thermal penetration depth. The ablation process changes the surface roughness.

The ablation threshold,  $F_{th}^1$ , for the epoxy with the excimer laser beam was found to be  $1.17 \text{ J/cm}^2$  with an incubation factor of  $\xi = 0.75$  and an optical penetration depth of  $\alpha^{-1} = 282 \text{ nm}$ . The ablation threshold value was lower for ABS with the excimer laser ( $F_{th} = 0.87 \text{ J/cm}^2$ ) compared to that with the femtosecond laser ( $F_{th} = 1.642 \text{ J/cm}^2$ ). This is due to the different in ablation mechanisms. The eximer laser ablation of ABS is governed by thermal ablation with single-photon absorption, whilst the femtosecond laser ablation of ABS is governed by photoablation (in the low fluence regime) and thermal ablation (in the high fluence regime) with multi-photon absorption. The optical penetration depth value was higher for ABS interaction with the excimer laser beam,  $\lambda = 248 \text{ nm}$  ( $\alpha^{-1} = 223 \text{ nm}$ ) compared to that for the femtosecond laser beam,  $\lambda = 800 \text{ nm}$  ( $\alpha^{-1} = 2.917 \text{ nm}$ ). This is due to the difference in photon energy of the laser beam of different wavelength.

In addition to material removal, laser ablation also changes the chemical composition of the treated layer mainly in the polymeric materials. The main observation of chemical changes was where the chain scission process through the reduction in unsaturated or saturated carbon-carbon chains and an increase in other functional groups such as oxygen rich (C-O and C=O) and nitrogen rich functional group (C-N) was observed. This is achieved through reactions between the free radical carbons with oxygen, nitrogen and water vapour in air. The increase in laser fluence and NOPs increased the oxygen and nitrogen rich functional groups on the epoxy resin surface when it was irradiated with the excimer laser. Nitrogen rich functional group was added into the polymeric chain of the ABS after laser ablation where the free radical carbons produced had a higher affinity towards nitrogen molecules than oxygen molecules.

The factors that affect paint adhesion on CFRP surface are types of contaminants, surface morphology and surface chemical composition. Surface cleanliness is the most crucial factor in determining the adhesiveness of a CFRP surface where contaminants containing fluorine from the release films or other ancillary consumable during the manufacturing process reduce paint adhesion strength of

CFRP found on the rough CFRP surface. The smooth CFRP surface had a higher paint adhesive strength than the rough CFRP surface (104 %) due to the absent of surface contaminants. The paint adhesion strength of the rough CFRP surface increased when the contaminants were removed through pre-treatment process such as laser treatment or sand-papering.

The second most influential factor for surface adhesion is the surface chemical composition of the polymers and the third most influential factor is the surface morphology (e.g. surface roughness) of the polymers. The sand-papered surfaces, although having a higher surface roughness, had lower paint adhesion strength as compared to the laser pre-treated samples using the optimal laser parameter. This is because laser pre-treated surface has a higher polar functional group density as compared to the sand-papered surface. The polar functional groups react and form better cross-link with the coatings which in turn enhance the adhesion of the paint on the CFRP surface. The increase in surface roughness provides a larger surface area for bonding between the paint and the substrate hence enhance paint adhesion of CFRP.

Factors affecting ABS surface dust adhesion performance are similar to those of CFRP which are surface roughness and surface chemical composition. An increase in surface roughness increases the surface area available for dust to adhere onto the surface resulting in more dust attachment. The femtosecond laser textured ABS produced porous micro-scale structures which acted as a repository area for the dust to hold on to. In addition, the change in surface roughness changes the drag coefficient of the air flow result in higher removal force exerted by the air flow onto the dust particles. Furthermore, the effect of different surface textures also changes the localised aerodynamic flow on the surface which seems to increase the removal force of the air flow as shown from the dust adhesion results for the line texture. On the other hand, an increase in the polar functional groups increases the adhesion of the dust particles onto the surface due to induce dipole moment between the charged dust particles and the ABS surface.

By carefully selecting the laser processing parameters, the increase in paint adhesion strength on CFRP was higher than sand-papered CFRP surfaces. The optimal excimer laser parameters for the smooth CFRP surface were found to be at a laser fluence of  $175 \pm 10 \text{ mJ/cm}^2$  with  $3 \pm 1$  NOPs at a frequency of

10  $Hz$  and 0 % overlap using the hybrid mask. For the rough CFRP surface, the optimal laser processing parameters were  $225 \pm 25 \text{ mJ/cm}^2$  with  $20 \pm 5$  NOPs at a frequency of 30  $Hz$  and a 50 % overlap using the square mask.

Surface tribology is another research topic in this thesis where the application involves improving friction and wear of nickel alloy. Laser surface texturing (producing micro dimples of 100  $\mu m$  diameter) showed an improvement in HR4 nickel alloy wear rates under both dry and oil lubricated environments. The micro dimples were produced through selecting suitable laser parameters around the ablation threshold to achieve a reasonable surface finish and machining time. The ablation threshold (in low fluence ablation region) for the HR4 nickel alloy with the femtosecond laser was found to be  $F_{th1} = 0.39 \text{ J/cm}^2$  with an incubation factor of  $\xi = 0.8$  and an optical penetration depth of 47.3  $nm$ . From the threshold value, it was observed that metallic materials show lower ablation thresholds as compared to that of polymeric materials. This indicates the difference in ablation mechanisms between the two classes of material.

Under the dry environment, a higher dimple area ratio reduced the wear rate of a surface. For the wear test duration of 900  $s$ , the optimal dimple area ratio was 20 % with a wear rate reduction of 64 % relative to the un-textured nickel alloy surface. The main wear mechanism involved was abrasive wear and the dimples acted as a reservoir to store wear particles produced which helps reduce the wear rate of the surface. Under the oil lubricated environment, the friction coefficient is dependent on the surface contact pressure, sliding speed and the viscosity of the lubricant. The wear rate is dependent on the film thickness formed between the two surfaces and is correlated to the friction coefficients. The optimal dimple area ratio for the minimum wear rate was at 20 % dimple area ratio when the dimple depth was 2.5  $\mu m$  with a reduction of 35 % relative to the un-textured nickel alloy surface.

The wear rate of a dimpled surface is dependent on three factors which are: dimple diameter to contact area diameter ratio, dimple depth and dimple area ratio. An increase in the dimple area ratio increases the contact pressure of the surface, which increases the wear rate of the surface. However, this also increases the reservoir capacity which decreases the wear rate of the surface. The increase in dimple depth decreases the thickness of the lubricant film under oil lubricated



environment which results in a reduced wear rate. The effect of the dimple as a lubricant reservoir is dependent on the dimple diameter to contact area diameter ratio where the effect decreases with the increasing ratio. The wear mechanism under room temperature environment is governed by abrasive wear.

The investigation into all three applications of laser surface texturing - paint adhesion, dust adhesion and tribology performance improvement showed positive results indicating laser surface texturing is a promising surface modification process for these applications. Through the understanding the laser beam material interactions with various materials, optimal laser parameters for surface engineering have been identified to achieve desired performances in the chosen applications.

# Chapter 9

## Future Work

### 9.1 Laser Beam Interaction with Materials

In this research, excimer and femtosecond laser interactions with polymers and femtosecond laser interactions with nickel alloy has been investigated. A comparison between different laser wavelength (IR and UV wavelength) and pulse width (nanosecond and femtosecond) on polymer ablation has been investigated. Other types of comparisons such as the effect of visible laser wavelengths and picosecond pulses can be carried out in the future to observe the dependency and changes in mechanisms when material interacting with laser beams of different properties. The dependency of ablation threshold on other laser parameters such as frequency can also be investigated. Characterisation of surface chemical composition changes of polymer after ablation using Time-of-Flight Secondary Ion Mass Spectrometry (TOF-SIMS) can be carried out to gather more accurate information on the changes in polymer chain size to further understand the existence of chain scission and/ or cross-link formation processes. The plume ejected during ablation process can also be collected and analysed to investigate the size and type of materials removed from the surface. Modelling of laser ablation process using molecular dynamic (MD) or smoothed-particle hydrodynamic (SPH) analysis can be carried out in the future to investigate ablation mechanisms of different materials with different laser types and can be used to compare with the experimental results.

## **9.2 Paint Adhesion Improvement by Laser Surface Processing**

Paint adhesion performance on laser surface pre-treated CFRP has been investigated, with the condition that all the laser parameters used do not expose the carbon fibre underneath the matrix. Study of paint adhesion performance under an exposed carbon fibre condition can be carried out in the future. In addition, the use of different mask design on changes in surface morphology can also be carried out in the future. The CFRP surface chemical composition changes on laser surface pre-treatment under different environmental conditions such as in argon, nitrogen or oxygen gas can be carried out in the future. Laser pre-treatments under different environment conditions can affect the formation of functional group types (carbon rich or oxygen rich functional groups) on the CFRP polymer surface and hence the effect of having specific functional groups on the CFRP on paint adhesion can be investigated in the future.

## **9.3 Tribology Performance Improvement by Laser Surface Texturing**

The tribology performance of the textured nickel alloy has been investigated using one type of oil lubricant. The effect of different types of lubricant on wear rate and friction coefficient performance of dimpled surface can be investigated. Only one dimple size ( $100\ \mu m$ ) has been used in the experiment. Therefore the effect of different dimple sizes can be investigated in the future. In addition, the effect of different contact area ratios relative to the dimple size can be investigated in the future as well. The effect of dimpled surfaces on solid lubricant under high temperature and pressure can also be investigated in the future, to study the effect of such surfaces under extreme conditions closer to the practical applications in the superplastic forming process.

## **9.4 Dust Adhesion Control with Laser Surface Texturing**

The investigation of dust adhesion characteristics on laser pre-treated surfaces has been concentrating on the effect of surface modification (ablation and texturing) on dust adhesion. Changes in other conditions such as having dust particles of different initial charges can be used to further investigate the charging effect in dust adhesion phenomena. As mentioned in the thesis, direct laser surface texturing produces a porous surface of sub-micron structure which aids in dust adhesion. Hence by using other techniques such as injection moulding, effects of pure surface texture on dust adhesion can be investigated, as surface textures without sub-micron structures and alteration of the surface functional groups can be produced. Aerodynamic modelling of airflow changes caused by different surface textures can be carried out in the future to visualise the texture effect under different airflow conditions in the cyclone environment. Such visualisation can also be achieved through airflow visualisation techniques through injecting fluorescence liquid of low viscosity.

# References

- [1] C. Kittel. *Introduction to solid state physics*. Wiley, New York, 1971.
- [2] C.Y. Yeo, S.C. Tam, S. Jana, and Michael W.S. Lau. A technical review of the laser drilling of aerospace materials. *J. Mater. Process. Technol.*, 42:15–49, 1994.
- [3] N.G. Semaltianos, W. Perrie, P. French, M. Sharp, G. Dearden, S. Logothetidis, and K.G. Watkins. Femtosecond laser ablation characteristics of nickel-based superalloy C263. *Applied Physics A*, 94:999–1009, 2009.
- [4] Yong Jee, Michael F. Becker, and Rodger M. Walser. Laser-induced damage on single-crystal metal surfaces. *J. Opt. Soc. Am. B*, 5 (3):648–659, 1988.
- [5] S. Preuss, A. Demchuk, and M. Stuke. Sub-picosecond UV laser ablation of metals. *Applied Physics A*, 61:33–37, 1995.
- [6] S. Nolte, C. Momma, H. Jacobs, A. Tunnermann, B.N. Chichkov, B. Wellegehausen, and H. Welling. Ablation of metals by ultrashort laser pulses. *J. Opt. Soc. Am. B*, 14 (10):2716–2722, 1997.
- [7] J.F. Ready. *Industrial applications of lasers*. Academic Press, New York, 1978.
- [8] M. Shinoda, R.R. Gattass, and E. Mazur. Femtosecond laser-induced formation of nanometer-width grooves on synthetic single-crystal diamond surfaces. *J. of Appl. Phys.*, 105:053102, 2009.

- [9] Bert Huis in t Veld and Hans van der Veer. Initiation of femtosecond laser machined ripples in steel observed by scanning helium ion microscopy. *J. of Las. Micro / Nanoeng.*, 5:28–34, 2010.
- [10] Barada K. Nayak and Mool C. Gupta. Self-organized micro/nano structures in metal surfaces by ultrafast laser irradiation. *Optics and Lasers in Engineering*, 48:940 – 949, 2010.
- [11] M. Geiger, U. Popp, and U. Engel. Excimer laser micro texturing of cold forging tool surfaces - Influence on tool life. *CIRP Annals Manufacturing Technology*, 51(1):231 – 234, 2002.
- [12] X. Wang, K. Kato, and K. Aizawa. The effect of laser texturing of SiC surface on the critical load for the transition of water lubrication mode from hydrodynamic to mixed. *Tribol. Int.*, 34 (10):703–711, 2001.
- [13] G. Dumitru, V. Romano, H.P. Weber, H. Haefke, Y. Gerbig, and E. Pfluger. Laser microstructuring of steel surfaces for tribological applications. *Appl. Phys. A: Mater. Sci. Process.*, 70:485 – 487, 2000.
- [14] G. Dumitru, V. Romano, H.P. Weber, M. Sentis, and W. Marine. Femtosecond ablation of ultrahard materials. *Appl. Phys. A: Mater. Sci. Process.*, 74:729 – 739, 2002.
- [15] G. Dumitru, V. Romano, H.P. Weber, M. Sentis, and W. Marine. Ablation of carbide materials with femtosecond pulses. *Appl. Surf. Sci.*, 205:80 – 85, 2005.
- [16] Q. Benard, M. Fois, M. Grisel, and P. Laurens. Surface treatment of carbon-epoxy and glass-epoxy composites by an excimer laser beam. *International Journal of Adhesion and Adhesives*, 26:543–549, 2006.
- [17] M. Rotel, J. Zahavia, A. Buchman, and H. Dodiuk. Preadhesion laser surface treatment of carbon fibre reinforced PEEK composite. *The Journal of Adhesion*, 55:77–97, 1995.

- [18] J.K. Park and K. Mukherjee. Excimer laser surface treatment of sheet molding compound for adhesive bonding. *Materials and Manufacturing Processes*, 13:359–368, 1998.
- [19] David E. Packham, Andreas chsner, Robert D. Adams, and Lucas F. M. da Silva. *Handbook of adhesion technology: Theories of fundamental adhesion volume 2*. Springer Berlin Heidelberg, 2011.
- [20] S.R. Leadley and J.F. Watts. The use of monochromated XPS to evaluate acid-base interactions at the PMMA/oxidised metal interface. *International Journal of Adhesion and Adhesives*, 60 (1-4):175–196, 1997.
- [21] S.F. Tead, W.E. Vanderlinda, G. Marra, A.L. Ruoff, and E.J. Kramer. Polymer diffusion as a probe of damage in ion or plasma etching. *J. Appl. Phys.*, 68 (6):2972–2982, 1990.
- [22] P. Davies, C. Courty, N. Xanthopoulos, and H.J. Mathieu. Surface treatment for adhesive bonding of carbon fibre-poly(etherether ketone) composites. *Journal of Materials Science Letters*, 10:335–338, 1991.
- [23] C.K. Jung, I.S. Bae, S.B. Lee, J.H. Cho, E.S. Shin, S.C. Choi, and J.H. Boo. Development of painting technology using plasma surface technology for automobile part. *Thin Solid Films*, 506-507:316–322, 2006.
- [24] J.R.J. Wingfield. Treatment of composite surfaces for adhesive bonding. *International Journal of Adhesion and Adhesives*, 13:151–156, 1993.
- [25] J. Visser. Adhesion and removal of particles I. *Fouling Science and Technology*, 145:87–123, 1988.
- [26] Bharat Bhushan and B.K. Gupta. *Handbook of tribology: Materials, coatings and surface treatment*. McGraw-Hill Inc, 1991.
- [27] I. Etsion. Improving tribological performance of mechanical components by laser surface texturing. *Tribology Letters*, 17 (4):733 – 737, 2004.

- [28] X.L. Wang and S.M. Hsu. An integrated surface technology for friction control: A new paradigm effects of geometric shapes on friction. *The 4th China International Symposium on Tribology*, pages 12–20, 2004.
- [29] Haiwu Yu, Xiaoleo Wang, and Fei Zhou. Geometric shape effects of surface texture on the generation of hydrodynamic pressure between conformal contacting surfaces. *Tribol. Lett.*, 37:123 – 130, 2010.
- [30] Kouros Kalantar-zadeh and Benjamin Fry. *Nanotechnology-enabled sensors*. Springer-Verlag, Berlin Heidelberg, 2008.
- [31] Bruker. *An introduction to non-contact surface metrology*. Bruker, 2013.
- [32] H. Yan, R. Adelgren, M. Boguszko, G. Elliot, and D. Knight. Laser energy deposition in quiescent air. *AIAA J.*, 41 (10):1988–1995, 2003.
- [33] DeFelsko Corporation. *PosiTest pull-off adhesion tester*. DeFelsko Corporation, 2011.
- [34] P.A. Friedman, S.G. Luckey, W.B. Copple, R. Allor, C.E. Miller, and C. Young. Overview of superplastic forming research at ford motor company. *Journal of Materials Engineering and Performance*, 13(6):670 – 677, 2004.
- [35] MIBA Coating Group. *Pin on disc tester PoD2: State of the art PVD and PACVD coating systems thin film test equipment*. Teer Coatings Ltd., 2013.
- [36] William M. Steen and J. Mazumdera. *Laser material processing, 4th edition*. Springer Verlag, 2010.
- [37] R. Lambourne. *Paint and surface coatings: Theory and practice*. Ellis Horwood Ltd, UK, 1987.
- [38] Wiliam M. Steen. *Laser material processing, 3rd Edition*. Springer-Verlag London Limited, USA, 2003.



- [39] G. Beamson and D. Briggs. *High resolution XPS of organic polymers: The Scienta ESCA300 database*. Wiley, 1992.
- [40] Brenda M. Parker and Rex M. Waghorne. Testing epoxy composite surfaces for bondability. *Surface and Interface Analysis*, 17:471–476, 1991.
- [41] F.D. Egitto, F. Emmi, and R.S. Horwath. Plasma etchin of oganic materials I. polyimide in  $O_2 - CF_4$ . *J. Vac. Sci. Technol. B*, 3(3):893–904, 1985.
- [42] D.M. Choi, C.K. Park, K. Cho, and C.E. Park. Adhesion improvement of epoxy resin/polyethylene joints by plasma treatment of polyethylene. *Polymer*, 38(25):6243–6249, 1997.
- [43] F. Kokai, H. Saito, and T. Fujioka. X-ray photoelectron spectroscopy studies on modified polyimide surfaces after ablation with KrF excimer laser. *J. Appl. Phys.*, 66(7):3252–3255, 1989.
- [44] D.K. Chattopadhyay, Siva Sankar Panda, and K.V.S.N. Raju. Thermal and mechanical properties of epoxy acrylate/methacrylates UV cured coatings. *Progress in Organic Coatings*, 54:10–19, 2005.
- [45] Q. Benard, M. Foïs, M. Grisel, P. Laurens, and F. Joubert. Influence of the polymer surface layer on the adhesion of polymer matrix composites. *Journal of Thermoplastic Composite Materials*, 22:51–61, 2009.
- [46] N. Eustathopoulos, M.G. Nicholas, and B. Drevet. *Wettability at high temperatures*. Pergamon, Oxford, UK, 1999.
- [47] Avanish Kumar Dubey and Vinod Yadava. Laser beam machining - a review. *Int. J. Mach. Tools Manufac.*, 48:609–628, 2008.
- [48] E. Yasa and J.P. Kurth. Investigation of laser and process parameters for selective laser erosion. *Precision Eng.*, 34:101–112, 2010.
- [49] V.A. Katulin. Laser technology in industry. *Hyperfine Interactions*, 37:423–432, 1987.

- [50] Martin von Allmen and Andreas Blatter. *Laser-beam interactions with materials*. Springer, Berlin, 1995.
- [51] N.W. Ashcroft and N.D. Mermin. *Solid state physics*. Saunders College, Philadelphia, 1976.
- [52] D. Pines and P. Nozières. *The theory of quantum liquids*. Benjamin, New York, 1966.
- [53] Philip B. Allen. Theory of thermal relaxation of electrons in metals. *Phys. Rev. Lett.*, 59 (13):1460–1463, 1987.
- [54] T.Q. Qiu and C.L. Tien. Short-pulse laser heating on metals. *Int. J. Heat Mass Transfer*, 35 (3):719–726, 1992.
- [55] G. Grimvall. *The electronphonon interaction in metals*. North-Holland, Amsterdam, 1981.
- [56] P.B. Allen. Theory of thermal relaxation of electrons in metals. *Phys. Rev. Lett.*, 59 (13):1460–1463, 1987.
- [57] P.B. Allen. Empirical electron-phonon lambda values from resistivity of cubic metallic elements. *Phys. Rev. B*, 36 (5):2920–2923, 1987.
- [58] S.I. Anisimov, B.L. Kapeliovich, and T.L. Perelman. Electron emission from metal surfaces exposed to ultrashort laser pulses. *Sov. Phys. JETP*, 39 (2):375–377, 1974.
- [59] R.H.M. Groeneveld, R. Sprik, and A. Lagendijk. Femtosecond spectroscopy of electron-electron and electron-phonon energy relaxation in Ag and Au. *Phys. Rev. B*, 51 (17):11433–11445, 1995.
- [60] M.I. Kaganov, I.M. Lifshitz, and L.V. Tanatarov. Relaxation between electrons and the crystalline lattice. *Sov. Phys. JETP*, 4:173178, 1957.
- [61] Peter Schaaf. *Laser processing of materials: Fundamentals, applications and developments*. Springer-Verlag, Berlin Heidelberg, 2010.

- [62] M. Bertolotti. *Physical processes in laser-materials interactions*. Plenum, New York, 1983.
- [63] G.E.R. Schulze. *Metallographie*. Springer, Wien-New York, 1974.
- [64] W. Amende. *Arten von werkstoffen und bauteilen des maschinenbaus mit dem hochleistungslaser technologie aktuell 3*. VDI-Verlag, Dsseldorf, 1985.
- [65] D. Ashkenasi, A. Rosenfeld, H. Varel, M. Wahmer, and E.E.B. Campbell. Laser processing of sapphire with picosecond and sub-picosecond pulses. *Appl. Surf. Sci.*, 120:65–80, 1997.
- [66] Mark J. Jacksin. *Micro and nanomanufacturing*. Springer, USA, 2007.
- [67] R. Le Harzic, D. Breitling, M. Weikert, S. Sommer, C. Fohl, S. Valette, C. Donnet, E. Audouard, and F. Dausinger. Pulse width and energy influence on laser micromachining of metals in a range of 100 *fs* to 5 *ps*. *Appl. Surf. Sci.*, 249:322–331, 2005.
- [68] F.C. Burns and Stephen R. Cain. The effect of pulse repetition rate on laser ablation of polyimide and polymethylmethacrylate-based polymers. *J. Phys. D: Appl. Phys.*, 29:1349–1355, 1996.
- [69] Stephen R. Cain, F.C. Burns, Charles E. Otis, and Bodil Braren. Photothermal description of polymer ablation: Absorption behavior and degradation time scales. *J. Appl. Phys.*, 72 (11):5172–5178, 1992.
- [70] John A. Dean. *Lange’s Handbook of Chemistry, 15th Edition*. McGraw-Hill Inc, New York USA, 1999.
- [71] S.K. Nayak, S.N. Khanna, and P. Jena. Energy deposition in supersonic flows. *Physical Review B*, 56 (7):3787–3790, 1998.
- [72] B.N. Chichkov, C. Momma, S. Nolte, F. von Alvensleben, and A. Tunnermann. Femtosecond, picosecond and nanosecond laser ablation of solids. *Applied Physics A*, 63:109–115, 1996.

- [73] S. Ma, J.P. McDonald, B. Tryon, S.M. Yalisove, and T.M. Pollock. Femtosecond laser ablation regimes in a single-crystal superalloy. *Metallurgical and Materials Transactions A*, 38A:2349–2357, 2007.
- [74] A. Luft, U. Franz, A. Emsermann, and J. Kasper. A study of thermal and mechanical effect on materials induced by pulsed laser drilling. *Appl. Phys. A*, 63:93–101, 1996.
- [75] I. N. Zavestovskaya, O.A. Glazov, N.N. Demchenko, and N.A. Menkova. High power and ultrashort laser pulse ablation of metals: Threshold characteristics. *Proc. SPIE 6735: International Conference on Lasers, Applications, and Technologies*, 6735:673512– 2–8, 2007.
- [76] D. Ashkenasi, R. Stoian, and A. Rosenfeld. Single and multiple ultrashort laser pulse ablation threshold of  $Al_2O_3$  corundum at different etch phases. *Applied Surface Science*, 154-155:40–46, 2000.
- [77] R. Srinivasan and V. Mayne-Banton. Self-developing photoetching of poly(ethylene terephthalate) films by far-ultraviolet excimer laser radiation. *Appl. Phys. Lett.*, 41:576–578, 1982.
- [78] Y. Kawamura, K. Toyoda, and S. Namba. Effective deep ultraviolet photoetching of polymethyl methacrylate by an excimer laser. *Appl. Phys. Lett.*, 40 (5):374–375, 1982.
- [79] Thomas Lippert and J. Thomas Dickinson. Chemical and spectroscopy aspects of polymer ablation: Special features and novel directions. *Chem. Rev.*, 103:453–485, 2003.
- [80] V. Srinivasan, M.A. Smrtic, and S.V. Babu. Excimer laser etching of polymers. *J. Appl. Phys.*, 59 (11):3861–3867, 1986.
- [81] J.T.C. Yeh. Laser ablation of polymers. *J. Vac. Sci. Technol. A*, 4 (3):653–658, 1986.
- [82] R. Srinivasan and Bodil Braren. Ultraviolet laser ablation of organic polymers. *Chem. Rev.*, 89:1303–1316, 1989.

- [83] S. Lazare and V. Granier. Ultraviolet-laser photoablation of polymers a review and recent results. *Laser Chem.*, 10:2540, 1989.
- [84] P.E. Dyer. Excimer laser polymer ablation: Twenty years on. *Appl. Phys. A*, 77:167173, 2003.
- [85] R. Srinivasan and W. J. Leigh. Ablative photodecomposition: Action of far-ultraviolet (193 nm) laser radiation on poly(ethyleneterephthalate) films. *J. Amer. Chem. Soc.*, 104:6784–6785, 1982.
- [86] W.R. Harp, J.R. Dilwith, and J.F. Tu. Laser ablation using a long-pulsed, high-fluence CW single-mode fiber laser. *J. Mater. Process. Technol.*, 198:22–23, 2008.
- [87] J. Lowell and W.S. Truscott. Triboelectrification of identical insulators I. An experimental investigation. *J. Phys. D*, 19:1273–80, 1986.
- [88] Daniel J. Lacks and R. Mohan Sankaran. Contact electrification of insulating materials. *J. Phys. D.*, 44:453001, 2011.
- [89] T.F. Deutsch and M.W. Geis. Self-developing UV photoresist using excimer laser exposure. *J. Appl. Phys.*, 54:7201, 1983.
- [90] J.E. Andrew, P.E. Dyer, D. Foster, and P.H. Key. Direct etching of polymeric materials using a XeCl laser. *Appl. Phys. Lett.*, 43:717719, 1983.
- [91] E. Sutcliffe and R. Srinivasan. Dynamics of UV laser ablation of organic polymer surfaces. *J. Appl. Phys.*, 60:33153322, 1986.
- [92] G.D. Mahan, H.S. Cole, Y.S. Liu, and H.R. Philip. Theory of polymer ablation. *Appl. Phys. Lett.*, 53:23772379, 1988.
- [93] I.W. Boyd and R.B. Jackman. *Photochemical processing of electronic materials*. Academic, London, 1992.
- [94] N. Arnold, B. Luk'yanchuk, and N. Bityurin. A fast quantitative modelling of ns laser ablation based on non-stationary averaging technique. *Appl. Surf. Sci.*, 127:184192, 1998.

- [95] S.R. Cain, F.C. Burns, and C.E. Otis. On single-photon ultraviolet ablation of polymeric materials. *J. Appl. Phys.*, 71:4107–4117, 1992.
- [96] S.R. Cain. A photothermal model for polymer ablation: chemical modification. *J. Phys. Chem.*, 97 (29):7572–7577, 1993.
- [97] G.C. D’Couto and S.V. Babu. Heat transfer and material removal in pulsed UV laser-induced ablation of polymers: pulsewidth dependence. *J. Appl. Phys.*, 76:3052, 1994.
- [98] B. Luk’yanchuk, N. Bityurin, M. Himmelbauer, and N. Arnold. UV-laser ablation of polyimide: From long to ultra-short laser pulses. *Nucl. Instrum. Methods Phys. Res. B*, 122:347–355, 1997.
- [99] R.F. Cozzens and R.B. Fox. Infrared laser ablation of polymers. *Polym. Eng. Sci.*, 18 (11):900904, 1978.
- [100] J.H. Brannon and J.R. Lankard. Pulsed  $CO_2$  laser etching of polyimide. *Appl. Phys. Lett.*, 48:1226–1228, 1986.
- [101] P.E. Dyer, G.A. Oldershaw, and J. Sidhu.  $CO_2$  laser ablative etching of polyethylene terephthalate. *Appl. Phys. B*, 48 (6):489–493, 1989.
- [102] H. Schmidt, J. Ihlemann, B. Wolff-Rottke, K. Luther, and J. Troe. Ultraviolet laser ablation of polymers: Spot size, pulse duration and plume attenuation effects explained. *J. Appl. Phys.*, 83:5458–5468, 1998.
- [103] R. Srinivasan. Ablation of polymers and biological tissue by ultraviolet lasers. *Science*, 234 (4776):559–565, 1986.
- [104] B. Luk’yanchuk, N. Bityurin, S. Anisimov, and D. Buerle. The role of excited species in UV-laser materials ablation. *Appl. Phys. A*, 57 (4):367–374, 1993.
- [105] B. Luk’yanchuk, N. Bityurin, N. Arnold, and D. Buerle. The role of excited species in ultraviolet-laser materials ablation III. Non-stationary ablation of organic polymers. *Appl. Phys. A*, 62 (5):397–401, 1996.

- [106] N. Bityurin, A. Malyshev, B. Luk'yanchuk, S. Anisimov, and D. Baeuerle. Photophysical mechanism of UV laser action: The role of stress transients. *Proc. SPIE*, 2802:103–112, 1996.
- [107] S. Papernov and A.W. Schmidt. Laser-induced surface damage of optical materials: Absorption sources, initiation, growth, and mitigation. *Proc. SPIE*, 7132:1–27, 2008.
- [108] Z. Guosheng, P.M. Fauchet, and A.E. Siegman. Growth of spontaneous periodic surface structures on solids during laser illumination. *Phys. Rev. B*, 26 (10):5366–5381, 1982.
- [109] M.N.W. Groenendijk and J. Meijer. Surface microstructures obtained by femtosecond laser pulses. *CIRP Annals - Manufacturing Technology*, 55 (1):183–186, 2006.
- [110] Y.R. Jeng. Impact of plateued surfaces on tribological performance. *Tribol. Trans.*, 39 (2):354 – 361, 1996.
- [111] E. Willis. Surface finish in relation to cylinder liners. *Wear*, 109:351 – 366, 1986.
- [112] R. Rajan, D.N. Lambeth, M. Tromel, P. Goglia, and Y. Li. Laser texturing for low-flying-height media. *Journal of Applied Physics*, 69 (8):5745 – 5747, 1991.
- [113] L. Zhou, K. Kato, G. Vurens, and F.E. Talke. The effect of slider surface texture on flyability and lubricant migration under near contact conditions. *Tribol. Int.*, 36 (4 - 6):269 – 277, 2003.
- [114] K. Komvopoulos. Adhesion and friction forces in microelectromechanical systems: Mechanisms, measurement, surface modification techniques and adhesion theory. *J. Adhes. Sci. Technol.*, 17 (4):477 – 517, 2003.
- [115] M. Geiger, S. Roth, and W. Becker. Influence of laser-produced microstructures on the tribological behavior of ceramics. *Surf. Coat. Technol.*, 100-101:17–22, 1998.

- [116] T.V. Kononenko, S.V. Garnov, S.M. Pimenov, V.I. Konov, V. Romano, B. Borsos, and H.P. Weber. Laser ablation and micropatterning of thin TiN coatings. *Appl. Phys. A: Mater. Sci. Process.*, 71:627 – 631, 2000.
- [117] G. Dumitru, V. Romano, H.P. Weber, S. Pimenov, T. Kononenko, J. Hermann, S. Bruneau, Y. Gerbig, and M. Shupegin. Laser treatment of tribological DLC films. *Diamond Relat. Mater.*, 12:1034 – 1040, 2003.
- [118] M. Rotel, J. Zahavia, S. Tamir, A. Buchman, and H. Dodiuk. Pre-bonding technology based on excimer laser surface treatment. *Applied Surface Science*, 154:610–616, 2000.
- [119] Keiko Gotoh and Shino Kikuchi. Improvement of wettability and detergency of polymeric materials by excimer UV treatment. *Colloid Polymer Science*, 283:1356–1360, 2005.
- [120] P.E. Dyer, S.T. Lau, G.A. Oldershaw, and D. Schudel. An investigation of XeCl laser ablation of polyetheretherketone (PEEK)-carbon fibre composite. *Journal of Materials Research*, 7:1152–1157, 1992.
- [121] J. Breuer, S. Metev, and G. Sepold. Photolytic surface modification of polymers with UV-laser radiation. *Journal of Adhesion Science and Technology*, 9:351–363, 1995.
- [122] D.Y. Kim, K. Lee, and C. Lee. Surface modification of silicon and PTFE by laser surface treatment: Improvement of wettability. *Proceedings of SPIE*, 5063:66–70, 2003.
- [123] F. Y. Sakata, A.M.E. Santo, W. Miyakawa, R. Riva, and M.S.F. Lima. Influence of laser surface texturing on surface microstructure and mechanical properties of adhesive joined steel sheets. *Surface Engineering*, 25:180–186, 2008.
- [124] A. Samad-Zadeh, M. Harsono, A. Belikov, K. V. Shatilova, A. Skripnik, P. Stark, C. Egles, and G. Kugela. The influence of laser-textured dentinal surface on bond strength. *Dental Materials*, 27:1038–1044, 2011.



- [125] C. Poisson, V. Hervais, M. F. Lacrampe, and P. Krawczak. Optimization of PE/binder/PA extrusion blow-molded films. II. Adhesion properties improvement using binder/eva blends. *Journal of Applied Polymer Science*, 101 (1):118–127, 2006.
- [126] K.W. Allen. A review of contemporary views of theories of adhesion. *J. Adhesion*, 21:261–277, 1987.
- [127] B.V. Deryagin and N.A. Krotova. Doklady akad nauk. 61:849, 1948.
- [128] B.V. Deryagin, N.A. Krotova, and V.P. Smilga. Adgezija tverdyck tel. *Izdvo. Nauka, Moskva*, 1973.
- [129] W. Possart. Experimental and theoretical description of the electrostatic component of adhesion at polymer/metal contacts. *International Journal of Adhesion and Adhesives*, 8 (2):77–83, 1998.
- [130] S.S. Voyutskii. Autohesion and adhesion of high polymers. *Interscience*, 89, 1963.
- [131] William Wake. *Adhesion and the formulation of adhesives: 2nd Edition*. Applied Science, London, 1982.
- [132] Lj. Atanasoska, Steven G. Anderson, H.M. Meyer III, Zhangda Lin, and J.H. Weaver. Aluminium/polyimide interface formation: An x-ray photoelectron spectroscopy study of selective chemical bonding. *J. Vec. Sci. Technol. A*, 5 (6):3325–3333, 1987.
- [133] A.D. Katnani, A. Knoll, and M.A. Mycek. Effects of environment and heat treatment on an oxygen plasma-treated polyimide surface and its adhesion to a chromium overcoat. *J. Adhesion Sci. Technol.*, 3 (6):441–453, 1989.
- [134] F.D. Egitto, L.J. Matienzo, K.J. Blackwell, and A.R. Knoll. Oxygen plasma modification of polyimide webs: Effect of ion bombardment on metal adhesion. *J. Adhesion Sci. Technol.*, 8 (4):411–433, 1994.
- [135] F.D. Egitto and L.J. Matienzo. Plasma modification of polymer surfaces for adhesion improvement. *J. Res. Develop.*, 38 (4):423–439, 1994.

- [136] K.L. Mittal. Adhesion aspects of metallization of organic polymer surfaces. *J. Vac. Sci. Technol.*, 13 (1):19–25, 1976.
- [137] H. Yaghoubi, N. Taghavinia, and E.K. Alamdari. Self cleaning  $TiO_2$  coating on polycarbonate: Surface treatment, photocatalytic and nanomechanical properties. *Surface and Coatings Technology*, 204:1562–1568, 2010.
- [138] K.L. Mittal. *Polymer surface modification: Relevance to adhesion vol. 2*. VSP, Utrecht, 2000.
- [139] G.K.A. Kodokian and A.J. Kinloch. Surface pretreatment and adhesion of thermoplastic fibre-composites. *Journal of Materials Science Letters*, 7:625–627, 1988.
- [140] S. Iannace, T. Monetta, F. Bellucci, L. Ambrosio, and L. Nicolais. Effect of RF plasma treatment on adhesion of hydrophilic matrix reinforced composites. *Proceedings of the European Conference on Advanced Materials and Processes*, pages 663–370, 1995.
- [141] F. Caiazzo, P. Canonico, R. Nigro, and V. Tagliaferri. Electrode discharge for plasma surface treatment of polymeric materials. *Journal of Materials Processing Technology*, 58:96–99, 1996.
- [142] S.K. Om. Plasma surface engineering of plastics. *Surf. Eng. Nonmetallic Mater*, 6:892–899, 1993.
- [143] L. Carrino, W. Polini, and L. Sorrentino. Ageing time of wettability on polypropylene surfaces processed by cold plasma. *Journal of Materials Processing Technology*, 153-154:519–525, 2004.
- [144] A. Baalmann, K.D. Vissing, E. Born, and A. Gross. Surface treatment of polyetheretherketone (PEEK) composites by plasma activation. *Journal of Adhesion*, 46:57–66, 1994.
- [145] L.W. Crane, C.L. Hamermesh, and L.Maus. Surface treatment of cured epoxy graphite composites to improve adhesive bonding. *SAMPE Journal*, 12:6–9, 1976.

- [146] Q. Benard, M. Fois, and M. Grisel. Influence of fibre reinforcement and peel ply surface treatment towards adhesion of composite surface. *International Journal of Adhesion and Adhesives*, 24:404–409, 2005.
- [147] A.J. Kinlocha and C.M. Taiga. The adhesive bonding of thermoplastic composites. *Journal of Adhesion*, 21, 1987.
- [148] B.M. Parker and R.M. Waghornea. Surface pretreatment of carbon fibre reinforced composites for adhesive bonding. *Composites*, 13, 1982.
- [149] G.P.A. Turner. *Introduction to paint chemistry and principles of paint technology 2nd Edition*. Chapman and Hall Ltd , USA, 1980.
- [150] J. Visser. Van der Waals and other cohesive forces affecting powder fluidization. *Powder Technology*, 58:1–10, 1989.
- [151] J. Visser. Particle adhesion and removal: A review. *Particulate Science and Technology*, 13:169–196, 1995.
- [152] D.K. Davies. Charge generation on dielectric surfaces. *Brit. J. Appl. Phys. Ser. 2*, 2:1533–1537, 1969.
- [153] D.K. Davies. Static electrification. *Institute of Physics and the Physical Society, IPPS Conf.*, 4:29–36, 1967.
- [154] D.K. Davies. Surface charge and the contact of elastic solids. *J. Phys. D*, 6:1017–1024, 1973.
- [155] J. Visser. *Surface and colloid science*. John Wiley & Sons, New York, 1976.
- [156] C.J. Tsai, D.Y.H. Pui, and B.Y.H. Liu. Particle detachment from disk surface of computer disk drives. *J. Aerosol Sci.*, 22 (6):737–746, 1991.
- [157] H.C. Wang. Effects of inceptive motion on particle detachment from surfaces. *J. Aerosol Sci Technol.*, 13:386–393, 1990.
- [158] K.L. Johnson, K. Kendall, and A.D. Roberts. Surface energy and the contact of elastic solids. *Proceedings of the Royal Society A*, 324:301–313, 1971.

- [159] B.V. Derjaguin, V.M. Muller, and Yu. P. Toporov. Effect of contact deformations on the adhesion of particles. *Journal of Colloid and Interface Science*, 53:314–326, 1975.
- [160] C.J. Tsai, D.Y.H. Pui, and B.Y.H. Liu. Elastic flattening and particle adhesion. *Aerosol Science and Technology*, 15 (4):239–255, 1991.
- [161] Mehdi Soltani and Goodarz Ahmadi. On particle adhesion and removal mechanisms inturbulent flows. *J. Adhesion Sci. Technol.*, 8 (7):763–785, 1994.
- [162] M. Soltani and G. Ahmadi. On particle adhesion and removal mechanisms in turbulent flows. *J. Adhesion Sci. Technol.*, 8 (7):763–785, 1994.
- [163] F.P. Bowden and D. Tabor. *Friction and lubrication of solids, Part I*. Clarendon Press, Oxford UK, 1950.
- [164] F.P. Bowden and D. Tabor. *Friction and lubrication of solids, Part II*. Clarendon Press, Oxford UK, 1950.
- [165] J.F. Archard. Contact and rubbing of flat surfaces. *J. Appl. Phys.*, 24:981–988, 1953.
- [166] M.B. Peterson and W.O. Winer. *Wear control handbook: Wear theory and mechanisms*. ASME, New York, 1980.
- [167] B. Bhushan. *Tribology and mechanis of magnetic storage devices*. Springer-Verlag, New York, 1990.
- [168] K. Osada and K. Shirakawa. Influence of lubrication on aluminum super-plastic forming. *Material Science Forum*, 304 - 306:813 – 818, 1999.
- [169] K.P. Rao and J.J. Wei. Performance of a new dry lubricant in the forming of aluminum alloy sheets. *Wear*, 249:86 – 93, 2001.
- [170] B. Navinsek, P. Panjan, I. Urankar, P. Cvahte, and F. Gorenjak. Improvement of hot-working processes with PVD coatings and duplex treatment. *Surface and Coatings Technology*, 142 - 144:1148 – 1154, 2001.

- [171] C. Mitterer, F. Holler, F. Ustel, and D. Heim. Application of hard coatings in aluminium die casting - Soldering, erosion and thermal fatigue behaviour. *Surface and Coatings Technology*, 125:233 – 239, 2000.
- [172] Thomas Bjork, Mattias Berger, Richard Westgard, Sture Hogmark, and Jens Bergstrom. New physical vapour deposition coatings applied to extrusion dies. *Surface and Coatings Technology*, 146 - 147:33 – 41, 2001.
- [173] D.B. Hamilton, J.A. Walowit, and C.M. Allen. A theory of lubrication by microirregularities. *ASME Journal of Basic Engineering*, 88 (1):177 – 185, 1966.
- [174] J.N. Anno, J.A. Walowit, and C.M. Allen. Microasperity lubrication. *ASME Journal of Basic Engineering*, 91 (2):351 – 355, 1968.
- [175] J.N. Anno, J.A. Walowit, and C.M. Allen. Load support and leakage from microasperity - Lubricated face seals. *ASME Journal of Basic Engineering*, 9 (4):726 – 731, 1969.
- [176] I. Etsion and L. Burstein. A model of mechanical seals with regular micro-surface structure. *Tribology Transactions*, 39:677 – 683, 1996.
- [177] A. Wennerberg, T. Albrektsson, C. Johansson, and B. Andersson. Experimental study of turned and grit-blasted screw-shaped implants with special emphasis on effects of blasting material and surface topography. *Biomaterials*, 17:15 – 22, 1996.
- [178] R. Bathomarco, G. Solorzano, C. Elias, and R. Prioli. Atomic force microscopy analysis of different surface treatments of Ti dental implant surfaces. *Applied Surface Science*, 233:29 – 34, 2004.
- [179] U. Pettersson and S. Jacobson. Influence of surface texture on boundary lubricated sliding contacts. *Tribol. Int.*, 36 (11):857 – 864, 2003.
- [180] C. Madore, O. Piotrowski, and D. Landolt. Through-mask electrochemical micro-machining of titanium. *Journal of Electrochemical Society*, 146:2526 – 2532, 1999.

- [181] M. Wakuda, Y. Yamauchi, S. Kanzaki, and Y. Yasuda. Effect of surface texturing on friction reduction between ceramic and steel materials under lubricated sliding contact. *Wear*, 253:356 – 363, 2003.
- [182] A. Gaggl, G. Schultes, W. Muller, and H. Karcher. Scanning electron microscopical analysis of laser-treated titanium implant surface - A comparative study. *Biomaterials*, 21:1067 – 1073, 2000.
- [183] A.A. Voevodin and J.S. Zabinski. Laser surface texturing for adaptive solid lubrication. *Wear*, 261:1285 – 1292, 2006.
- [184] H. Ogawa, S. Sasaki, A. Korenaga, K. Miyake, M. Nakano, and T. Murakami. Effects of surface texture size on the tribological properties of slides. *J. Engineering Tribology Proc. IMechE*, 224:885–890, 2010.
- [185] Andriy Kovalchenko, Oyelayo Ajayi, Ali Erdemir, and George Fenske. The effect of laser texturing of steel surfaces and speed-load parameters on the transition of lubrication regime from boundary to hydrodynamic. *Tribology Transactions*, 47:299 – 307, 2004.
- [186] Andriy Kovalchenko, Oyelayo Ajayi, Ali Erdemir, George Fenske, and Izhak Etsion. The effect of laser surface texturing on transitions in lubrication regimes during unidirectional sliding contact. *Tribology International*, 38:219 – 225, 2005.
- [187] Andriy Kovalchenko, Oyelayo Ajayi, Ali Erdemir, and George Fenske. Friction and wear behavior of laser textured surface under lubricated initial point contact. *Wear*, 271:1719–1725, 2011.
- [188] C. Chouquet, J. Gavillet, C. Ducros, and F. Sanchette. Effect of DLC surface texturing on friction and wear during lubricated sliding. *Material Chemistry and Physics*, 123:367–371, 2010.
- [189] Perrite. *ABS 35 material datasheet*. Perrite, 2012.
- [190] W. M. Riggs, C.D. Wagner, L. E. Davis, and J. F. Moulder. *Handbook of x-ray photoelectron spectroscopy*. Perkin-Elmer Corporation, Physical Electronics Division, Minnesota, 1979.

- [191] B.R.K. Blackman, A.J. Kiloch, and J.F. Watts. The plasma treatment of thermoplastic fibre composites for adhesive bonding. *Composite*, 25 (5):332–341, 1994.
- [192] Keyence. *Sensors vision: Measurement and microscopes - VHX-500F light microscope*. Keyence, 2011.
- [193] F. Korte, J. Serbin, J. Koch, A. Egbert, C. Fallnich, A. Ostendorf, and B.N. Chichkov. Towards nanostructuring with femtosecond laser pulses. *Appl. Phys. A*, 77:229–235, 2003.
- [194] P.T. Mannion, J. Magee, E. Coyne, G.M. O’Connor, and T.J. Glynn. The effect of damage accumulation behavior on ablation threshold and damage morphology in ultrafast laser micro-machining of common metals in air. *Applied Surface Science*, 233:275–287, 2004.
- [195] A. Semerok, C. Chaleard, V. Detalle, J.L. Lacour, P. Mauchin, P. Meynadier, C. Nouvellon, B. Salle, P. Palianov, M. Pedrix, and G. Petite. Experimental investigations of laser ablation efficiency of pure metals with femto, pico and nanosecond pulses. *Appl. Surf. Sci.*, 138-139:311–314, 1999.
- [196] S. Kuper and M. Stuke. Ablation of polytetrafluoroethylene (Teflon) with femtosecond UV excimer laser pulses. *Appl. Phys. Lett.*, 54:4–6, 1989.
- [197] S.V. Babu, G.C. D’Couto, and F.D. Egitto. Excimer laser induced ablation of polyetheretherketone, polyimide and polytetrafluoroethylene. *J. Appl. Phys.*, 72:692–698, 1992.
- [198] S. Ruotsalainen, P. Laakso, R. Penttil, and H. Pantsar. Picosecond laser processing - Material removal rates of plastics. *Proceedings of the 11th NOLAMP Conference*, 2007.
- [199] Ishan Saxena, Kornel Ehmann, and Jian Cao. A comparative study of laser induced plasma micro-machining and laser ablation of low melting point. *9th International Workshop on Microfactories, Honolulu, USA*, 2014.

- [200] Erol Sancaktar and Hui Lu. The effects of excimer laser irradiation at 248 nm on the surface mass loss and thermal properties of PS, ABS, PA6, and PC polymers. *Journal of Applied Polymer Science*, 99:1024–1037, 2006.
- [201] M.K. Wei and H. Yang. Cumulative heat effect in excimer laser ablation of polymer PC and ABS. *Int. J. Adv. Manuf. Technol.*, 21:1029–1034, 2003.
- [202] S. Preuss, E. Matthias, and M. Stuke. Sub-picosecond UV-laser ablation of Ni films. *Appl. Phys. A*, 59 (1):79–82, 1994.
- [203] B.C. Stuart, M.D. Feit, S. Herman, A.M. Rubenchik, B.W. Shore, and M.D. Perry. Nanosecond-to-femtosecond laser-induced breakdown in dielectrics. *Phys. Rev. B*, 53 (4):1749–1761, 1996.
- [204] J. Gudde, J. Hohlfeld, J.G. Muller, and E. Matthias. Damage threshold dependence on electron-phonon coupling in Au and Ni films. *Applied Surface Science*, 127-129:40–45, 1998.
- [205] M. Lenzner, J. Kruger, W. Kautek, and F. Krausz. Precision laser ablation of dielectrics in the 10 fs regime. *Appl. Phys. A*, 68 (3):369–371, 1999.
- [206] S.S. Wellershoff, J. Hohlfeld, J. Gudde, and E. Matthias. The role of electron-phonon coupling in femtosecond laser damage of metals. *Appl. Phys. A*, 69:99–107, 1999.
- [207] S. Baudach, J. Bonse, and W. Kautek. Ablation experiments on polyimide with femtosecond laser pulses. *Appl. Phys. A: Materials Science and Processing*, 69:395–398, 1999.
- [208] F. Beinhorn, J. Ihlemann, K. Luther, and J. Troe. Plasma effects in picosecond-femtosecond UV laser ablation of polymers. *Appl. Phys. A*, 79:869–873, 2004.
- [209] S. Kuper and M. Stuke. Femtosecond UV excimer laser ablation. *Appl. Phys. B: Photo-Physics and Laser Chemistry*, 44:199–204, 1987.



- [210] R. Srinivasan, E. Sutcliffe, and B. Braren. Ablation and etching of polymethylmethacrylate by very short (160 *fs*) ultraviolet (308 *nm*) laser pulses. *Appl. Phys. Lett.*, 51:1285–1287, 1987.
- [211] Carmela De Marco, Shane M. Eaton, Rafaella Suriano, Stefano Turi, Marinella Levi, Roberta Ramponi, Giulio Cerullo, and Roberto Osellame. Surface properties of femtosecond laser ablated PMMA. *Applied Materials and Interfaces*, 2 (8):2377–2384, 2010.
- [212] X. Liu, X. Chen, W.T. Lotshaw, and A.C. Tien. Elimination of recast laser and microcracking in laser machining with femtosecond pulses. *Lasers and Electro-Optics*, 11:162, 1997.
- [213] Friedrich Dausinger. Femtosecond technology for precision manufacturing: Fundamental and technical aspects. *Third international symposium on laser precision microfabrication*, 4830:471–478, 2003.
- [214] J. Liu. Simple technique for measurements of pulsed gaussian-beam spot sizes. *Optics Letters*, 7 (5):196–198, 1982.
- [215] D.R. Lide. *CRC handbook of chemistry and physics, 71th edition*. Boca Raton: CRC Press, 1990.
- [216] Denise J.D. Moyer and J.P. Wightman. Characterization of surface pre-treatments of carbon fibre-polyimide matrix composites. *Surface and Interface Analysis*, 14:496–504, 1989.
- [217] Jong Min Kim, Jin Kook Kim, and Dai Gil Lee. Ultraviolet surface treatment for adhesion strength improvement of carbon/epoxy composite. *J. Adhesion Sci. Technol.*, 17(11):1523–1542, 2003.
- [218] Lino Ferreira, Marta B. Evangelista, M Cristina L. Martins, Pedro L. Granja, Jose L. Esteves, and Mario A. Barbosa. Improving the adhesion of poly(ethylene terephthalate) fibers to poly(hydroxyethyl methacrylate) hydrogels by ozone treatment: Surface characterization and pull-out tests. *Polymer*, 46:9840–9850, 2005.

- [219] Qi Song and Anil N. Netravali. Excimer laser surface modification of ultra-high-strength polyethylene fibers for enhanced adhesion with epoxy resins. part 1. effect of laser operating parameters. *J. Adhesion Sci. Technol.*, 12(9):957–982, 1998.
- [220] Firas Awaja and Paul J. Pigram. Surface molecular characterisation of different epoxy resin composites subjected to UV accelerated degradation using xps and tof-sims. *Polymer Degradation and Stability*, 94:651–658, 2009.
- [221] E.M. Liston, L. Martinu, and M.R. Wertheimer. Plasma surface modification of polymers for improved adhesion: A critical review. *J. Adhesion Sci. Technol.*, 7 (10):1091–1127, 1993.
- [222] N. Kroll and K.M. Watson. Theoretical study of ionization of air by intense laser pulses. *Phys. Rev. A. Gen. Phys.*, 5 (4):1179–1188, 1972.
- [223] Y.P. Raizer. *Gas discharge physics*. Springer-Verlag, Berlin Germany, 1991.
- [224] R. Adelgren, G. Elliott, D. Knight, A. Zheltovodov, and T.J. Beutner. Energy deposition in supersonic flows. *AIAA Paper*, page 0885, 2001.
- [225] P. Nelson, P. Veyrie, M. Berry, and Y. Durand. Experimental and theoretical studies of air breakdown by intense pulse of light. *Phys. Lett.*, 13:226–228, 1964.
- [226] I.P. Shkarofsky. Review of gas-breakdown phenomena induced by high power lasers. I. *RCA Rev.*, 35:48–78, 1974.
- [227] G. Bekefi. *Principles of laser plasmas*. Wiley, New York, 1976.
- [228] C.H. Chan, C.D. Moody, and W.B. McKnight. Significant loss mechanisms in gas breakdown at 10.6  $\mu$ . *J. App. Phys.*, 44 (3):1179–1188, 1973.
- [229] Magesh Thiagarajan. Experimental investigation of 193 nm laser breakdown in air. *IEEE Trans. Plasm. Sci.*, 36 (5):2512–2521, 2008.

- [230] Carlos A. Aguilar, Yi Lu, Samuel Mao, and Shaochen Chen. Direct micro-patterning of biodegradable polymers using ultraviolet and femtosecond lasers. *Biomaterials*, 26:7642–7649, 2005.
- [231] A.A. Serafetinides, C.D. Skordoulis, M.I. Makropoulou, and A.K. Kar. Picosecond and subpicosecond visible laser ablation of optically transparent polymers. *Appl. Surf. Sci.*, 135:276–282, 1998.
- [232] Z. Wang, M. Hong, Y. Lu, D. Wu, B. Lan, and T. Chong. Femtosecond laser ablation of polytetrafluoroethylene (Teflon) in ambient air. *J. Appl. Phys.*, 93 (10):6375–6380, 2003.
- [233] R. Sauerbrey and G.H. Petti. Theory for the etching of organic materials by ultraviolet laser pulses. *Appl. Phys. Lett.*, 55:421–423, 1989.
- [234] G.H. Pettit and R. Sauerbrey. Pulsed ultraviolet laser ablation. *Appl. Phys. A*, 56:51–63, 1993.
- [235] H.S. Cole, Y.S. Liu, and H.R. Philipp. Dependence of photoetching rates of polymers at 193 nm on optical absorption depth. *Appl. Phys. Lett.*, 48:76–77, 1986.
- [236] J.H. Brannon, J.R. Lankard, A.I. Baise, F. Burns, and J. Kaufman. Excimer laser etching of polyimide. *J. Appl. Phys.*, 58:2036–2043, 1985.
- [237] S. Baudach, J. Bonse, J. Kurger, and W. Kautek. Ultrashort pulse laser ablation of polycarbonate and polymethylmethacrylate. *Appl. Surf. Sci.*, 154-155:555–560, 2000.
- [238] Juana Abenojar, Rafael Torregrosa-Coque, Miguel Angel Martnez, and Jos Miguel Martn-Martnez. Surface modifications of polycarbonate (PC) and acrylonitrile butadiene styrene (ABS). *Surface & Coatings Technology*, 203:2173–2180, 2009.
- [239] Xuejiao Tang, Meng Cao, Chengliang Bi, Lijuan Yan, and Baogui Zhang. Research on a new surface activation process for electroless plating. *Materials Letters*, 62:1089–1091, 2008.

- [240] Firas Awaja, Michael Gilbert, Georgina Kelly, Bronwyn Fox, and Paul J. Pigram. Adhesion of polymer. *Progress in Polymer Science*, 34:948–968, 2009.
- [241] Lingfei Ji, Lin Li, Hugh Devlin, Zhu Liu, Jiao Jiao, and David Whitehead. Ti:sapphire femtosecond laser ablation of dental enamel, dentine and cementum. *Lasers Med. Sci.*, 27:197–204, 2012.
- [242] W. Kautek, S. Mitterer, J. Kruger, W. Husinsky, and G. Grabner. Femtosecond-pulsed laser ablation of human corneas. *Appl. Phys. A*, 58:513–518, 1994.
- [243] J. Guillet. *Polymer photophysics ad photochemistry. An introduction to the study of photoprocess in macromolecules*. Cambridge University Press, Cambridge, UK, 1985.
- [244] R. BerndKeller, W.N. Su, and P. Eyerer. Temperature dependent optical properties of polymers as a basis for laser process modeling.
- [245] Thomas Lippert. Laser application of polymers. *Adv Polym Sci*, 168:51–246, 2004.
- [246] T. Lippert, L.S. Bennett, T. Nakamura, H. Niino, A. Ouchi, and A. Yabe. Comparison of the transmission behavior of a triazeno-polymer with a theoretical model. *Applied Physics A*, 63 (3):257–265, 1996.
- [247] H. Furutani, H. Fukumura, H. Masuhara, T. Lippert, and A. Yabe. Laser-induced decomposition and ablation dynamics studied by nanosecond interferometry. 1. A triazenopolymer film. *The Journal of Physical Chemistry A*, 101 (32):5742–5747, 1997.
- [248] Martin K. Beyer and Hauke Clausen-Schaumann. Mechanochemistry: The mechanical activation of covalent bonds. *Chemical Reviews*, 105 (8):2921–2948, 2005.
- [249] J. Lawrence and L. Li. Modification of the wettability characteristics of polymethyl methacrylate (PMMA) by means of  $CO_2$ , Nd: YAG, excimer

- and high power diode laser radiation. *Material Science and Engineering: A*, 303 (1-2):142–149, 2001.
- [250] H.J. Busscher, A.W.J. van Pelt, P. de Boer, H.P. de Jong, and J. Arends. The effect of surface roughening of polymers on measured contact angles of liquids. *Colloids and Surfaces*, 9 (4):319331, 1984.
  - [251] Y.Luo, S.G. Luckey, W.B. Copple, and P.A. Friedman. Comparison of advance SPF die technologies in the forming of a production panel. *Journal of Materials Engineering and Performance*, 17(2):142 – 152, 2008.
  - [252] Paul E. Krajewski and Arianna T. Morales. Tribological issues during quick plastic forming. *Journal of Materials Engineering and Performance*, 13(6):700 – 709, 2004.
  - [253] E.S. Nachman and S. Kalpakjian. *Lubricants and lubrication in metal working operations*. New York : Marcel Dekker, 1985.
  - [254] J.A. Schey. *Tribology in metalworking: Fiction, lubrication and wear*. Metals Park, OH : American Society for Metals, 1983.
  - [255] L. Lazzarotto, L. Dubar, A. Dubois, P. Ravassard, J.P. Bricout, and J. Oudin. A selection methodology for lubricating oils in cold metal forming process. *Wear*, 215:1 – 9, 1998.
  - [256] Lidia Galda, Pawel Pawlus, and Jaroslaw Sep. Dimples shape and distribution effect on characteristics of stribeck curve. *Tribology International*, 42:1505–1512, 2009.
  - [257] L. Mouriera, D. Mazuyer, A.A. Lubrecht, and C. Donnet. Transient increase of film thickness in micro-textured EHL contacts. *Tribol. Int.*, 39 (12):1745–1756, 2006.
  - [258] I. Krupka and M. Hartl. The effect of surface texturing on thin EHD lubrication films. *Tribology International*, 40:1100–1110, 2007.
  - [259] Elmar Achenbach. On particle adhesion and removal mechanisms inturbulent flows. *J. Fluid Mech.*, 65 (1):113–125, 1974.

- [260] Ronald H. Radeztsky Jr., Mark S. Reibert, and William S. Saric. On particle adhesion and removal mechanisms in turbulent flows. *AIAA Journal*, 37 (11):1370–1377, 1999.